



TECHNISCHE
UNIVERSITÄT
DARMSTADT

THE IN-MEDIUM SIMILARITY RENORMALIZATION GROUP
FOR *AB INITIO* NUCLEAR STRUCTURE:
METHOD ADVANCES AND NEW APPLICATIONS

**Vom Fachbereich Physik
der Technischen Universität Darmstadt**

zur Erlangung des Grades
eines Doktors der Naturwissenschaften (Dr. rer. nat.)

**genehmigte Dissertation von
Jan Lucas Hoppe, M.Sc.
geboren in Offenbach am Main**

Referent: Prof. Achim Schwenk, Ph.D.
Korreferent: Priv.-Doz. Dr. Kai Hebeler

Tag der Einreichung: 09.05.2022

Tag der Prüfung: 20.06.2022

Darmstadt 2022

D17

The in-medium similarity renormalization group for *ab initio* nuclear structure:
method advances and new applications

Die In-Medium Similarity Renormalization Group für die *ab initio* Kernstrukturphysik:
Methodenentwicklung und neue Anwendungen

Genehmigte Dissertation von Jan Lucas Hoppe, M.Sc. geboren in Offenbach am Main
Darmstadt, Technische Universität Darmstadt

Referent: Prof. Achim Schwenk, Ph.D.

Korreferent: Priv.-Doz. Dr. Kai Hebeler

Tag der Einreichung: 09.05.2022

Tag der Prüfung: 20.06.2022

Jahr der Veröffentlichung der Dissertation auf TUpriints: 2022

Darmstadt 2022 - D17

Bitte zitieren Sie dieses Dokument als:

URN: urn:nbn:de:tuda-tuprints-215761

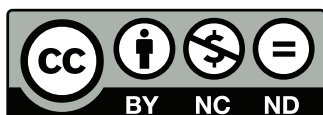
URL: <https://tuprints.ulb.tu-darmstadt.de/id/eprint/21576>

Dieses Dokument wird bereitgestellt von tuprints,

E-Publishing-Service der TU Darmstadt

<http://tuprints.ulb.tu-darmstadt.de/>

tuprints@ulb.tu-darmstadt.de



Die Veröffentlichung steht unter folgender Creative Commons Lizenz:

CC BY-NC-ND 4.0 International - Attribution, NonCommercial, NoDerivatives

<https://creativecommons.org/licenses/by-nc-nd/4.0/>

Abstract

Over the past two decades, *ab initio* nuclear structure calculations of atomic nuclei have seen major advances. The use of systematically improvable methods with controlled truncations has enabled studies over a large range of mass numbers and for a diverse set of nuclear observables. These developments were mainly driven by wave-function expansion methods that are based on a many-body expansion around a reference state, while admitting a mild computational scaling in mass number. However, substantial increases in computational cost and memory requirements when describing heavier and more exotic nuclei or when aiming at more precise predictions still present severe challenges in *ab initio* theory.

In this thesis, we address these challenges and present promising approaches that allow to extend current frontiers and enable converged *ab initio* calculations for higher mass numbers and with increased precision. We study light, medium-mass, and heavy closed-shell nuclei within the in-medium similarity renormalization group (IMSRG) using two- and three-body interactions derived within the framework of chiral effective field theory.

In particular, we investigate optimizations of the reference state using the natural orbital basis, employ importance-truncation techniques to compress many-body operators, and apply a new normal-ordering framework that allows to circumvent standard truncations when including three-nucleon interactions. The natural orbital basis, defined as the eigenbasis of a perturbatively improved one-body density matrix, is explored in detail. Significant benefits in many-body calculations are obtained using truncated natural orbitals that are constructed in a large space and applied in a reduced space for the many-body solution. This approach results in faster model-space convergence and frequency-independent ground-state observables. Furthermore, we demonstrate how importance-truncation techniques can be applied in the IMSRG to compress many-body operators and to substantially reduce the memory requirements. Considering only the most important contributions of the two-body operators, a major part of the matrix elements can be neglected while introducing only minor errors in medium-mass nuclei. Both advances using natural orbitals and importance-truncation techniques are also of great interest for relaxing the presently established many-body truncation in the IMSRG approach, which is currently prohibitive beyond small model spaces due to the tremendous increase in computational costs.

The explicit inclusion of three-body operators provides additional computational challenges for *ab initio* calculations. Standard normal-ordering applications to approximate three-body interactions typically necessitate a truncation on the number of three-body matrix elements, which becomes significant for calculations of heavy nuclei. The novel normal-ordering framework in this thesis avoids this truncation and requires substantially less memory by performing the normal ordering directly in the Jacobi basis. We systematically study the convergence behavior and explore benefits of the new framework for light up to heavy nuclei, especially targeting ^{132}Sn and ^{208}Pb .

These developments open new ways for extending first-principle calculations of atomic nuclei to heavier and more exotic systems over the whole range of the nuclear chart.

Zusammenfassung

Die In-Medium Similarity Renormalization Group für die ab initio Kernstrukturphysik: Methodenentwicklung und neue Anwendungen

Im Laufe der letzten zwei Jahrzehnte haben *ab initio* Berechnungen von Atomkernen in der Kernstrukturphysik erhebliche Fortschritte gemacht. Vor allem die Verwendung von systematisch verbesserbaren Methoden mit kontrollierten Approximationen ermöglicht Untersuchungen über einen großen Bereich der Nuklidkarte. Vorangetrieben wurden diese Entwicklungen hauptsächlich durch Näherungsverfahren, welche auf einer Vielteilchenentwicklung um einen Referenzzustand beruhen. Jedoch stellen signifikant ansteigende Rechenzeiten und Speicheranforderungen für die systematische theoretische Beschreibung von schwereren und exotischeren Kernen nach wie vor eine große Herausforderung in der Kernstrukturphysik dar.

Die vorliegende Dissertation befasst sich mit diesen Herausforderungen und konzentriert sich im Besonderen auf die Verbesserung und Beschleunigung von Vielteilchenrechnungen. Wir stellen vielversprechende Ansätze vor, die es erlauben, derzeitige Grenzen zu erweitern und konvergierte *ab initio* Berechnungen für höhere Massenzahlen sowie mit verbesserter Genauigkeit zu ermöglichen. Hierzu untersuchen wir leichte bis schwere Kerne mit abgeschlossenen Schalen innerhalb der In-Medium Similarity Renormalization Group (IMSRG) unter Verwendung von chiralen Zwei- und Dreiteilchenwechselwirkungen.

Insbesondere untersuchen wir Optimierungen des Referenzzustands unter Verwendung der natürlichen Orbitalbasis und Anwendung von Importance-Trunkierungstechniken zur Komprimierung von Vielteilchenoperatoren. Die natürliche Orbitalbasis, welche als Eigenbasis einer störungstheoretisch verbesserten Einteilchendichtematrix definiert ist, wird im Detail erforscht. Die Verwendung trunkierter natürlicher Orbitale, konstruiert in einem großen Modellraum, angewendet in einem reduzierten Modellraum, führt zu einer verbesserten Modellraumkonvergenz sowie zu frequenzunabhängigen Grundzustandsobservablen. Darüber hinaus zeigen wir, wie Importance-Trunkierungstechniken in der IMSRG angewendet werden können, um den Speicherbedarf erheblich zu reduzieren. Berücksichtigt man nur die wichtigsten Beiträge der Zweiteilchenoperatoren, kann ein Großteil der Matrixelemente vernachlässigt werden, was zu lediglich geringen Fehlern für mittelschwere Kerne führt. Sowohl die Fortschritte basierend auf der natürlichen Orbitalbasis, als auch die Importance-Trunkierungsmethoden stellen vielversprechende Methoden dar, um die gegenwärtig etablierte Vieleilchentrukkierung in der IMSRG zu verbessern, welche derzeit aufgrund des enormen Anstiegs des Rechenaufwands auf kleine Modellräume beschränkt ist. Die explizite Einbeziehung von Dreiteilchenoperatoren stellt zusätzliche rechnerische Herausforderungen für *ab initio* Berechnungen dar. Standard Normalordnungsmethoden erfordern üblicherweise eine Begrenzung der Anzahl von Dreiteilchenmatrixelementen, was einen erheblichen Einfluss bei Berechnungen von schweren Kernen haben kann. Wir stellen eine neue Normalordnungsmethode in der Jacobibasis vor, welche diese Trunkierung vermeidet, wesentlich weniger Speicherplatz benötigt und studieren Vorteile für leichte bis schwere Kerne, insbesondere für ^{132}Sn und ^{208}Pb .

Die in dieser Arbeit vorgestellten Entwicklungen eröffnen neue Wege zur Erweiterung und Verbesserung der Grundlagenrechnungen von Atomkernen, besonders hinsichtlich schwererer und exotischerer Systeme.

Contents

1	Introduction	1
1.1	Low-energy nuclear physics	1
1.2	<i>Ab initio</i> nuclear structure theory	2
1.3	Status and frontiers of <i>ab initio</i> nuclear structure	5
1.4	Scope of this thesis	11
2	Nuclear Forces and Chiral Effective Field Theory	13
2.1	Quantum chromodynamics	14
2.2	Chiral effective field theory	17
2.2.1	Formalism and hierarchy of nuclear forces	17
2.2.2	Construction of nuclear interactions	21
2.3	Renormalization group methods	25
2.4	Singular value decomposition	28
3	In-Medium Similarity Renormalization Group	33
3.1	Second quantization and normal ordering	34
3.2	Hartree-Fock method	38
3.3	Selected many-body approaches	43
3.3.1	No-core shell model	44
3.3.2	Coupled cluster theory	45
3.3.3	Many-body perturbation theory	47
3.4	IMSRG approach	51
3.4.1	Generator choices	55
3.4.2	Angular-momentum-coupled flow equations	57
3.4.3	General operators and charge radii in the IMSRG	58
3.4.4	Magnus approach	60
3.5	IMSRG with three-body operators	62
3.5.1	Approximate IMSRG(3) truncation schemes	67
3.6	Applications of low-rank potentials in the IMSRG	70
4	Natural Orbital Basis	73
4.1	Single-particle basis and basis optimization	74
4.1.1	Natural orbital basis	75
4.1.2	Perturbatively improved density matrix	76
4.1.3	Basis transformation	78
4.1.4	Intrinsic kinetic energy	79
4.1.5	Normal ordering in the NAT basis	80
4.1.6	Single-reference case	81

4.2	Diagnostics for the density matrix	82
4.2.1	“Softness” of the interaction	82
4.2.2	Single-particle wave functions	83
4.2.3	Positive definiteness as diagnostic tool	84
4.3	Natural orbital basis in the IMSRG	85
4.3.1	Differences between NCSM and IMSRG	87
4.3.2	Reduced-basis calculations from NAT/HF constructed in full space . .	88
4.4	Exploration of Skyrme EDF basis sets	90
4.5	Systematic study of IMSRG(3) truncations	93
4.5.1	Application to ${}^4\text{He}$ and ${}^{16}\text{O}$	94
4.5.2	Analysis of truncation performance	97
5	Importance Truncation	99
5.1	Basic principle	100
5.1.1	Perturbative analysis	101
5.2	Application to the IMSRG	102
5.2.1	Interaction blocks	104
5.2.2	Definition of importance measures	106
5.2.3	Perturbative treatment of truncated Hamiltonian	108
5.3	Medium-mass applications	109
5.3.1	Interaction sensitivity	111
5.3.2	Mass number sensitivity	113
5.3.3	First computational investigations	114
6	Normal Ordering in the Jacobi Basis	115
6.1	Normal ordering in plane-wave Jacobi basis	117
6.1.1	Transformation to Jacobi HO basis	122
6.1.2	Transformation to single-particle basis	123
6.2	Truncation benchmark for light nuclei	125
6.2.1	Matrix-element comparison	125
6.2.2	Ground-state properties	126
6.3	Application to heavy systems	127
6.3.1	Charge radii	131
7	Summary and Outlook	133
	List of Abbreviations	137

1

Introduction

1.1 *Low-energy nuclear physics*

Understanding how atomic nuclei are bound and how their constituents compound matter is the main endeavor of modern nuclear physics. The challenging task of describing the fundamental force of strong interaction among protons and neutrons is therefore one of the central goals of theoretical nuclear physics. As a result, nuclear theory calculations aim for the description of a large variety of systems, ranging from a small system consisting of only two bound particles, over light, medium-mass, and heavy nuclei up to stellar objects with extreme conditions, such as neutron stars. In particular, nuclear structure calculations for a variety of observables, e.g., ground- and excited-state properties, charge radii, or electromagnetic observables can be compared to experimental results, where available, and allow for a comprehensive check of the theory. Furthermore, theoretical predictions for cases presently still outside the reach of experiments are key for astrophysics and guide future experimental efforts.

Approximately 3300 bound nuclei are experimentally known today [1, 2]. The nuclear chart displays these nuclei characterized by their proton number Z and neutron number N , with the proton and neutron drip lines determining the limits of bound nuclei on the top and bottom of the nuclear chart, respectively. These limits are defined as the one- or two-proton and one- or two-neutron separation energy becoming negative and consequently prohibiting the existence of bound nuclei beyond the drip lines (see Fig. 1.4 for a subset of the nuclear chart). Theoretical calculations predict the existence of about 7000-9000 nuclei, depending on if continuum effects are included in the description or not [1, 3]. This highlights the importance of reliable nuclear theory predictions, especially towards the (neutron) drip line and higher mass numbers, where a large part of the nuclear chart is still unknown.

Systematically improvable *ab initio* methods with controlled approximations provide a promising and powerful tool to drive progress towards these directions by performing nuclear structure calculations with predictive power and an assessment of theory uncertainties.

In addition to nuclear structure, nuclear reaction theory and studying how nuclei react in different decay and reaction processes provides an essential aspect of the field of nuclear theory. For example studies of the formation of heavy elements in the nucleosynthesis is an important part of our understanding of the evolution of stars and formation of neutron stars.

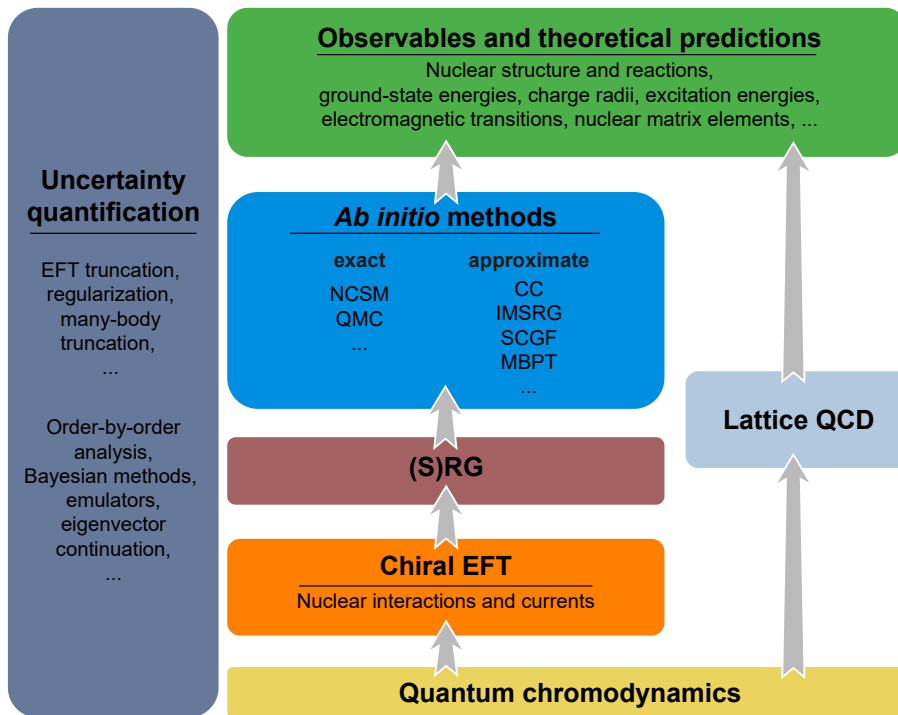


Figure 1.1: Workflow towards the calculation of nuclear observables and theoretical predictions starting from the underlying theory of QCD. The right path shows the direct application of lattice QCD methods, which is currently still limited to very small mass numbers. The left path shows the strategy pursued in this thesis: Nuclear interactions that are derived within chiral EFT and possibly softened by a subsequent SRG evolution provide the input for various exact and approximate *ab initio* many-body methods to solve the nuclear many-body problem and calculate observables (see text for details). We emphasize that the many-body methods on the right-hand side of the blue box in general are also exact and we here refer to their approximate counterparts within a given truncation scheme. The leftmost panel indicates the importance of uncertainty quantification and systematic estimates of the errors introduced by truncations and approximations of the theory and the many-body method. Figure adapted from Ref. [4].

1.2 *Ab initio* nuclear structure theory

In order to describe the structure and properties of finite nuclei, the nonrelativistic many-body Schrödinger equation for an A -body system is solved, requiring two ingredients: a nuclear potential describing the interaction among the constituent protons and neutrons, also referred to as nucleons; and a framework to numerically solve the resulting equation. Figure 1.1 summarizes the general idea of *ab initio* calculations, starting from the underlying theory of the strong interaction, quantum chromodynamics (QCD), and displays two possible paths to arrive at predictions for nuclear observables, which are discussed in more detail in the following. This thesis follows the left path with a particular emphasis on developments and applications of the many-body method to calculate nuclear observables, displayed by the blue box in Fig. 1.1.

Even though in low-energy nuclear theory we mainly focus on protons and neutrons, as being the constituents which compound nuclei, the nucleons themselves are composite

particles consisting of quarks, which are fundamental spin-1/2 particles. The fundamental force of the strong interaction between quarks mediated by gluons is described by QCD. It has two key properties: the asymptotic freedom for very large energies on the one hand, caused by the coupling constant approaching zero for high-energy scales; and the rapid growth of the coupling constant for low energies on the other hand, causing the quarks to be confined in color-neutral objects, called mesons and baryons, consisting of two and three quarks, respectively. The large coupling constant at the low-energy regime, where nuclear structure theory is situated, significantly complicates a direct description based on the fundamental theory and makes the application of any perturbative approaches unfeasible.

Approaches to directly solving nuclear theory problems from the underlying theory QCD, following the right path in Fig. 1.1, are of course desirable and in practice realized by discretizing space and time on a four-dimensional grid in lattice QCD calculations [5]. However, the tremendous computational demands for such calculations currently limit their applicability to single mesons, baryons, or very light nuclei [6–8]. Therefore, calculations for a wide range of nuclei directly based on the underlying theory are still not feasible at present.

These problems can be remedied by the formulation of a low-energy effective theory of QCD, which is directly connected to the fundamental theory. In this thesis, we specifically focus on chiral effective field theory (EFT), the orange box in Fig. 1.1. Chiral EFT is a low-energy effective theory, based on the pioneering works of Weinberg in the 1990s [9–11], that is consistent with the symmetries of QCD, in particular the spontaneously and explicitly broken chiral symmetry. The effective degrees of freedom at low energies of chiral EFT are nucleons and pions instead of the fundamental degrees of freedom of QCD, quarks and gluons. While the low-energy details are described explicitly, the high-energy physics are not resolved by the theory and enter the description by so called low-energy constants (LEC) that are fitted to experiment. In recent years, chiral EFT has become the dominant approach for deriving nuclear interactions that are based on the underlying theory and can be constructed in a systematically improvable way, with many-body forces entering naturally [12]. Interaction models based on phenomenological approaches, such as the Nijmegen [13], Argonne v_{18} [14], or CD-Bonn [15] potential, even though yielding a good description of experimental data, lack this clear connection to the underlying theory provided by chiral potentials and do not allow for consistent many-body potentials and currents. Commonly, (similarity) renormalization group [(S)RG] methods [16, 17] are used along with chiral interactions to obtain low-resolution Hamiltonians, which lead to faster model-space convergence in practical calculations or enable perturbative descriptions [18].

Multiple computational frameworks can be applied to numerically solve the many-body Schrödinger equation. The key idea behind *ab initio* many-body methods is to solve the A -body problem in a systematic expansion, where going to higher order of the many-body expansion in a given truncation scheme results in more precise calculations, and truncations at a finite order allow for uncertainty quantification. This approach enables one to perform calculations for nuclear observables and make theoretical predictions with predictive power by using just few-body input to describe the many-body system, most commonly employing chiral nucleon-nucleon (NN) and three-nucleon (3N) potentials with a clear connection to the underlying theory.

Generally speaking, we can distinguish two classes of many-body methods to solve the A -body Schrödinger equation (see the two columns in the blue box in Fig. 1.1): exact approaches that yield numerically exact results and scale exponentially in the mass number on the one

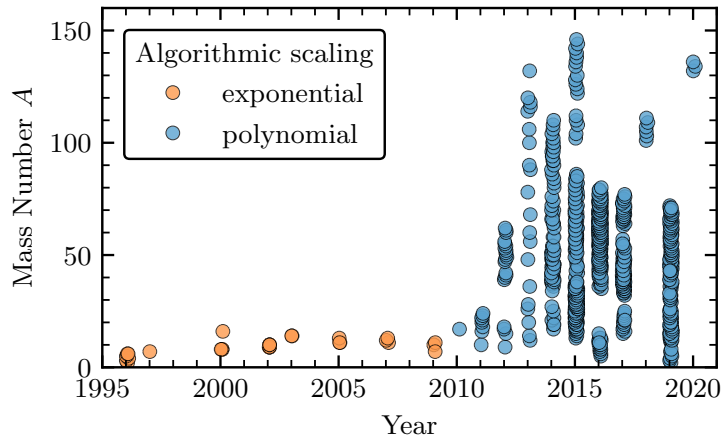


Figure 1.2: Accessible mass number A by *ab initio* methods with exponential (orange) and polynomial (blue) scaling from 1995 to 2020. Figure taken from Ref. [4] with data from Ref. [19].

hand; and approximate methods that perform a systematic correlation expansion around a chosen reference state with controlled approximations, resulting in a polynomial scaling with system size on the other hand.

Examples of exact methods with an exponential scaling in A are the no-core shell model (NCSM) [20–23], which directly diagonalizes the Hamiltonian in the space of configurations, or quantum Monte Carlo (QMC) calculations [24–27]. Examples for approximate methods that employ a given truncation scheme and therefore scale polynomially in A (at low truncation orders) are given by coupled-cluster (CC) theory [28, 29], the in-medium similarity renormalization group (IMSRG) [30–32], self-consistent Green’s function (SCGF) methods [33, 34], and many-body perturbation theory (MBPT) [18, 35–37]. Their difference in scaling behavior is highlighted in Fig. 1.2

The variety of different computational approaches to solve the A -body problem allows for a meaningful comparison between various *ab initio* many-body methods by calculating the same observable using identical input interactions and a range of mass numbers that can be targeted by all considered methods. The oxygen isotopic chain provides an ideal testbed for such benchmark calculations. By being a rather light system, it is accessible for exact and approximate methods and the existence of experimental data provides an additional possibility of comparison. In Fig. 1.3, ground-state energies of the oxygen isotopic chain are compared for a large set of many-body methods, showing the remarkable consistency between all methods as well as good agreement with experiment [19].

Quantifying uncertainties of nuclear theory calculations is an area of active research and constitutes an essential step towards more accurate predictions and calculations. These developments are leading nuclear theory into a precision era and allow for a meaningful comparison between experiment and theory within error bars. Systematic errors and approximations for both the chiral potential and the *ab initio* method arise by truncations at finite order in the chiral expansion, different fitting protocols as well as regulator characteristics in the construction of the interaction, and truncations in the many-body expansion. The systematically improvable approach of chiral EFT offers the possibility to estimate the uncertainty based on the discarded information at the next order in the order-by-order expansion [38]. Typically the EFT truncation error gives the most dominant contribution to the total uncertainty. More elaborate approaches use Bayesian methods for an improved uncertainty

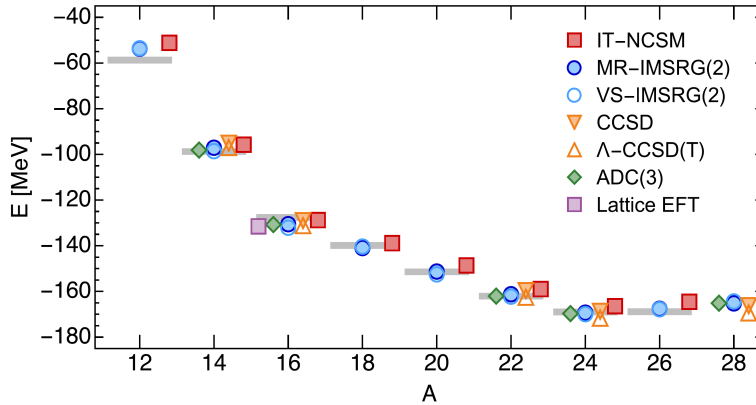


Figure 1.3: Ground-state energies of the oxygen isotopic chain, using the same consistently SRG-evolved chiral NN+3N input interaction [22, 46, 47] for all employed many-body methods. Results are shown for the importance-truncated NCSM (IT-NCSM), multi-reference (MR) and valence-space (VS) extensions of the IMSRG(2), CC with singles and doubles (CCSD), CC with approximate triples [Λ -CCSD(T)], the Algebraic Diagrammatic Construction [ADC(3)] within the SCGF method, and lattice EFT calculations. Additionally, the grey bars indicate experimental values from Ref. [48]. Figure taken from Ref. [19].

quantification [39–42] based on a statistical analysis. Recently, the use of emulators, e.g., eigenvector continuation [43], has shown to be a highly efficient and versatile tool to help with quantifying errors [44] and studying ground-state observables for a large parameter space of LEC combinations in a computationally inexpensive way [45].

1.3 Status and frontiers of *ab initio* nuclear structure

Over the last decade, computational methods for the *ab initio* solution of the nuclear many-body Schrödinger equation have witnessed major improvements, extending their reach of accessible closed- and open-shell nuclei over a wide range of mass numbers in the nuclear chart. The tremendous progress over the last ten years is summarized in Fig. 1.4, showing the reach of *ab initio* methods covering only light and selected medium-mass nuclei in 2010 (yellow), and improving up to mass numbers $A \approx 132$ accessible in 2020 (blue) [49, 50]. Very recently, even exploratory studies of heavier nuclei, such as ^{208}Pb came into reach [51]. These advances are mainly based on three aspects: the construction of improved high-precision chiral NN and 3N interactions together with the application of SRG techniques to evolve nuclear interactions to lower resolution scales, leading to improved accuracy and accelerated model-space convergence; the developments of wave-function expansion methods with a polynomial scaling in mass number; and the strong increase in computational resources, enabling larger memory and more computing power. In particular the difference in the scaling behavior was a key factor for extending the range of *ab initio* methods by overcoming the severe computational limitations for increased mass numbers and led to an explosion in the amount of accessible nuclei.

Nevertheless, multiple frontiers in *ab initio* theory remain. Improved chiral input Hamiltonians that lead to more consistent calculations for multiple observables over a large range of mass numbers need to be constructed. Additionally, developments for the many-body

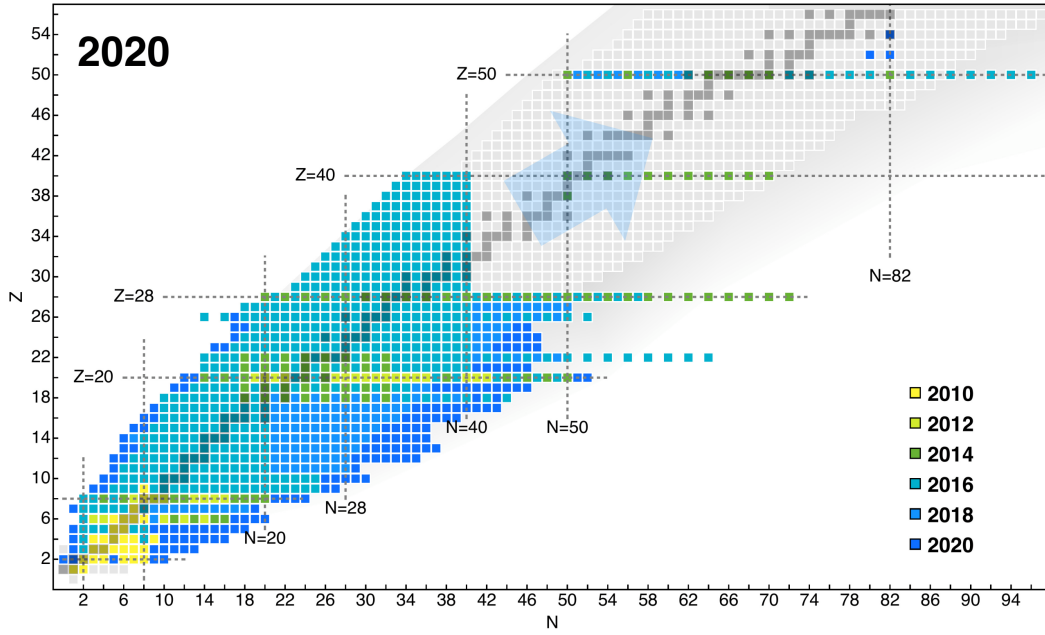


Figure 1.4: Nuclear chart with proton number Z and neutron number N on the y -, and x -axes, respectively. The colored boxes show the accessible mass numbers for *ab initio* nuclear structure calculations in the corresponding years over the last decade, from 2010 (yellow) to 2020 (blue). Dashed horizontal and vertical lines indicate good shell closures, referred to as magic numbers, based on the nuclear shell model for proton (neutron) numbers Z (N) = 2, 8, 20, 28, 40, 50, and 82. Figure taken from Ref. [19].

methods are required to extend their reach to heavier and more exotic systems and achieve theoretical predictions with higher precision. We highlight some of our current understanding on these issues in the following.

When moving to higher mass numbers, the consistency between different *ab initio* methods, observed for the oxygen isotopes in Fig. 1.3, remains unchanged, as can be seen for the calcium isotopic chain in Fig. 1.5. However, the predictions significantly deviate from experiment and show a strong overbinding for this particular outdated chiral interaction employed in Ref. [37]. Similar trends of overbinding ground-state energies and underestimating charge radii, can be observed for predictions of higher mass numbers and other chiral Hamiltonians. This signals that the reason for the mismatch of theory and experiment is not rooted in the choice of the specific many-body method but in the chiral potential. Interactions leading to good agreement with experimental data for one region, e.g., light or medium-mass nuclei typically fall short of reproducing heavy nuclei or infinite nuclear matter saturation properties, and vice versa [29, 37, 52, 53]. Nuclear matter is an idealized theoretical construct with an infinite number of nucleons in an infinite volume, where the density is uniform and Coulomb interactions are neglected. Depending on the fraction of protons, we distinguish infinite neutron matter, for a proton fraction of zero, and (symmetric) nuclear matter for equal proton and neutron densities. One exception of the characteristics mentioned above, is an interaction constructed in Ref. [54], often called the “magic” interaction, which leads to a remarkably good description of ground-state energies over a large range of mass numbers, from ${}^4\text{He}$ to ${}^{132}\text{Sn}$ [49, 50, 55], while simultaneously reproducing realistic saturation properties, despite only being fit to few-body data.

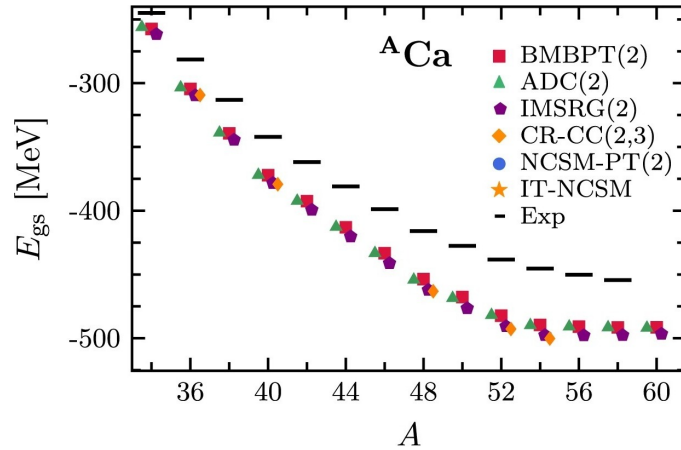


Figure 1.5: Ground-state energies for the calcium isotopic chain for different many-body methods, using the same interaction as in Fig. 1.3, compared to experimental (black bars). Results are shown for the Bogoliubov many-body perturbation theory up to second order (BMBPT(2)), the Algebraic Diagrammatic Construction within Gorkov SCGF theory (ADC(2)), IMSRG(2), closed-shell coupled cluster (CR-CC(2,3)), perturbatively-improved NCSM (NCSM-PT(2)), and the IT-NCSM. Figure adapted from Ref. [37].

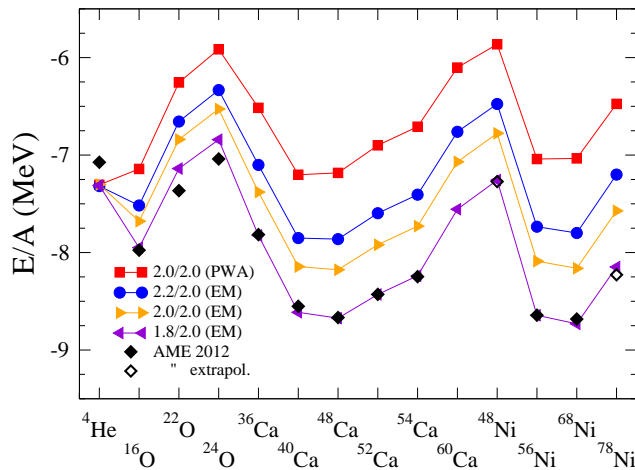


Figure 1.6: Ground-state energy per particle calculated in the IMSRG for selected closed-shell nuclei using four different Hamiltonians compared to experimental results. The purple curve corresponds to the “magic” 1.8/2.0 EM interaction. Figure taken from Ref. [55].

The good performance of this interaction can also be identified by the purple line in Fig. 1.6, nicely agreeing with experiment. However, the reason for the exceptional performance of this particular chiral interaction, which treats NN and 3N forces at inconsistent chiral orders, until now remains an open question. A detailed study of the Hamiltonians, constructed in Ref. [54], and their predictions for finite nuclei was performed in Ref. [55] and is shown in Fig. 1.6, suggesting that the good performance of the “magic” interaction is connected to its nuclear matter saturation properties. Following this indication, chiral 3N interactions together with NN interactions of Ref. [56] were fit to the empirical saturation point of nuclear matter and the ^3H binding energy [57], where reasonable saturation properties were obtained for all interactions. Applications of these interactions in *ab initio* many-body calculations however revealed that a clear understanding of the connection between nuclear matter and finite nuclei is still lacking [52, 53].

All these observations reveal shortcomings of chiral Hamiltonians and provide room for improvements in the construction of chiral NN and 3N interactions. This motivates ongoing efforts for the construction of high-precision chiral interactions with the goal of consistent predictions for nuclear observables over a large range of mass numbers all the way up to reasonable saturation properties of nuclear matter. In practice, various approaches, e.g., using different observables and fitting protocols for the determination of the LECs, applying different functional forms of the regulator and ranges of the cutoff value, or additionally incorporating the Δ -isobar degree of freedom in the description are performed [24, 58–64]. This results in a variety of chiral interactions being applied to both nuclear structure studies for finite nuclei and investigations of infinite matter. Furthermore, recent studies for the error propagation of 3N LECs to observables of light systems using Bayesian methods and eigenvector continuation emulators showed that in the future more sophisticated uncertainty quantification should be applied for a comparison of theory and experiment [65].

Three-nucleon forces, in addition to NN forces, have been shown to play a major role for realistic predictions of finite nuclei [22, 66–68] as well as to obtain reasonable saturation properties of symmetric nuclear matter [54]. Therefore, incorporating the effects of 3N interactions is an essential step towards accurate theoretical calculations. Storing three-body operator matrix elements however requires a tremendous amount of memory, especially when represented in a single-particle basis, as usually done for *ab initio* methods. This motivates the use of approximate treatments and storing schemes by introducing an additional truncation in three-body space, referred to as $E_{3\max}$, which tames the memory requirements to more reasonable quantities. This approach has been proven to work very well for light and medium-mass nuclei. However, when approaching heavy nuclei, 3N contributions from larger model spaces become important and are required to obtain converged calculations. Consequently, results more sensitively depend on the applied cuts, and the tremendous increase in memory for larger $E_{3\max}$ limits the scope of *ab initio* many-body methods. Only recently, developments for storing three-body operator matrix elements [50] allowed one to extend the model-space truncations to larger values and enabled converged calculations of heavier nuclei, see Fig. 1.7. Nevertheless, memory limitations still prevent *ab initio* methods from going to very heavy nuclei and alternative approaches and approximation schemes to incorporate 3N forces are investigated.

The wave-function expansion methods discussed in this thesis generally aim at approximating the exact wave function by starting from a chosen reference state and account for the missing correlation effects in the many-body expansion. The reference state can be a simple harmonic oscillator state or a more refined estimate, such as a Hartree-Fock (HF) or natural orbital basis state. While closed-shell nuclei are well described with symmetry-conserving single Slater-determinant approximations of the ground state, open-shell nuclei require more general reference states and still provide challenges for *ab initio* calculations [37, 69–76]. Especially once approaching open-shell mid-mass and heavier systems, where exact methods are not feasible anymore, refined reference states as well as many-body expansion methods are required. This leads to increased computational demands and necessitates formal developments. In practice, most commonly multi-reference and symmetry-breaking reference states are employed, e.g., breaking the conservation of particle number by Bogoliubov vacua or using deformed reference states, breaking the conservation of the total angular momentum. Formal progress of extending the many-body methods to incorporate such reference states allows one to systematically target open-shell systems in nuclear theory. Extensions of closed-shell *ab*

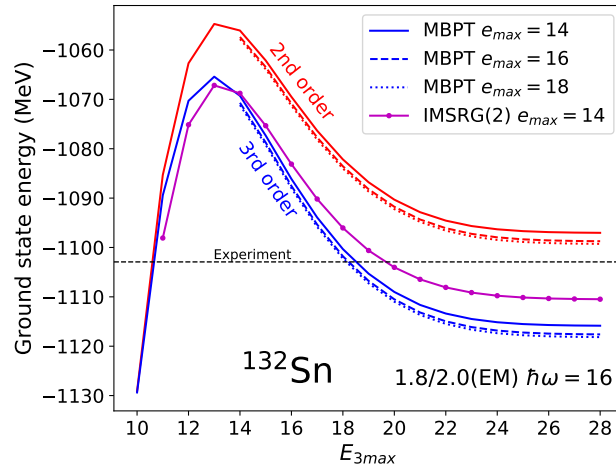


Figure 1.7: Ground-state energy of ^{132}Sn as a function of the $E_{3\text{max}}$ truncation in the space of three-body matrix elements. Recent advances of extending the $E_{3\text{max}}$ cut to higher values of up to $E_{3\text{max}} = 28$ [50], allow one to obtain converged results for heavier systems, here shown by applications in the IMSRG (purple curve) for an $e_{\text{max}} = 14$ truncation of the single-particle basis. Figure taken from Ref. [50].

initio methods that are with success applied to nuclear structure are, e.g., Gorkov SCGF [69, 77], Bogoliubov MBPT [37, 78], deformed CC [74] as well as Bogoliubov CC theory [79], or the projected generator coordinate method perturbation theory [80–82]. However, the nucleus, as a finite quantum systems, technically does not break any symmetries. Eventually restoring the symmetry in actual calculations still presents a major challenge on a formal and computational level and is subject of ongoing research in nuclear theory, see, e.g., Ref. [83] for first applications of angular-momentum-projected CC calculations.

Moreover, multiple challenges of describing nuclear observables in *ab initio* theory remain, and we list some key aspects in the following. Predicting nuclear matrix elements with rigorous uncertainty estimates plays an important role for the investigation of beyond standard model physics. In particular the hypothetical neutrinoless double- β decay provides a promising candidate to observe such effects by breaking the lepton number conservation [84–86]. Precise theory predictions of the involved nuclear matrix elements are crucial to guide next-generation experiments. Current calculations in different many-body methods however still vary by approximately a factor of three and require large model spaces to obtain converged results [87–89]. Studying excited-state properties, 2^+ excitation energies of closed-shell nuclei have been found to be sensitive to higher excitations of the reference state [55, 90], which are usually not incorporated in standard working truncations of the many-body method. Moreover, calculations of electromagnetic observables, in particular the strength of electric quadrupole transitions, even though showing qualitative agreement with experiment, typically predict too small values in *ab initio* calculations [91, 92]. This highlights the need for more precise *ab initio* calculations, consistent currents, and improved many-body methods.

In principal, more precise results for wave-function expansion methods can be obtained by capturing the correlation effects in more detail, either going to higher orders in the correlation expansion, or applying more refined reference states that possibly already account for parts of the correlation. Although extending the many-body expansion to higher orders is a highly preferable goal, efforts along these lines are severely limited by high computation times and large memory requirements.

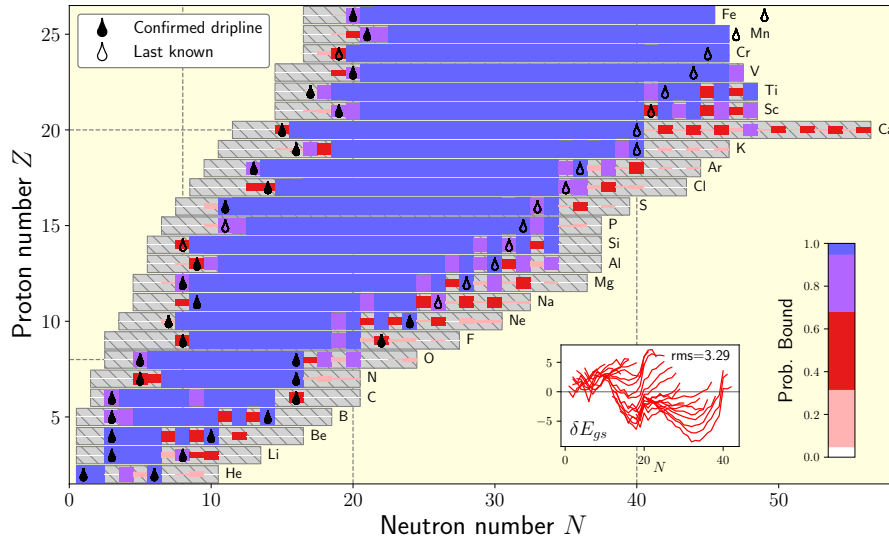


Figure 1.8: Nuclear chart with ground-state energies calculated in the VS-IMSRG. The colored boxes show the probability for each nucleus to be bound with respect to one- or two-neutron as well as one- or two-proton removal in the corresponding area of the nuclear chart. The gray area indicates all calculated mass numbers and the inset shows the difference of ground-state energies to the experimental values, with a root-mean-square deviation of 3.29 MeV. Figure taken from Ref. [75].

Future developments in *ab initio* theory in general go in two directions: First, the construction of improved nuclear forces for high-precision calculations with an appropriate uncertainty quantification. The goal for these forces is that they lead to reasonable agreement of theory and experiment over a wide range of mass numbers and consistently reproduce observables for light, medium-mass and heavy nuclei, as well as realistic saturation properties of nuclear matter, which is currently still lacking [18, 29, 37, 52, 53]. Second, advances for the many-body methods themselves will enable more precise calculations by going to higher orders in the many-body expansion with controlled approximations being able to target larger model-space truncations and obtain converged results in heavier systems. These efforts are however currently limited by the substantial increase in computational cost for higher-order calculations and the required memory for storing many-body operators in large model spaces.

This thesis addresses some of the current major challenges for *ab initio* theory, specifically focusing on developments and applications for the many-body approach, applying the IMSRG as the primary many-body method. The *ab initio* IMSRG is a powerful tool to calculate a diverse set of nuclear observables in a computationally efficient way by decoupling the reference state from all excited states, applying a continuous sequence of unitary transformations to the normal-ordered Hamiltonian. We focus on studying ground-state observables of closed-shell nuclei using the single-reference IMSRG, however extensions of the standard IMSRG that use shell-model approaches to diagonalize an effective valence-space Hamiltonian in the valence-space IMSRG (VS-IMSRG) [30, 93, 94] or employ multi-reference states in the multi-reference IMSRG (MR-IMSRG) [68, 72] are capable of targeting open-shell nuclei and excited-state properties. Figures 1.6 and 1.8 highlight the strength and versatility of the IMSRG by showing ground-state energies for a variety of closed-shell nuclei using different Hamiltonians, and a recent study of ground-state energies of about 700 closed- and open-shell nuclei in the VS-IMSRG [75], respectively. The latter additionally calculates predictions for the proton and neutron drip lines over a large range of mass numbers.

1.4 Scope of this thesis

In this thesis, we propose advances for the IMSRG, aiming at improved model-space convergence, optimized memory consumption, and controlled approximation schemes that allow for more accurate *ab initio* calculations and higher mass numbers, as well as pushing the many-body truncation to the next order.

It has been realized that optimizing the employed reference state can significantly improve the many-body calculation. We show how incorporating correlation effects beyond the mean-field level into the reference state yields results with improved convergence behavior with respect to the model-space size and significantly lowers or even completely resolves the dependence on basis set parameters of the employed single-particle basis. This is accomplished by using the natural orbital basis constructed from a perturbatively improved density matrix.

Furthermore, memory requirements, especially for storing three-body operator matrix elements in large model spaces, provide a fundamental limitation for *ab initio* theory, e.g., limiting converged results for heavy nuclei. Tensor-factorization approaches and importance-truncation (IT) techniques offer a possibility to compress and approximate many-body operators, thereby effectively lowering the computational cost and memory consumption. We demonstrate their benefits and derive first applications to the IMSRG.

Going to higher order in the many-body expansion of the IMSRG and including three-body operators in the IMSRG(3) truncation is currently still limited to rather small model spaces, based on the computational cost and high memory requirements for the three-body operators. Improving the convergence behavior for full and approximate IMSRG(3) calculations is hence a crucial step towards the goal of more precise calculations in large spaces. The benefits observed from the natural orbital basis provide a promising tool along these lines. Additionally, the application of importance-truncation techniques is of great interest for pushing the IMSRG to the IMSRG(3) truncation, where compressed or truncated operators could bring large model-space applications into reach.

Normal-ordering techniques allow to approximate three-body interactions in a computationally efficient way by incorporating them as effective interactions of lower many-body rank. However, standard approaches still require three-body operators stored in a single-particle basis, consequently being limited by the large memory requirements of the employed basis. We display how using the Jacobi basis circumvents these limitations and present a novel normal-ordering framework that avoids the $E_{3\max}$ truncation in the single-particle basis (see also Ref. [95]) and study its application in IMSRG calculations.

This thesis is structured as follows. In Ch. 2, we introduce chiral EFT as a low-energy effective theory of QCD and outline the construction of chiral interactions, specifically considering NN and 3N interactions using different regularization schemes and fitting approaches. We show how the free-space SRG can be used to soften nuclear potentials by evolving them to lower resolution scales and how tensor-factorization techniques, in particular the singular value decomposition, can be applied to obtain low-rank approximations of chiral potentials.

In Ch. 3, we define operators in a second-quantized form and introduce the concept of normal ordering with respect to a chosen reference state. Typically, HF states, stemming from a mean-field solution, yield a good estimate for the reference state. We therefore outline the general approach to derive the HF solution, before shortly discussing three selected many-body methods relevant for this thesis: the no-core shell model, coupled-cluster theory, and many-

body perturbation theory. The many-body workhorse of this thesis, the *ab initio* IMSRG, is afterwards explained in detail. By using the fundamental commutator expressions of the IMSRG, we derive the flow equations for two truncation schemes, given by the IMSRG(2) and IMSRG(3), and discuss possible generator choices that lead to the desired decoupling of the ground state.

The dependence on different reference states is studied in detail in Ch. 4 by applications of the natural orbital basis, defined as the eigenstates of the one-body density matrix. Specially, we employ a perturbatively improved density matrix up to second-order perturbation theory. Finally, we investigate different basis sets for the IMSRG(2) and apply the natural orbital basis for approximate and full IMSRG(3) truncations in small model spaces.

The framework of importance truncation *a priori* measures the importance of different contributions of the many-body operator and provides an alternative approach to the singular value decomposition to effectively reduce the size of the many-body problem. In Ch. 5, we show how importance-truncation techniques can be applied to the IMSRG and investigate predictions for ground-state observables using importance-truncated operators.

Chapter 6 presents a novel way of normal ordering the three-body interaction directly in the relative Jacobi momentum-space basis, in contrast to the traditional approach of normal ordering in the single-particle basis. New quantum numbers, describing the additional center-of-mass dependence of the normal-ordered two-body interaction, have to be introduced. The convergence behavior with respect to these quantum numbers and the benefits of the new normal-ordering framework are explored in detail, using the IMSRG to study ground-state observables of light, medium-mass, and heavy nuclei.

Finally, we conclude this thesis by giving a summary and outlook in Ch. 7.

2

Nuclear Forces and Chiral Effective Field Theory

The construction of nuclear interactions that describe the force between nucleons is a key element for microscopic investigations of nuclear observables and has a long history in nuclear physics. Early approaches were mostly based on phenomenological models, with meson-exchanges models, as described in Refs. [15, 96], or combined with a hard-core for the short-range repulsion, as e.g., for the Argonne v_{18} [14] potential, and a Yukawa one-pion exchange interaction [97] for the long-rang part. In the early 1970s QCD was established as the underlying theory of the strong interaction, which describes the interaction between the fundamental degrees of freedom, quarks and gluons. However, the nonperturbative character of the theory at the low-energy regime, where nuclear physics is situated, prevents a direct construction of nuclear interactions. Furthermore, the fact that the nuclear interaction is not unique and its construction is scheme and scale dependent complicates the derivation of nuclear forces. Realistic phenomenological interactions, even though being capable of describing nuclear observables in good agreement with experiment, evidently lack a clear connection to the underlying theory. Chiral EFT provides a remedy to this issue by deriving nuclear interactions based on a low-energy effective theory of QCD, with the same underlying symmetries. It therefore offers the key advantages of a systematically improvable description with controlled uncertainty estimates that is directly connected to the fundamental force of the strong interaction. In this thesis, we use two- and three-nucleon forces constructed within the framework of chiral EFT and apply them in many-body calculations to investigate the structure of finite nuclei.

This chapter is organized as follows. In Sec. 2.1, we discuss the main properties of QCD, with its spontaneous and explicit chiral symmetry breaking and the problems that arise at low energies due to the running coupling constant of the theory. We then review the construction of nuclear interactions in chiral EFT in Sec. 2.2. We closely follow Refs. [12, 98, 99] and refer to these publications and references within for further details. Finally, we conclude this chapter with a discussion of the free-space SRG as a method to soften the chiral input interactions by evolving them to lower resolution scales in Sec. 2.3, and an introduction to the singular value decomposition to obtain low-rank approximations of chiral interactions in Sec. 2.4.

2.1 Quantum chromodynamics

The degrees of freedom of the underlying theory of the strong interaction QCD are quarks, which are elementary spin-1/2 particles, and gluons, the gauge bosons of the theory as mediators of the force. QCD is a local, non-Abelian gauge theory with the special unitary group of degree three [SU(3)]. Six quark flavors, which carry different mass and electric charge labeled up (u), down (d), strange (s), charm (c), bottom (b), and top (t), are the ingredients that compound matter together with their corresponding antiparticles, indicated by a bar on top of the abbreviation. We start to take a closer look at the underlying theory by writing down the Lagrangian and discussing its symmetries and characteristics. The QCD Lagrangian is given by

$$\mathcal{L}_{\text{QCD}} = \sum_{j=u,d,s,c,b,t} \bar{q}_j (i\not{D} - m_j) q_j - \frac{1}{2} \mathcal{G}_{\mu\nu}^a \mathcal{G}^{\mu\nu,a}, \quad (2.1)$$

where q_j is the quark field with corresponding quark mass m_j . The term $\not{D} = \gamma^\mu (\partial_\mu + ig_s A_\mu)$ represents the covariant derivative, using the Dirac matrix γ^μ for the Feynman-slash notation, the strong coupling constant g_s , the gluon field A_μ , and $\mathcal{G}_{\mu\nu}^a$ is the gluon-field-strength tensor given by

$$\mathcal{G}_{\mu\nu}^a = \partial_\mu A_\nu^a - \partial_\nu A_\mu^a + g_s f^{abc} A_\mu^b A_\nu^c, \quad (2.2)$$

using the definition $A_\mu \equiv A_\mu^a T^a$ with the generators of the SU(3) group T^a for the indices $a, b, c = 1, \dots, 8$ and the structure constant f^{abc} . The sum in Eq. (2.1) in general runs over all quark flavors, u, d, s, c, b , and t . However, in the low-energy regime only the lightest quarks, the up, down, and strange quark, are most important, such that we limit the sum to the subset u, d, s in the following. Table 2.1 summarizes the masses and electric charges of the six quark flavors, showing the significant increase in mass when going from the strange to the charm quark, justifying the limitation of the sum in Eq. (2.1) to only three quark flavors for low energies. For comparison, the nucleon mass is given by $M \approx 939$ MeV, well below the masses of charmed hadrons, e.g., the J/ψ meson is three times as heavy as the nucleon. In addition to the electric charge, quarks carry a quantum “number” called color charge, given by red (r), green (g), or blue (b). Any combination of color charge with its corresponding anticolor ($\bar{r}, \bar{g}, \bar{b}$) carried by an antiquark, or a combination of all three (anti)color charges is color neutral (white) as in the RGB color model for light. The number of color variations $n_C = 3$ also explains the degree of the SU(3) symmetry group of the theory.

The coupling constant α_s of QCD varies as a function of the scale Q [100]. It is therefore called a running constant

$$\alpha_s(Q) \approx \frac{2\pi}{\left(11 - \frac{2}{3}n_f\right) \ln\left(\frac{Q}{\Lambda_{\text{QCD}}}\right)}, \quad (2.3)$$

with the number of quark flavors n_f and the characteristic QCD scale Λ_{QCD} , which is scheme dependent and typically in the range of 200–300 MeV. Note that Eq. (2.3) just gives α_s approximately and higher-order terms in the renormalization group equation of the running coupling constant are neglected (see Ref. [101] for details).

quark flavor	mass (MeV)	electric charge (e)
u p	2.16 $^{+0.49}_{-0.26}$	$+\frac{2}{3}$
d own	4.67 $^{+0.48}_{-0.17}$	$-\frac{1}{3}$
s trange	93 $^{+11}_{-5}$	$-\frac{1}{3}$
c harm	1270 ± 20	$+\frac{2}{3}$
b ottom	$4180 \text{ }^{+30}_{-20}$	$-\frac{1}{3}$
t op	172760 ± 300	$+\frac{2}{3}$

Table 2.1: Quark flavors with their masses and electric charges. Values are taken from the Particle Data Group [102].

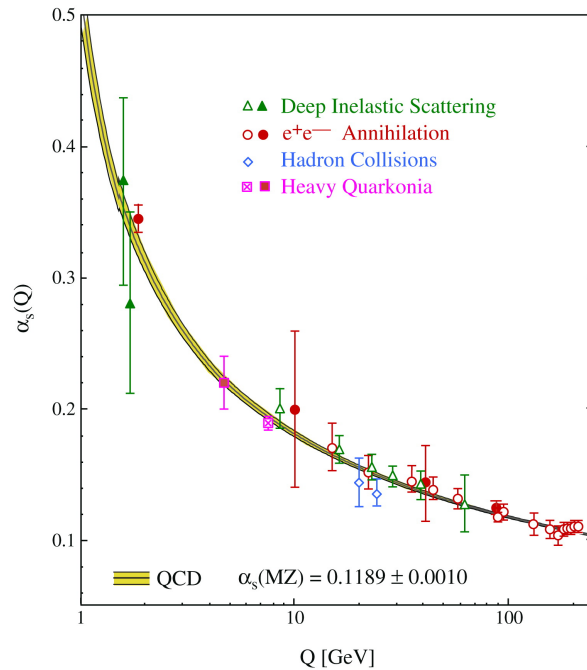


Figure 2.1: Coupling constant α_s of QCD as a function of energy scale Q for the world average value $\alpha_s(Q = M_{Z^0}) = 0.1189 \pm 0.0010$ at the Z^0 boson mass (status of the year 2006). The open and filled symbols show experimental values at next-to-leading order and next-to-next-to-leading order perturbation theory for different experimental approaches, given by deep inelastic scattering (green), positron-electron annihilation (red), hadron collisions (blue), and heavy quarkonia (purple) experiments. See Ref. [101], where this figure is taken from, for further details.

In Fig. 2.1, we show the coupling constant of the strong interaction as a function of Q together with experimental values based on different experimental approaches. One can identify two important regimes: First, for high energies, the coupling becomes small allowing for perturbative QCD calculations and eventually leading to the phenomenon of asymptotic freedom in the limit of very large energies, indicated by the flattening of the curve in the lower right of Fig. 2.1. Second, for low energies, the coupling constant grows rapidly and eventually $\alpha_s > 1$, making any perturbative description of the theory in this regime unfeasible.

Related to the strong coupling at low energies, the observation of individual quarks at low temperature and low density is not possible due to the confinement given by the strong interaction in this regime. As a result, hadronic degrees of freedom composed of color-neutral combinations of quarks arise and are the observed degrees of freedom at low energies. We distinguish between different hadrons based on the number of constituent quarks: hadrons consisting of three quarks with neutral color charge called baryons, e.g., neutrons or protons, and states of a quark and antiquark pair called mesons, e.g., pions or ρ mesons. More exotic combinations such as pentaquark [103–105] or tetraquark [106, 107] states with five and four quarks, respectively, are possible and have been observed or suggested in experiments, e.g., at the Large Hadron Collider (LHC). See also Ref. [108] for a recent review on experimental evidence of such more exotic states.

Approaches to calculate nuclear observables in the low-energy regime directly from QCD and deriving, e.g., properties of light and heavy mesons [6], nucleon-nucleon scattering [109], baryon-baryon interactions [110, 111], or the axial coupling of the nucleon to high precision [112] have been very successful by using lattice QCD (LQCD). This method employs a discretized lattice in space-time and uses Monte-Carlo methods for the solution of the resulting path integrals. For a more detailed discussion of the method and its application to nuclear physics, we refer to Refs. [5, 113]. Even larger systems like light nuclei or hypernuclei with $A \leq 4$ have already been calculated from LQCD by the Nuclear Physics with Lattice QCD (NPLQCD) collaboration [7, 8] but at larger pion masses. However, due to the complexity of the systems and the computational challenges involved, LQCD calculations for nuclear many-body problems are currently still limited to very small system sizes with just a few particles and mostly large values for the quark masses, leading to unphysical pion masses. Chiral effective field theory, a low-energy effective theory of QCD introduced in the next section, makes the connection to the underlying theory based on the global symmetries of the QCD Lagrangian, where the key global symmetry of QCD (in the low-energy regime) is chiral symmetry, which we explore now.

In the following, we assume that quark masses are exactly equal to zero such that the mass term for the quark fields q_j in Eq. (2.1) vanishes and we only have to consider the kinetic part with the covariant derivative. Applying projection operators for the right- and left-handed components of the quark fields, given by

$$P_R = \frac{1}{2}(1 + \gamma_5), \quad (2.4a)$$

$$P_L = \frac{1}{2}(1 - \gamma_5), \quad (2.4b)$$

respectively, we can rewrite the QCD Lagrangian for zero quark masses, here indicated by the 0 superscript, in terms of separate right- and left-handed quark fields

$$q_{R_j} = P_R q_j, \quad (2.5a)$$

$$q_{L_j} = P_L q_j, \quad (2.5b)$$

resulting in

$$\mathcal{L}_{\text{QCD}}^0 = \sum_{j=u,d,s} (\bar{q}_{R_j} i \not{D} q_{R_j} + \bar{q}_{L_j} i \not{D} q_{L_j}) - \frac{1}{2} \mathcal{G}_{\mu\nu}^a \mathcal{G}^{\mu\nu,a}, \quad (2.6)$$

with the trace over the gluon field strength tensor being unaffected. This form of the Lagrangian is now invariant under separate transformations of the right- and left-handed components of the quark fields, as no term couples the two components. The underlying symmetry group is $U(3)_L \times U(3)_R$, which can be reformulated as a $U(1)_A \times U(1)_V \times SU(3)_R \times SU(3)_L$ symmetry. The baryon number conservation is reflected by the $U(1)_V$ symmetry, and the $SU(3)_R \times SU(3)_L$ symmetry is called *chiral symmetry*, which can also be written in terms of $SU(3)_{L-R} \times SU(3)_{L+R} = SU(3)_A \times SU(3)_V$.

However, chiral symmetry is spontaneously broken. This can be seen by identifying parity doublets, states with equal quantum numbers but opposite parity, which are supposed to have identical masses in case of an exact chiral symmetry. Considering, e.g., the ρ vector meson with mass $M_\rho = 775$ MeV and negative parity ($J^\Pi = 1^-$) compared to the a_1 pseudovector meson with equal quantum numbers but positive parity, i.e., $J^\Pi = 1^+$, and mass $M_{a_1} = 1230$ MeV signals a mass difference and the resulting spontaneously broken symmetry. According to the Goldstone theorem [114], every spontaneously broken (continuous) symmetry implies the existence of massless excitations of the vacuum, so-called Goldstone bosons, one for each generator of the symmetry, resulting in eight Goldstone bosons for the spontaneously broken chiral symmetry.

In addition to the spontaneous symmetry breaking, chiral symmetry is also explicitly broken by the nonvanishing quark masses, as can be seen from the mass term of the Lagrangian in Eq. (2.1) for the right- and left-handed fields

$$\sum_{j=u,d,s} \bar{q}_j m_j q_j = \sum_{\substack{j=u,d,s \\ i=u,d,s}} \bar{q}_{Ri} M_{ij} q_{Lj} + \text{H.c.}, \quad M = \begin{pmatrix} m_u & & \\ & m_d & \\ & & m_s \end{pmatrix}, \quad (2.7)$$

where M is the mass matrix for the u , d , and s quark, mixing right and left-handed components in contrast to $\mathcal{L}_{\text{QCD}}^0$. The explicit symmetry breaking gives rise to massive Goldstone bosons, so-called pseudo-Goldstone bosons. In QCD, these eight pseudo-Goldstone bosons are the π^+ , π^- , π^0 , K^+ , K^- , K^0 , \bar{K}^0 , and η mesons, with the pions being the lightest of these particles consisting only of u and d quarks. Taking into account the small mass difference of the u and d quark, compared to the s quark, the subgroup $SU(2)_V \subset SU(3)_V$ is a good approximate symmetry, corresponding to the isospin symmetry of two quark flavors, explaining e.g., the small mass difference between the proton ($M_p = 938.27$ MeV) and the neutron ($M_n = 939.57$ MeV).

2.2 Chiral effective field theory

2.2.1 Formalism and hierarchy of nuclear forces

In this subsection, we introduce an effective field theory that is consistent with the low-energy symmetries of QCD and provides an efficient and powerful tool to derive nuclear forces and currents, enabling calculations of nuclear properties and observables with a direct link to the underlying fundamental theory. Specifically, we focus on chiral EFT, which was first

introduced in the seminal works of Weinberg [9–11] in the early 1990s. We do not aim to give a complete account of all aspects of the theory here, instead, we focus on the elementary ideas and concepts for the derivation of nuclear forces within the framework of chiral EFT. We refer to Refs. [12, 99, 115] for more detailed reviews about this topic.

A key concept of any effective field theory is the separation of scales, where typically a soft scale \mathcal{Q} and a hard scale Λ are identified with $\mathcal{Q} \ll \Lambda$. The soft scale defines the phenomena to be resolved by the theory, whereas the hard scale sets a resolution limit with physics beyond this scale not explicitly resolved by the theory. This allows for an order-by-order expansion in \mathcal{Q}/Λ , where at order ν the contributions scale like $(\mathcal{Q}/\Lambda)^\nu$. A schematic illustration of this approach is the multipole expansion of an extended charge distribution, where one expands the potential far away from the source by different multipole orders. Incorporating the next order increases the precision of the description, and one can truncate the expansion at a chosen order to obtain a desired accuracy.

In the following, these general ideas are applied to a low-energy effective theory of QCD. The details of the high-energy physics, related to short-range phenomena, are not explicitly resolved by the low-energy expansion but can be incorporated in terms of contact interactions, whose strength is determined by low-energy constants (LECs), which have to be determined by fitting to experimental data or, if possible, calculated based on the underlying theory, see, e.g., Refs. [116–120]. In chiral EFT, nucleons and pions are the relevant degrees of freedom, rather than the fundamental degrees of freedom quarks and gluons of QCD. The important scales are given by the soft scale of typical momenta of the order of the pion mass $M_\pi = 140$ MeV and the hard scale by the physics that is left, roughly of the order of the mass of the next heaviest meson, the ρ meson $M_\rho = 775$ MeV. This results in an estimated breakdown scale of chiral EFT of $\Lambda_b \approx 500$ MeV.

The relevant task for deriving nuclear interactions consists of constructing the most general Lagrangian based on the relevant degrees of freedom consistent with chiral symmetry

$$\mathcal{L}_{\text{eff}} = \mathcal{L}_{\pi\pi} + \mathcal{L}_{\pi N} + \mathcal{L}_{NN} + \dots, \quad (2.8)$$

where we have expanded the Lagrangian into three contributions, given by the pion-pion ($\pi\pi$), pion-nucleon (πN), and NN parts, with the ellipsis denoting higher-order terms. In general, an infinite number of terms contribute to the chiral Lagrangian, but by expanding \mathcal{L} in terms of $(\mathcal{Q}/\Lambda)^\nu$ and using a power counting to organize the arising terms by their importance, only a finite number of terms contributes to each order ν . Based on such a power-counting scheme, we can organize the arising nucleon-nucleon, three-nucleon, and higher many-body interactions and order the complete chiral Lagrangian in terms of orders of ν to obtain a hierarchy of nuclear forces. The idea is that with every additional order ν the theory becomes more accurate, where lower orders are more important. The most commonly applied power counting scheme is Weinberg power counting [9–11], which for A nucleons is given by

$$\nu = -2 + 2A - 2C + 2L + \sum_i \Delta_i, \quad (2.9)$$

with the number of separately connected diagrams C , the number of loops L , the sum over all vertices i , and Δ_i defined as

$$\Delta_i = d_i + \frac{n_i}{2} - 2, \quad (2.10)$$

where d_i is the number of derivatives or insertion of pion masses, and n_i the number of nucleon fields at a given vertex. An important fact is that $\Delta_i \geq 0$ ensures $\nu \geq 0$ such that the low-energy expansion is bounded from below. There are ongoing discussions about what the correct power counting scheme for nuclear interactions is, see, e.g., Refs. [121–126] for more detailed information and some alternative approaches. For all interactions used in this thesis Weinberg power counting discussed above is the underlying power counting scheme.

At leading order (LO), $\nu = 0$, the only contribution to the potential is given by the one-pion exchange (OPE) potential and the two-nucleon contact interaction

$$V_{\text{OPE}}(\mathbf{Q}) = -\frac{g_A^2}{4F_\pi^2} \frac{(\boldsymbol{\sigma}_1 \cdot \mathbf{Q})(\boldsymbol{\sigma}_2 \cdot \mathbf{Q})}{Q^2 + M_\pi^2} \boldsymbol{\tau}_1 \cdot \boldsymbol{\tau}_2, \quad (2.11)$$

$$V_{\text{contact}} = C_S + C_T \boldsymbol{\sigma}_1 \cdot \boldsymbol{\sigma}_2, \quad (2.12)$$

with the momentum transfer $\mathbf{Q} = \mathbf{p}' - \mathbf{p}$ given by the initial and final relative momentum \mathbf{p} and \mathbf{p}' , respectively, the axial-vector coupling constant $g_A = 1.27$, the pion decay constant $F_\pi = 92.4$ MeV, the spin and isospin Pauli matrices $\boldsymbol{\sigma}_i = (\sigma_x, \sigma_y, \sigma_z)$ and $\boldsymbol{\tau}_i = (\tau_x, \tau_y, \tau_z)$ of the first ($i = 1$) and second ($i = 2$) nucleon, and the two LECs C_S and C_T of the contact interaction. The LEC combination with the operators $\mathbb{1}$ and $\boldsymbol{\sigma}_1 \cdot \boldsymbol{\sigma}_2$ is a particular choice, related to the Fierz ambiguity [127, 128] and only two out of four operator structures are required for the LO contact interaction. The LO chiral potential is consequently given by

$$V_{\text{NN}}^{\text{LO}}(\mathbf{Q}) = C_S + C_T \boldsymbol{\sigma}_1 \cdot \boldsymbol{\sigma}_2 + V_{\text{OPE}}(\mathbf{Q}). \quad (2.13)$$

Note that the contact interaction is momentum independent, meaning that it only contributes to S-wave channels. Two LECs for the two S -waves occur at this order. Going to higher orders, momentum-dependent interactions and three-body forces contribute. These depend on additional LECs, which have to be fitted to experiment as well. Even though the direct determination of LECs from first principles by, e.g., lattice QCD calculations is desirable and an active field of research, the tremendous computational prerequisites make such an approach unfeasible at present [129].

A detailed overview of the diagrammatic expansion of the nuclear interaction at each order in the expansion based on the power counting in Eq. (2.9) is shown in Fig. 2.2, where in general we distinguish two main contributions: nucleon contact interactions, which cover the short-range part of the nuclear interaction; and one- and multiple-pion exchange diagrams, which parameterize the long- and intermediate-range part of the interaction. The different LECs are given by white and colored symbols, where white symbols only contribute to the NN force and colored symbols additionally (or exclusively in some cases) contribute in the description of the 3N force.

Going from LO to next-to-leading order (NLO) at $\nu = 2$, seven additional LECs enter for the NN force, see the red box in the top right corner for the NLO NN panel in Fig. 2.2, and the description of the interaction at intermediate distances becomes improved by the leading-order two-pion exchange (2PE) potential. Note that there are no contributions for $\nu = 1$ due to parity conservation and time-reversal symmetry [12]. Explicit forms of the potential at NLO, or higher orders will not be given here for brevity, and we refer to Refs. [12, 99, 115] for an in-depth derivation of the individual $\pi\pi$, πN , and NN contributions to the chiral potential.

Using the power counting, we can directly predict the orders at which three- and higher-

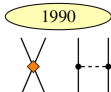
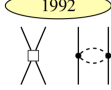
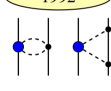
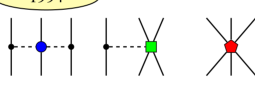
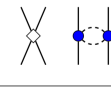
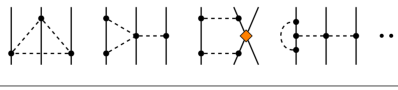

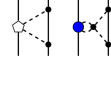
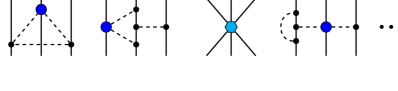

	NN	3N	4N
LO $\mathcal{O}(Q^0/\Lambda^0)$	 1990 2	—	—
NLO $\mathcal{O}(Q^2/\Lambda^2)$	 1992 7	—	—
N ² LO $\mathcal{O}(Q^3/\Lambda^3)$	 1992 0	 1994 2	—
N ³ LO $\mathcal{O}(Q^4/\Lambda^4)$	 2000–2002 12	 2008–2011 0	 2006 0
N ⁴ LO $\mathcal{O}(Q^5/\Lambda^5)$	 2015 0	 2011– ?	 ?

Figure 2.2: Hierarchy of nuclear forces for the individual orders of the chiral expansion (Q^ν/Λ^ν) starting at LO, $\nu = 0$, up to next-to-next-to-next-to-next-to-leading order (N⁴LO) at $\nu = 5$ in rows one to five. Note that NLO starts at $\nu = 2$, as $\nu = 1$ is not allowed due to parity conservation and time reversal symmetry. The columns indicate two-nucleon, three-nucleon, and four-nucleon interactions. Solid and dashed lines represent nucleons and pions, respectively. Colored symbols (diamonds, squares, circles, penta-, and hexagons) indicate vertices of different order, where white vertices only enter the NN interaction and colored vertices also enter the 3N interaction. The years in the yellow ellipses in the top left corner show the date the contributions in the corresponding panel have been worked out, and the colored boxes in the top right corner of each panel give the number of additional LECs entering the many-body force at this order. Figure taken from Ref. [130].

body forces enter in the expansion. By setting $L = \sum_i \Delta_i = 0$ and $C = 1$, we see that three-nucleon (3N) forces first enter at NLO, but their contribution cancels at this order [131]. First nonvanishing 3N forces appear at next-to-next-to-leading order (N²LO). Four-nucleon (4N) forces first enter at $\nu = 4$, corresponding to next-to-next-to-next-to-leading order (N³LO).

At N²LO, the description of the intermediate-range improves by incorporating the subleading two-pion exchange potential and nonvanishing 3N forces enter for the first time. Nucleon-nucleon forces have currently been derived up to fifth order (N⁴LO) in the chiral expansion [56]. While 3N forces at this order are still under development, 3N forces at N³LO (subleading 3N forces) have been derived [132–134] and partial-wave decomposed [130, 135, 136], allowing for consistent interactions up to the 3N level at fourth order in the chiral expansion.

The systematically improvable approach of chiral EFT has the key advantage that it can be used to derive uncertainty estimates arising from the EFT truncation in the order-by-order expansion. The concept of uncertainty quantification (UQ) has become a crucial ingredient for high-precision calculations in nuclear theory and is key for a reliable comparison to experiment and predicting observables. While earlier approaches were mostly based on parameter variations (e.g., varying the LECs) and studying the resulting changes for nuclear observables, the EFT uncertainty can be estimated by the discarded contributions at the

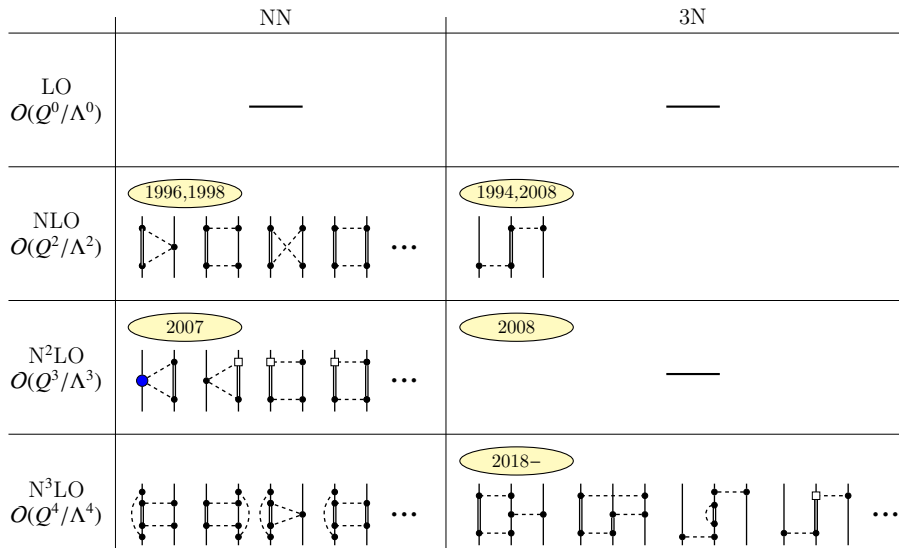


Figure 2.3: Same as Fig. 2.2 but for the additional diagrams contributing in Δ -full chiral EFT. Double solid lines denote virtual excitations of the nucleon to the Δ isobar. Figure taken from Ref. [130].

next higher order [38]. A more refined uncertainty estimate is obtained by modern methods that employ advanced statistical tools, resulting in sophisticated UQ approaches based on, e.g., Bayesian methods (see Refs. [39, 41, 42, 137]) and are further capable of quantifying correlated uncertainties.

Alternative choices of the low-energy degrees of freedom give rise to slightly different effective theories, e.g., pionless EFT [138] (see Ref. [118] for an application to finite nuclei), with just nucleon contact interactions, and Δ -full chiral EFT, which incorporates the delta isobar $\Delta(1232)$ as an explicit low-energy degree of freedom [60, 62, 139, 140]. The three most common nuclear EFTs are discussed in detail in a recent review [126]. With a mass splitting of approximately 293 MeV between the delta and the nucleon, the energy scale associated with a virtual excitation of the nucleon to the delta is $\approx 2M_\pi$, which is well below the chiral breakdown scale Λ_b . The diagrammatic expansion for Δ -full chiral EFT slightly changes compared to the Δ -less chiral EFT presented in Fig. 2.2, and the LECs have to be readjusted in some cases. We show the additional diagrams occurring for the Δ -full theory in Fig. 2.3. Note that there is no change at LO, but 3N forces already enter at NLO by the so-called Fujita-Miyazawa term [141].

In this thesis, we focus on chiral NN and 3N forces up to N³LO derived within Δ -less chiral EFT. We neglect contributions of 4N forces, which first enter at N³LO. Based on the hierarchy of nuclear forces $V_{\text{NN}} \gg V_{\text{3N}} \gg V_{\text{4N}}$ their impact is expected to be small compared to the NN and 3N contributions [142, 143].

2.2.2 Construction of nuclear interactions

Evaluating the individual contributions of the chiral interaction gives rise to ultraviolet (UV) divergences, e.g., in the evaluation of loop integrals for high momenta, which have to be regularized. When applying a given chiral potential in the Lippmann-Schwinger equation, the high-momentum contributions in the integral can be cut off by using a regulator function with

a chosen cutoff value Λ , usually of the order of the chiral breakdown scale Λ_b . In theory, in the limit of infinite chiral order, the regulator and its specific functional form and cutoff value would not affect the final result for observables. However, in practical calculations at finite order, results do depend on the regulator, giving rise to so-called regulator artifacts, such as cutoff artifacts. Variations of the cutoff value offer the possibility to study their impact on the final result.

Typically, one distinguishes regulators applied to the contact interactions and the pion-exchange parts of the potential, given by the short- and long-range regulator, respectively. The freedom to choose any appropriate functional form for the regulator together with variations of the specific cutoff value results in a large variety of regularized potentials. Often the cutoff value Λ in momentum space is used in the name specifier of the interaction, e.g., the EMN 450 interaction of Ref. [56] with $\Lambda = 450$ MeV.

We can distinguish three families of chiral interactions, depending on the different regularization schemes applied to the short- and long-range part: local, semilocal, and nonlocal interactions. Local potentials (see, e.g., Refs. [24, 144, 145]), only depend on the momentum transfer $\mathbf{Q} = \mathbf{p}' - \mathbf{p}$ in momentum space, or the relative distance \mathbf{r} in coordinate space and require a regulator that preserves this locality. Local interactions are especially applied in QMC calculations, which rely on local input Hamiltonians. Semilocal interactions (see, e.g., Refs. [38, 146, 147]) employ a mixture of local and nonlocal regulators, where typically the long-range part is regularized locally and the short-range part nonlocally. Finally, nonlocal potentials (see, e.g., Refs. [46, 56, 59]) use a nonlocal regulator for both the short- and long-range part, which only depends on the magnitude of the relative momenta $p = |\mathbf{p}|$ and $p' = |\mathbf{p}'|$ without any angular dependence as observed for local regulators. Table 2.2 shows a selected set of examples for these three types of interactions with the corresponding functional form of the regulators. Both regularization in coordinate and momentum space are used in practice. In Ref. [38], an estimate of the relation between the cutoff values in the two spaces is given by $\Lambda = 2/R_0$ based on the Fourier transform of a Gaussian. However, a universal relation between the two cutoff values is not always directly possible and the functional form of the regulator should also be considered for a meaningful comparison [148].

Throughout this thesis, in the majority of calculations we use (nonlocal) chiral interactions with a nonlocal regulator as, e.g., used for the NN potential by Entem, Machleidt, and Nosyk (EMN) of Ref. [56]

$$f(p)_{\Lambda_{\text{NN}}} = \exp \left[- \left(\frac{p^2}{\Lambda_{\text{NN}}^2} \right)^n \right], \quad (2.14)$$

with regulator exponent n and cutoff value Λ_{NN} for the NN interaction given in the name specifier. The 3N interaction is regularized in a similar fashion by

$$f(p, q)_{\Lambda_{\text{3N}}} = \exp \left[- \left(\frac{p^2 + \frac{3}{4}q^2}{\Lambda_{\text{3N}}^2} \right)^n \right], \quad (2.15)$$

using the magnitude of the Jacobi momenta $p = |\mathbf{p}|$ and $q = |\mathbf{q}|$, the regulator exponent n (mostly set to $n = 4$), and the 3N cutoff value Λ_{3N} , set to the same value as used in the NN potential when using the EMN potentials. The Jacobi momenta \mathbf{p} and \mathbf{q} are given by the relative momentum of the particles one and two and the momentum of the third particle relative to the center-of-mass momentum (cm) of the first two particles, respectively. The

	regulator functions		regulator exponent(s)	chiral order cutoff range
	short-range (contact)	long-range (pion exchanges)		
local				
GT+ [24, 144]	$\alpha e^{-\bar{r}^n}$	$1 - e^{-\bar{r}^n}$	$n = 4$	up to N ² LO $R_0 = 0.9 - 1.2$ fm
semilocal				
EKM [38, 146]	$e^{-\bar{p}^{n_1}} e^{-\bar{p}'^{n_1}}$	$(1 - e^{-\bar{r}^2})^{n_2}$	$n_1 = 2$ $n_2 = 6$	up to N ⁴ LO $R_0 = 0.8 - 1.2$ fm $\Lambda_{\text{NN}} \approx 493 - 329$ MeV
nonlocal				
EMN [56]	$e^{-\bar{p}^{2n_1}} e^{-\bar{p}'^{2n_1}}$	$e^{-\bar{p}^{2n_2}} e^{-\bar{p}'^{2n_2}}$	$n_1 > \nu/2$ $n_2 = 2$ (4)	up to N ⁴ LO $\Lambda_{\text{NN}} = 450 - 550$ MeV

Table 2.2: Short- and long-range regulators in coordinate and momentum space for selected local [24, 144], semilocal [38, 146], and nonlocal [56] NN potentials with $\bar{r} \equiv r/R_0$ and $\bar{p} \equiv p/\Lambda_{\text{NN}}$ in the first and second and column, where $\alpha = (\pi\Gamma(3/4)R_0^3)^{-1}$ is a normalization constant and ν is the order of the chiral expansion. We use the abbreviations GT+ for the local potentials of Gezerlis, Tews *et al.*, EKM for the semilocal potentials of Epelbaum, Krebs, and Meißner, and EMN for the nonlocal potentials of Entem, Machleidt, and Nosyk. For the EMN potentials, the regulator exponent $n_2 = 2$ is applied to the pion exchanges and $n_2 = 4$ for the one-pion exchange beyond NLO. The highest available chiral order and the cutoff ranges are given in the fourth column. Table adjusted from Ref. [148].

particular functional form of Eq. (2.15) is motivated by the relative kinetic energy of the three-body system, which can be written in terms of the Jacobi momenta \mathbf{p} and \mathbf{q} [130, 149].

In addition to the regularization, which results in different families of chiral interactions, the fitting protocol of the LECs as outlined in Sec. 2.2 plays a key role in constructing nuclear interactions and has a critical impact on predictions for finite nuclei or nuclear matter. Most commonly, the NN LECs are fit to nucleon-nucleon partial-wave phase shifts using laboratory energies up to $E_{\text{lab}} \simeq 300$ MeV, e.g., based on the Nijmegen partial-wave analysis (PWA) [13]. The determination of the 3N low-energy couplings requires additional information from three or higher-body systems, resulting in various fitting procedures that use different few- and many-body observables as well as nuclear matter properties in practical applications. For the leading 3N force at N²LO five LECs contribute. Three of these, labeled by c_1 , c_3 , and c_4 are already determined in the NN sector as can be seen by the blue circle in Fig. 2.2 for the 2π -exchange potential of the NN force at N²LO. The remaining two LECs are given by the 1π -exchange contact c_D and the 3N contact c_E , shown by the green square and red pentagon of the corresponding diagrams in Fig. 2.2, respectively. They have to be determined explicitly in the 3N (or higher-body) sector. The two contributions to the 3N potential are given by

$$V_{1\pi\text{-cont.}} = -\frac{g_A}{8F_\pi^2} \frac{c_D}{F_\pi^2 \Lambda_b} \sum_{i \neq j \neq k} \frac{\boldsymbol{\sigma}_j \cdot \mathbf{Q}_j}{Q_j^2 + M_\pi^2} (\boldsymbol{\tau}_i \cdot \boldsymbol{\tau}_j) (\boldsymbol{\sigma}_i \cdot \mathbf{Q}_j), \quad (2.16)$$

$$V_{3\text{N cont.}} = \frac{c_E}{2F_\pi^4 \Lambda_b} \sum_{j \neq k} (\boldsymbol{\tau}_j \cdot \boldsymbol{\tau}_k), \quad (2.17)$$

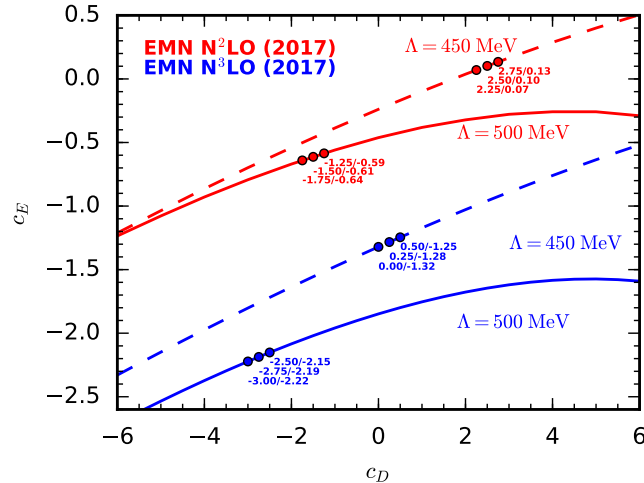


Figure 2.4: Combinations of the 3N couplings c_D and c_E reproducing the triton binding energy $E(^3H) = -8.482$ MeV for the NN+3N EMN interaction [56, 57] at N²LO (red) and N³LO (blue) for the cutoff values $\Lambda = 450$ MeV (dashed lines) and $\Lambda = 500$ MeV (solid lines). The three points on each line with annotated c_D/c_E values indicate the best reproduction of the empirical saturation density and energy. Figure taken from Ref. [57].

with the momentum transfer $\mathbf{Q}_i = \mathbf{k}'_i - \mathbf{k}_i$ given by the initial and final single-particle momenta \mathbf{k}_i and \mathbf{k}'_i of the i -th particle, respectively, and the chiral breakdown scale set to $\Lambda_b = 700$ MeV in Ref. [149].

Two observables, ideally with minimal correlation, are required for the determination of c_D and c_E . In practice, this is commonly done by using two few-body observables. In particular, the triton ground-state energy together with, e.g., its β -decay half-life or the charge radius of ^4He . Fitting first to the ^3H ground-state energy results in combinations of c_D and c_E values which all reproduce $E(^3\text{H})$, as exemplarily shown in Fig. 2.4 for the EMN interaction at N²LO and N³LO. A second observable is required to fix a specific point on the c_D - c_E curve for the final determination of the 3N force. A naive first guess would be the ground-state energy of ^4He in addition to the triton, but these two observables are not independent of each other with their correlation given by the Tjon line [150, 151]. A possible choice for two less correlated observables is the ground-state energy of ^3H and the charge radius of ^4He as used in Ref. [54]. Remarkably, the interactions derived in Ref. [54], which are just fit to few-body data, lead to good reproduction of empirical nuclear matter properties in terms of saturation density and energy.

Another choice in the fitting procedure is the β -decay half-life of the triton in addition to its ground-state energy as was first done in Ref. [152]. Chiral EFT has the advantage that nuclear currents can be derived consistently to the nuclear interactions and consequently depend on the same LECs. These nuclear currents are then used to calculate electroweak observables, like the ^3H β -decay. Recently, also empirical saturation properties of infinite nuclear matter have been employed in the fitting strategies of the 3N force [57]. The three combinations of c_D/c_E values annotated next to the circles in Fig. 2.4 lead to the best reproduction of the empirical saturation point for each interaction in terms of both saturation density and energy.

Predictions using chiral interactions that are fit to only NN data and few-body observables usually considerably deviate from experiment for medium-mass and heavy nuclei [29, 58, 59].

Therefore approaches to obtain an improved description of light- and medium-mass nuclei are performed by incorporating properties of nuclei beyond the few-body sector (of only three- and four-body systems) into the fit of the 3N force. This strategy was first employed in Ref. [58], where energies and charge radii of selected carbon and oxygen isotopes were used in a simultaneous fit of the 3N and NN force. This particular interaction only reproduces NN phase shifts to rather low energies, but predicts nuclei up to the medium-mass regime in better agreement with experiment. A very recent Δ -full interaction derived in Ref. [61], which also performs a simultaneous fit of the 2N and 3N force using ground-state properties of $A = 2$ –4 systems as well as saturation properties of nuclear matter, leads to promising results of ground-state energies and charge radii for a large range of finite nuclei up to mass numbers $A = 132$. However, its predicted NN phase shifts deviate from experiment in the P -wave channels [153].

In order to obtain a reliable extraction of the 3N couplings c_D and c_E in the large parameter space, the various sources of uncertainties, including EFT truncation errors, should be considered in the fitting procedure of statistical methods. Taking advantage of the method of eigenvector continuation [43, 44] for the construction of emulators, Ref. [154] analyzed the statistical uncertainties for the consistent solution of the triton binding energy, its β -decay rate, and the ground-state energy and charge radius of ${}^4\text{He}$ for fitting c_D and c_E using a Bayesian framework including theoretical and experimental errors. This analysis provides clear evidence that EFT truncation errors should be included in the fit to obtain meaningful and consistent results.

In this thesis, we mainly focus on two chiral interactions: The first given by the EMN NN interaction derived in Ref. [56] up to $N^4\text{LO}$ with cutoff values from $\Lambda = 400$ –550 MeV together with 3N forces constructed in Ref. [57] up to $N^3\text{LO}$ by fitting the 3N LECs to the ${}^3\text{H}$ binding energy and nuclear matter saturation properties, utilizing the same cutoff value as for the NN force. This allows for a consistent treatment of two- and three-body forces at $N^3\text{LO}$. We will refer to this interaction by “ $N^3\text{LO}$ ” followed by the cutoff value and indicate cases where we use the NN-only interaction. The second interaction, constructed in Ref. [54], is based on an NN force at $N^3\text{LO}$ and a 3N force at $N^2\text{LO}$, with the 3N couplings fit to only few-body data, specifically the ${}^3\text{H}$ binding energy and the charge radius of ${}^4\text{He}$. We refer to this interaction by “1.8/2.0 EM” in the following. Even though the many-body forces are treated at inconsistent chiral orders ($N^3\text{LO}$ and $N^2\text{LO}$) and the NN and 3N cutoffs are given by different values ($\Lambda_{\text{NN}} = 500$ MeV and $\Lambda_{3\text{N}} = 2.0$ fm $^{-1}$ [394 MeV]), this interaction leads to a remarkably good reproduction of ground-state energies of finite nuclei over a wide range of masses [49, 55, 75], while underpredicting their charge radii [55].

2.3 Renormalization group methods

Nuclear interactions are often characterized in terms of their perturbativeness (or softness), which indicates the degree of decoupling between high- and low-momentum modes in the potential and is closely related to its order-by-order convergence behavior in a perturbative many-body expansion [18]. Typically, chiral interactions show strong low- to high-momentum couplings as indicated by the dark red off-diagonal area in the left panel of Fig. 2.5. These couplings significantly complicate investigations at low-energy scales, as most basis-expansion-based methods profit from rather soft input interactions to achieve converged results in

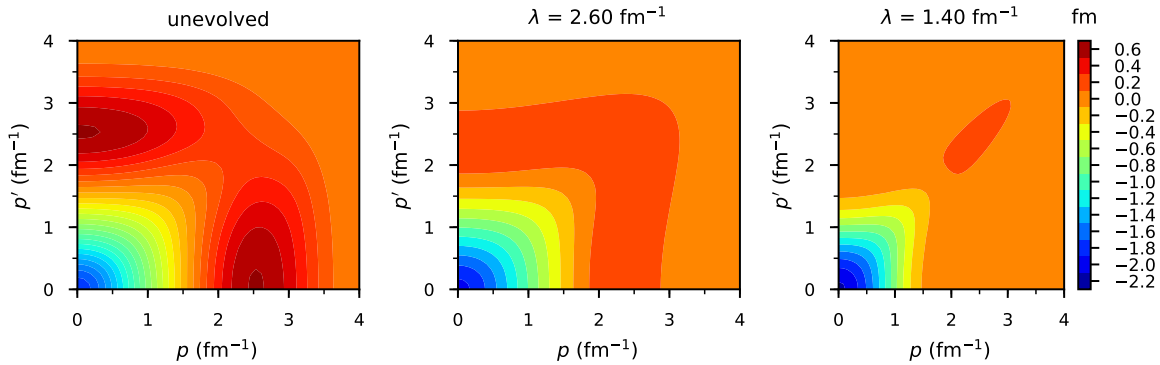


Figure 2.5: SRG evolution of the $N^3\text{LO}$ 500 NN interaction in momentum space in the 1S_0 partial-wave channel as a function of the magnitude of the initial and final relative momenta p and p' , respectively. The initial (unevolved) potential is shown in the left panel, and the SRG-evolved potentials to resolution scales $\lambda = 2.6 \text{ fm}^{-1}$ and $\lambda = 1.4 \text{ fm}^{-1}$ are shown in the middle and right panels, respectively.

reasonable model-space sizes, and perturbative calculations get more involved or even unfeasible at all for nonperturbative (hard) potentials [155]. Simply neglecting the troublesome couplings by cutting off all contributions from high momenta, e.g., by a regulator function, does not remedy the problem, as low-energy observables and phase-shifts do not stay invariant. A powerful method to decouple the momenta and obtain (softer) nuclear interactions at reduced resolution scales, while leaving low-energy observables invariant, is the SRG developed by Wegner [156, 157] as well as Glazek and Wilson [158, 159] in the 1990s. The SRG employs flow equations to drive the Hamiltonian to a band-diagonal form. Specifically, low-to high-momentum couplings with momentum transfers larger than the SRG resolution scale λ are exponentially suppressed. Figure 2.5 demonstrates the application of the SRG to a chiral NN interaction. Starting from the initial potential with strong off-diagonal couplings in the left panel, it shows the decoupling and resulting band-diagonal form as the potential is evolved to lower resolution scales λ in the middle and right panel.

The high-momentum couplings of the Hamiltonian get decoupled by a continuous sequence of unitary transformations $U(s)$ with the flow parameter s

$$H(s) = U(s)H(0)U^\dagger(s), \quad (2.18)$$

and we obtain the flow equation for the Hamiltonian by differentiating with respect to s

$$\begin{aligned} \frac{dH(s)}{ds} &= \frac{dU}{ds}H(0)U^\dagger + UH(0)\frac{dU^\dagger}{ds} \\ &= \frac{dU}{ds}U^\dagger UH(0)U^\dagger + UH(0)U^\dagger U\frac{dU^\dagger}{ds} \\ &= \frac{dU}{ds}U^\dagger H(s) + H(s)U\frac{dU^\dagger}{ds} \\ &= [\eta(s), H(s)], \end{aligned} \quad (2.19)$$

where we dropped the s -dependence of the transformation for brevity, used $\mathbb{1} = U^\dagger U$, $\frac{d}{ds}(UU^\dagger) = 0$, and replaced $\frac{dU}{ds}U^\dagger$ by the anti-Hermitian generator $\eta(s)$. The SRG resolution scale λ , also shown in Fig. 2.5, is directly related to the flow parameter by $\lambda = s^{-1/4}$

and characterizes the degree of decoupling as well as the width of the band diagonal.

An alternative approach to decoupling high- and low-momenta is given by the RG method, which leads to a block-diagonal form of the low-momentum interaction, usually referred to as $V_{\text{low } k}$. In this method, a set of coupled differential equations is solved to achieve the decoupling and contributions above a chosen cutoff value are set to zero afterwards, therefore reducing the size of the block matrix for smaller cutoff values Λ . Moreover, RG methods have recently been applied to short-range correlation physics to investigate the relation between a high- and low-resolution description [160, 161]. The following discussion and all applications in this thesis focus on the SRG approach.

In general, any anti-Hermitian operator can be employed for the generator in Eq. (2.19), where the specific form defines the decoupling pattern for the Hamiltonian. The generator can be expressed in terms of a commutator relation

$$\eta(s) = [G(s), H(s)] , \quad (2.20)$$

with a Hermitian operator $G(s)$ and the flowing Hamiltonian. A widely used choice for $G(s)$ is the intrinsic kinetic energy operator T_{int} . This choice will lead to the desired decoupling, as the kinetic energy operator is diagonal in momentum space. We obtain a fix point of the evolution once the Hamiltonian is diagonal and therefore commutes with T_{int} and the generator $\eta(s) = [T_{\text{int}}, H(s)]$ turns zero. A large variety of generator choices is possible and has been investigated in the literature, see, e.g., Refs. [162–164].

However, this decoupling is not achieved for free and many-body forces get induced during the flow. Based on the commutator equation in Eq. (2.19), we induce many-body operators of higher ranks during the commutator evaluation, with the maximum rank r given by

$$r([A, B]) = r(A) + r(B) - 1 . \quad (2.21)$$

This can most easily be seen by the schematic example of a two-body force and a two-body generator in second quantization (see Sec. 3.1 for an introduction to operators in second quantization and operator products). The result of the commutator reads

$$\left[\sum a^\dagger a^\dagger a a, \sum a^\dagger a^\dagger a a \right] = \dots + \sum a^\dagger a^\dagger a a + \sum a^\dagger a^\dagger a^\dagger a a a , \quad (2.22)$$

where we highlight the induced three-body contribution in red that results from evaluating one contraction between the operators. Truncating the unitary transformation at a chosen many-body rank (smaller than the system size A) breaks its unitarity and calculated observables of higher-particle rank do not remain unchanged by this truncation and consequently show a resolution-scale dependence on the SRG parameter λ . Nevertheless, observables up to the chosen many-body rank still remain invariant under the transformation. For instance, consistently evolving the NN and 3N contributions and applying a truncation at the three-body level keeps the binding energy in $A = 3$ system, i.e., the triton, invariant, while ground-state energies of finite nuclei with mass numbers of $A > 3$ may show sensitivity to λ . Figure 2.6 shows the invariance of the triton binding energy if all induced terms are kept up to the three-body level by comparing the triton binding energy as a function of λ for an SRG-evolved NN-only force with and without keeping the induced three-body contributions, and a consistently SRG-evolved NN+3N interaction with keeping the induced 3N contributions. Consequently, one does not aim for a completely diagonal form of the

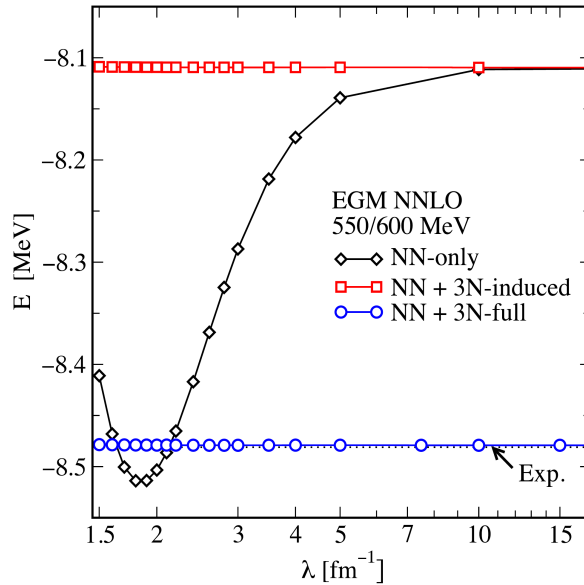


Figure 2.6: Triton ground-state energy as a function of the SRG resolution scale λ for the chiral N^2LO NN interaction of Ref. [165] (EGM) and N^2LO 3N forces [149]. Results are shown for the evolved NN-only interaction (black diamonds), the evolved NN interaction keeping the induced 3N contributions labeled NN+3N-induced (red squares), and the consistently evolved NN and 3N interaction again keeping the induced 3N contributions labeled NN+3N-full (blue circles) compared to the experimental value (black-dotted line). Adjusted Figure of Ref. [166] taken from Ref. [72] with data courtesy of K. Hebeler.

potential in the limit $s \rightarrow \infty$ ($\lambda \rightarrow 0$), as induced many-body forces will get significantly enhanced, but rather evolves to a finite value of s , where the interaction is reasonably soft and the induced many-body forces are mostly small or of negligible size. Typical values for soft SRG-evolved interactions are around $\lambda = 1.8 \text{ fm}^{-1}$.

In this thesis, we use the SRG to soften the chiral input interactions and obtain potentials at lower resolution scales. Considering the two interactions introduced in Sec. 2.2, we investigate both unevolved and consistently SRG-evolved NN+3N forces in momentum space for the N^3LO interaction, which also incorporate the induced 3N contributions [166]. Higher many-body forces beyond the three-body level, which are induced during the evolution, are neglected. The 1.8/2.0 EM interaction consists of a mixture of evolved NN and unevolved 3N interactions, with the NN force being SRG-evolved to $\lambda = 1.8 \text{ fm}^{-1}$ and the 3N interaction being fitted in combination with this NN interaction.

2.4 Singular value decomposition

Nuclear many-body interactions are conveniently stored in a relative momentum-space basis using a discretized Gauss momentum mesh. Especially storing three-body operator matrix elements, which are important for a quantitative description of finite nuclei and nuclear matter properties (see, e.g., Refs. [130, 167]), provides a key challenge regarding the required memory. This becomes even more severe for operator matrix elements stored in a single-particle basis (see Sec. 3.1), which is the standard input to most many-body basis-expansion

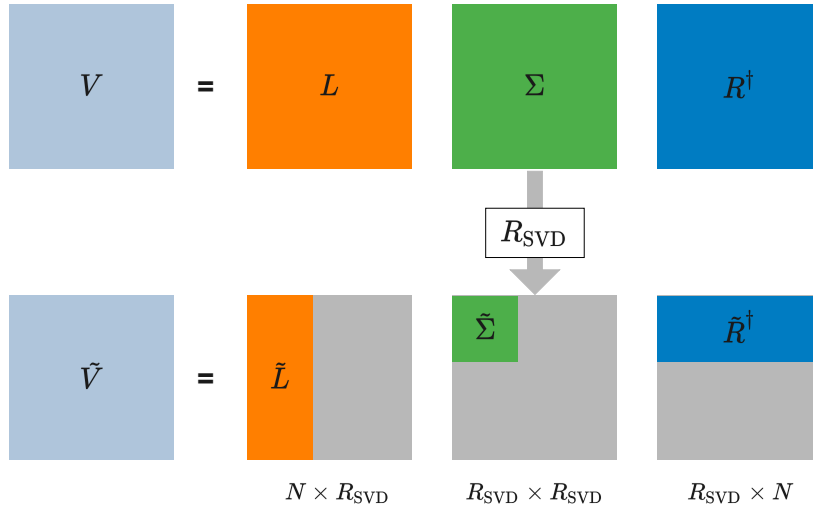


Figure 2.7: Schematic representation of the SVD approach. The upper panel shows the full SVD considering all singular values, yielding an exact decomposition of the matrix V . The lower panel shows the truncated SVD, truncating all singular values beyond rank R_{SVD} , leading to an approximate representation of V indicated by \tilde{V} , a truncated diagonal matrix $\tilde{\Sigma}$ of dimension $R_{\text{SVD}} \times R_{\text{SVD}}$, and truncated matrices of left and right singular vectors, \tilde{L} and \tilde{R}^\dagger , respectively, where we assumed the initial matrix V to be of dimension N .

methods. Hence, finding alternative suitable operator basis choices to effectively reduce the memory footprint of the employed many-body operators would allow for substantial benefits in practical applications.

In this section, we introduce tensor-factorization techniques, which provide a powerful tool to approximate high-dimensional objects by sums of low-dimensional ones (see, e.g., Refs. [168–170]). This reduces the required storage and possibly lowers the computational cost for calculations involving the compressed objects. In particular, we present the singular value decomposition (SVD) following our work in Ref. [171] as one possible application of tensor-factorization methods to approximate chiral interactions by a low-rank decomposition. These low-rank interactions discard unimportant information of the full interaction matrix, given by small decomposition factors of the SVD, and hence significantly reduce the required storage at the price of a small decomposition error. Applications of the SVD have already been successfully applied in sensitivity studies of energy density functionals [172], for investigations of shell-model interactions [173–175], in electrodisintegration studies [176], or as tools for generalized eigenvalue problems [177]. Moreover, low-rank interactions have also been obtained based on expansions in Weinberg eigenvalues [148, 178, 179].

The SVD of a matrix V is defined by

$$V = L\Sigma R^\dagger, \quad (2.23)$$

where L and R^\dagger are the matrices of left and right singular vectors, respectively, and the diagonal matrix $\Sigma = \text{diag}(s_i)$ contains the set of nonnegative singular values s_i in descending order. The columns of the matrices of left and right singular vectors L and R^\dagger , respectively, are orthonormal, i.e., L and R^\dagger are unitary matrices. The SVD is a particularly versatile factorization ansatz because it naturally extends to non-Hermitian and nonsquare matrices

based on the decomposition using distinct matrices L and R^\dagger . This is a feature not shared by some other common matrix decomposition approaches, such as the eigenvalue decomposition $V = QDQ^\dagger$, where Q is a square matrix with columns given by the eigenvectors and D is the diagonal matrix of eigenvalues, or the Cholesky decomposition $V = KK^\dagger$, where K is a lower triangular matrix. These methods typically require one single matrix and its inverse or transposed for the decomposition as well as additional prerequisites for V .

In the following, we apply the truncated SVD

$$\tilde{V} \equiv \tilde{L}\tilde{\Sigma}\tilde{R}^\dagger, \quad (2.24)$$

where all singular values s_i beyond a chosen decomposition rank R_{SVD} are discarded, i.e.,

$$\tilde{\Sigma} \equiv \text{diag}(s_1, \dots, s_{R_{\text{SVD}}}, 0, \dots, 0), \quad (2.25)$$

such that only the first R_{SVD} columns of L and R_{SVD} rows of R^\dagger need to be stored, indicated by the tilde on top of the objects in Eq. (2.24). The truncated matrices consequently have dimensions of $N \times R_{\text{SVD}}$, $R_{\text{SVD}} \times R_{\text{SVD}}$, and $R_{\text{SVD}} \times N$, for \tilde{L} , $\tilde{\Sigma}$, and \tilde{R}^\dagger , respectively. This is schematically shown in Fig. 2.7, where the upper panel shows the decomposition for the full matrix, taking into account all singular values in Σ , and the lower panel shows the truncated SVD, considering only the first R_{SVD} singular values. According to the Eckart-Young theorem [180], the truncated SVD matrix \tilde{V} provides the best rank- R_{SVD} approximation to V in the sense of minimizing

$$\|\Delta V\|_{\text{F}}^2 \equiv \|V - \tilde{V}\|_{\text{F}}^2, \quad (2.26)$$

where $\|\cdot\|_{\text{F}}$ denotes the Frobenius norm. Comparing the storage requirements of the full interaction matrix, given by N^2 for a matrix of dimension N , to the storage requirements of the truncated factors, given by $2NR_{\text{SVD}} + R_{\text{SVD}}$ [see Eq. (2.24) and Fig. 2.7], allows one to define the compression

$$C_{R_{\text{SVD}}} \equiv \frac{N^2}{2NR_{\text{SVD}} + R_{\text{SVD}}} \quad (2.27)$$

as the ratio of the initially required storage divided by the storage after factorization. The higher the compression, the higher the computational savings. However, higher compression typically comes at the price of inducing higher decomposition errors by truncating at smaller R_{SVD} , such that in practice a balance has to be found.

In this thesis, we apply the SVD to chiral NN interactions in a partial-wave decomposed momentum-space basis, defined as

$$\langle p(LS)JTM_T | V_{\text{NN}} | p'(L'S)JTM_T \rangle, \quad (2.28)$$

with the initial (final) orbital angular momentum L (L'), the two-body spin S , the total-angular momentum J , whose projection M_J we omit as the NN interaction does not depend on it, and the two-body isospin T with projection M_T . In particular, we investigate the magnitude of the singular values as well as the predictions of low-rank chiral potentials stemming from a truncated SVD for NN phase shifts. We additionally apply low-rank interactions in the IMSRG in Sec. 3.6 and study their performance for calculations of ground-

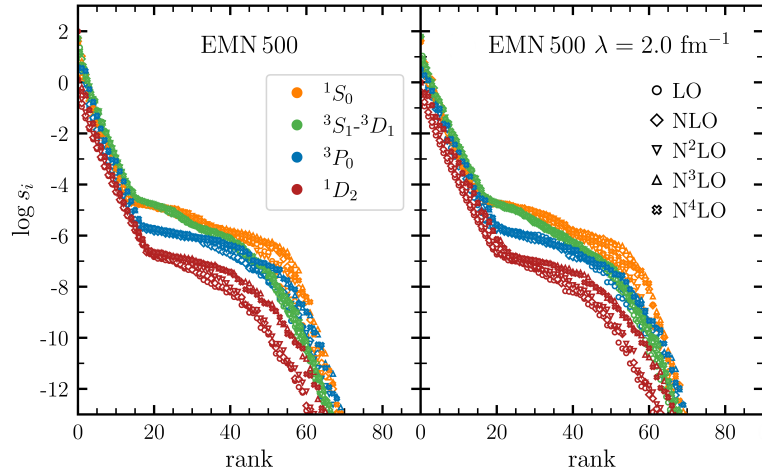


Figure 2.8: Singular values s_i of the unevolved (left) and SRG-evolved to $\lambda = 2.0 \text{ fm}^{-1}$ (right) EMN 500 interaction of Ref. [56] on a logarithmic scale as a function of SVD rank. We show the different partial-wave channels 1S_0 , 3S_1 - 3D_1 , 3P_0 , and 1D_2 in orange, green, blue, and red, respectively, and consider the potentials at multiple chiral orders from LO to N⁴LO indicated by different symbols. In the coupled 3S_1 - 3D_1 deuteron channel, the rank was divided by two in order to account for the effective doubling of the matrix dimension. Figure taken from Ref. [171].

state energies of finite nuclei. All results shown in this section and in Sec. 3.6 are part of our already published work in Ref. [171] and we refer to this reference for more details and further applications.

In Fig. 2.8, we show the magnitude of the singular values s_i for the unevolved and SRG-evolved EMN 500 NN interaction of Ref. [56] at different chiral orders, ranging from LO to N⁴LO, and in different partial-wave channels. We observe a rapid fall-off of singular values down to magnitudes below 10^{-4} – 10^{-5} from rank $R_{\text{SVD}} \approx 20$ on. This behavior is the same in all partial-wave channels. The rank is effectively doubled in the deuteron channel due to the coupling of the 3S_1 - 3D_1 blocks and we divided the rank by two for a better comparison of the different partial-wave channels. Moreover, partial waves with higher angular momenta, e.g., the 3P_0 and 1D_2 channels, generally have smaller singular values. All of the above features are independent of the chiral order, and no systematic differences arise at different chiral orders. This shows that the low-rank properties of chiral interactions are not spoiled by the presence of more complicated operator structures that enter with higher-order pion exchanges or higher-order short-range interactions. Comparing the two panels in Fig. 2.8 indicates that the SRG-evolution does not affect the singular value behavior either. Although momentum-space matrix elements are different for the unevolved and SRG-evolved interaction, the SRG has little effect on the SVD fall-off of singular values.

As a next step, we benchmark the predictions of low-rank nuclear potentials in the two-body system and investigate NN scattering phase shifts obtained by solving the Lippmann-Schwinger integral equation for the truncated SVD interaction \tilde{V}

$$\begin{aligned} \langle p(LS)J|T|p'(L'S)J \rangle &= \langle p(LS)J|\tilde{V}|p'(L'S)J \rangle \\ &+ \frac{2}{\pi} \sum_{L''} \int_0^\infty dq q^2 \frac{\langle p(LS)J|\tilde{V}|q(L''S)J \rangle \langle q(L''S)J|T|p'(L'S)J \rangle}{E - \frac{q^2}{M} + i\epsilon}, \end{aligned} \quad (2.29)$$

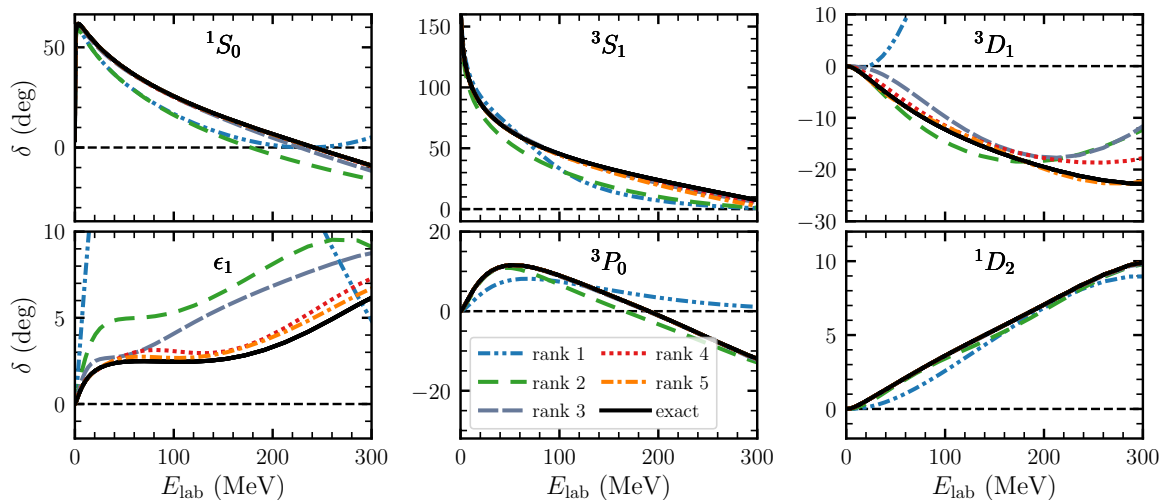


Figure 2.9: Nucleon-nucleon phase shifts of the $N^3\text{LO } 500$ interaction as a function of the laboratory energy E_{lab} for the partial-wave channels 1S_0 , 3S_1 , 3D_1 , 3P_0 , and 1D_2 as well as the mixing angle ϵ_1 for the deuteron channel in the bottom left panel. We show results for different SVD ranks of $R_{\text{SVD}} = 1\text{--}5$ indicated by different line styles and colors compared to exact results given by the black solid line. Figure taken from Ref. [171].

where T denotes the scattering T matrix that is evaluated right-on-shell, i.e., $E = \frac{p'^2}{2M}$, and we suppress the dependence on the isospin and its projection for brevity.

In Fig. 2.9, we compare NN scattering phase shifts for different low-rank approximations of the unevolved $N^3\text{LO } 500$ interaction to exact results up to laboratory energies of $E_{\text{lab}} = 300$ MeV, using the same set of partial-wave channels as in Fig. 2.8. For very small SVD ranks, i.e., $R_{\text{SVD}} = 1$ or 2, scattering phase shifts obtained from the low-rank potentials show significant deviations compared to the exact calculations in the shown energy range. By including more components in the decomposition, the deviation to the exact result is systematically reduced, and at ranks $R_{\text{SVD}} \gtrsim 5$ we observe a very quantitative reproduction of the exact phase shifts over the entire energy regime. The difference $\Delta\delta$ to exact results for $R_{\text{SVD}} = 5$ is below 1 degree in all partial-wave channels, with only noticeable differences at higher E_{lab} . In the deuteron channel, we also show the mixing angle ϵ_1 , which is sensitive to all contributing subblocks in the 3S_1 - 3D_1 channel (including the off-diagonal 3SD_1 and 3DS_1 blocks with $L = 0, L' = 2$ and $L = 2, L' = 0$, respectively). For energies $E_{\text{lab}} > 150$ MeV, the difference to the exact mixing angle is about $\Delta\epsilon_1 = 1$ degree for $R_{\text{SVD}} = 5$. When increasing the rank to $R_{\text{SVD}} = 15$ (not shown in Fig. 2.9) virtually exact results are obtained. These benchmarks clearly demonstrate the low-rank properties of the chiral two-body interaction.

3

In-Medium Similarity Renormalization Group

In this chapter, we introduce the nonperturbative IMSRG as a versatile and powerful tool to solve the nuclear many-body problem for a large range of mass numbers from light up to medium-heavy nuclei of $A \approx 132$ [49, 50, 55]. The IMSRG aims at decoupling the ground state from all excited states by a continuous sequence of unitary transformations of the normal-ordered Hamiltonian. It therefore allows to study ground- and excited-state observables of finite nuclei in a computationally efficient way. Considering all A -body operators in an A -body system would result in an exact solution of the many-body problem. However, the computational challenges involved in treating all A -body operators make a complete consideration intractable, and a reasonable truncation scheme of including only a restricted number of many-body operators is required. Practical calculations in converged model-space sizes are currently limited to the normal-ordered two-body level for the operators and allow for a mild polynomial scaling in mass number. The IMSRG in a given truncation scheme belongs to the class of approximate many-body methods (see Fig. 1.1) accounting for additional correlation effects on top of an A -body reference state, such as CC, SCGF, and MBPT theory. In this thesis, we focus on the application to closed-shell nuclei with a single Slater determinant reference state and limit our studies to ground-state observables. Extensions of the closed-shell single-reference IMSRG in terms of the valence-space IMSRG (VS-IMSRG) [32, 70, 94], the multi-reference IMSRG (MR-IMSRG) [72], and the Bogoliubov IMSRG (BIMSG) are however capable of targeting open-shell systems, with both the VS- and MR-IMSRG being successfully applied to finite nuclei (see, e.g., Refs. [68, 75, 181, 182]). Additionally, the diagonalization of an effective valence-space Hamiltonian in the VS-IMSRG allows for the study of excited-state observables, such as excitation energies or electromagnetic transition strengths.

The structure of this chapter is as follows. In Sec. 3.1, we discuss the general representation of operators and states in second quantization as well as the framework of normal ordering with respect to a chosen reference state in a single-particle basis. The Hartree-Fock approach is outlined in Sec. 3.2, and we give a short overview of three selected many-body methods: the NCSM, CC theory, and MBPT in Sec. 3.3, before focusing in more detail on the IMSRG in Sec. 3.4. We introduce the commonly employed truncation scheme of the *ab initio* IMSRG at the two-body level, the IMSRG(2), give the corresponding fundamental commutators, and show possible generator choices to obtain the desired decoupling of the ground state. Finally, we conclude this chapter by discussing the extension of the IMSRG many-body truncation to the next order by including three-body operators in the IMSRG(3) in Sec. 3.5.

3.1 Second quantization and normal ordering

In this section, we introduce the basic concepts of operators and many-body states in a second-quantized form and discuss the framework of normal ordering with respect to a chosen reference state. The fermionic creation operator a^\dagger and annihilation operator a either create or destroy a particle, respectively, in a specified single-particle state,

$$a_p^\dagger |0\rangle = |p\rangle, \quad (3.1)$$

$$a_q |p\rangle = \delta_{pq} |0\rangle, \quad (3.2)$$

where $|0\rangle$ is the vacuum state containing no particles and $|p\rangle$ is a single-particle state with one fermion in the state indicated by the collective index p . The operators obey the anticommutation relations given by

$$\{a_p^\dagger, a_q\} = \delta_{pq}, \quad (3.3a)$$

$$\{a_p^\dagger, a_q^\dagger\} = 0, \quad (3.3b)$$

$$\{a_p, a_q\} = 0. \quad (3.3c)$$

Making use of the creation and annihilation operators, we formulate an A -body state $|\Phi\rangle$ in the Hilbert space constructed by the product of A single-particle states, indicated by a string of creation operators acting on the vacuum

$$|\Phi\rangle = |p_1 p_2 \cdots p_A\rangle = a_{p_1}^\dagger a_{p_2}^\dagger \cdots a_{p_A}^\dagger |0\rangle = \prod_{i=1}^A a_{p_i}^\dagger |0\rangle. \quad (3.4)$$

Such an antisymmetrized product state of single-particle states is called a Slater determinant [183], with the antisymmetry immediately following from the anticommutation relations in Eq. (3.3). In addition to the single-particle and many-body states, any general A -body operator can be represented in second-quantized form. For example, a two-body operator, such as the two-body interaction $V^{(2)}$, in second-quantized form reads

$$V^{(2)} = \frac{1}{(2!)^2} \sum_{pqrs} \langle pq | V^{(2)} | rs \rangle a_p^\dagger a_q^\dagger a_s a_r, \quad (3.5)$$

where we assume that the matrix elements $\langle pq | V^{(2)} | rs \rangle = V_{pqrs}$ are fully antisymmetrized. The formulation naturally extends to three- and higher n -body operators by the prefactor $(1/n!)^2$ and the corresponding n creation and n annihilation operators together with the n -body matrix elements. We can thus write a three-body interaction $V^{(3)}$ as

$$V^{(3)} = \frac{1}{36} \sum_{pqrstu} \langle pqr | V^{(3)} | stu \rangle a_p^\dagger a_q^\dagger a_r^\dagger a_u a_t a_s. \quad (3.6)$$

The two-body operator in Eq. (3.5) [as well as three-body operator in Eq. (3.6)] is already in normal-ordered form, denoted by sorting all creation operators to the left and all annihilation operators to the right-hand side. This is accomplished by using the anticommutation relations in Eq. (3.3). The string of creation and annihilation operators normal-ordered with respect

to the vacuum always vanishes,

$$\langle 0 | : a_p^\dagger a_q^\dagger a_s a_r : | 0 \rangle = 0, \quad (3.7)$$

due to Eqs. (3.1) and (3.2), where the colons indicate the normal ordering of the string of operators.

A more generic representation of normal-ordered operators can be obtained by performing the normal ordering with respect to a chosen reference state $|\Phi\rangle$ instead of the vacuum state $|0\rangle$, leading to an in-medium optimized form of the operator [184]. In general, this can be any A -body state, but in this thesis we focus on single Slater-determinant reference states, as e.g., an HF reference state (see Sec. 3.2). Employing more sophisticated reference states, such as a multi-reference or symmetry-breaking reference state in the normal ordering leads to more complicated expressions (see, e.g., Refs. [72, 185, 186]) and will not be discussed in detail in this thesis. Normal ordering with respect to a given reference state is obtained by using Wick's theorem [187], summing over all possible single, double, ..., and full contractions, where one contraction is defined as the reference-state expectation value of the contracted operators

$$\overline{a_p^\dagger a_q} = \langle \Phi | a_p^\dagger a_q | \Phi \rangle. \quad (3.8)$$

For the case of one pair of creation and annihilation operators we just have one possible contraction and consequently Wick's theorem gives

$$a_p^\dagger a_q = : a_p^\dagger a_q :_{|\Phi\rangle} + \overline{a_p^\dagger a_q}, \quad (3.9)$$

with the colon index indicating the normal ordering with respect to the reference state $|\Phi\rangle$. Using Wick's theorem for a generic string of A creation and A annihilation operators, we are able to obtain the normal-ordered expression

$$\begin{aligned} a_{p_1}^\dagger a_{p_2}^\dagger \cdots a_{p_A}^\dagger a_{q_A} \cdots a_{q_2} a_{q_1} &= : a_{p_1}^\dagger a_{p_2}^\dagger \cdots a_{p_A}^\dagger a_{q_A} \cdots a_{q_2} a_{q_1} :_{|\Phi\rangle} \\ &+ \sum_{\text{single contractions}} : \overbrace{a_{p_1}^\dagger a_{p_2}^\dagger \cdots a_{p_A}^\dagger a_{q_A} \cdots a_{q_2} a_{q_1}} :_{|\Phi\rangle} \\ &+ \sum_{\text{double contractions}} : \overbrace{a_{p_1}^\dagger a_{p_2}^\dagger \cdots a_{p_A}^\dagger a_{q_A} \cdots a_{q_2} a_{q_1}} :_{|\Phi\rangle} \\ &+ \dots \\ &+ \sum_{\text{full contractions}} : \overbrace{a_{p_1}^\dagger a_{p_2}^\dagger \cdots a_{p_A}^\dagger a_{q_A} \cdots a_{q_2} a_{q_1}} :_{|\Phi\rangle}, \end{aligned} \quad (3.10)$$

where the sums indicate all possible single, double, ..., and full contractions. Note that the contractions are just defined for neighboring operators and we have to anticommute the corresponding operators next to each other in the normal-ordered string, leading to additional phases in the evaluation. The same arguments as for the vacuum normal ordering in Eq. (3.7) yield

$$\langle \Phi | : a_{p_1}^\dagger a_{p_2}^\dagger \cdots a_{p_A}^\dagger a_{q_A} \cdots a_{q_2} a_{q_1} :_{|\Phi\rangle} | \Phi \rangle = 0 \quad (3.11)$$

for an operator normal ordered with respect to the reference state $|\Phi\rangle$. We will drop the

reference state index of the normal-ordered operators for brevity in the following. By applying the anticommutation relation for the contractions, we can determine two nonvanishing contributions for the reference state $|\Phi\rangle$

$$\overline{a_p^\dagger a_q} = \langle \Phi | a_p^\dagger a_q | \Phi \rangle = \gamma_{pq}, \quad (3.12a)$$

$$\overline{a_p a_q^\dagger} = \langle \Phi | a_p a_q^\dagger | \Phi \rangle = \langle \Phi | \delta_{pq} - a_q^\dagger a_p | \Phi \rangle = \delta_{pq} - \gamma_{pq}, \quad (3.12b)$$

where γ_{pq} is the one-body density matrix, and two vanishing contributions

$$\overline{a_p a_q} = \langle \Phi | a_p a_q | \Phi \rangle = 0, \quad (3.13a)$$

$$\overline{a_p^\dagger a_q^\dagger} = \langle \Phi | a_p^\dagger a_q^\dagger | \Phi \rangle = 0, \quad (3.13b)$$

with the two terms in Eq. (3.13) vanishing independently of the reference state. Working in the eigenbasis of the one-body density matrix $\gamma_{pq} = n_p \delta_{pq}$ with occupation numbers $n_p \in \{0, 1\}$ given by the eigenvalues, allows for simplifications of the following expressions. We can distinguish two classes of single-particle states, hole and particle states, depending on their occupation number in the reference state

$$n_p = \begin{cases} 1, & \text{if } p \text{ is a hole state,} \\ 0, & \text{if } p \text{ is a particle state.} \end{cases} \quad (3.14)$$

The two nonvanishing contractions in Eq. (3.12) in the eigenbasis can be written as

$$\overline{a_p^\dagger a_q} = n_p \delta_{pq}, \quad (3.15a)$$

$$\overline{a_p a_q^\dagger} = \delta_{pq} (1 - n_p). \quad (3.15b)$$

The contractions in Eqs. (3.15a) and (3.15b) only contribute for hole and particle states, respectively, due to the corresponding occupation number. We will come back to the eigenbasis of the one-body density matrix in more detail when defining the natural orbital single-particle basis in Sec. 4.1.1.

A key factor when solving the many-body Schrödinger equation and deriving the IMSRG flow equations is the intrinsic Hamiltonian. In vacuum normal order, the Hamiltonian, here up to the three-body level, is given by

$$H = \left(1 - \frac{1}{A}\right) T^{(1)} + T^{(2)} + V^{(2)} + V^{(3)}, \quad (3.16)$$

with the two-body interaction $V^{(2)}$, the three-body interaction $V^{(3)}$, and the one- and two-body parts of the kinetic energy $T^{(1)}$ and $T^{(2)}$, respectively, defined by

$$T^{(1)} = \sum_p \frac{\mathbf{p}_p^2}{2M}, \quad (3.17a)$$

$$T^{(2)} = -\frac{1}{A} \sum_{p < q} \frac{\mathbf{p}_p \mathbf{p}_q}{M}, \quad (3.17b)$$

where \mathbf{p}_p and \mathbf{p}_q are the momenta of particles p and q , respectively, and M is the nucleon mass. In the following, we write all operators in second quantization and utilize Wick's theorem to derive the normal-ordered intrinsic Hamiltonian with respect to a single-reference state. The application of Wick's theorem is exemplarily illustrated for the normal ordering of the two-body interaction $V^{(2)}$, employing the anticommutation relations of Eq. (3.3) and the contraction definitions of Eq. (3.15):

$$\begin{aligned}
& \frac{1}{4} \sum_{pqrs} V_{pqrs} a_p^\dagger a_q^\dagger a_s a_r \\
&= \frac{1}{4} \sum_{pqrs} V_{pqrs} : a_p^\dagger a_q^\dagger a_s a_r : \\
&+ \frac{1}{4} \sum_{pqrs} V_{pqrs} \left(: \overline{a_p^\dagger a_q^\dagger a_s a_r} : + : \overline{a_p^\dagger a_q^\dagger a_s} a_r : + : \overline{a_p^\dagger a_q^\dagger} a_s a_r : + : \overline{a_p^\dagger a_q^\dagger a_s} a_r : \right) \\
&+ \frac{1}{4} \sum_{pqrs} V_{pqrs} \left(: \overline{a_p^\dagger a_q^\dagger a_s} a_r : + : \overline{a_p^\dagger a_q^\dagger} a_s a_r : \right) \\
&= \frac{1}{4} \sum_{pqrs} V_{pqrs} : a_p^\dagger a_q^\dagger a_s a_r : + \sum_{pqs} V_{pqp}s n_p : a_q^\dagger a_s : + \frac{1}{2} \sum_{pq} V_{ppq} n_p n_q,
\end{aligned} \tag{3.18}$$

where we used that the matrix elements $V_{pqrs} = \langle pq | V^{(2)} | rs \rangle$ are fully antisymmetrized to simplify the four (two) terms arising from the single (double) contractions. The final three terms in the last row contribute to the normal-ordered two-, one-, and zero-body part of the Hamiltonian, respectively, as indicated by the corresponding number of normal-ordered creation and annihilation operators.

Applying Wick's theorem to all operators on the right-hand side of Eq. (3.16), the complete normal-ordered Hamiltonian up to the three-body rank reads

$$H = E + \sum_{pq} f_{pq} : a_p^\dagger a_q : + \frac{1}{4} \sum_{pqrs} \Gamma_{pqrs} : a_p^\dagger a_q^\dagger a_s a_r : + \frac{1}{36} \sum_{pqrst} W_{pqrst} : a_p^\dagger a_q^\dagger a_r^\dagger a_u a_t a_s :, \tag{3.19}$$

with the normal-ordered zero-, one-, two-, and three-body parts E , f_{ij} , Γ_{ijkl} , and W_{ijklmn} , respectively, given by

$$E = \left(1 - \frac{1}{A}\right) \sum_p T_{pp}^{(1)} n_p + \frac{1}{2} \sum_{pq} (T_{ppq}^{(2)} + V_{ppq}^{(2)}) n_p n_q + \frac{1}{6} \sum_{pqr} V_{pqr}^{(3)} n_p n_q n_r, \tag{3.20a}$$

$$f_{12} = \left(1 - \frac{1}{A}\right) T_{12}^{(1)} + \sum_p (T_{1p2p}^{(2)} + V_{1p2p}^{(2)}) n_p + \frac{1}{2} \sum_{pq} V_{1pq2pq}^{(3)} n_p n_q, \tag{3.20b}$$

$$\Gamma_{1234} = T_{1234}^{(2)} + V_{1234}^{(2)} + \sum_p V_{12p34p}^{(3)} n_p, \tag{3.20c}$$

$$W_{123456} = V_{123456}^{(3)}, \tag{3.20d}$$

where external indices of the Hamiltonian are indicated by numbers and internal indices by p , q , and r . We emphasize that the normal-ordered zero-, one-, and two-body part contain contributions from the three-body interaction $V^{(3)}$ due to the normal ordering.

The product of two normal-ordered operators can be calculated by applying the so-called generalized Wick theorem to evaluate contractions between two normal-ordered operators. The product of an A - and B -body operator, both normal-ordered with respect to the same reference state, can therefore be expressed as

$$\begin{aligned}
& : a_{p_1}^\dagger \dots a_{p_A}^\dagger a_{q_A} \dots a_{q_1} : \times : a_{r_1}^\dagger \dots a_{r_B}^\dagger a_{s_B} \dots a_{s_1} : \\
& = (-1)^{AB} : a_{p_1}^\dagger \dots a_{p_A}^\dagger a_{r_1}^\dagger \dots a_{r_B}^\dagger a_{q_A} \dots a_{q_1} a_{s_B} \dots a_{s_1} : \\
& \quad + (-1)^{AB} \sum_{\text{single contractions}} : \overbrace{a_{p_1}^\dagger \dots a_{p_A}^\dagger a_{r_1}^\dagger \dots a_{r_B}^\dagger a_{q_A} \dots a_{q_1} a_{s_B} \dots a_{s_1}} : \\
& \quad + (-1)^{AB} \sum_{\text{double contractions}} : \overbrace{a_{p_1}^\dagger \dots a_{p_A}^\dagger a_{r_1}^\dagger \dots a_{r_B}^\dagger a_{q_A} \dots a_{q_1} a_{s_B} \dots a_{s_1}} : \\
& \quad + \dots,
\end{aligned} \tag{3.21}$$

with contractions only being evaluated between the operator strings of the A - and B -body operator and not within the same operator. Ordering all B creation operators of the initial B -body operator to the left past the A annihilation operators of the A -body operator results in the phase prefactor $(-1)^{AB}$ in the above equation. Multiplying normal-ordered operators by using the generalized Wick theorem will become important when we derive the flow equations for the IMSRG framework in Sec. 3.3.

3.2 Hartree-Fock method

The Hartree-Fock method is a variational mean-field approach to determine the single Slater-determinant approximation to the ground-state wave function that results in a minimization of the ground-state energy (see, e.g., Ref. [188]). Each nucleon moves in a mean-field potential given by the average interaction with all other nucleons and no explicit two-, three- or higher-body interactions among the single particles are considered. The “best” single Slater determinant is found using the variational principle, leading to the lowest energy expectation value in the space of single Slater determinants. The HF reference state therefore provides a good starting point for any many-body calculation that performs a correlation expansion around a single-reference state. Hartree-Fock approaches are not only limited to applications in nuclear theory but are also standard methods in other research fields, e.g., quantum chemistry. In the following, we introduce the main concepts and the application of the HF method to nuclear theory (for finite nuclei).

The exact many-body ground-state wave function $|\Psi\rangle$ minimizes the energy functional

$$E[|\Psi\rangle] = \frac{\langle\Psi|H|\Psi\rangle}{\langle\Psi|\Psi\rangle}, \tag{3.22}$$

where the denominator ensures the normalization. In general, the ground-state wave function can be very complicated in structure depending on the studied system and is given by a superposition of many Slater determinants. Considering the many-body state in terms of a single Slater determinant is therefore only an approximation and the energy functional for

the approximate state $|\Psi^{\text{approx}}\rangle$ is given by

$$E[|\Psi^{\text{approx}}\rangle] = \frac{\langle \Psi^{\text{approx}} | H | \Psi^{\text{approx}} \rangle}{\langle \Psi^{\text{approx}} | \Psi^{\text{approx}} \rangle}. \quad (3.23)$$

We aim to solve for the single Slater determinant $|\Psi^{\text{approx}}\rangle = |\text{HF}\rangle$ with the lowest energy expectation value or, in other words, find the wave function that minimizes the energy functional (3.22) in the space of single Slater determinants.

The Slater determinant for A nucleons is constructed from the corresponding number of single-particle states in the HF basis

$$|\text{HF}\rangle = |p_1 p_2 \cdots p_A\rangle = \prod_{i=1}^A c_{p_i}^\dagger |0\rangle, \quad (3.24)$$

where each single-particle state in the HF basis can be expressed in terms of the underlying chosen single-particle basis. Most commonly, the harmonic oscillator (HO) basis presents an appropriate choice. Expanding the single-particle HF states in the HO basis gives

$$|p\rangle_{\text{HF}} = \sum_q C_{qp} |q\rangle_{\text{HO}}, \quad (3.25)$$

with the expansion coefficients C_{qp} of the basis transformation

$$C_{qp} = {}_{\text{HO}}\langle q | p \rangle_{\text{HF}}, \quad (3.26)$$

where the subscripts HO and HF identify states in the corresponding single-particle basis and the creation operators c_p^\dagger in the HF basis and a_q^\dagger in the HO basis are given by

$$c_p^\dagger = \sum_q C_{qp} a_q^\dagger, \quad (3.27a)$$

$$a_q^\dagger = \sum_p C_{qp}^* c_p^\dagger, \quad (3.27b)$$

respectively. The transformation is unitary, with $C^\dagger C = \mathbb{1}$, and consequently the resulting HF single-particle states constitute an orthonormal basis. We used a collective label to represent the quantum numbers of the single-particle states in the above equations with

$$|p\rangle_{\text{HO}} = |n(ls)jm_p m_{t_p}\rangle_{\text{HO}}, \quad (3.28)$$

where n denotes the radial quantum number, l the orbital angular momentum, $s = 1/2$ the spin, j the total angular momentum with its projection $m_p = -j, \dots, j$, and m_{t_p} the isospin projection distinguishing proton and neutron states with $m_{t_p} = +1/2$ and $m_{t_p} = -1/2$, respectively. Note that the unitary transformation from the HO to the HF states only mixes radial excitations and all other quantum numbers are identical for the single-particle states $|p\rangle_{\text{HO}}$ and $|p\rangle_{\text{HF}}$, due to the spherical symmetry and conservation of the total angular momentum exploited for all calculations in this thesis.

In order to solve for the HF Slater determinant $|\text{HF}\rangle$ that minimizes the energy functional in Eq. (3.23), we use the nuclear Hamiltonian in vacuum normal order [compare Eq. (3.16)]

up to the two-body part written in second-quantized form

$$H = \sum_{pq} H_{pq}^{(1)} : a_p^\dagger a_q : + \frac{1}{4} \sum_{pqrs} H_{pqrs}^{(2)} : a_p^\dagger a_q^\dagger a_s a_r : , \quad (3.29)$$

with the one-body matrix elements $H_{pq}^{(1)}$ and the antisymmetrized two-body matrix elements $H_{pqrs}^{(2)}$. The one- and two-body density matrix for the HF Slater determinant are defined by

$$\gamma_{pq} = \langle \text{HF} | a_p^\dagger a_q | \text{HF} \rangle , \quad (3.30a)$$

$$\gamma_{pqrs} = \langle \text{HF} | a_p^\dagger a_q^\dagger a_s a_r | \text{HF} \rangle = \gamma_{qs} \gamma_{pr} - \gamma_{qr} \gamma_{ps} , \quad (3.30b)$$

respectively, where we assumed that the HF state is normalized $\langle \text{HF} | \text{HF} \rangle = 1$. The two-body density matrix factorizes for the case of a single Slater determinant by using Wick's theorem into a combination of one-body density matrices. Using the creation and annihilation operators c_p^\dagger and c_q in the HF basis based on Eq. (3.27a), the one-body density matrix in Eq. (3.30a) can be rewritten in terms of the transformation coefficients:

$$\gamma_{pq} = \sum_{rs} C_{pr}^* C_{qs} \langle \text{HF} | c_r^\dagger c_s | \text{HF} \rangle = \sum_i C_{pi}^* C_{qi} , \quad (3.31)$$

where we assumed that the one-body density matrix is diagonal in the HF basis, with $\gamma_{pq} = n_p \delta_{pq}$ and eigenvalues (occupation numbers) $n_p = 1$ for hole and $n_p = 0$ for particle states. Due to the occupation number, the sum on the right-hand side of Eq. (3.31) only runs over hole states i , with $n_i = 1$ occupied in the reference state. Note that the occupation numbers are defined by n_p with the single-particle index p , not to be confused with the radial quantum number n of the single-particle state defined in Eq. (3.28). The one-body density matrix has to fulfill the constraints of Hermiticity and idempotency leading to

$$\gamma^\dagger = \gamma , \quad (3.32a)$$

$$\gamma^2 = \gamma . \quad (3.32b)$$

Using the above definition of the density matrices, we rewrite the functional in Eq. (3.23) for the HF Slater determinant to a functional of the one-body density matrix by multiplying $|\text{HF}\rangle$ from the left

$$E[\gamma] = \sum_{pq} H_{pq}^{(1)} \gamma_{pq} + \frac{1}{2} \sum_{pqrs} H_{pqrs}^{(2)} \gamma_{rs} \gamma_{pq} , \quad (3.33)$$

where we used that the two-body matrix elements are antisymmetric and relabeled the indices of the two-body interaction.

The variational principle with small variations $\delta\gamma$ of γ is employed to find the single-particle states that construct the HF Slater determinant leading to the lowest energy expectation value

$$\delta E[\gamma] = E[\gamma + \delta\gamma] - E[\gamma] . \quad (3.34)$$

By keeping only terms up to linear order in $\delta\gamma$, Eq. (3.34) reads

$$\begin{aligned}
\delta E [\gamma] &= \sum_{pq} H_{pq}^{(1)} \delta\gamma_{pq} + \frac{1}{2} \sum_{pqrs} H_{pqrs}^{(2)} (\gamma_{rs} \delta\gamma_{pq} + \delta\gamma_{rs} \gamma_{pq}) \\
&= \sum_{pq} H_{pq}^{(1)} \delta\gamma_{pq} + \sum_{pqrs} H_{pqrs}^{(2)} \gamma_{rs} \delta\gamma_{pq} \\
&= \sum_{pq} \left(H_{pq}^{(1)} + \sum_{rs} H_{pqrs}^{(2)} \gamma_{rs} \right) \delta\gamma_{pq} \\
&= \sum_{pq} h_{pq} [\gamma] \delta\gamma_{pq}.
\end{aligned} \tag{3.35}$$

We again employed the antisymmetry of the matrix elements $H_{pqrs}^{(2)}$ and defined the one-body HF mean-field operator $h [\gamma]$

$$h[\gamma] = \sum_{pq} \left(H_{pq}^{(1)} + \sum_{rs} H_{pqrs}^{(2)} \gamma_{rs} \right). \tag{3.36}$$

The one-body HF operator consists of the one-body part of the Hamiltonian and an effective one-body potential based on averaging over the two-body interaction of all constituent nucleons by summing over the density. This can be straightforwardly extended to three- and higher-body terms, based on the many-body rank of the starting Hamiltonian in Eq. (3.29). We briefly discuss the inclusion of three-body forces at the end of this section.

In order to minimize the energy functional and obtain the HF Slater determinant, we solve the stationary condition

$$\delta E [\gamma] = 0, \tag{3.37}$$

resulting in

$$0 = \sum_{pq} h_{pq} [\gamma] \delta\gamma_{pq}. \tag{3.38}$$

The variation of the density matrix $\gamma + \delta\gamma$ still has to fulfill the same idempotency and Hermiticity constraints as the original density matrix in Eqs. (3.32a) and (3.32b) with the idempotency $(\gamma + \delta\gamma)^2 = \gamma + \delta\gamma$ leading to

$$\delta\gamma = \gamma\delta\gamma + \delta\gamma\gamma. \tag{3.39}$$

Multiplying γ or $(1 - \gamma)$ from left and right on both sides of Eq. (3.39) and using the idempotence of the density matrix results in

$$\gamma \delta\gamma \gamma = 0, \tag{3.40a}$$

$$(1 - \gamma)\delta\gamma(1 - \gamma) = 0, \tag{3.40b}$$

indicating that variations for the hole-hole and particle-particle block vanish based on the occupation number $n_p = 1$ and $n_p = 0$ for hole and particle states, respectively. Consequently, only variations for particle-hole and hole-particle combinations contribute to the sum in the

stationary condition in Eq. (3.38)

$$0 = \sum_{ia} h_{ia} [\gamma] \delta\gamma_{ia} + \text{H.c.}, \quad (3.41)$$

where, as before, we used the notation of i and a running over hole and particle indices, respectively, and H.c. stands for Hermitian conjugate. This equation can be restated as a commutator expression of the one-body HF operator and the one-body density matrix

$$[h[\gamma], \gamma] = 0, \quad (3.42)$$

showing the existence of a common eigenbasis for $h[\gamma]$ and γ . We formulate the eigenvalue problem for $h[\gamma]$, allowing us to solve for the corresponding eigenvectors and eigenvalues

$$h[\gamma] |p\rangle_{\text{HF}} = \varepsilon_p |p\rangle_{\text{HF}}, \quad (3.43)$$

with the HF single-particle state $|p\rangle_{\text{HF}}$ and the eigenvalue ε_p of p given by the so-called single-particle energy (SPE). The associated eigenvectors correspond to the transformation coefficients C_{pq} of the single-particle state from the HO to the HF basis, as outlined in Eq. (3.25). The SPEs are given by

$$\varepsilon_p = H_{pp}^{(1)} + \sum_i H_{pipi}^{(2)}, \quad (3.44)$$

and the total HF energy by

$$E_{\text{HF}} = \sum_i \varepsilon_i - \frac{1}{2} \sum_{ij} H_{ijij}^{(2)}, \quad (3.45)$$

where again the indices i and j run over occupied states in the reference state. Note that E_{HF} is not simply given by the sum of the single-particle energies but additionally incorporates effects of the two-body interaction. The self-consistent eigenvalue problem in Eq. (3.43) can be solved by iteration, with the one-body HO density matrix as a possible starting point. The iteration procedure is as follows: We first update the one-body HF operator in Eq. (3.36) based on the previous one-body density matrix and diagonalize $h[\gamma]$ afterwards. The resulting eigenvalues correspond to the new SPEs and the eigenvectors to the transformation coefficients of the single-particle states in Eq. (3.25). Based on the new transformation coefficients we construct the updated one-body density matrix as shown in Eq. (3.31), and start the next iteration step. These steps are iterated until a convergence criterion is reached. Most commonly, the change of the SPEs in each iteration step is used as a reasonable indicator to identify a convergence threshold. Typical values of the norm difference, once convergence is reached, are of the order of $\approx 10^{-8}$ MeV. The initial Hamiltonian (in HO basis) can be transformed to the HF basis by applying the unitary transformation, given by the final eigenvectors, to the one-, two-, and any possible higher-body part. Obviously, the one-body part, also referred to as Fock matrix, of the HF Hamiltonian is diagonal. A basis that diagonalizes the Fock matrix is called canonical basis. By solving for the HF basis, we additionally diagonalize the one-body density matrix simultaneously. Such basis choices that lead to a diagonal one-body density matrix are called natural orbitals. Consequently, the canonical and natural orbital basis coincide for the HF approach.

One advantageous property of working in a canonical basis is given by Brillouin's theorem [188] stating that all 1p1h excitations of the reference state vanish. The matrix elements for such excitations are given by

$$f_{ia} = \langle \text{HF} | H : a_a^\dagger a_i : | \text{HF} \rangle = \langle \text{HF} | H | \text{HF}_i^a \rangle, \quad (3.46)$$

with the singly-excited HF Slater determinant $|\text{HF}_i^a\rangle$, also known as 1p1h excitation. These matrix elements are zero in the case of a canonical basis with a diagonal Fock matrix, as Eq. (3.41) ensures that all off-diagonal matrix elements h_{ia} and h_{ai} are 0. The HF Slater determinant therefore does not mix with any singly-excited states. Nevertheless, couplings off higher-excited states to other single excitations, e.g., $\langle \text{HF}_i^a | H | \text{HF}_{ij}^{ab} \rangle$ still contribute. Brillouin's theorem is especially beneficial for many-body perturbation theory applications in a canonical basis, e.g., an HF basis as discussed in Sec. 3.3.3, by reducing the number of contributing expressions at each order based on the vanishing one-body part for singly-excited states.

The above derivation can be straightforwardly extended to consider three-body interactions by keeping the three-body contribution $H^{(3)}$ for the Hamiltonian in Eq. (3.29) and applying similar arguments as for the two-body interaction. The additional three-body density matrix also factorizes for a single Slater determinant, yielding

$$\begin{aligned} \gamma_{pqrst} &= \langle \text{HF} | a_p^\dagger a_q^\dagger a_r^\dagger a_u a_t a_s | \text{HF} \rangle \\ &= \gamma_{ru}(\gamma_{qt}\gamma_{ps} - \gamma_{qs}\gamma_{pt}) + \gamma_{rt}(\gamma_{qs}\gamma_{pu} - \gamma_{qu}\gamma_{ps}) + \gamma_{rs}(\gamma_{qu}\gamma_{pt} - \gamma_{qt}\gamma_{pu}), \end{aligned} \quad (3.47)$$

and the HF mean-field operator gets an additional contribution of the three-body interaction averaged by the sum over two one-body density matrices

$$h[\gamma] = \sum_{pq} \left(H_{pq}^{(1)} + \sum_{rs} H_{prqs}^{(2)} \gamma_{rs} + \frac{1}{2} \sum_{rstu} H_{prtqsu}^{(3)} \gamma_{rs} \gamma_{tu} \right). \quad (3.48)$$

The resulting single-particle energies and total HF energy considering up to three-body interactions are given by

$$\varepsilon_p = H_{pp}^{(1)} + \sum_i H_{pipi}^{(2)} + \frac{1}{2} \sum_{ij} H_{pijpij}^{(3)}, \quad (3.49)$$

$$E_{\text{HF}} = \sum_i \varepsilon_i - \frac{1}{2} \sum_{ij} H_{ijij}^{(2)} - \frac{1}{3} \sum_{ijk} H_{ijkijk}^{(3)}, \quad (3.50)$$

respectively.

3.3 Selected many-body approaches

Even though the IMSRG is the workhorse for most of the results presented in this thesis, we briefly outline three selected many-body methods here that will be considered in this thesis and offer additional benchmark possibilities, consistency checks, as well as comparisons of computational scaling and final results. We first discuss the NCSM as an exact method for solving the nuclear A -body problem. Given the computational costs and exponential scaling

the accessible mass numbers within this method are, however, limited to light nuclei. In contrast to that, CC theory and MBPT (in a given truncation scheme) are approximate many-body methods that perform an expansion of the wave function and nonperturbatively and perturbatively, respectively, build in correlation effects on top of a reference state. These methods have the key advantage that they scale polynomially in mass number, enabling the description of systems of up to $A \approx 132$ interacting nucleons. The HF solution given in Sec. 3.2, serves as a good starting point for most of such many-body expansion methods that are based on a single Slater-determinant reference state, starting from the lowest energy expectation value.

3.3.1 No-core shell model

A direct way to solve the nuclear many-body problem is to construct the Hamiltonian in a basis of many-body states, given by the reference state and its particle-hole excitations, and diagonalize the Hamiltonian. This results in an exact solution of the many-body Schrödinger equation in terms of the eigenvalues and corresponding eigenstates of the A -body Hamiltonian. These can then be used to calculate observables, e.g., ground- and excited-state energies. In the NCSM [20, 23], this is typically done by using a finite harmonic oscillator single-particle basis with a truncation of the many-body model space N_{\max} that limits the maximal number of single-particle excitations on top of the minimum excitation number N_{\min} of the target nucleus

$$\sum_{i=1}^A 2n_i + l_i \leq N_{\max} + N_{\min}, \quad (3.51)$$

with the radial quantum number n and the orbital angular momentum l of orbital i . The minimal excitation number depends on the number of particles and is, e.g., given by $N_{\min} = 0$ for ${}^4\text{He}$ or $N_{\min} = 8$ for ${}^{12}\text{C}$. All particles are treated as active, meaning that they can be excited to any single-particle state allowed by N_{\max} . This is indicated by the term “no-core” and the summation bound from $i = 1$ to $i = A$ in Eq. (3.51), in contrast to standard shell-model approaches, where typically only the valence particles on top of a static core are active. It is important to note that the N_{\max} truncation of the many-body model space limiting the single-particle excitations is different from the truncation of the single-particle basis $e_{\max} = (2n + l)_{\max}$ that limits the number of single-particle states, which will be used for the IMSRG in Sec. 3.4. The NCSM is a variational method and therefore the binding energy increases for increased basis truncation N_{\max} , allowing for an extrapolation to infinite basis size and a final N_{\max} -independent result. On the other hand, a major drawback of the NCSM is its exponential scaling with system size, leading to rapidly growing basis dimensions for increased mass numbers. Even though one does not perform the full diagonalization and is only interested in the first (few) smallest eigenvalues, diagonalization approaches based on Krylov subspace methods, e.g., the Lanczos algorithm [189], are still fundamentally limited by the basis size. Hence, the NCSM is only applicable to rather light systems with mass numbers around $A \approx 12$. Importance-truncation techniques, which select the most important configurations in the many-body space and diagonalize the Hamiltonian in the subsequent subspace, have pushed this boundary and enabled calculations of mass numbers up to $A \approx 25$ for the importance-truncated NCSM (IT-NCSM) [21, 190]. We will come back to the topic of importance truncation when discussing its general ideas in more detail and possible applications to the IMSRG in Sec. 5.

3.3.2 Coupled cluster theory

Coupled cluster theory, introduced in the 1960s in Refs. [191–194], has undergone a revival in nuclear theory and has been with great success applied to the *ab initio* calculation of atomic nuclei [28, 29, 74]. The many-body wave function for the solution of the many-body Schrödinger equation is derived by an exponential ansatz, accounting for particle-hole excitations on top of a chosen reference state $|\Phi\rangle$

$$|\Psi_{\text{CC}}\rangle = e^T |\Phi\rangle, \quad (3.52)$$

with the many-body wave function $|\Psi_{\text{CC}}\rangle$ and the cluster operator $T = T^{(1)} + T^{(2)} + \dots + T^{(A)}$ containing up to A -body contributions in an A -body system. The individual contributions, here shown up to the three-body operator $T^{(3)}$, are defined by

$$T = \sum_{ai} t_{ai} : a_a^\dagger a_i : + \frac{1}{4} \sum_{abij} t_{abij} : a_a^\dagger a_b^\dagger a_j a_i : + \frac{1}{36} \sum_{abcijk} t_{abcijk} : a_a^\dagger a_b^\dagger a_c^\dagger a_k a_j a_i + \dots, \quad (3.53)$$

with the so-called cluster amplitudes given by the matrix elements $t_{a\dots i\dots}$ for the corresponding many-body rank and indices i, j, k, \dots (a, b, c, \dots) running over hole (particle) states. Note that the cluster amplitudes are antisymmetric under the exchange of indices in the hole and particle space separately. From Eq. (3.53) it is clear that the cluster operator generates 1p1h, 2p2h, three-particle-three-hole (3p3h), and higher particle-hole excitations of the reference state, defined by $|\Phi_{ij\dots}^{ab\dots}\rangle = : a_a^\dagger a_b^\dagger \dots a_j a_i \dots : |\Phi\rangle$. In practice, the inclusion of all particle-hole excitations up to the A -body level is unfeasible and truncating the cluster operator to a limited number of particle-hole excitations gives rise to different truncation schemes of CC theory. By truncating T after the 2p2h level, we obtain CC with singles and doubles (CCSD), while incorporating the 3p3h term yields CC with additional triples (CCSDT). Due to the tremendous computational requirements for the full inclusion of triples excitations in CC theory, calculations with full triples effects are currently still unfeasible for mid-mass applications. However, various techniques to approximately include triples effects have been derived, e.g., by iterative and noniterative triples [195–198]. Even if the cluster operator T is truncated at the 2p2h level, as is done in CCSD, the exponential ansatz of the transformation in Eq. (3.52) mixes arbitrarily high particle-hole excitations to the reference state. This can be easily seen by expanding e^T in terms of a Taylor series that generates particle-hole excitations of the reference state beyond the 2p2h level.

A key object in CC theory is the similarity-transformed Hamiltonian, motivated by the transformation of the wave function in Eq. (3.52), given by

$$H_{\text{CC}} = e^{-T} H e^T. \quad (3.54)$$

Here H is the normal-ordered Hamiltonian with respect to an A -body product reference state, most commonly a single Slater determinant, e.g., an HO or HF reference state. The transformed Hamiltonian H_{CC} , or so-called coupled cluster effective Hamiltonian, is evaluated by applying the Baker-Campbell-Hausdorff (BCH) expansion using nested commutators

$$H_{\text{CC}} = H + [H, T] + \frac{1}{2!} [[H, T], T] + \frac{1}{3!} [[[H, T], T], T] + \frac{1}{4!} [[[[H, T], T], T], T] + \dots, \quad (3.55)$$

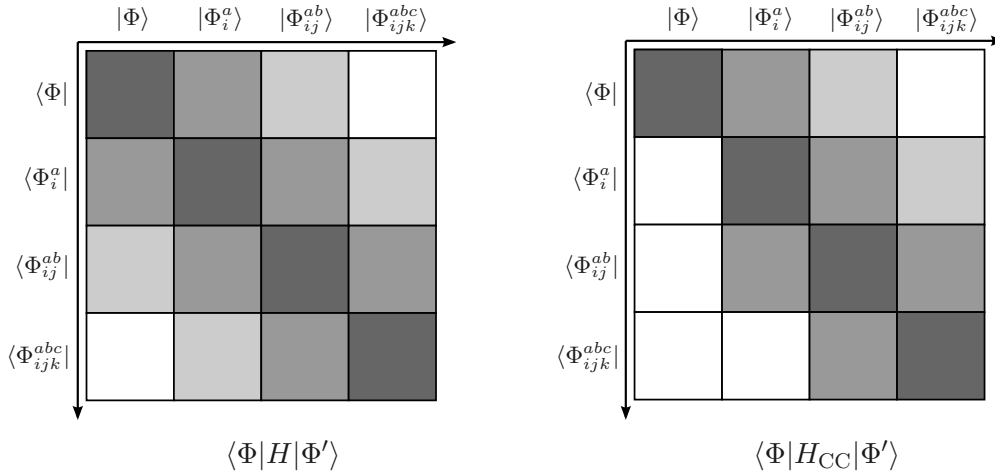


Figure 3.1: Initial Hamiltonian H (left) compared to the similarity transformed CC Hamiltonian H_{CC} (right), which indicates the decoupling of the reference state in the first column and the non-Hermiticity of the final operator by the remaining couplings in the first row. Note that the two-body Hamiltonian here only couples $(n \pm 2)p(n \pm 2)h$ states. Figure adapted from Ref. [31].

where the series terminates naturally after a given order, as the individual contributions of T commute. Furthermore, only connected diagrams contribute in the above commutator expansion, making CC a size-extensive many-body method, meaning that calculations scale linearly in mass number A .

Depending on the many-body truncation of the operators H and T , the series truncates after fourfold (sixfold) nested commutators for the case of two-body (three-body) operators, corresponding to CCSD (CCSDT). This is in contrast to the application of the BCH series in the Magnus approach of the IMSRG, which is discussed in Sec. 3.4.4, where a convergence threshold has to be set in order to truncate the BCH series. Note however that $-T \neq T^\dagger$, and consequently the transformation is not unitary and the resulting transformed Hamiltonian H_{CC} is non-Hermitian. Nevertheless, the transformation leaves the (energy-)eigenvalues invariant.

The ground-state wave function is obtained by decoupling all particle-hole excitations for the transformed Hamiltonian, which in the case of CCSD read

$$\langle \Phi | e^{-T} H e^T | \Phi \rangle = E, \quad (3.56a)$$

$$\langle \Phi_i^a | e^{-T} H e^T | \Phi \rangle = 0, \quad (3.56b)$$

$$\langle \Phi_{ij}^{ab} | e^{-T} H e^T | \Phi \rangle = 0, \quad (3.56c)$$

where E is the ground-state energy corresponding to the eigenvalue problem $H e^T | \Phi \rangle = E e^T | \Phi \rangle$. The above system of coupled nonlinear equations, also called amplitude equations, has to be solved to obtain the cluster amplitudes of T for the desired decoupling. This is accomplished by iterative approaches. The resulting decoupling for the CC Hamiltonian is schematically shown in the right panel of Fig. 3.1. While the left column clearly indicates the decoupling of the reference state from 1p1h and 2p2h excitations as demanded in the CC equations (3.56), the first row shows the remaining couplings to particle-hole excitations due

to the non-unitarity of the transformation. Identifying the various contributions that arise by solving the CC equations, one can show that CCSD is complete up to third order in MBPT while additionally nonperturbatively incorporating many diagrams of higher order [199].

3.3.3 Many-body perturbation theory

For perturbative interactions, the HF solution already provides a good approximation to the exact solution of the many-body problem and the remaining (small) correlation effects can be accounted for in a perturbative way. This is the main ansatz for (many-body) perturbation theory, where the Hamiltonian is split into an unperturbed part H_0 and a perturbation H_1 with the auxiliary dependence on the parameter λ

$$H = H_0 + \lambda H_1 . \quad (3.57)$$

The exact unperturbed solution to the many-body problem is known and given by

$$H_0 |\Phi_n\rangle = E_n^{(0)} |\Phi_n\rangle , \quad (3.58)$$

where $|\Phi_n\rangle$ is the unperturbed wave function and given by the reference state. For example, $|\Phi_0\rangle = |\Phi\rangle$ can be an HO, HF, or natural orbital single Slater-determinant reference state. The exact solution to the many-body Schrödinger equation for the full Hamiltonian is given by

$$H |\Psi_n\rangle = E_n |\Psi_n\rangle , \quad (3.59)$$

where $|\Psi_n\rangle$ is the n -th eigenstate of the system. We will focus on ground-state observables here and therefore limit the discussion to the ground-state wave functions and energies by omitting the index $n = 0$ in the following.

We use the power series ansatz

$$E = \sum_{p=0}^{\infty} \lambda^p E^{(p)} , \quad (3.60a)$$

$$|\Psi\rangle = \sum_{p=0}^{\infty} \lambda^p |\Psi^{(p)}\rangle , \quad (3.60b)$$

for the exact energy and many-body state, respectively, and set $|\Psi^{(0)}\rangle = |\Phi\rangle$ to the unperturbed wave function at $p = 0$ with intermediate normalization

$$\langle \Phi | \Psi \rangle = 1 . \quad (3.61)$$

In practical calculations, the series in Eq. (3.60) are truncated at finite order and we consider MBPT energy corrections up to third order in this thesis. Higher-order contributions are expected to give only small corrections when using soft (perturbative) interactions. We define the projection operators P and Q on the reference state and the residual states, respectively

by

$$P = |\Phi\rangle \langle \Phi|, \quad (3.62a)$$

$$Q = \mathbb{1} - P = \sum_{n \neq 0} |\Phi_n\rangle \langle \Phi_n|, \quad (3.62b)$$

which give $P|\Phi\rangle = |\Phi\rangle$ and $Q|\Phi\rangle = 0$ for the reference state. Applying the operator $\mathbb{1} = P + Q$ to the exact wave function yields

$$|\Psi\rangle = |\Phi\rangle + Q|\Psi\rangle, \quad (3.63)$$

and subsequently multiplying $|\Phi\rangle$ to the Schrödinger equation (3.59) from the left results in

$$\langle \Phi | E | \Psi \rangle = \langle \Phi | H | \Phi \rangle + \langle \Phi | H Q | \Psi \rangle, \quad (3.64a)$$

$$E = E_{\text{ref.}} + \langle \Phi | H Q | \Psi \rangle, \quad (3.64b)$$

where we defined the reference state energy $E_{\text{ref.}}$ as the reference state expectation value of the full Hamiltonian $E_{\text{ref.}} = \langle \Phi | H_0 | \Phi \rangle + \langle \Phi | H_1 | \Phi \rangle = E^{(0)} + E^{(1)}$. The expansion of the energy correction in MBPT is commonly done for $\Delta E = E - E_{\text{ref.}}$. By using a Slater-determinant reference state, the difference ΔE corresponds to the correlation energy of the system that is missing on top of the reference state energy $E_{\text{ref.}}$ to obtain the exact energy.

The specific splitting into H_0 and H_1 in Eq. (3.57) gives rise to different MBPT partitioning schemes. Most commonly, the partitioning is performed with H_0 being the diagonal one-body operator of the Hamiltonian, also referred to as the diagonal case of perturbation theory, which may result in the so-called Møller-Plesset (MP) partitioning, which will be used for all perturbative energy and state corrections for the rest of this thesis. Using this choice of partitioning, the unperturbed Hamiltonian can be written in its eigenbasis as

$$H_0 = \sum_p \varepsilon_p a_p^\dagger a_p, \quad (3.65)$$

with the SPE ε_p of orbital p given by the diagonal elements of the Fock operator $\varepsilon_p = f_{pp}$. An alternative partitioning, which will not be further discussed here, is given by the Epstein-Nesbet choice, where the diagonal part of the Hamiltonian in a given many-body basis is chosen for the unperturbed Hamiltonian H_0 .

One can use Rayleigh-Schrödinger perturbation theory and the many-body resolvent operator

$$R = \frac{Q}{E^{(0)} - H_0} = \sum_{n \neq 0} \frac{|\Phi_n\rangle \langle \Phi_n|}{E^{(0)} - E_n^{(0)}}, \quad (3.66)$$

to obtain the formal expressions of the energy and wave function corrections. We just give the final results here and refer to Ref. [199] for the technical and detailed derivation. The power series ansatz in Eq. (3.60) using the resolvent operator, $Q^2 = Q$ for the projection

operator, and $\lambda \rightarrow 1$ can be rewritten to

$$|\Psi\rangle = \sum_{n=0}^{\infty} \left(R(H_1 - \Delta E) \right)^n |\Phi\rangle, \quad (3.67a)$$

$$\Delta E = \sum_{n=0}^{\infty} \langle \Phi | H_1 \left(R(H_1 - \Delta E) \right)^n |\Phi\rangle, \quad (3.67b)$$

for the wave function and the correlation energy, respectively. As ΔE is just a number and commutes with the resolvent operator, and $R|\Phi\rangle = 0$ due to the action of the projection operator Q (3.62b), the energy corrections to the lowest orders are given by

$$E^{(0)} = \langle \Phi | H_0 | \Phi \rangle, \quad (3.68a)$$

$$E^{(1)} = \langle \Phi | H_1 | \Phi \rangle, \quad (3.68b)$$

$$E^{(2)} = \langle \Phi | H_1 R H_1 | \Phi \rangle, \quad (3.68c)$$

$$E^{(3)} = \langle \Phi | H_1 R (H_1 - E^{(1)}) R H_1 | \Phi \rangle, \quad (3.68d)$$

...

By using $E_{\text{ref.}} = E^{(0)} + E^{(1)}$, the first correction to the energy enters at second order. For the Møller-Plesset partitioning and using Slater determinants constructed from single-particle states, the energy denominators in the resolvent operator are simply given by the difference of the single-particle energies of the reference state and the n -th unperturbed wave function $|\Phi_n\rangle$

$$E^{(0)} - E_n^{(0)} = \varepsilon_i + \varepsilon_j + \dots - \varepsilon_a - \varepsilon_b - \dots, \quad (3.69)$$

assuming $|\Phi_n\rangle = |\Phi_{ij\cdots}^{ab\cdots}\rangle$, which most of the time involves one-particle-one-hole (1p1h) $|\Phi_i^a\rangle$ and two-particle-two-hole (2p2h) $|\Phi_{ij}^{ab}\rangle$ excitations of the reference state. We employ the short hand notation

$$\varepsilon_{ij}^{ab} = \varepsilon_i + \varepsilon_j - \varepsilon_a - \varepsilon_b, \quad (3.70)$$

for the energy denominators.

Working in the eigenbasis of the unperturbed Hamiltonian H_0 and employing a single Slater-determinant reference state, we can rewrite the resolvent operator using the formulation of particle-hole excitations on top of the reference state $|\Phi\rangle$

$$R = \sum_{ai} \frac{|\Phi_i^a\rangle \langle \Phi_i^a|}{\varepsilon_i^a} + \frac{1}{4} \sum_{abij} \frac{|\Phi_{ij}^{ab}\rangle \langle \Phi_{ij}^{ab}|}{\varepsilon_{ij}^{ab}} + \dots, \quad (3.71)$$

where as before the labels a, b, \dots and i, j, \dots run over particle and hole indices, respectively. Employing a perturbation Hamiltonian H_1 with only two-body interactions, we obtain the second-order energy correction in Møller-Plesset partitioning for a canonical reference state by inserting Eq. (3.71) into Eq. (3.68c):

$$E^{(2)} = \frac{1}{4} \sum_{abij} \frac{\Gamma_{abij} \Gamma_{ijab}}{\varepsilon_{ij}^{ab}}, \quad (3.72)$$

where Γ is the normal-ordered 2-body part of the Hamiltonian with respect to the reference state $|\Phi\rangle$ and contributions from the one-body part vanish in a canonical basis due to Brillouin's theorem [188]. For a noncanonical reference state an additional one-body contribution occurs based on the 1p1h excitation in the first term of the resolvent operator

$$E_{\text{noncan.}}^{(2)} = \sum_{ia} \frac{f_{ai} f_{ia}}{\varepsilon_i^a}, \quad (3.73)$$

with the normal-ordered one-body part f of the Hamiltonian. At third order, three terms contribute for a canonical reference state

$$\begin{aligned} E^{(3)} &= \langle \Phi | H_1 R H_1 R H_1 | \Phi \rangle \\ &= E_{\text{pp}}^{(3)} + E_{\text{hh}}^{(3)} + E_{\text{ph}}^{(3)} \\ &= \frac{1}{8} \sum_{abcdij} \frac{\Gamma_{ijab} \Gamma_{abcd} \Gamma_{cdij}}{\varepsilon_{ij}^{ab} \varepsilon_{ij}^{cd}} \\ &\quad + \frac{1}{8} \sum_{abijkl} \frac{\Gamma_{ijab} \Gamma_{kl ij} \Gamma_{abkl}}{\varepsilon_{ij}^{ab} \varepsilon_{kl}^{ab}} \\ &\quad - \sum_{abcijk} \frac{\Gamma_{ijab} \Gamma_{kbic} \Gamma_{ackj}}{\varepsilon_{ij}^{ab} \varepsilon_{kj}^{ac}}, \end{aligned} \quad (3.74)$$

where one can distinguish the pp, hh, and ph expressions for the particle-particle (Γ_{abcd}), hole-hole ($\Gamma_{kl ij}$), and particle-hole (Γ_{kbic}) contributions of the two-body Hamiltonian, respectively in Eq. (3.74). Employing a noncanonical reference state results in 11 additional diagrams (14 diagrams in total) for the third-order energy correction. Following the diagrammatic expansion in Ref. [199], the additional energy corrections at third order are given by

$$\begin{aligned} E_{\text{noncan.}}^{(3)} &= \frac{1}{2} \sum_{abcij} \frac{\Gamma_{abij} \Gamma_{abcj} f_{ci}}{\varepsilon_{ij}^{ab} \varepsilon_i^c} - \frac{1}{2} \sum_{abijk} \frac{\Gamma_{abij} \Gamma_{ijkb} f_{ak}}{\varepsilon_{ij}^{ab} \varepsilon_k^a} + \frac{1}{2} \sum_{abcij} \frac{\Gamma_{abij} f_{ac} \Gamma_{cbij}}{\varepsilon_{ij}^{ab} \varepsilon_{ij}^{bc}} \\ &\quad - \frac{1}{2} \sum_{abijk} \frac{\Gamma_{abij} f_{ik} \Gamma_{abkj}}{\varepsilon_{ij}^{ab} \varepsilon_{jk}^{ab}} + \frac{1}{2} \sum_{abcij} \frac{f_{ai} \Gamma_{ajcb} \Gamma_{cbij}}{\varepsilon_i^a \varepsilon_{ij}^{bc}} + \frac{1}{2} \sum_{abijk} \frac{f_{ai} \Gamma_{ibkj} \Gamma_{abkj}}{\varepsilon_i^a \varepsilon_{jk}^{ab}} \\ &\quad + \sum_{abij} \frac{\Gamma_{abij} f_{jb} f_{ai}}{\varepsilon_{ij}^{ab} \varepsilon_i^a} + \sum_{abij} \frac{f_{ai} f_{jb} \Gamma_{abij}}{\varepsilon_i^a \varepsilon_j^b} + \sum_{abij} \frac{f_{ai} f_{jb} \Gamma_{abij}}{\varepsilon_i^a \varepsilon_{ij}^{ab}} \\ &\quad + \sum_{abi} \frac{f_{ai} f_{ab} f_{bi}}{\varepsilon_i^a \varepsilon_i^b} - \sum_{aij} \frac{f_{aj} f_{ij} f_{ai}}{\varepsilon_i^a \varepsilon_j^a}. \end{aligned} \quad (3.75)$$

Equations (3.72)-(3.75) demonstrate the benefits of using a canonical (e.g., an HF) reference state for MBPT applications, with just one diagram contributing to the energy correction at second order and three diagrams at third order, in contrast to two and 14 diagrams at second and third order, respectively for noncanonical reference states. Deriving the MBPT formulas up to high orders in the expansion and explicitly calculating all possible contractions by using Wick's theorem can become quite cumbersome. Therefore, a diagrammatic expansion is often used that can be straightforwardly translated into an equation for each diagram with a small set of rules. In this expansion, only linked diagrams contribute based on the linked-diagram theorem of Goldstone [200]. We refer to Ref. [199] for a detailed derivation of the diagrammatic expansion of antisymmetrized Goldstone diagrams in MBPT and a proof of the

linked-diagram theorem. Especially when going to higher orders, the number of contributing diagrams increases rapidly. Therefore, the automated generation of many-body diagrams on a computer provides substantial benefits for the derivation and calculation of higher-order contributions (see, e.g., Refs. [57, 201–204]).

Considerable savings in the computational cost and scaling behavior can be obtained by using the conservation of the total angular momentum for closed-shell nuclei and working in an angular-momentum-coupled basis with spherically symmetric reference states. The working equations grow more complicated in the angular-momentum-coupled scheme with operator matrix elements of more involved structure. All energy corrections given in this subsection are shown in an uncoupled (m -scheme) form, however the angular-momentum-coupled expressions can be straightforwardly derived by using the AMC tool [205] of Ref. [206].

Even though we focus on applications to finite nuclei in this thesis with the framework of MBPT being successfully applied to nuclear structure calculations in a wide range of different mass numbers [35, 37, 207, 208], the general ideas and concepts of MBPT discussed here can also be applied for studies of infinite nuclear matter (see, e.g., Refs. [54, 57, 136, 142, 209–212]).

3.4 IMSRG approach

In the following, we give a comprehensive introduction to the nonperturbative IMSRG and discuss its commonly used working truncation, the IMSRG(2), with operators truncated at the normal-ordered two-body level. In addition, we review different generator choices to obtain the desired decoupling of the ground state. The *ab initio* IMSRG, in a given truncation scheme, falls into the same category of approximate many-body methods with a mild polynomial scaling in mass number, as MBPT and CC theory discussed in the previous section. Similarly to the free-space SRG in Sec. 2.3, we evolve the nuclear Hamiltonian by a continuous sequence of unitary transformations in the IMSRG. However for the in-medium SRG, we transform the normal-ordered Hamiltonian with respect to a chosen reference state, i.e., a single Slater determinant in our case, indicated by the term *in medium*. In contrast to the free-space counterpart, we decouple the reference state from all particle-hole excitations in the limit $s \rightarrow \infty$ for the in-medium method, thereby approximating the exact ground state and allowing for calculations of nuclear observables. The transformed Hamiltonian can be written as in the free-space case [cf. Eq. (2.18)]

$$H(s) = U(s)H(0)U^\dagger(s), \quad (3.76)$$

with the initial normal-ordered Hamiltonian $H(s=0)$ and the unitary transformation $U(s)$. As for the free-space counterpart, we derive the flow equation for the Hamiltonian

$$\frac{dH(s)}{ds} = [\eta(s), H(s)], \quad (3.77)$$

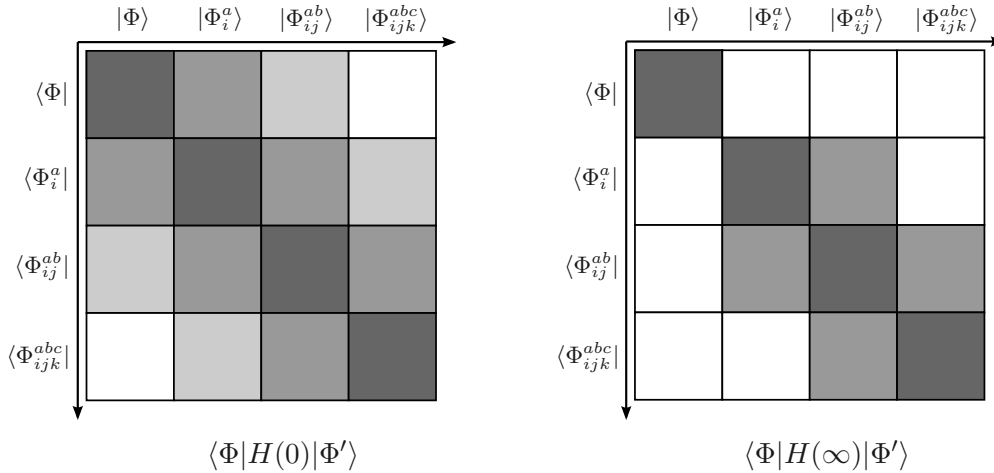


Figure 3.2: Initial normal-ordered Hamiltonian $H(0)$ (left) at the beginning of the IMSRG flow compared to the IMSRG Hamiltonian $H(\infty)$ (right) after decoupling all particle-hole excitations in the limit $s \rightarrow \infty$ in the flow. Note that the two-body Hamiltonian here only couples $(n \pm 2)p(n \pm 2)h$ states. Figure adapted from Ref. [31].

where the anti-Hermitian generator $\eta(s)$ that defines the decoupling pattern is given by

$$\eta(s) = \frac{dU(s)}{ds} U^\dagger(s). \quad (3.78)$$

The generator will be discussed in more detail in Sec. 3.4.1. The initial coupling of the ground state $|\Phi\rangle$, to nph excitations ($|\Phi_i^a\rangle$, $|\Phi_{ij}^{ab}\rangle$, $|\Phi_{ijk}^{abc}\rangle$, ...) is schematically shown in the left panel of Fig. 3.2 by the gray and light-gray squares. After solving the IMSRG flow equations, the decoupling of the reference state in the limit $s \rightarrow \infty$ is depicted in the right panel of Fig. 3.2, showing the suppression of the off-diagonal parts of $H(\infty)$ in the first row and column by the white squares. Additionally, Fig. 3.2 depicts the unitarity of the transformation, preserving the Hermiticity of the Hamiltonian. This is in contrast to the similarity-transformed CC Hamiltonian shown in Fig. 3.1, which is non-Hermitian as discussed in Sec. 3.3.2. To fully decouple the reference state from all particle-hole excitations, the flow equation in Eq. (3.77) has to be solved for the limit $s \rightarrow \infty$ with the normal-ordered Hamiltonian at $s = 0$ given by Eq. (3.19) (up to the three-body rank). The repeated evaluation of the commutator expressions during the flow induces many-body operators up to the A -body level in an A -body system by calculating the product of normal-ordered operators using the generalized Wick theorem [186, 187]. This is analogous to the discussion of induced many-body forces in the free-space SRG in Sec. 2.3. The commutator of two generic normal-ordered operators $A^{(K)}$ and $B^{(L)}$ with particle rank K and L , respectively, can be evaluated to a normal-ordered operator $C^{(M)}$ by using the generalized Wick theorem (3.21) with many-body parts from particle rank $|K - L|$ up to $K + L - 1$ contributing to C

$$[A^{(K)}, B^{(L)}] = \sum_{M=|K-L|}^{K+L-1} C^{(M)}. \quad (3.79)$$

For example, the commutator of two two-body operators would lead to a zero-, one-, two-, and three-body contribution. Solving the flow equation and including up to A -body forces and A -body operators is computationally intractable in practical applications. Consequently, a truncation scheme for the commutator expansion is required. Currently, the standard truncation scheme for the IMSRG is the IMSRG(2) truncation, where all operators and commutators are truncated at the normal-ordered two-body (NO2B) level (see, e.g., Refs. [213, 214]). This leads to two effects for the IMSRG: First, the residual three-body force W of the normal-ordered operator in Eq. (3.19) is neglected. Second, all normal-ordered three-body (and higher-body) parts that would arise during the flow, i.e., the three-body part of the commutator $[A^{(2)}, B^{(2)}]$ discussed above, are neglected as well. Some attempts to approximately capture the effects of neglected induced three-body contributions in the IMSRG(2) have been explored [215], but a systematic understanding has not been formed. Notice however, that contributions from the 3N interaction are still considered in actual calculations by the normal-ordered two-body approximation and affect the normal-ordered zero-, one-, and two-body part, as can be seen in Eqs. (3.20a)-(3.20c). We will come back to the IMSRG truncation and the inclusion of three-body operators when discussing the extension of the many-body method to the IMSRG(3) truncation in Sec. 3.5. For the moment, we limit the discussion to the normal-ordered Hamiltonian up to the two-body level and normal-ordered generators with a one- and two-body part $\eta(s) = \eta^{(1)}(s) + \eta^{(2)}(s)$.

With the IMSRG(2) truncation at hand, we derive the corresponding flow equations in order to solve the many-body problem, where the commutator expression of Eq. (3.77) can be expanded to

$$\frac{dE(s) + df(s) + d\Gamma(s)}{ds} = [\eta(s)^{(1)} + \eta(s)^{(2)}, E(s) + f(s) + \Gamma(s)]. \quad (3.80)$$

Following Eq. (3.79), the fundamental commutators of the IMSRG(2) are given by

$$[\eta(s)^{(1)}, f(s)] = [\eta(s)^{(1)}, f(s)]^{(0)} + [\eta(s)^{(1)}, f(s)]^{(1)}, \quad (3.81)$$

$$[\eta(s)^{(1)}, \Gamma(s)] = [\eta(s)^{(1)}, \Gamma(s)]^{(1)} + [\eta(s)^{(1)}, \Gamma(s)]^{(2)}, \quad (3.82)$$

$$[\eta(s)^{(2)}, f(s)] = [\eta(s)^{(2)}, f(s)]^{(1)} + [\eta(s)^{(2)}, f(s)]^{(2)}, \quad (3.83)$$

$$[\eta(s)^{(2)}, \Gamma(s)] = [\eta(s)^{(2)}, \Gamma(s)]^{(0)} + [\eta(s)^{(2)}, \Gamma(s)]^{(1)} + [\eta(s)^{(2)}, \Gamma(s)]^{(2)}, \quad (3.84)$$

where the resulting many-body ranks on the right-hand side are indicated by the commutator superscript and the term $[\eta(s)^{(2)}, \Gamma(s)]^{(3)}$ in the last row is neglected in the IMSRG(2) and therefore not shown in Eq. (3.84). The commutator of the generator with the scalar value $E(s)$ in Eq. (3.80) vanishes. We order the fundamental commutators by their many-body rank and assign the corresponding terms to the zero-, one-, and two-body parts $\frac{dE(s)}{ds}$, $\frac{df(s)}{ds}$, and $\frac{d\Gamma(s)}{ds}$ of the flowing Hamiltonian, respectively, to obtain a set of coupled ordinary differential equations. These equations can be simplified by using the generalized Wick's theorem to evaluate the product of normal-ordered operators and working in the eigenbasis of the one-body density matrix, as defined in Eqs. (3.15a) and (3.15b). In the following, we explicitly derive the fundamental commutator of the one-body generator and the one-body Hamiltonian that contributes to the one-body part of the flowing Hamiltonian, given by the last term in

Eq. (3.81) and drop the s -dependence for brevity

$$\begin{aligned}
[\eta^{(1)}, f]^{(1)} &= \sum_{pqr} \left\{ \eta_{pq} f_{rs} (: \overline{a_p^\dagger a_q a_r^\dagger a_s} : + : a_p^\dagger \overline{a_q a_r^\dagger a_s} :) - f_{rs} \eta_{pq} (: \overline{a_r^\dagger a_s a_p^\dagger a_q} : + : a_r^\dagger \overline{a_s a_p^\dagger a_q} :) \right\} \\
&= \sum_{pqr} \eta_{pq} f_{rp} (n_p : a_q a_r^\dagger : - \bar{n}_p : a_r^\dagger a_q :) + \sum_{pqs} \eta_{pq} f_{qs} (\bar{n}_q : a_p^\dagger a_s : - n_q : a_s a_p^\dagger :) \\
&= \sum_{pqr} \eta_{qp} f_{pr} (\bar{n}_p : a_r^\dagger a_q : + n_p : a_r^\dagger a_q :) + \sum_{pqs} \eta_{pq} f_{qs} (\bar{n}_q : a_p^\dagger a_s : + n_q : a_p^\dagger a_s :) \\
&= \sum_{pqr} (\eta_{qp} f_{pr} + \eta_{rp} f_{pq}) : a_r^\dagger a_q : ,
\end{aligned} \tag{3.85}$$

where n_p is the occupation number of orbital p , and $\bar{n}_p \equiv 1 - n_p$. We appropriately relabeled the summation indices of the second term in the third row and used that the matrix elements f_{pq} and η_{pq} are Hermitian and anti-Hermitian, respectively. In a similar fashion, all fundamental commutators in Eqs. (3.81)-(3.84) can be calculated to derive the complete IMSRG(2) flow equations in a symmetry-unrestricted (so-called m -scheme) form. We additionally use the permutation operator P_{ij} , which exchanges the indices i and j of the matrix elements in the subsequent term, and exploit the Hermiticity of the Hamiltonian and the anti-Hermiticity of the generator to simplify the expressions. The resulting m -scheme IMSRG(2) flow equations are given by

$$\frac{dE}{ds} = \sum_{pq} (n_p - n_q) \eta_{pq} f_{qp} + \frac{1}{2} \sum_{pqrt} n_p n_q \bar{n}_r \bar{n}_t \eta_{pqrt} \Gamma_{rtpq} , \tag{3.86}$$

$$\begin{aligned}
\frac{df_{12}}{ds} &= \sum_p (1 + P_{12}) \eta_{1p} f_{p2} + \sum_{pq} (n_p - n_q) (\eta_{pq} \Gamma_{q1p2} - f_{pq} \eta_{q1p2}) \\
&\quad + \frac{1}{2} \sum_{pqr} (n_p n_q \bar{n}_r + \bar{n}_p \bar{n}_q n_r) (1 + P_{12}) \eta_{r1pq} \Gamma_{pqr2} ,
\end{aligned} \tag{3.87}$$

$$\begin{aligned}
\frac{d\Gamma_{1234}}{ds} &= \sum_p \left((1 - P_{12}) (\eta_{1p} \Gamma_{p234} - f_{1p} \eta_{p234}) - (1 - P_{34}) (\eta_{p3} \Gamma_{12p4} - f_{p3} \eta_{12p4}) \right) \\
&\quad + \frac{1}{2} \sum_{pq} (1 - n_p - n_q) (\eta_{12pq} \Gamma_{pq34} - \Gamma_{12pq} \eta_{pq34}) \\
&\quad + \sum_{pq} (n_p - n_q) (1 - P_{12}) (1 - P_{34}) \eta_{1qp4} \Gamma_{p23q} .
\end{aligned} \tag{3.88}$$

Numbers (1, 2, 3, 4) in the above equations indicate external indices of the flowing Hamiltonian and internal summation indices are given by characters (p, q, r, t) . The commutator derived in Eq. (3.85) can be identified in the first sum of the flowing one-body part in Eq. (3.87) by replacing the indices 1 and 2 with q and r , respectively. The commutator expansion of the flow equation ensures that only connected diagrams contribute for the IMSRG, making it a size-extensive many-body method [31]. The computational cost of solving the IMSRG(2) scales like $\mathcal{O}(N^6)$ with N being the size of the single-particle basis. One can show that the IMSRG(2) truncation is complete up to third order in perturbation theory and additionally nonperturbatively resums particle-particle- and hole-hole-ladder as well as particle-hole-ring diagrams [31].

In practice, the set of coupled ordinary differential equations (ODE) is solved by integrating Eqs. (3.86)-(3.88) from $s = 0$ to $s \rightarrow \infty$ applying standard ODE solver methods, such as

a Runge-Kutta approach [216–218]. The ground-state energy of the system is then given by the expectation value of the transformed Hamiltonian $\langle \Phi | H(s \rightarrow \infty) | \Phi \rangle = E(s \rightarrow \infty)$. Instead of solving the flow equations up to the limit $s \rightarrow \infty$, it is more convenient to define a convergence criterion for the decoupling and stop the calculation at a finite value of s . Commonly employed criteria are the norm of the generator $\|\eta(s)\|$ or the energy correction at second-order perturbation theory $E^{(2)}$, which both signal the size of the matrix elements that couple the ground state to higher particle-hole excitations. Values below a given threshold indicate only small remaining coupling to particle-hole excitations and therefore only minor changes to $H(s)$ for the rest of the flow. An alternative method for solving the IMSRG flow equations is given by the Magnus approach, which will be discussed in more detail in Sec. 3.4.4.

3.4.1 Generator choices

In general, any functional form of the generator that fulfills the anti-Hermiticity constraint and leads to the desired decoupling of the reference state from all particle-hole excitations is imaginable in the IMSRG flow equations. This results, as for the free-space SRG, in a variety of possible generator choices, where some may perform better or worse in terms of their computational efficiency, convergence, or suppression and decoupling behavior. In the following, we list the most commonly applied generators to decouple the Hamiltonian and solve the IMSRG flow equations.

In order to decouple the ground state, we strive to suppress the off-diagonal part of the flowing Hamiltonian, given by the particle-hole excitations, indicated by the gray squares in Fig. 3.2. In the case of a two-body Hamiltonian, these are defined by all one-particle-one-hole (1p1h) and two-particle-two-hole (2p2h) excitations $|\Phi_i^a\rangle$ and $|\Phi_{ij}^{ab}\rangle$, respectively. The matrix elements of these excitations can be written by

$$\langle \Phi_i^a | H | \Phi \rangle = \langle \Phi | : a_i^\dagger a_a : H | \Phi \rangle = f_{ai}, \quad (3.89a)$$

$$\langle \Phi | H | \Phi_i^a \rangle = \langle \Phi | H : a_a^\dagger a_i : | \Phi \rangle = f_{ia}, \quad (3.89b)$$

$$\langle \Phi_{ij}^{ab} | H | \Phi \rangle = \langle \Phi | : a_i^\dagger a_j^\dagger a_b a_a : H | \Phi \rangle = \Gamma_{abij}, \quad (3.89c)$$

$$\langle \Phi | H | \Phi_{ij}^{ab} \rangle = \langle \Phi | H : a_a^\dagger a_b^\dagger a_j a_i : | \Phi \rangle = \Gamma_{ijab}, \quad (3.89d)$$

such that the off-diagonal Hamiltonian based on these matrix elements reads

$$H^{od}(s) = \sum_{ai} f_{ai}(s) : a_a^\dagger a_i : + \frac{1}{4} \sum_{abij} \Gamma_{abij}(s) : a_a^\dagger a_b^\dagger a_j a_i : + \text{H.c.}, \quad (3.90)$$

where H.c. indicates the Hermitian conjugates defined in Eq. (3.89).

The first generator choice we present here is the so-called White generator motivated based on the work of White in Ref. [219], which combines the one- and two-body matrix elements of the off-diagonal Hamiltonian in Eq. (3.90) with an energy denominator Δ

$$\eta(s)_{\text{White}} = \sum_{ai} \frac{f_{ai}(s)}{\Delta_{ai}(s)} : a_a^\dagger a_i : + \frac{1}{4} \sum_{abij} \frac{\Gamma_{abij}(s)}{\Delta_{abij}(s)} : a_a^\dagger a_b^\dagger a_j a_i : - \text{H.c.}, \quad (3.91)$$

where the denominators have to change sign under transposition of the first and second index of the one-body part and the first two and last two indices of the two-body part to fulfill the

constraint of anti-Hermiticity of the generator. A fixed point of the flow equation is reached once the off-diagonal part of the flowing Hamiltonian is fully suppressed. As a result, the matrix elements of the generator become 0, and thus, the generator and the Hamiltonian commute. A possible choice of the energy denominators is the Møller-Plesset denominators

$$\Delta_{ai} = \varepsilon_a - \varepsilon_i, \quad (3.92a)$$

$$\Delta_{abij} = \varepsilon_a + \varepsilon_b - \varepsilon_i - \varepsilon_j, \quad (3.92b)$$

with the SPEs $\varepsilon_i = f_{ii}$ given by the one-body part of the flowing Hamiltonian. Note that the SPEs and therefore the energy denominators depend on the flow parameter s , but we drop the dependence here for simplicity. Equations (3.92a) and (3.92b) obey the required antisymmetry under transposition, $\Delta_{ai} = -\Delta_{ia}$ and $\Delta_{abij} = -\Delta_{ijab}$. An alternative choice is the Epstein-Nesbet denominators, which additionally incorporate the two-body matrix elements Γ_{pqrs} ,

$$\Delta_{ai} = \varepsilon_a - \varepsilon_i + (n_a - n_i)\Gamma_{aiai}, \quad (3.93a)$$

$$\begin{aligned} \Delta_{abij} = & \varepsilon_a + \varepsilon_b - \varepsilon_i - \varepsilon_j + (1 - n_a - n_b)\Gamma_{abab} - (1 - n_i - n_j)\Gamma_{ijij} \\ & + (n_a - n_i)\Gamma_{aiai} + (n_a - n_j)\Gamma_{ajaj} + (n_b - n_i)\Gamma_{bibi} + (n_b - n_j)\Gamma_{bjbj}. \end{aligned} \quad (3.93b)$$

Again both expressions change sign under transposition.

Problems in the IMSRG flow using this generator can arise when the energy denominators become small or even vanish completely, leading to an enhancement of the off-diagonal elements during the flow instead of a suppression. This is, e.g., the case for systems with small energy gaps between the highest occupied and the lowest unoccupied orbitals. A remedy for this complication is given by the so-called arctan version of the White generator. The arctangent function tames possibly large matrix elements of the one- and two-body generator caused by small energy denominators to values in the interval $(-\pi/2, \pi/2)$,

$$\begin{aligned} \eta(s)_{\text{arctan}} = & \frac{1}{2} \sum_{ai} \arctan \left(\frac{2f_{ai}(s)}{\Delta_{ai}(s)} \right) : a_a^\dagger a_i : \\ & + \frac{1}{8} \sum_{abij} \arctan \left(\frac{2\Gamma_{abij}(s)}{\Delta_{abij}(s)} \right) : a_a^\dagger a_b^\dagger a_j a_i : -\text{H.c.}, \end{aligned} \quad (3.94)$$

where the prefactors for the one- and two-body part can be understood by the Taylor series expansion of the arctangent function for small arguments.

In a similar fashion, the problem of very small or vanishing energy denominators can be circumvented by employing the signum function, as is done for the so-called imaginary time generator motivated by the quantum Monte Carlo method

$$\begin{aligned} \eta(s)_{\text{imag. t}} = & \sum_{ai} \text{sgn}(\Delta_{ai}(s)) f_{ai}(s) : a_a^\dagger a_i : \\ & + \frac{1}{4} \sum_{abij} \text{sgn}(\Delta_{abij}(s)) \Gamma_{abij}(s) : a_a^\dagger a_b^\dagger a_j a_i : -\text{H.c.} \end{aligned} \quad (3.95)$$

In this thesis, we employ the arctan generator to solve the IMSRG flow equations, if not stated otherwise, but also investigate the dependence of the results on the generator choice in selected cases.

3.4.2 Angular-momentum-coupled flow equations

Nuclear Hamiltonians obey a set of symmetries that can be explicitly exploited to lower computational requirements for storing operator matrix elements and performing many-body calculations. These symmetries are: rotational invariance ($[H, J^2] = [H, J_z] = 0$) for the total angular momentum J and its projection on the z -component J_z , parity conservation ($[H, \Pi] = 0$), and isospin conservation ($[H, T_z] = 0$) for the projection T_z of the total isospin T . Exploiting these symmetries leads to a block-diagonal structure in the quantum numbers ($J\Pi T_z$), where off-diagonal matrix elements vanish and we store, e.g., the two-body matrix elements in separate blocks. The block structure is preserved for the normal-ordered Hamiltonian if a symmetry-conserving reference state is employed, which is the case for all systems and computational bases considered in this thesis. Applications of symmetry-broken reference states lead to many-body operators with reduced symmetries compared to their non-normal-ordered representations (see, e.g., Refs.[220, 221]).

In the following, we adapt our previous definition of the single-particle states $|p\rangle = |n(ls)jm_p m_{t_p}\rangle$ of Eq. (3.28) and write $|\tilde{p}\rangle = |n(ls)jm_{t_p}\rangle$ for single-particle states independent of the angular momentum projection m_p , with $|\tilde{p}m_p\rangle = |p\rangle$.

Operator matrix elements, independent of the total angular momentum projection m , in the so-called j -coupled scheme are given by an additional superscript, indicating the total angular momentum. The one-body matrix elements are given by

$$O_{\tilde{p}\tilde{q}}^j = \delta_{m_p m_q} \delta_{j_p j_q} \langle \tilde{p}m_p | O | \tilde{q}m_q \rangle, \quad (3.96)$$

and are diagonal in the angular-momentum projection $m_p = m_q$ and the angular momentum itself $j_p = j_q = j$.

The coupled two-body basis states are obtained by coupling the individual angular momenta j_p and j_q to the total two-body angular momentum J_{pq} with projection M_{pq} by a Clebsch–Gordan coefficient [222],

$$|(\tilde{p}\tilde{q})J_{pq}M_{pq}\rangle = \sum_{m_p m_q} \left(\begin{array}{cc} j_p & j_q \\ m_p & m_q \end{array} \middle| \begin{array}{c} J_{pq} \\ M_{pq} \end{array} \right) |pq\rangle. \quad (3.97)$$

Using the coupled basis, we can rewrite the two-body matrix elements of a scalar operator in a j -coupled form by coupling the angular momenta of the bra and the ket state,

$$\begin{aligned} O_{\tilde{p}\tilde{q}\tilde{r}\tilde{s}}^J &= \langle (\tilde{p}\tilde{q})JM_J | O | (\tilde{r}\tilde{s})JM_J \rangle \\ &= \sum_{\substack{m_p m_q \\ m_r m_s}} \left(\begin{array}{cc} j_p & j_q \\ m_p & m_q \end{array} \middle| \begin{array}{c} J \\ M_J \end{array} \right) \left(\begin{array}{cc} j_r & j_s \\ m_r & m_s \end{array} \middle| \begin{array}{c} J \\ M_J \end{array} \right) \langle pq | O | rs \rangle, \end{aligned} \quad (3.98)$$

where the superscript J denotes the total two-body angular momentum of the reduced (unnormalized) two-body matrix element. The conservation of the total angular momentum leads to $J_{pq} = J_{rs} = J$ and the matrix element is diagonal in this quantum number and its projection $M_J = M_{pq} = M_{rs}$ as well as independent of the latter and we set $M_{pq} = M_{rs} = J$. Two-body operators stored in the j -coupled form (the so-called “me2j” format) typically require about 0.7 GB memory in a compressed format. We drop the tilde over the momentum indices in the following for simplicity when working with angular-momentum-coupled states, the difference to the uncoupled expressions will be clear depending on the superscript. Applying the symmetry reduction to the m -scheme IMSRG flow equations

in Eqs. (3.86)-(3.88), we obtain the IMSRG(2) “ j -scheme” flow equations for the angular-momentum-coupled expressions. This can be most easily accomplished by using the `amc` tool [205] of Ref. [206].

$$\frac{dE}{ds} = \sum_{pq} (n_p - n_q) \hat{j}^2 \eta_{pq}^j f_{qp}^j + \frac{1}{2} \sum_{pqrtJ} n_p n_q \bar{n}_r \bar{n}_t \hat{J}^2 \eta_{pqrt}^J \Gamma_{rtpq}^J, \quad (3.99)$$

$$\begin{aligned} \frac{df_{12}^j}{ds} &= \sum_p (1 + P_{12}) \left(\eta_{1p}^j f_{p2}^j \right) + \frac{1}{\hat{j}^2} \sum_{pqJ} (n_p - n_q) \hat{J}^2 \left(\eta_{pq}^j \Gamma_{q1p2}^J - f_{pq}^j \eta_{q1p2}^J \right) \\ &+ \frac{1}{2} \frac{1}{\hat{j}^2} \sum_{pqrJ} (n_p n_q \bar{n}_r + \bar{n}_p \bar{n}_q n_r) (1 + P_{12}) \hat{J}^2 \eta_{r1pq}^J \Gamma_{pqr2}^J, \end{aligned} \quad (3.100)$$

$$\begin{aligned} \frac{d\Gamma_{1234}^J}{ds} &= \sum_p (1 - (-1)^{j_1+j_2-J} P_{12}) \left(\eta_{1p}^j \Gamma_{p234}^J - f_{1p}^j \eta_{p234}^J \right) \\ &- \sum_p (1 - (-1)^{j_3+j_4-J} P_{34}) \left(\eta_{p3}^j \Gamma_{12p4}^J - f_{p3}^j \eta_{12p4}^J \right) \\ &+ \frac{1}{2} \sum_{pq} (1 - n_p - n_q) \left(\eta_{12pq}^J \Gamma_{pq34}^J - \Gamma_{12pq}^J \eta_{pq34}^J \right) \\ &+ \sum_{pqJ'} (n_p - n_q) \left(1 - (-1)^{j_1+j_2-J} P_{12} - (-1)^{j_3+j_4-J} P_{34} + (-1)^{j_1+j_2+j_3+j_4} P_{12} P_{34} \right) \\ &\quad \times \hat{J}'^2 \left\{ \begin{matrix} j_1 & j_2 & J \\ j_3 & j_4 & J' \end{matrix} \right\} \bar{\eta}_{14pq}^{J'} \bar{\Gamma}_{pq32}^{J'}, \end{aligned} \quad (3.101)$$

where $\hat{J} = \sqrt{2J+1}$ and we dropped the indices of the total two-body angular momentum J of the j -coupled matrix elements. The overlined operators $\bar{\eta}_{14pq}^{J'}$ and $\bar{\Gamma}_{pq32}^{J'}$ in the last row of Eq. (3.101) are the Pandya-transformed matrix elements obtained by the Pandya transformation [223]

$$\bar{\Gamma}_{1432}^{J'} \equiv - \sum_J \hat{J}^2 \left\{ \begin{matrix} j_1 & j_4 & J' \\ j_3 & j_2 & J \end{matrix} \right\} \Gamma_{1234}^J, \quad (3.102)$$

with the $6j$ -symbol reordering the coupling of the angular momenta (see, e.g., Ref. [222]). This transformation allows one to perform the tensor contraction in the last line of Eq. (3.101) as a matrix matrix multiplication, thus, being computationally more efficient. The resulting two-body matrix element is initially given in the form $\bar{\Gamma}_{1432}^{J'}$, however the Pandya transformation is its own inverse, such that we employ an additional Pandya transformation to obtain the desired output matrix element Γ_{1234}^J indicated by the sum over J' and the $6j$ -symbol in the last line of Eq. (3.101). Typical IMSRG(2) calculations in converged model spaces of $e_{\max} = 14$ take about 16 hours on a supercomputing node with around 24 cores.

3.4.3 General operators and charge radii in the IMSRG

The unitary transformation and flow equation of the Hamiltonian in Eqs. (3.76) and (3.77) can be adapted to any other additional operator O of interest. Applying the unitary transformation $U(s)$ to the normal-ordered operator O with respect to the same reference state as the Hamiltonian yields

$$O(s) = U(s)O(0)U^\dagger(s), \quad (3.103)$$

and can be expressed as a flow equation for the transformed operator $O(s)$

$$\frac{dO(s)}{ds} = [\eta(s), O(s)] . \quad (3.104)$$

The set of flow equations for each additional operator results in an increased number of coupled differential equations that have to be solved together with the Hamiltonian. This increases computational expenses in terms of both memory requirements and runtime, which is why typically the number of additional operators in the IMSRG is limited to very few operators.

In the following, we demonstrate the advantages of the IMSRG to calculate other observables than just the ground-state energy by considering the point-proton mean-square radius operator, which is the main component for the calculation of charge radii of finite nuclei. The operator is given by

$$R_p^2 = \frac{1}{Z} \sum_{i=1}^A \frac{1 + \tau_3^{(i)}}{2} (\mathbf{r}_i - \mathbf{R})^2 , \quad (3.105)$$

with proton number Z , the isospin projection $\tau_3^{(i)}$ of the i -th particle with $(1 + \tau_3^{(i)})/2$ projecting on protons, the coordinate \mathbf{r}_i of the i -th particle, and the cm coordinate \mathbf{R} . The charge radius based on the point-proton radius operator is obtained by adding the relativistic Darwin-Foldy correction $3/(4M^2) = 0.033 \text{ fm}^2$ [224–226], the spin-orbit correction $\langle r^2 \rangle_{so}$ [227], and considering the mean-square radius of the proton and neutron $\langle r_p^2 \rangle$ and $\langle r_n^2 \rangle$, respectively,

$$R_{ch} = \sqrt{R_p^2 + \langle r_p^2 \rangle + \frac{N}{Z} \langle r_n^2 \rangle + \frac{3}{4M^2} + \langle r^2 \rangle_{so}} , \quad (3.106)$$

where $N = A - Z$ is the neutron number and M is the nucleon mass. Different experimental techniques to measure the proton charge radius produce different values, giving rise to the so-called proton-radius puzzle. To be precise, measurements performed on muonic hydrogen [228, 229] disagree significantly with measurements performed on atomic hydrogen [230]. These controversies led to ongoing investigations [231–233] in order to find an explanation, however, new evidence has not been able to fully resolve the proton-radius puzzle so far [234, 235]. In this thesis we use the values $\langle r_p^2 \rangle = 0.770 \text{ fm}^2$ and $\langle r_n^2 \rangle = -0.1149 \text{ fm}^2$. Note that two-body currents, which would give additional corrections to the charge radius, are not considered here. The spin-orbit correction is calculated by

$$\langle r^2 \rangle_{so} = -\frac{1}{Z} \sum_{i=1}^A \frac{\mu_i}{M^2} (\kappa_i + 1) , \quad (3.107)$$

with the magnetic moment μ_i of particle i , given by $\mu_p = 2.793\mu_N$ and $\mu_n = -1.913\mu_N$ [102] for protons and neutrons, respectively, and the nuclear magneton μ_N and the parameter κ_i defined by

$$\kappa_i = \begin{cases} l_i & \text{if } j_i = l_i - \frac{1}{2} , \\ -(l_i + 1) & \text{if } j_i = l_i + \frac{1}{2} . \end{cases} \quad (3.108)$$

The IMSRG charge radius R_{ch} is obtained by evolving the operator R_p^2 along with the Hamiltonian up to a finite value of the flow parameter s , where the chosen convergence criteria are met and the ground state is decoupled. Adding the corresponding corrections given in Eq. (3.106) to the evolved operator finally gives the charge radius for the studied system.

3.4.4 Magnus approach

In practice, the solution of the set of coupled ODEs, given by the flow equations in Eqs. (3.99)-(3.101), can be quite involved and requires the usage of high-order ODE solvers, e.g., Runge-Kutta solvers [218] or other sophisticated solver methods, to obtain numerically stable results. These solvers necessitate the storage of multiple copies of the solution vector throughout the flow, leading to tremendous memory costs in model-space sizes required for converged results. Any additional operator targeted in the IMSRG, e.g., the point-proton mean-square radius operator for calculations of the charge radius described in Sec. 3.4.3, has to be evolved in parallel with the Hamiltonian, roughly leading to a doubling of the computational costs and memory demands. An alternative approach to solving the IMSRG flow equations, with the possibility to circumvent some of the key challenges mentioned above, is the Magnus expansion of Refs. [236, 237], which results in significantly reduced memory footprints and lowered computation costs. In this method, one directly solves for the unitary transformation based on a simple first-order Euler method, while preserving the same numerical accuracy as for standard ODE solver applications, see also Ref. [160] for a recent free-space SRG application of the Magnus expansion. In the Magnus approach, the solution to the differential equation of the unitary transformation

$$\frac{dU(s)}{ds} = -\eta(s)U(s), \quad (3.109)$$

is given by an exponential ansatz

$$U(s) = e^{\Omega(s)}, \quad (3.110)$$

with the anti-Hermitian Magnus operator $\Omega(s)$, which fulfills $\Omega(s)^\dagger = -\Omega(s)$ and $\Omega(0) = 0$, such that $U(s)U^\dagger(s) = \mathbb{1}$ and $U(0) = 1$, as required. This allows one to write the transformation of the Hamiltonian or any other operator in the IMSRG as

$$H(s) = e^{\Omega(s)}H(0)e^{-\Omega(s)}. \quad (3.111)$$

In contrast to the standard approach of solving the flow equations for the Hamiltonian, we solve the flow equations for the Magnus operator

$$\frac{d\Omega(s)}{ds} = \sum_{k=0}^{\infty} \frac{B_k}{k!} ad_{\Omega(s)}^k(\eta(s)), \quad (3.112)$$

with the Bernoulli numbers B_k and the nested commutators $ad_{\Omega(s)}^k$ defined as

$$ad_{\Omega(s)}^0(\eta(s)) = \eta(s), \quad (3.113a)$$

$$ad_{\Omega(s)}^k(\eta(s)) = \left[\Omega(s), ad_{\Omega(s)}^{k-1}(\eta(s)) \right]. \quad (3.113b)$$

Technically, the differential equation for the Magnus operator in Eq. (3.112) is solved by a naive first-order Euler method and provides numerically stable results that are rather insensitive to the Euler step size and, at convergence, in agreement with exact methods. This allows for a simplified solution of the IMSRG flow based on a computationally cheaper and straightforward method compared to standard ODE solvers. Knowing the Magnus operator $\Omega(s)$, the transformed Hamiltonian in Eq. (3.111) can be obtained by using the BCH formula

$$H(s) = \sum_{k=0}^{\infty} \frac{1}{k!} ad_{\Omega(s)}^k(H(0)), \quad (3.114)$$

with the definition of the nested commutators as before. This series involves an infinite number of terms and does not terminate naturally, in contrast to, e.g., the transformation of the Hamiltonian in CC theory in Eqs. (3.54) and (3.55) discussed in Sec. 3.3.2, such that a truncation scheme is required. In the Magnus(2) approach all operators and commutators are truncated at the NO2B level, in consistency with the IMSRG(2). It is important to note that even though the Magnus operator $\Omega(s)$ is truncated, the transformation stays unitary due to the exponential ansatz. However, even in the Magnus(2) the series for the Magnus operator in Eq. (3.112) and the transformation of the Hamiltonian in Eq. (3.114) do not terminate automatically and still involve an infinite number of terms. In practical calculations, these are truncated beyond a chosen threshold value, as the magnitude of higher-order terms typically decreases monotonically. The truncation criteria may be defined by

$$\left| \frac{B_k \|ad_{\Omega(s)}^k(\eta(s))\|}{k! \|\Omega(s)\|} \right| < \epsilon_{\text{deriv}}, \quad (3.115)$$

$$\left| \frac{\left(ad_{\Omega(s)}^k(H(0))\right)^{(0)}}{k!} \right| < \epsilon_{\text{BCH}}, \quad (3.116)$$

for the truncation of Eq. (3.112) and Eq. (3.114), respectively, where we use the zero-body part of the nested commutator expression in Eq. (3.116). Additionally, we can split up the application of the Magnus expansion to solve the IMSRG flow equations in multiple steps of updating the Magnus operator each time the operator (or its norm) gets large. This approach more closely resembles the solution of using standard ODE solvers. In practice, we solve Eq. (3.112) and transform the initial Hamiltonian based on Eq. (3.114) until the norm $\|\Omega(s)\|$ exceeds a chosen threshold value. We now use the transformed Hamiltonian $H(s)$ at this point in the flow as new initial Hamiltonian, update the Magnus operator based on the new Hamiltonian, and continue solving the flow equations with the updated operators until we reach the next update step of $\Omega(s)$.

Having direct access to the unitary transformation based on Eq. (3.110), the Magnus expansion provides a desirable feature: Any additional operator O can now be transformed with minimal additional cost of only evaluating the BCH formula for the operator [cf. Eq. (3.114)]

$$O(s) = e^{\Omega(s)} O(0) e^{-\Omega(s)} = \sum_{k=0}^{\infty} \frac{1}{k!} ad_{\Omega(s)}^k(O(0)). \quad (3.117)$$

This is in contrast to evolving the operator along with the Hamiltonian, which results in additional flow equations and an extended set of coupled ODEs. In this thesis, we use

the Magnus expansion with the arctan generator of Eq. (3.94) to solve the IMSRG(2) flow equations.

3.5 IMSRG with three-body operators

The IMSRG(2) predicts nuclear observables, e.g., ground-state energies and charge radii, of medium-mass (and up to some heavy) nuclei in good agreement with experiment and is with great success applied for *ab initio* investigations of finite nuclei, see, e.g., Refs. [49, 50, 55, 75]. However, it has been shown that triples effects that are neglected in the IMSRG(2) truncation are important for many observables and theoretical predictions, e.g., 2^+ excitation energies [55, 90], nuclear β -decay matrix elements [238], or the dipole polarizability [239, 240]. Incorporating these effects in the many-body method by means of three-particle-three-hole (3p3h) excitations of the reference state is therefore key for meaningful comparisons and theoretical predictions. Extending the IMSRG to the next order in the many-body truncation, the IMSRG(3), and including initial and induced three-body operators up to the three-body rank during the flow, provides an important step towards more accurate results and systematically improves the many-body method. In this section, we review the basic steps necessary to obtain the extended set of fundamental commutators and derive the IMSRG(3) flow equations. We define different approximate truncation schemes of the IMSRG(3) based on computational cost and perturbative arguments. These results are part of our publication [241], to which I contributed with support for the implementation, especially regarding the use of different single-particle bases. Here, we only review the basic aspects and show selected results in Sec. 4.5, but refer to Ref. [241] for further details.

By including three-body operators in the IMSRG, two effects occur: The initial (normal-ordered) Hamiltonian as well as the generator can contain residual three-body interactions, given by the three-body term W in Eq. (3.19) for the Hamiltonian and $\eta^{(3)}$ for the generator. Additionally, new commutator contributions arise and we truncate the commutator expressions at the three-body level, now also including the induced three-body terms during the flow that have been neglected in the IMSRG(2) in Eqs. (3.81)-(3.84). The extended set of fundamental commutators in the IMSRG(3) based on the flow equation (3.77) for a three-body Hamiltonian and three-body generator includes 15 new terms compared to the IMSRG(2) commutator expressions (however only ten of these consist of new analytic structure) and is given by

$$\left[\eta(s)^{(1)}, f(s)\right] = \left[\eta(s)^{(1)}, f(s)\right]^{(0)} + \left[\eta(s)^{(1)}, f(s)\right]^{(1)}, \quad (3.118)$$

$$\left[\eta(s)^{(1)}, \Gamma(s)\right] = \left[\eta(s)^{(1)}, \Gamma(s)\right]^{(1)} + \left[\eta(s)^{(1)}, \Gamma(s)\right]^{(2)}, \quad (3.119)$$

$$\left[\eta(s)^{(2)}, f(s)\right] = \left[\eta(s)^{(2)}, f(s)\right]^{(1)} + \left[\eta(s)^{(2)}, f(s)\right]^{(2)}, \quad (3.120)$$

$$\begin{aligned} \left[\eta(s)^{(2)}, \Gamma(s)\right] &= \left[\eta(s)^{(2)}, \Gamma(s)\right]^{(0)} + \left[\eta(s)^{(2)}, \Gamma(s)\right]^{(1)} + \left[\eta(s)^{(2)}, \Gamma(s)\right]^{(2)} \\ &\quad + \left[\eta(s)^{(2)}, \Gamma(s)\right]^{(3)}, \end{aligned} \quad (3.121)$$

$$\left[\eta(s)^{(1)}, W(s)\right] = \left[\eta(s)^{(1)}, W(s)\right]^{(2)} + \left[\eta(s)^{(1)}, W(s)\right]^{(3)}, \quad (3.122)$$

$$\left[\eta(s)^{(3)}, f(s)\right] = \left[\eta(s)^{(3)}, f(s)\right]^{(2)} + \left[\eta(s)^{(3)}, f(s)\right]^{(3)}, \quad (3.123)$$

$$\left[\eta(s)^{(2)}, W(s)\right] = \left[\eta(s)^{(2)}, W(s)\right]^{(1)} + \left[\eta(s)^{(2)}, W(s)\right]^{(2)} + \left[\eta(s)^{(2)}, W(s)\right]^{(3)}, \quad (3.124)$$

$$\left[\eta(s)^{(3)}, \Gamma(s)\right] = \left[\eta(s)^{(3)}, \Gamma(s)\right]^{(1)} + \left[\eta(s)^{(3)}, \Gamma(s)\right]^{(2)} + \left[\eta(s)^{(3)}, \Gamma(s)\right]^{(3)}, \quad (3.125)$$

$$\begin{aligned} \left[\eta(s)^{(3)}, W(s)\right] &= \left[\eta(s)^{(3)}, W(s)\right]^{(0)} + \left[\eta(s)^{(3)}, W(s)\right]^{(1)} + \left[\eta(s)^{(3)}, W(s)\right]^{(2)} \\ &+ \left[\eta(s)^{(3)}, W(s)\right]^{(3)}, \end{aligned} \quad (3.126)$$

where the three-body term $\left[\eta(s)^{(2)}, \Gamma(s)\right]^{(3)}$ in Eq. (3.121) vanishes in the IMSRG(2) truncation. Induced many-body contributions beyond the three-body level, e.g., the four-body term $\left[\eta(s)^{(2)}, W(s)\right]^{(4)}$, which would arise in Eq. (3.124), are neglected in the IMSRG(3). The three-body Hamiltonian now additionally couples 3p3h excitations to the reference state, with the corresponding matrix elements written as

$$\langle \Phi_{ijk}^{abc} | H | \Phi \rangle = \langle \Phi | : a_i^\dagger a_j^\dagger a_k^\dagger a_c a_b a_a : H | \Phi \rangle = W_{abcijk}, \quad (3.127a)$$

$$\langle \Phi | H | \Phi_{ijk}^{abc} \rangle = \langle \Phi | H : a_a^\dagger a_b^\dagger a_c^\dagger a_k a_j a_i : | \Phi \rangle = W_{ijkabc}, \quad (3.127b)$$

similar the two-body case in Eq. (3.89). The off-diagonal Hamiltonian is accordingly given by

$$\begin{aligned} H^{od}(s) &= \sum_{ai} f_{ai}(s) : a_a^\dagger a_i : + \frac{1}{4} \sum_{abij} \Gamma_{abij}(s) : a_a^\dagger a_b^\dagger a_j a_i : \\ &+ \frac{1}{36} \sum_{abcijk} W_{abcijk}(s) : a_a^\dagger a_b^\dagger a_c^\dagger a_k a_j a_i : + \text{H.c.} \end{aligned} \quad (3.128)$$

In order to obtain the correct decoupling behavior and also decouple 3p3h excitations from the reference state during the IMSRG flow, the generator definitions in Sec. 3.4.1 have to be extended by the three-body part $\eta(s)^{(3)}$. The matrix elements of the White generator are given by

$$\eta(s)_{abcijk}^{(3)} = \frac{W_{abcijk}(s)}{\Delta_{abcijk}(s)}, \quad (3.129)$$

with the Møller-Plesset energy denominator

$$\Delta_{abcijk} = \varepsilon_a + \varepsilon_b + \varepsilon_c - \varepsilon_i - \varepsilon_j - \varepsilon_k. \quad (3.130)$$

The arctan generator is defined as

$$\eta(s)_{abcijk}^{(3)} = \frac{1}{2} \arctan \left(\frac{2W_{abcijk}(s)}{\Delta_{abcijk}(s)} \right), \quad (3.131)$$

and the imaginary-time generator reads

$$\eta(s)_{abcijk}^{(3)} = \text{sgn}(\Delta_{abcijk}(s)) W_{abcijk}(s). \quad (3.132)$$

The Hermitian conjugate matrix elements of the three generator types are obtained by transposition of the particle and hole indices, and again, the energy denominator ensures the anti-Hermiticity of the generator.

In the following, we derive the IMSRG(3) m -scheme flow equations to decouple the

reference state and drive the off-diagonal Hamiltonian in Eq. (3.128) to zero. As before, we sort the commutator contributions by their particle rank, now going up to rank three, to obtain a set of coupled ordinary differential equations. For simplicity, we first give a schematic derivation of the individual IMSRG(3) fundamental commutators of Eqs. (3.118)-(3.126) by two generic many-body operators A and B of rank K and L , respectively and resulting operator C . For $[A^{(K)}, B^{(L)}] \rightarrow C$, the operator C contains all possible many-body ranks M allowed by the commutator evaluation [cf. Eq. (3.79)] and the IMSRG(3) truncation. The many-body rank of the operator $C^{(M)}$ is implicitly given by the number of indices of the matrix element and we only indicate the zero-body part with a superscript (0).

$$\blacksquare [A^{(1)}, B^{(1)}] \rightarrow \circ$$

$$C^{(0)} = \sum_{pq} (n_p \bar{n}_q - \bar{n}_p n_q) A_{pq} B_{qp}, \quad (3.133a)$$

$$C_{12} = \sum_p (A_{1p} B_{p2} - B_{1p} A_{p2}). \quad (3.133b)$$

$$\blacksquare [A^{(1)}, B^{(2)}] \rightarrow \circ$$

$$C_{12} = \sum_{pq} (n_p \bar{n}_q - \bar{n}_p n_q) A_{pq} B_{1q2p}, \quad (3.134a)$$

$$C_{1234} = 2 \sum_p (A_{1p} B_{p234} - A_{p3} B_{12p4}). \quad (3.134b)$$

$$\blacksquare [A^{(2)}, B^{(2)}] \rightarrow \circ$$

$$C^{(0)} = \frac{1}{4} \sum_{pqrs} (n_p n_q \bar{n}_r \bar{n}_s - \bar{n}_p \bar{n}_q n_r n_s) A_{pqrs} B_{rspq}, \quad (3.135a)$$

$$C_{12} = \frac{1}{2} \sum_{pqr} (n_p n_q \bar{n}_r + \bar{n}_p \bar{n}_q n_r) (A_{1r pq} B_{pq2r} - B_{1r pq} A_{pq2r}), \quad (3.135b)$$

$$C_{1234} = \frac{1}{2} \sum_{pq} (\bar{n}_p \bar{n}_q - n_p n_q) (A_{12pq} B_{pq34} - B_{12pq} A_{pq34}) \\ - 4 \sum_{pq} (n_p \bar{n}_q - \bar{n}_p n_q) A_{p23q} B_{1qp4}, \quad (3.135c)$$

$$C_{123456} = 9 \sum_p (A_{3p45} B_{126p} - B_{3p45} A_{126p}). \quad (3.135d)$$

$$\blacksquare [A^{(1)}, B^{(3)}] \rightarrow \circ$$

$$C_{1234} = \sum_{pq} (n_p \bar{n}_q - \bar{n}_p n_q) A_{pq} B_{12q34p}, \quad (3.136a)$$

$$C_{123456} = 3 \sum_p (A_{3p} B_{12p456} - A_{p6} B_{12345p}). \quad (3.136b)$$

$$\blacksquare [A^{(2)}, B^{(3)}] \rightarrow \circ$$

$$C_{12} = \frac{1}{4} \sum_{pqrs} (n_p n_q \bar{n}_r \bar{n}_s - \bar{n}_p \bar{n}_q n_r n_s) A_{pqrs} B_{rs1pq2}, \quad (3.137a)$$

$$C_{1234} = \sum_{pqr} (n_p n_q \bar{n}_r + \bar{n}_p \bar{n}_q n_r) (A_{r1pq} B_{pq234r} - A_{pqr3} B_{12r pq4}), \quad (3.137b)$$

$$C_{123456} = \frac{3}{2} \sum_{pq} (\bar{n}_p \bar{n}_q - n_p n_q) (A_{12pq} B_{pq3456} - A_{pq45} B_{123pq6}) \\ + 9 \sum_{pq} (\bar{n}_p n_q - n_p \bar{n}_q) A_{3pq6} B_{12q45p}. \quad (3.137c)$$

$$\blacksquare [A^{(3)}, B^{(3)}] \rightarrow \circ$$

$$C^{(0)} = \frac{1}{36} \sum_{pqrst} (n_p n_q n_r \bar{n}_s \bar{n}_t \bar{n}_u - \bar{n}_p \bar{n}_q \bar{n}_r n_s n_t n_u) A_{pqrst} B_{stupqr}, \quad (3.138a)$$

$$C_{12} = \frac{1}{12} \sum_{pqrst} (n_p n_q n_r \bar{n}_s \bar{n}_t + \bar{n}_p \bar{n}_q \bar{n}_r n_s n_t) (A_{st1pqr} B_{pqrst2} - B_{st1pqr} A_{pqrst2}), \quad (3.138b)$$

$$C_{1234} = \frac{1}{6} \sum_{pqrs} (\bar{n}_p \bar{n}_q \bar{n}_r n_s - n_p n_q n_r \bar{n}_s) (A_{12spqr} B_{pqr34s} - B_{12spqr} A_{pqr34s}) \\ + \sum_{pqrs} (n_p n_q \bar{n}_r \bar{n}_s - \bar{n}_p \bar{n}_q n_r n_s) A_{pq1rs3} B_{rs2pq4}, \quad (3.138c)$$

$$C_{123456} = \frac{1}{6} \sum_{pqr} (n_p n_q n_r + \bar{n}_p \bar{n}_q \bar{n}_r) (A_{123pqr} B_{pqr456} - B_{123pqr} A_{pqr456}) \\ + \frac{9}{2} \sum_{pqr} (n_p n_q \bar{n}_r + \bar{n}_p \bar{n}_q n_r) (A_{pq345r} B_{12r pq6} - B_{pq345r} A_{12r pq6}). \quad (3.138d)$$

The computational cost of each commutator scales naively like $\mathcal{O}(N^{K+L+M})$ in the size of the single-particle basis N , with M being the many-body rank of the resulting operator C . The cost of the full IMSRG(3) solution is dominated by the most expensive commutator, the $[A^{(3)}, B^{(3)}] \rightarrow C^{(3)}$ commutator, and as a result scales like $\mathcal{O}(N^9)$.

In a next step, we utilize the generic expressions derived above for the fundamental IMSRG(3) commutators given in Eqs. (3.118)-(3.126) and ensure the antisymmetry of the two- and three-body matrix elements throughout the IMSRG evolution by applying the permutation operator. We use the permutation operator P_{12} for the two-body matrix elements and additionally introduce the permutation operator $P(12/3) \equiv 1 - P_{13} - P_{23}$ for the combination of three indices to antisymmetrize the three-body contributions. The m -scheme flow equations for the IMSRG(3) are then given by

$$\frac{d}{ds} E = \sum_{pq} (n_p \bar{n}_q - \bar{n}_p n_q) \eta_{pq} f_{qp} + \frac{1}{4} \sum_{pqrt} (n_p n_q \bar{n}_r \bar{n}_t - \bar{n}_p \bar{n}_q n_r n_t) \eta_{pqrt} \Gamma_{rt pq} \\ + \frac{1}{36} \sum_{pqrtuv} (n_p n_q n_r \bar{n}_t \bar{n}_u \bar{n}_v - \bar{n}_p \bar{n}_q \bar{n}_r n_t n_u n_v) \eta_{pqrtuv} W_{tuv pqr}, \quad (3.139)$$

$$\begin{aligned}
\frac{d}{ds}f_{12} &= \sum_p (\eta_{1p}f_{p2} - f_{1p}\eta_{p2}) + \sum_{pq} (n_p\bar{n}_q - \bar{n}_p n_q) (\eta_{pq}\Gamma_{1q2p} - f_{pq}\eta_{1q2p}) \\
&+ \frac{1}{2} \sum_{pqr} (n_p n_q \bar{n}_r + \bar{n}_p \bar{n}_q n_r) (\eta_{1r pq} \Gamma_{pq2r} - \Gamma_{1r pq} \eta_{pq2r}) \\
&+ \frac{1}{4} \sum_{pqrt} (n_p n_q \bar{n}_r \bar{n}_t - \bar{n}_p \bar{n}_q n_r n_t) (\eta_{pqrt} W_{rt1pq2} - \Gamma_{pqrt} \eta_{rt1pq2}) \\
&+ \frac{1}{12} \sum_{pqrtu} (n_p n_q n_r \bar{n}_t \bar{n}_u + \bar{n}_p \bar{n}_q \bar{n}_r n_t n_u) (\eta_{tu1pqr} W_{pqrtu2} - W_{tu1pqr} \eta_{pqrtu2}) ,
\end{aligned} \tag{3.140}$$

$$\begin{aligned}
\frac{d}{ds}\Gamma_{1234} &= (1 - P_{12}) \sum_p (\eta_{1p}\Gamma_{p234} - f_{1p}\eta_{p234}) - (1 - P_{34}) \sum_p (\eta_{p3}\Gamma_{12p4} - f_{p3}\eta_{12p4}) \\
&+ \frac{1}{2} \sum_{pq} (\bar{n}_p \bar{n}_q - n_p n_q) (\eta_{12pq}\Gamma_{pq34} - \Gamma_{12pq}\eta_{pq34}) \\
&- (1 - P_{12})(1 - P_{34}) \sum_{pq} (n_p \bar{n}_q - \bar{n}_p n_q) \eta_{p23q} \Gamma_{1qp4} \\
&+ \sum_{pq} (n_p \bar{n}_q - \bar{n}_p n_q) (\eta_{pq} W_{12q34p} - f_{pq} \eta_{12q34p}) \\
&+ \frac{1}{2} (1 - P_{12}) \sum_{pqr} (n_p n_q \bar{n}_r + \bar{n}_p \bar{n}_q n_r) (\eta_{r1pq} W_{pq234r} - \Gamma_{r1pq} \eta_{pq234r}) \\
&- \frac{1}{2} (1 - P_{34}) \sum_{pqr} (n_p n_q \bar{n}_r + \bar{n}_p \bar{n}_q n_r) (\eta_{pqr3} W_{12r pq4} - \Gamma_{pqr3} \eta_{12r pq4}) \\
&+ \frac{1}{6} \sum_{pqrt} (\bar{n}_p \bar{n}_q \bar{n}_r n_t - n_p n_q n_r \bar{n}_t) (\eta_{12tpqr} W_{pqr34t} - W_{12tpqr} \eta_{pqr34t}) \\
&+ \frac{1}{4} (1 - P_{12})(1 - P_{34}) \sum_{pqrt} (n_p n_q \bar{n}_r \bar{n}_t - \bar{n}_p \bar{n}_q n_r n_t) \eta_{pq1rt3} W_{rt2pq4} ,
\end{aligned} \tag{3.141}$$

$$\begin{aligned}
\frac{d}{ds}W_{123456} &= P(12/3)P(45/6) \sum_p (\eta_{3p45}\Gamma_{126p} - \Gamma_{3p45}\eta_{126p}) \\
&+ P(12/3) \sum_p (\eta_{3p}W_{12p456} - f_{3p}\eta_{12p456}) - P(45/6) \sum_p (\eta_{p6}W_{12345p} - f_{p6}\eta_{12345p}) \\
&+ \frac{1}{2} P(12/3) \sum_{pq} (\bar{n}_p \bar{n}_q - n_p n_q) (\eta_{12pq} W_{pq3456} - \Gamma_{12pq} \eta_{pq3456}) \\
&- \frac{1}{2} P(45/6) \sum_{pq} (\bar{n}_p \bar{n}_q - n_p n_q) (\eta_{pq45} W_{123pq6} - \Gamma_{pq45} \eta_{123pq6}) \\
&+ P(12/3)P(45/6) \sum_{pq} (\bar{n}_p n_q - n_p \bar{n}_q) (\eta_{3pq6} W_{12q45p} - \Gamma_{3pq6} \eta_{12q45p}) \\
&+ \frac{1}{6} \sum_{pqr} (n_p n_q n_r + \bar{n}_p \bar{n}_q \bar{n}_r) (\eta_{123pqr} W_{pqr456} - W_{123pqr} \eta_{pqr456}) \\
&+ \frac{1}{2} P(12/3)P(45/6) \sum_{pqr} (n_p n_q \bar{n}_r + \bar{n}_p \bar{n}_q n_r) (\eta_{pq345r} W_{12r pq6} - W_{pq345r} \eta_{12r pq6}) .
\end{aligned} \tag{3.142}$$

Exploiting the conservation of the total angular momentum and working in an angular-momentum-coupled basis for spherically symmetric systems (e.g., closed-shell nuclei), as outlined in Sec. 3.4.2, significantly reduces the memory requirements of storing matrix elements. This is especially important for the three-body operators and their multiple copies,

which are required when solving the IMSRG flow equations that dominate the memory costs. Additionally, working with the coupled expressions for the fundamental commutators also lowers the computational efforts for the commutator evaluation. However, the equations get more involved and more complicated expressions arise for the antisymmetrization of the j -coupled terms. The coupled one- and two-body basis states as well as the one- and two-body operator matrix elements in an angular-momentum-coupled basis have already been discussed in Eqs. (3.96)-(3.98) for the IMSRG(2). The coupled three-body basis states can be written as

$$|[(\tilde{p}\tilde{q})J_{pq}M_{pq}\tilde{r}]\mathcal{J}M_{\mathcal{J}}\rangle = \sum_{\substack{m_p m_q \\ M_{pq} m_r}} \begin{pmatrix} j_p & j_q & J_{pq} \\ m_p & m_q & M_{pq} \end{pmatrix} \begin{pmatrix} J_{pq} & j_r & \mathcal{J} \\ M_{pq} & m_r & M_{\mathcal{J}} \end{pmatrix} |pqr\rangle, \quad (3.143)$$

where we couple the angular momentum of particle p and q to J_{pq} as in the two-body case, and subsequently couple J_{pq} with the angular momentum j_r of particle r to the total three-body angular momentum \mathcal{J} with its projection $M_{\mathcal{J}}$. Note that in general, also other coupling orders are possible, e.g., first coupling the angular momenta of q and r and then coupling J_{qr} with j_p to the total angular momentum. The corresponding three-body matrix elements for a scalar operator and the j -coupled basis are given by

$$\begin{aligned} O_{\tilde{p}\tilde{q}\tilde{r}\tilde{s}\tilde{t}\tilde{u}}^{\mathcal{J},J_{pq},J_{st}} &= \langle [(\tilde{p}\tilde{q})J_{pq}M_{pq}\tilde{r}]\mathcal{J}M_{\mathcal{J}} | O | [(\tilde{s}\tilde{t})J_{st}M_{st}\tilde{u}]\mathcal{J}M_{\mathcal{J}} \rangle \\ &= \sum_{\substack{m_p m_q \\ M_{pq} m_r}} \sum_{\substack{m_s m_t \\ M_{st} m_u}} \begin{pmatrix} j_p & j_q & J_{pq} \\ m_p & m_q & M_{pq} \end{pmatrix} \begin{pmatrix} J_{pq} & j_r & \mathcal{J} \\ M_{pq} & m_r & M_{\mathcal{J}} \end{pmatrix} \\ &\quad \times \begin{pmatrix} j_s & j_t & J_{st} \\ m_s & m_t & M_{st} \end{pmatrix} \begin{pmatrix} J_{st} & j_u & \mathcal{J} \\ M_{st} & m_u & M_{\mathcal{J}} \end{pmatrix} \langle pqr | O | stu \rangle, \end{aligned} \quad (3.144)$$

where the superscripts indicate the total three-body angular momentum \mathcal{J} and the intermediate angular momenta J_{pq} and J_{st} of the bra and ket state, respectively. Due to angular-momentum conservation both J_{pq} with j_r and J_{st} with j_u couple to the same total angular momentum \mathcal{J} and we set $M_{\mathcal{J}} = \mathcal{J}$. Note however that J_{pq} and J_{rs} in general can be different and that the matrix element is independent of $M_{\mathcal{J}}$. We will not give the angular-momentum-coupled expressions for the fundamental commutators here, but refer to the Appendix of Ref. [241] for the analog of the fundamental commutators in Eqs. (3.133)-(3.138) in a j -coupled form. The IMSRG(3) j -scheme flow equations can then be derived based on the coupled expressions and applying the antisymmetrizer to the angular-momentum-coupled terms.

3.5.1 Approximate IMSRG(3) truncation schemes

The full inclusion of triples corrections in the IMSRG presents a major challenge in terms of both computational costs and memory requirements, and scales like $\mathcal{O}(N^9)$ including all fundamental commutators of Eqs. (3.118)-(3.126). Therefore finding a way to approximate the IMSRG(3) truncation would pave the way to large model-space IMSRG calculations that approximately include the effects of three-body operators. Approximate triples have already been successfully used in other many-body methods, such as CC theory [28, 198, 242-245], and are standard approaches in quantum chemistry, e.g., the iterative CCSD-T(1) truncation scales like $\mathcal{O}(A^3 N^4)$ (with mass number A) opposed to the $\mathcal{O}(A^3 N^6)$ scaling of CCSDT. In

Commutator	Cost	Perturbative order
$[2, 2] \rightarrow 3$	$\mathcal{O}(N^7)$	g^4
$[2, 3] \rightarrow 2$	$\mathcal{O}(N^7)$	g^4
$[1, 3] \rightarrow 3$	$\mathcal{O}(N^7)$	g^4
$[3, 3] \rightarrow 0$	$\mathcal{O}(N^6)$	g^4
$[2, 3] \rightarrow 1$	$\mathcal{O}(N^6)$	g^5
$[1, 3] \rightarrow 2$	$\mathcal{O}(N^6)$	g^5
$[3, 3] \rightarrow 1$	$\mathcal{O}(N^7)$	g^6
$[2, 3] \rightarrow 3$	$\mathcal{O}(N^8)$	g^5
$[3, 3] \rightarrow 2$	$\mathcal{O}(N^8)$	g^5
$[3, 3] \rightarrow 3$	$\mathcal{O}(N^9)$	g^6

Table 3.1: Computational cost and perturbative order of the IMSRG(3) fundamental commutators of Eqs. (3.133)-(3.138). The perturbative order is based on a perturbative analysis of the individual contributions in Ref. [241], following Ref. [31].

the following, we present approximate IMSRG(3) truncation schemes by including in each scheme selected fundamental commutators (see Table 3.1) on top of the IMSRG(2). The different truncation schemes are then summarized in Fig. 3.3.

In Ref. [31], a perturbative analysis of the IMSRG is presented for the case where the NO2B approximation and an HF reference state are used. This analysis reveals the MBPT diagrammatic content of the many-body method, and we use it as a tool to understand the contributions of different commutators in the IMSRG(3) and estimate their perturbative order. In the following, we use the results derived in Ref. [241] and refer to this reference and Ref. [31] for a more in-depth discussion of the perturbative analysis and formal derivation. We list the computational cost $\mathcal{O}(N^{K+L+M})$ as well as the perturbative order of the ten additional fundamental commutators entering the IMSRG(3) in Table 3.1, where g is the auxiliary parameter of the perturbed Hamiltonian and we use the shorthand notation $[K, L] \rightarrow M$ for the commutators $[A^{(K)}, B^{(L)}] \rightarrow C^{(M)}$ of corresponding many-body rank.

A key result of the analysis in Ref. [31] is that the IMSRG(2) is complete up to third order in MBPT and additionally contains many fourth-order diagrams. At the NO2B level, the IMSRG(3) accounts for the induced three-body effects, which are what is missing for the complete inclusion of fourth-order diagrams in the IMSRG(2), making the IMSRG(3) fourth-order complete (at the NO2B level) [31].

The first major truncation beyond IMSRG(2) we use, includes the minimum commutators necessary to make the truncation fourth-order complete in MBPT. These are the $[2, 2] \rightarrow 3$, $[2, 3] \rightarrow 2$, $[1, 3] \rightarrow 3$, and $[3, 3] \rightarrow 0$ commutators. We refer to this truncation as the IMSRG(3)-MP4 approximation. The IMSRG(3)-MP4 is most similar to iterated coupled-cluster methods like CCSDT-1 [28, 242, 244], as both methods are fourth-order complete. However, CCSDT-1 scales like $\mathcal{O}(A^3N^4)$, while the IMSRG(3)-MP4 scales like $\mathcal{O}(N^7)$.

Beyond the IMSRG(3)-MP4 truncation, we consider two approaches to including further commutators. The first is inclusion based on computational cost, including first the cheapest of the remaining commutators before including the more expensive commutators [246]. The rationale here is that by using this approach one can include as much “physics” as possible

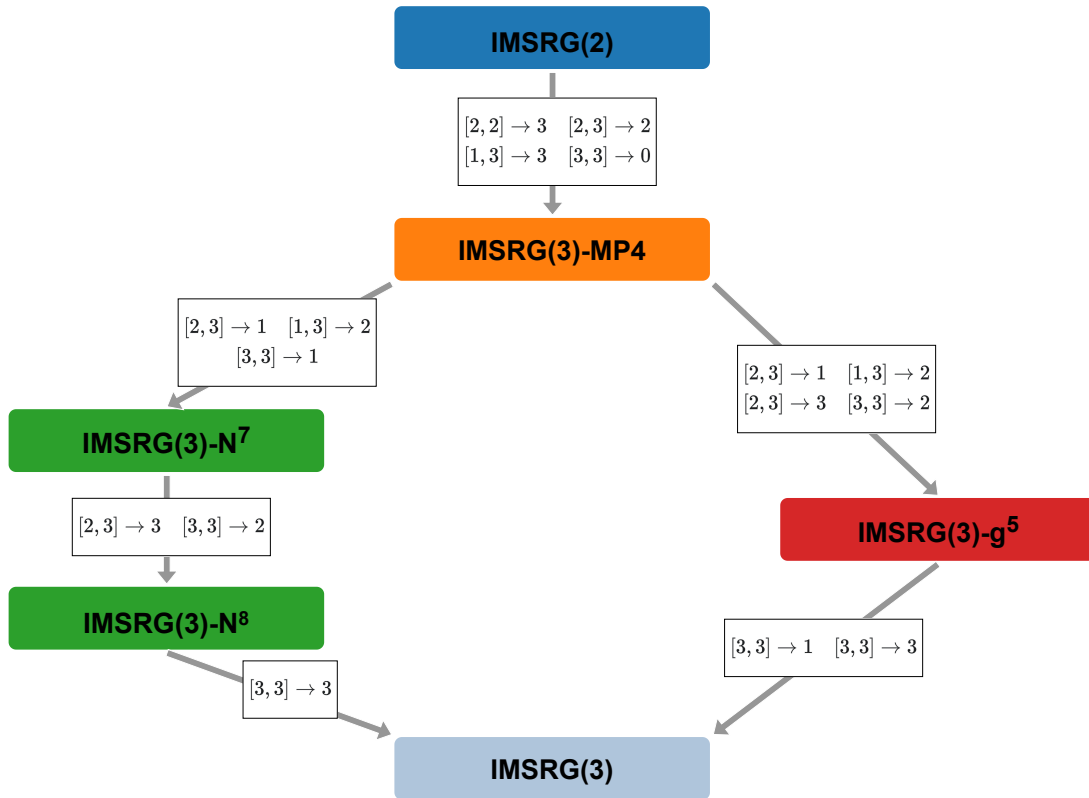


Figure 3.3: Approximate IMSRG(3) truncations schemes. We show the IMSRG(3)-MP4, the computational-cost-based IMSRG(3)- N^7 and IMSRG(3)- N^8 (left), and the perturbative-order-based IMSRG(3)- g^5 (right) truncations in orange, green, and red, respectively. The additional fundamental commutators included on top of the previous truncation are given at the corresponding arrows.

while increasing the computational cost incrementally, hopefully leading to a fairly faithful reproduction of the full IMSRG(3) results. The second approach is based on the perturbative analysis, where remaining commutators are included in the order of their perturbative importance. This physically motivated approach attempts to capture as best as possible the available physics in a consistent manner before including “higher-order” effects. One would hope to see that these higher-order effects generate only small changes in energies and in practical calculations some “complete” lower-order approximation could be used.

Following the first approach (the left path in Fig. 3.3), including the $[2, 3] \rightarrow 1$, $[1, 3] \rightarrow 2$, and $[3, 3] \rightarrow 1$ commutators on top of the IMSRG(3)-MP4 approximation yields a truncation that includes all IMSRG(3) commutators that cost $\mathcal{O}(N^7)$ or less. We refer to this truncation as the IMSRG(3)- N^7 truncation. The inclusion of the $[2, 3] \rightarrow 3$ and $[3, 3] \rightarrow 2$ commutators on top of this truncation yields the IMSRG(3)- N^8 truncation, which includes all commutators that cost $\mathcal{O}(N^8)$ or less. This truncation differs from the full IMSRG(3) only by the missing $[3, 3] \rightarrow 3$ commutator.

Following the second approach (the right path in Fig. 3.3), we note that the IMSRG(3)-MP4 truncation already follows this approach, including all of the IMSRG(3) commutators that are $\mathcal{O}(g^4)$ or less, with the exception of the $[1, 2] \rightarrow 2$ commutator, which is $\mathcal{O}(g^5)$ and is included in the IMSRG(2) truncation. The next truncation we present includes the remaining $\mathcal{O}(g^5)$ commutators, the $[2, 3] \rightarrow 1$, $[1, 3] \rightarrow 2$, $[2, 3] \rightarrow 3$, and $[3, 3] \rightarrow 2$ commutators, on top

of the IMSRG(3)-MP4 truncation. We refer to this truncation as the IMSRG(3)- g^5 truncation. This truncation includes two commutators that cost $\mathcal{O}(N^8)$, which subsequently defines the cost of the truncation. The two remaining commutators are $\mathcal{O}(g^6)$, so this is the only complete perturbatively guided truncation between the IMSRG(3)-MP4 and full IMSRG(3) truncation. All four approximate truncation schemes discussed above are systematically studied in Sec. 4.5 and compared to full IMSRG(3) calculations for ${}^4\text{He}$ and ${}^{16}\text{O}$ in small ($e_{\text{max}} = 2$) model spaces.

3.6 Applications of low-rank potentials in the IMSRG

In this section, we apply low-rank approximations of chiral NN interactions, using the SVD approach introduced in Sec. 2.4, to the IMSRG and study their performance and predictions for ground-state energies of finite nuclei. The results presented here have been published in Ref. [171], where I contributed with performing the many-body calculations to test the SVD rank-reduced interactions in medium-mass nuclei. We carry out the truncated SVD for the potential in the partial-wave momentum-space basis and subsequently transform the interaction to a single-particle HO basis as suitable input to the IMSRG. We emphasize that in this exploratory application, we do not fully take advantage of the low-rank structure of the potential in the many-body calculation, but rather reconstruct the full matrix from the approximate interaction by filling the truncated blocks with zeros. By this approach we can straightforwardly use the standard transformation codes to the single-particle basis and the standard IMSRG solver of Ref. [247]. Completely exploiting the power of the SVD and using the low-rank properties of the interaction would require reformulating the many-body method itself based on the factors in the decomposition. This is beyond the scope of this thesis, however work along these lines is in progress [248].

In Fig. 3.4, we compare the HF and IMSRG(2) ground-state energy per particle at various SVD ranks $R_{\text{SVD}} = 1\text{--}5$ to exact results using untruncated NN interactions for selected closed-shell oxygen, calcium, and nickel isotopes employing the N^3LO 450 and 500 NN interactions. The IMSRG(2) calculations are performed using an HF reference state and we employ a model space of $e_{\text{max}} = 14$ with $\hbar\omega = 28$ MeV. From the top panel we see that the ground-state energy per particle converges rapidly as a function of SVD rank and the full result is quantitatively reproduced already when keeping only five singular values in the decomposition in each partial-wave channel. In most cases, lower values of R_{SVD} yield less binding both at the HF and IMSRG(2) level. Although in all cases the full potential provides a bound HF solution, for ${}^{24}\text{O}$ and ${}^{78}\text{Ni}$ the HF determinant is unbound for the EMN 500 interaction at $R_{\text{SVD}} = 1$. This pathology is cured when increasing the decomposition rank to $R_{\text{SVD}} = 2$. We did not find a similar behavior when using the EMN 450 interaction. Moreover, the quality of the low-rank approximation is stable as a function of mass number, i.e., the energy per particle is equally well reproduced at low ranks for the closed-shell oxygen and nickel isotopes.

A more careful analysis of the relative error in the lower panel of Fig. 3.4 reveals that already at $R_{\text{SVD}} = 3$ the decomposition error for the IMSRG energy is only about three percent for all studied nuclei. Further increasing the rank to $R_{\text{SVD}} = 5$ yields excellent reproduction of the exact results indicated by the black dashed line. We stress that the convergence in general is not variational and that the relative error in the lower panel can be smaller or larger than zero for different ranks. For the heaviest nucleus investigated so far the error on the IMSRG(2) binding energy for $R_{\text{SVD}} = 5$ is 2.5 MeV. For the systems studied here

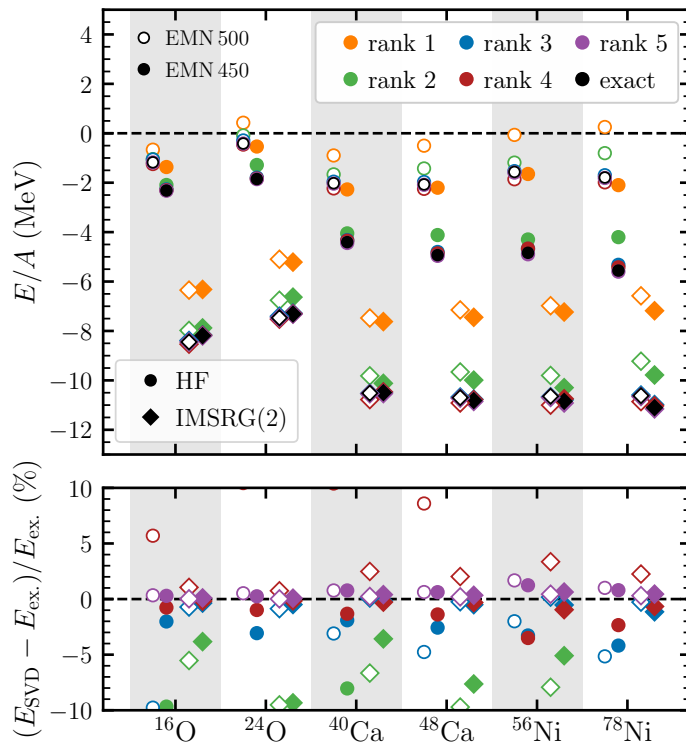


Figure 3.4: Ground-state energy per particle (upper panel) of selected closed-shell oxygen, calcium, and nickel isotopes at the HF level (circles) and using the IMSRG(2) approximation (diamonds) based on the N^3LO 500 (open symbols) and N^3LO 450 (solid symbols) NN interactions for SVD ranks $R_{\text{SVD}} = 1\text{--}5$ compared to exact results (black symbols). We additionally show the corresponding relative errors for the HF and IMSRG(2) energies of the low-rank potentials compared to their exact counterparts in the lower panel. All calculations use a model space of $e_{\text{max}} = 14$ and an oscillator frequency of $\hbar\omega = 28$ MeV. Figure taken from Ref. [171].

the relative error of IMSRG(2) ground-state energies seems to be smaller compared to the HF results at the same R_{SVD} . However, the absolute error in both cases is comparable and the decrease in relative error reflects the larger magnitude of the IMSRG(2) binding energy due to the additional correlations accounted for by the IMSRG solution.

While the decomposition was performed in momentum space, the various basis transformations may potentially spoil the low-rank properties of the tensor factorization. In particular, the basis transformations involving couplings of cm and intrinsic degrees of freedom may require the SVD to be reformulated. However, since the SVD is performed in individual partial-wave channels, fundamental symmetries of the nuclear interaction, e.g., rotational invariance and parity conservation, are automatically preserved. This is particularly important, since the conservation of spatial symmetries in a tensor-factorization environment is highly nontrivial and more complex tensor formats will generally break symmetries of the many-body operators.

4

Natural Orbital Basis

Most many-body frameworks that perform a correlation expansion around a reference state require the introduction of a computational (single-particle) basis for the representation of the many-body operators, which are commonly written in a second-quantized form. In the limit of a one-body Hilbert space of infinite dimension, different choices of the computational basis yield identical results. However, due to computational limitations, in practice one is always restricted to using a finite basis size and, consequently, calculated observables will depend on the underlying computational basis.

It has been recently realized in nuclear physics that the optimization of the single-particle basis provides a powerful tool to stabilize many-body calculations and enables a more reliable extraction of physical observables from large-scale calculations [249, 250]. Choosing the single-particle basis in nuclear many-body theory primarily requires addressing the following questions:

- What is the best choice for obtaining rapid convergence with respect to the model-space size?
- What is the best strategy to minimize the dependence of physical observables on basis set parameters?
- To what extent is the factorization of center-of-mass and intrinsic motion contaminated?

In practice, optimizing with respect to all of the above points simultaneously is not possible. Historically, most many-body calculations either employ HO or HF single-particle states. Harmonic oscillator basis states rigorously ensure factorization of center-of-mass and intrinsic degrees of freedom of the many-body wave function when combined with a N_{\max} truncation, as in NCSM approaches [20, 23]. However, in practice, a strong dependence on the basis set parameters such as the oscillator frequency of the confining potential is observed, especially for heavier nuclei or for observables that are more sensitive to the long-range part of the nuclear wave function. This makes the extraction of such observables challenging. Using HF orbitals based on a prior mean-field solution typically lowers the frequency dependence, while numerically still leading to a factorization of the center-of-mass and intrinsic wave function in large enough model spaces [251]. However, selected nuclear observables may still show sensitivity to the oscillator frequency in the HF basis as observed, e.g., for charge radii of medium-mass nuclei in IMSRG calculations [52].

Recently, applications of natural orbitals (NAT), defined as the eigenvectors of the one-body density matrix, revealed faster model-space convergence and significantly reduced sensitivity to basis parameters in large-scale NCSM calculations [250]. Furthermore, they have

been shown to drastically reduce the required amount of 3p3h amplitudes in CC applications [74], allowing for novel calculations with leading triples corrections, e.g., for deformed nuclei [74] and nuclear matrix elements of the neutrinoless double- β decay [238].

In this chapter, we present the natural orbital single-particle basis as an efficient basis choice for many-body applications based on our publication in Ref. [252], leading to significant improvements such as faster model-space convergence and lower sensitivity to basis set parameters. Specifically, we systematically compare HF and NAT orbitals and benchmark the advantages observed in NCSM calculations using the NAT basis for the IMSRG. Substantial computational savings in practice are obtained by the construction of natural orbitals in a large single-particle basis. This step enables for performing the many-body calculation in a reduced space of much lower dimension, thus offering help to extend the reach of *ab initio* methods towards heavier masses and higher orders in the many-body expansion.

Most of the results presented in this chapter are part of our already published work in Refs. [241, 252], and we closely follow the course of these publications in the following. In Sec. 4.1, we review the construction of the NAT single-particle basis based on a perturbatively improved density matrix. The HO, HF, and NAT single-particle bases are compared in detail in Sec. 4.2, and the HF and NAT bases are studied for applications to medium-mass systems using the IMSRG formalism in Sec. 4.3. Mixed basis sets using orbitals from an energy density functional (EDF) calculation are explored and compared to the HF and NAT basis in Sec. 4.4. Additionally, we show results for using the NAT basis in the IMSRG(3) for small model spaces in Sec. 4.5.

4.1 Single-particle basis and basis optimization

While HO basis sets have been used extensively for a long time in various many-body frameworks, they constitute an agnostic choice with respect to any specific properties of the target system, e.g., in terms of mass number or mean-field effects. This can be addressed by using HF orbitals instead. Hartree-Fock orbitals account for bulk properties of the nucleus stemming from a variational minimization of the ground-state energy. Observables like the energy or the radius are therefore well captured at the HF level as long as the nuclear interaction is soft enough, and the single-particle wave functions possess an improved radial dependence as opposed to the Gaussian falloff of HO eigenfunctions. Proton and neutron single-particle potentials in general differ in the HF approach, thus accounting for mean-field contributions induced by Coulomb and isospin-breaking effects. Still, the HF procedure by construction only provides an optimization of hole single-particle states while leaving the particle states untouched beyond fixing the normalization. However, wave-function expansion methods aim at capturing dynamic correlations linked to particle-hole excitations, which also involve single-particle orbitals that are not optimized by the HF approach. Therefore, incorporating such effects in the construction of the computational basis is key when trying to robustly determine observables to high precision. In this chapter, we discuss one possible way to incorporate such effects in the basis construction by calculating natural orbitals based on a perturbatively improved density matrix up to second order in MBPT, which additionally optimizes the particle orbitals in contrast to the HF approach.

Nucleon-nucleon as well as 3N interactions are conveniently stored in a partial-wave decomposed form in relative momentum space that allows for storage in a relatively cheap

way. However, most many-body methods require input two- and three-body interactions formulated in a single-particle basis to solve the nuclear many-body problem. We refer to Refs. [253–255] for a detailed derivation of the transformation of the NN and 3N potential matrix elements from a relative momentum-space basis to a single-particle basis, where especially the transformation of the 3N interaction to the single-particle HO basis can be computationally challenging.

4.1.1 Natural orbital basis

Natural orbitals are defined as the eigenbasis of the one-body density matrix with its matrix elements given by

$$\gamma_{pq} \equiv \frac{\langle \Psi | : a_p^\dagger a_q : | \Psi \rangle}{\langle \Psi | \Psi \rangle}, \quad (4.1)$$

where $|\Psi\rangle$ denotes the exact ground state and the denominator ensures the normalization, i.e., $\text{tr}(\gamma) = A$. The calculation of the exact one-body density matrix requires the full solution of the Schrödinger equation, which is out of reach beyond the lightest systems. However, early attempts in quantum chemistry revealed that approximate natural orbitals can be very useful [256, 257]. Such basis sets are obtained by using an approximate many-body state $|\Psi^{\text{approx}}\rangle$ to obtain an approximate one-body density matrix,

$$\gamma_{pq}^{\text{approx}} \equiv \frac{\langle \Psi^{\text{approx}} | : a_p^\dagger a_q : | \Psi^{\text{approx}} \rangle}{\langle \Psi^{\text{approx}} | \Psi^{\text{approx}} \rangle}. \quad (4.2)$$

In regions of the nuclear chart where the exact wave function is computationally inaccessible, this provides an alternative option for defining a basis for the many-body calculation. In practice, a reasonable trade-off between the accuracy of the many-body truncation for the construction of the approximate wave function and the associated computational cost needs to be found.

In the case where the approximate wave function is an HF Slater determinant $|\text{HF}\rangle$ the density matrix

$$\gamma_{pq}^{\text{HF}} \equiv \langle \text{HF} | : a_p^\dagger a_q : | \text{HF} \rangle, \quad (4.3)$$

already derived in Eq. (3.30a) in Sec. 3.2, has the particularly simple form

$$\gamma^{\text{HF}} = \begin{pmatrix} \mathbb{1}_{\text{hh}} & 0 \\ 0 & 0 \end{pmatrix}, \quad (4.4)$$

where $\mathbb{1}_{\text{hh}}$ denotes the identity matrix in the subblock of hole states and we assumed that the HF state is normalized to unity by $\langle \text{HF} | \text{HF} \rangle = 1$. Furthermore, the density matrix corresponds to a normalized many-body state, meaning that its trace yields the particle number of the state, i.e., $\text{tr}(\gamma^{\text{HF}}) = A$.

For an HF reference state, the canonical orbitals, defined as the eigenbasis of the one-body (HF) Hamiltonian, and the natural orbitals based on the HF density matrix in Eq. (4.4) coincide. Therefore, one must include correlations beyond mean field in the construction of the density matrix to gain a benefit from the natural orbitals.

4.1.2 Perturbatively improved density matrix

As discussed at the beginning of this section, accounting for particle-hole couplings in the density matrix is essential for providing a more refined computational basis. The simplest approach to including such effects is by employing a perturbatively corrected one-body density matrix. Following the description in Ref. [258], the one-body density matrix up to second order in the interaction (λ^2), based on expanding the eigenstate of the approximate wave function up to second order in MBPT (MP2), can be written as

$$\gamma^{\text{MP2}} \equiv \gamma^{\text{HF}} + \gamma^{(02)} + \gamma^{(20)} + \gamma^{(11)} + \mathcal{O}(\lambda^3), \quad (4.5)$$

where

$$\gamma_{pq}^{(mn)} \equiv \langle \Phi^{(m)} | : a_p^\dagger a_q : | \Phi^{(n)} \rangle \quad (4.6)$$

is the MBPT contribution for the density matrix arising from the bra and ket wave function corrections of the reference state $|\Phi\rangle$ at orders m and n , respectively. Terms of order λ^3 or higher in the interaction are discarded. Moreover, terms of the form $\gamma^{(01)/(10)}$ are absent when using a canonical HF reference state due to Brillouin's theorem [188] (see Sec. 3.2). Explicit expressions for the various contributions in terms of single-particle orbitals are given by

$$D_{i'a'}^{(\text{hp})_1} = \frac{1}{2} \sum_{abi} \frac{\Gamma_{i'iab} \Gamma_{aba'i}}{\epsilon_{i'}^{a'} \epsilon_{i'}^{ab}}, \quad (4.7a)$$

$$D_{i'a'}^{(\text{hp})_2} = -\frac{1}{2} \sum_{aij} \frac{\Gamma_{i'aij} \Gamma_{ija'a}}{\epsilon_{i'}^{a'} \epsilon_{ij}^{a'a}}, \quad (4.7b)$$

$$D_{i'j'}^{(\text{hh})} = -\frac{1}{2} \sum_{abi} \frac{\Gamma_{i'iab} \Gamma_{abj'i}}{\epsilon_{i'}^{ab} \epsilon_{j'i}^{ab}}, \quad (4.7c)$$

$$D_{a'b'}^{(\text{pp})} = \frac{1}{2} \sum_{aij} \frac{\Gamma_{a'aij} \Gamma_{ijb'a}}{\epsilon_{ij}^{a'a} \epsilon_{ij}^{b'a}}, \quad (4.7d)$$

where the labels i, j, k, \dots (a, b, c, \dots) correspond to single-particle states occupied (unoccupied) in the reference determinant, i.e., the HF state in our case. The matrix elements Γ_{pqrs} of the normal-ordered Hamiltonian are given in the HF basis, thus corresponding to an HF partitioning in the MBPT expansion of the density matrix [18]. Furthermore, the shorthand notation

$$\epsilon_{ij}^{ab} = \epsilon_i + \epsilon_j - \epsilon_a - \epsilon_b \quad (4.8)$$

as for MBPT in Eq. (3.70) is used, with $\epsilon_p \equiv f_{pp}$ denoting the HF SPE of orbital p . Consequently, the MP2 density matrix is given by

$$\gamma^{\text{MP2}} = \begin{pmatrix} \gamma^{\text{hh}} & \gamma^{\text{hp}} \\ \gamma^{\text{ph}} & \gamma^{\text{pp}} \end{pmatrix}, \quad (4.9)$$

where the hole-particle and particle-hole blocks are nonzero and given by

$$\gamma^{\text{hp}} = D^{(\text{hp})_1} + D^{(\text{hp})_2} = \left(\gamma^{\text{ph}} \right)^\top, \quad (4.10)$$

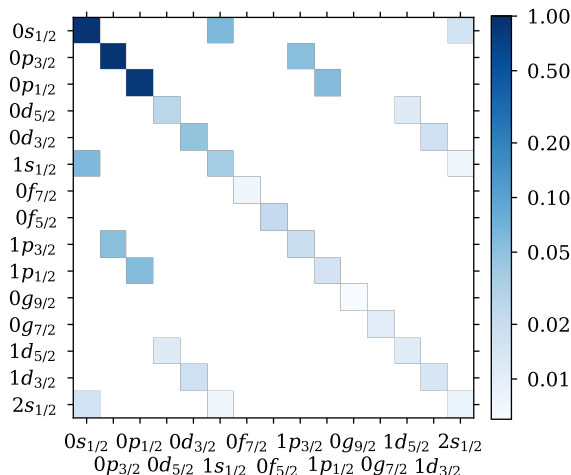


Figure 4.1: Correlated one-body proton density matrix γ^{MP2} in the HF basis for ^{16}O in an $e_{\text{max}} = 4$ model space using the N^3LO 450 interaction based on the N^3LO NN potential from Ref. [56] with N^3LO 3N forces constructed in Ref. [57]. The first three proton orbitals ($0s_{1/2}$, $0p_{3/2}$, and $0p_{1/2}$) are occupied in the ^{16}O reference state, while the remaining ones are unoccupied. The perturbative corrections beyond HF can be seen in the diagonal particle-particle contributions and the off-diagonal particle-hole and hole-particle contributions. Note that for this $N = Z$ nucleus the neutron one-body density matrix is very similar.

and the hole-hole and particle-particle blocks given by

$$\gamma^{\text{hh}} = \gamma^{\text{HF}} + D^{(\text{hh})}, \quad (4.11\text{a})$$

$$\gamma^{\text{pp}} = D^{(\text{pp})}, \quad (4.11\text{b})$$

respectively. Note that in contrast to the HF density matrix, the MP2 density matrix contains particle-particle and particle-hole couplings as shown for ^{16}O in Fig. 4.1. Since

$$\sum_i D_{ii}^{(\text{hh})} + \sum_a D_{aa}^{(\text{pp})} = 0, \quad (4.12)$$

the second-order density matrix still fulfills the trace normalization condition $\text{tr}(\gamma^{\text{MP2}}) = A$ as in the HF case.

In practice, the construction of the MP2 density matrix is realized using a spherically constrained scheme, i.e., enforcing angular-momentum conservation throughout the initial HF solution and the following MBPT calculation. Specifically, the single-particle orbitals, which are $(2j + 1)$ -fold degenerate, are characterized by the quantum numbers n , l , j , and m_t [cf. Eqs. (3.28)]. As before, n is the radial quantum number, l the orbital angular momentum, j the total angular momentum, and m_t the isospin projection. In actual calculations, we truncate the single-particle states at $e \leq e_{\text{max}}$, with quantum numbers $e = 2n + l$ and $e_{\text{max}} = (2n + l)_{\text{max}}$.

Consequently, the resulting MP2 density matrix is block diagonal in the quantum numbers ljt as only states with different radial quantum number n couple. The diagonalization of the MP2 density matrix is performed in ljt subblocks to ensure symmetry conservation. The resulting eigenvectors and eigenvalues correspond to the transformation coefficients from the HF to the NAT basis and the occupation numbers of the natural orbitals, respectively.

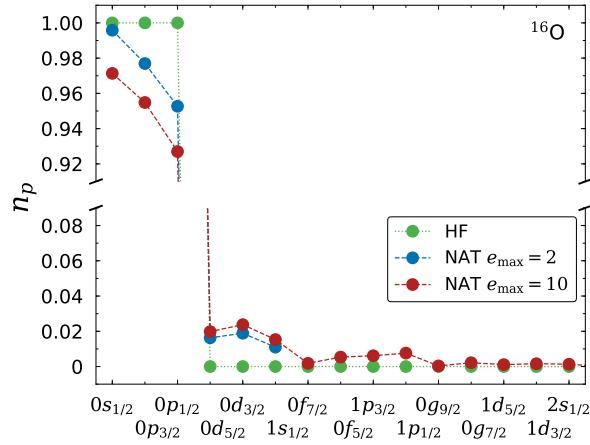


Figure 4.2: Occupation numbers n_p of the single-particle proton orbitals for the HF and NAT basis in ^{16}O , using the 1.8/2.0 EM interaction [54] and an oscillator frequency $\hbar\omega = 16$ MeV. We show results for two model-space truncations $e_{\max} = 2$ and $e_{\max} = 10$ in the NAT basis construction. As for Fig. 4.1, the occupations of the neutron orbitals are nearly identical.

4.1.3 Basis transformation

The natural orbital states are obtained as linear combinations of the HF states, mixing radial excitations only:

$$|n\alpha_p\rangle_{\text{NAT}} = \sum_{n'}^{\text{NAT}} C_{nn'}^{\alpha_p} |n'\alpha_p\rangle_{\text{HF}}, \quad (4.13)$$

where α_p is a collective index for the quantum numbers l_p , j_p , and m_{t_p} and ${}^{\text{NAT}}C_{nn'}^{\alpha_p}$ denotes the expansion coefficients in the HF basis obtained by the diagonalization, i.e.,

$${}_{\text{HF}}\langle n'\alpha_p | n\alpha_p \rangle_{\text{NAT}} = {}^{\text{NAT}}C_{nn'}^{\alpha_p}, \quad (4.14)$$

where the projection m_p of the total angular momentum is suppressed since the transformation coefficients and single-particle states do not depend on it as long as rotational symmetry is enforced. By expanding the HF states in the HO basis, we can also express the natural orbital states in the HO basis:

$$\begin{aligned} |n\alpha_p\rangle_{\text{NAT}} &= \sum_{n'n''} {}^{\text{NAT}}C_{nn'}^{\alpha_p} {}_{\text{HF}}C_{n'n''}^{\alpha_p} |n''\alpha_p\rangle_{\text{HO}} \\ &= \sum_{n''} {}^{\text{NAT}/\text{HF}}C_{nn''}^{\alpha_p} |n''\alpha_p\rangle_{\text{HO}}, \end{aligned} \quad (4.15)$$

where the coefficients ${}^{\text{NAT}/\text{HF}}C_{nn''}^{\alpha_p}$ now combine the transformation from the HO to the HF and from the HF to the NAT basis.

Note that the set of occupation numbers for the natural orbitals $n_p \in [0, 1]$ obtained from the eigenvalues now leads to a fractional filling of all orbitals, in contrast to the occupation numbers $n_p \in \{0, 1\}$ obtained from the HF solution discussed in Sec. 3.2. This feature is illustrated in Fig. 4.2 comparing the NAT and HF occupation numbers for an ^{16}O reference state.

Since the reference state for the MP2 density matrix is not a single Slater determinant due to mixing of particle-hole excitations, the occupation numbers must differ from the mean-field

picture. As discussed in the following, this also affects the normal-ordering procedure with respect to natural-orbital basis states.

While the employed MP2 density matrix provides a simple approximation to the exact one-body density matrix, nonperturbative many-body schemes can be used to refine the approximation, e.g., a Λ approach in CC theory [199], dressed propagators from Green's function theory [259], or a fully correlated configuration interaction (CI) calculation [260]. A balance between accuracy and computational complexity needs to be found, and a low-order MBPT approach provides a reasonable approximation to the one-body density matrix at low computational cost.

4.1.4 Intrinsic kinetic energy

The intrinsic Hamiltonian, here as before considered up to three-body contributions, can be split into a kinetic part and an interaction part,

$$H = T - T_{\text{cm}} + V^{(2)} + V^{(3)} = T_{\text{int}} + V^{(2)} + V^{(3)}, \quad (4.16)$$

with the intrinsic kinetic energy T_{int} , obtained by subtracting the cm kinetic energy T_{cm} from the full kinetic energy T . The intrinsic kinetic energy can be represented either as a sum of one- and two-body operators, as shown in Eq. (3.17),

$$T_{\text{int}}^{(1+2)} = \left(1 - \frac{1}{A}\right) \sum_p \frac{\mathbf{p}_p^2}{2M} - \frac{1}{A} \sum_{p<q} \frac{\mathbf{p}_p \cdot \mathbf{p}_q}{M}, \quad (4.17)$$

or as a pure two-body operator,

$$T_{\text{int}}^{(2)} = \frac{1}{A} \sum_{p<q} \frac{(\mathbf{p}_p - \mathbf{p}_q)^2}{2M}. \quad (4.18)$$

Of course, both cases are equal and can be transformed into each other by

$$\begin{aligned} \sum_{p<q} \frac{(\mathbf{p}_p - \mathbf{p}_q)^2}{2M} &= \sum_{p<q} \frac{(\mathbf{p}_p^2 + \mathbf{p}_q^2 - 2\mathbf{p}_p \cdot \mathbf{p}_q)}{2M} \\ &= (A-1) \sum_p \frac{\mathbf{p}_p^2}{2M} - \sum_{p<q} \frac{\mathbf{p}_p \cdot \mathbf{p}_q}{M}. \end{aligned} \quad (4.19)$$

The one- and two-body matrix elements of the Hamiltonian obviously differ depending on the choice of T_{int} . Nevertheless, both cases result in the same HF determinant with identical total HF energy, as studied in detail in Refs. [261, 262]. The HF single-particle energies are different for both choices and can be related by a unitary transformation of the occupied single-particle states [261]. These findings are based on the assumption of a reference state with well-defined particle number A . For a discussion of particle-number breaking theories, e.g., the Hartree-Fock-Bogoliubov approach, see Ref. [263].

The partitioning of the kinetic energy operator also affects the construction of the natural orbital basis. By employing $T_{\text{int}}^{(2)}$, the initial Hamiltonian (before normal ordering) no longer has a one-body part, and the two-body matrix elements in the construction of γ^{MP2} [see Eqs. (4.7a)–(4.7d)] differ from the ones obtained by using the one- plus two-body form of the kinetic energy, resulting in altered transformation coefficients and NAT occupation numbers.

The partitioning also changes the single-particle energies, further changing the resulting γ^{MP2} density matrix.

In general, we apply the intrinsic kinetic energy operator of Eq. (4.17) with a one- and two-body part for the IMSRG calculations performed in this thesis. However, in the following we additionally study the impact of using a pure two-body kinetic energy operator $T_{\text{int}}^{(2)}$.

4.1.5 Normal ordering in the NAT basis

When employing a multi-reference state that is no longer a single Slater determinant, the notion of normal ordering introduced in Sec. 3.1 needs to be extended to cope with the multi-configurational character of the vacuum. Such an extension can be naturally addressed in terms of the generalized Mukherjee-Kutzelnigg normal ordering [185]. Even though this scheme is not used for practical applications in this thesis, it is still worth anticipating the additional complications that arise from normal ordering with respect to a multi-reference state.

For an arbitrary many-body operator O containing up to two-body contributions:

$$O = O^{(0)} + O^{(1)} + O^{(2)}, \quad (4.20)$$

performing the normal ordering with respect to a non-product-type vacuum yields [190]

$$\tilde{o}^{(0\text{B})} = o^{(0\text{B})} + \sum_{pq} o_{pq}^{(1\text{B})} \gamma_{pq} + \frac{1}{4} \sum_{pqrs} o_{pqrs}^{(2\text{B})} \gamma_{pqrs}, \quad (4.21\text{a})$$

$$\tilde{o}_{pq}^{(1\text{B})} = o_{pq}^{(1\text{B})} + \sum_{rs} o_{prqs}^{(2\text{B})} \gamma_{rs}, \quad (4.21\text{b})$$

$$\tilde{o}_{pqrs}^{(2\text{B})} = o_{pqrs}^{(2\text{B})}, \quad (4.21\text{c})$$

involving one- and two-body density matrices γ_{pq} and γ_{pqrs} , respectively, and we use the tilde to distinguish the reference-state normal-ordered matrix elements from the initial ones. The two-body density matrix, which contributes to the zero-body part of the normal-ordered operator, is given by

$$\gamma_{pqrs} = \frac{\langle \Psi | : a_p^\dagger a_q^\dagger a_s a_r : | \Psi \rangle}{\langle \Psi | \Psi \rangle} \quad (4.22)$$

and can be decomposed into a factorized part of products of one-body density matrices and an irreducible two-body part λ_{pqrs} ,

$$\gamma_{pqrs} = \left(\gamma_{qs} \gamma_{pr} - \gamma_{qr} \gamma_{ps} \right) + \lambda_{pqrs}. \quad (4.23)$$

The appearance of λ_{pqrs} is a consequence of the reference state being no longer of mean-field character [see Eq. (3.30b) for the two-body density matrix of an HF reference state]. In practice, such states are obtained, e.g., from particle-number-broken and -restored Hartree-Fock-Bogoliubov vacua [68] or small-scale CI diagonalizations [264]. In the following, the irreducible two-body part is discarded for simplicity and a mean-field-like approximation is employed:

$$\gamma_{pqrs} \approx \gamma_{qs} \gamma_{pr} - \gamma_{qr} \gamma_{ps}. \quad (4.24)$$

Equation (4.24) is exact as long as a many-body state of product type is used. While in principle it is straightforward to derive two-body density matrices in MBPT, the factorized approximation is expected to provide a reasonably good choice for the basis optimization.

Considerable simplifications are obtained by working in the natural orbital basis, i.e.,

$$\gamma_{pq} = n_p \delta_{pq}, \quad n_p \in [0, 1], \quad (4.25)$$

where the lack of a well-defined particle-hole picture means that the occupation numbers are no longer strictly zero or one. Expressions for the normal-ordered matrix elements in Eq. (4.21) in the natural orbital basis are

$$\tilde{o}^{(0B)} = o^{(0B)} + \sum_p o_{pp}^{(1B)} n_p + \frac{1}{2} \sum_{pq} o_{ppqq}^{(2B)} n_p n_q, \quad (4.26a)$$

$$\tilde{o}_{pq}^{(1B)} = o_{pq}^{(1B)} + \sum_r o_{pqr}^{(2B)} n_r, \quad (4.26b)$$

$$\tilde{o}_{pqrs}^{(2B)} = o_{pqrs}^{(2B)}, \quad (4.26c)$$

now involving single-particle summations running over the full one-body Hilbert space for the summation indices p , q , and r instead of hole orbitals only, a consequence of the smeared-out Fermi distributions in the occupation numbers n_p , as shown in Fig. 4.2.

4.1.6 Single-reference case

In the simplest case, a single Slater-determinant reference state, see Eq. (3.4), is employed in the many-body expansion, and we use the definition of hole and particle states with $n_p = 1$ and $n_p = 0$, respectively of Eq. (3.14). Performing the single-reference normal ordering with respect to this reference state, the corresponding normal-ordered matrix elements of the operator are obtained as (see, e.g., Ref. [184])

$$\tilde{o}^{(0B)} = o^{(0B)} + \sum_i o_{ii}^{(1B)} + \frac{1}{2} \sum_{ij} o_{ijij}^{(2B)} + \frac{1}{6} \sum_{ijk} o_{ijkijk}^{(3B)}, \quad (4.27a)$$

$$\tilde{o}_{pq}^{(1B)} = o_{pq}^{(1B)} + \sum_i o_{pqi}^{(2B)} + \frac{1}{2} \sum_{ij} o_{pijqij}^{(3B)}, \quad (4.27b)$$

$$\tilde{o}_{pqrs}^{(2B)} = o_{pqrs}^{(2B)} + \sum_i o_{pqirsi}^{(3B)}, \quad (4.27c)$$

$$\tilde{o}_{pqrstu}^{(3B)} = o_{pqrstu}^{(3B)}, \quad (4.27d)$$

where the labels i and j indicate hole states occupied in the reference state $|\Phi\rangle$. In Eq. (4.27), three-body contributions are explicitly included. In practice, the NO2B approximation is employed [213, 214], where the residual three-body part in Eq. (4.27d) is discarded to lower the computational complexity.

Because the MP2 density matrix does not correspond to a single Slater determinant, an auxiliary many-body state $|\text{NAT}\rangle$ is constructed by filling the first A states with the highest occupation numbers. Similar to Eq. (3.4), these orbitals are filled with updated occupations $n_p \in \{0, 1\}$ to conserve the particle-number expectation value, thus establishing a well-defined particle-hole picture. Consequently, in the following applications standard Slater-determinant-based codes can be used for the many-body expansion. Note that, even though this reference

state has product-type character, the information about the correlated density matrix is encoded in the transformation matrix from the HO to the NAT basis [see Eq. (4.15)] for the one- and two-body parts of the intrinsic Hamiltonian. By using such an auxiliary vacuum, the reference-state expectation value is larger than the HF expectation value since there is no underlying variational principle, i.e.,

$$\langle \text{NAT} | H | \text{NAT} \rangle > \langle \text{HF} | H | \text{HF} \rangle. \quad (4.28)$$

4.2 Diagnostics for the density matrix

In this section, natural orbitals, given by the eigenstates of the one-body density matrix, are studied in detail and compared to the commonly used HF single-particle basis. We demonstrate, how using natural orbitals constructed from a perturbatively improved density matrix lead to significantly reduced frequency dependence of the single-particle wave functions. These results allow us to gain a better understanding of the relationship between the various computational bases and their sensitivity to the nuclear Hamiltonian used in their construction. We focus on the two chiral interactions discussed in Sec. 2.2.2, the N³LO interaction with the NN potential from Ref. [56] and N³LO 3N forces constructed in Ref. [57] using the cutoff values $\Lambda = 400\text{--}500$ MeV and the 1.8/2.0 EM interaction of Ref. [54].

4.2.1 “Softness” of the interaction

“Soft” interactions are low-resolution interactions that show weak coupling between low- and high-energy states. The softness of an interaction, i.e., the degree of decoupling between low and high momenta in the Hamiltonian, can be varied by changing the regulator scale for Hamiltonians constructed from an EFT as well as by applying SRG methods to decouple or integrate out high-momentum degrees of freedom [184, 265] (see Sec. 2.3). Soft interactions applied in many-body methods have been shown to improve convergence with respect to basis truncation and order in the many-body expansion. In particular, the use of an SRG-evolved Hamiltonian is required to enable a perturbative solution even for closed-shell systems [18]. A Weinberg-eigenvalue analysis, which provides a metric of the perturbativeness of an interaction, shows that the softness is intimately linked to the SRG resolution scale [148, 178].

Because the one-body density matrix is constructed from an MBPT expansion, we expect the density matrix and the resulting NAT basis to be more sensitive to the basis frequency and truncation for hard interactions. For unevolved chiral potentials, the mean-field wave function may exhibit unphysical properties, giving rise to an unbound HF solution. With such a poor reference state, the many-body expansion is significantly more complicated, in particular if perturbative techniques are employed. The key idea of a many-body expansion is to start from a qualitatively correct reference state while residual dynamic correlation effects are brought in as (small) corrections. This rationale is obviously broken once the mean-field reference is unbound or not under control, manifesting in final results via, e.g., strong frequency dependence.

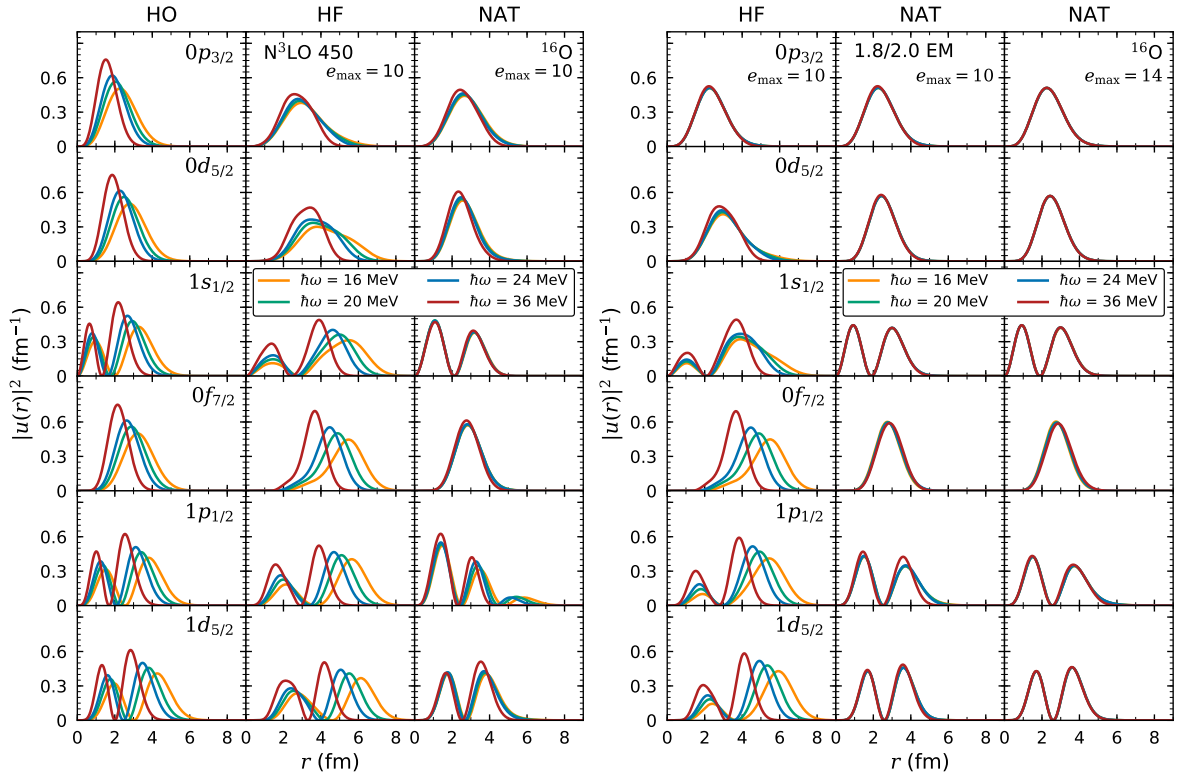


Figure 4.3: Squared absolute value of the radial wave function $u(r)$ of ^{16}O as a function of r for different proton orbitals in the HO, HF, and NAT bases. We show results for the occupied $0p_{3/2}$ orbital (first row) and some of the first unoccupied orbitals (second through sixth rows) for the $\text{N}^3\text{LO 450}$ interaction (left) and the 1.8/2.0 EM interaction (right) using oscillator frequencies $\hbar\omega = 16\text{--}36$ MeV for the HO, HF, and NAT basis. The HF and NAT orbitals include single-particle HO states up to $e_{\text{max}} = 10$ and $E_{3\text{max}} = 14$, as well as up to $e_{\text{max}} = 14$ for the NAT basis in last column of the right plot.

4.2.2 Single-particle wave functions

While the HF approach targets the optimization of the occupied single-particle states from a variational approach, the unoccupied orbitals are left unmodified up to normalization. Therefore, the HF basis is expected to properly describe occupied orbitals while failing for unoccupied ones. The natural orbital basis, however, accounts for particle-hole admixtures and particle-particle couplings and therefore may qualitatively improve the description of unoccupied states as will be tested in the subsequent calculations. In the following, a single-particle basis is employed including states up to a principal quantum number e_{max} . Additionally, we introduce a truncation $E_{3\text{max}}$ in three-body space keeping only configurations with $e_1 + e_2 + e_3 \leq E_{3\text{max}} < 3e_{\text{max}}$ due to the extensive size of three-body matrix elements.

In the left plot of Fig. 4.3, we show the squared absolute value of the radial wave functions for different oscillator frequencies using the HO, HF, and NAT bases and the $\text{N}^3\text{LO 450}$ interaction. Different rows correspond to different single-particle orbitals; only the first row ($0p_{3/2}$) corresponds to an occupied orbital in ^{16}O . Clearly, using a HO basis leads to strong frequency dependence in all cases, even for the occupied $0p_{3/2}$ state. Hence, HO wave functions are ruled out as a reliable computational basis and are not considered further in this thesis. While the $0p_{3/2}$ orbitals are more robust in the HF case as expected, unoccupied HF orbitals

show frequency dependence comparable to that of HO orbitals, a consequence of the fact that unoccupied orbitals are not optimized in the HF approach. Switching to natural orbitals nicely resolves many of the remaining artifacts, revealing only minor frequency dependence for both occupied and unoccupied states.

As the softer 1.8/2.0 EM interaction from Ref. [54] leads to much better reproduction of ground-state energies at the HF level [55], this also improves the quality of the MP2 density matrix. In the right plot of Fig. 4.3, we compare HF (left) and natural orbitals (middle) in a model space with $e_{\max} = 10$ for this interaction, while additionally benchmarking the effect of natural orbitals when going to a larger basis size of $e_{\max} = 14$ (right). While the frequency dependence for this softer interaction is much milder in the HF case, high-lying single-particle states still significantly depend on $\hbar\omega$. A residual frequency dependence is still seen in the $1p_{1/2}$ orbital at $e_{\max} = 10$ in the natural orbital basis, but fully vanishes when going to larger spaces of $e_{\max} = 14$.

In summary, properties of the HF solution strongly impact the qualitative behavior of the natural orbital single-particle wave functions and a bound mean-field solution is key for providing a reliable reference point for a many-body expansion.

4.2.3 Positive definiteness as diagnostic tool

The density matrix is a positive-definite operator and thus its eigenvalues, the occupation numbers, are nonnegative. Therefore, unphysical negative occupations or occupations larger than one should not show up during the diagonalization. Previous investigations in quantum chemistry showed that the appearance of negative occupation numbers can be linked to a breakdown of a single-reference description and hint at the onset of strong static correlations [266]. Therefore, we aim to utilize occupation numbers as a diagnostic tool and investigate their sensitivity to the softness of the nuclear interaction. As the HF ground-state energy is directly related to the softness of the interaction, a correlation between the HF energy and the size of negative occupations is expected.

Figure 4.4 depicts the magnitude of the negative occupations using the $N^3\text{LO}$ interactions for various cutoff values in ^{16}O , ^{22}O , and ^{12}C . In both oxygen nuclei, we observe a decrease in size for softer interactions, as indicated by going from the harder potentials with cutoff $\Lambda = 500$ MeV to $\Lambda = 400$ MeV, in both the NN-only and the NN+3N cases. Consequently, an unbound HF solution strongly affects the appearance of unphysical negative occupations. In general, using the two-body form of the kinetic energy operator $T_{\text{kin}}^{(2)}$ results in smaller negative occupations for both nuclei. We also verified that softening the interaction by a consistent SRG evolution of NN and 3N contributions [52, 166] significantly reduces the magnitude of the negative occupations, eventually letting them vanish completely. Increasing the model-space size seems to increase the magnitude of these occupations. Moreover, the effect is generally less pronounced for heavier nuclei, e.g., in ^{78}Ni (not shown).

In addition, we investigate the size of negative occupations in the case of ^{12}C . Due to the cluster structures and weak shell closure in ^{12}C , the quality of single-reference many-body approaches is expected to deteriorate in comparison to the doubly magic nucleus ^{16}O . An analysis of the single-particle spectrum revealed only a small shell gap in the single-particle spectrum, thus significantly enhancing the size of perturbative corrections to the MP2 density matrix in the particle-particle and hole-hole channel [see Eqs. (4.7c) and (4.7d)]. Consequently, highly erratic occupation numbers are observed in the bottom panel of Fig. 4.4. Empirically, we find that the use of $T_{\text{int}}^{(2)}$ with a slightly larger shell gap was superior to $T_{\text{int}}^{(1+2)}$,

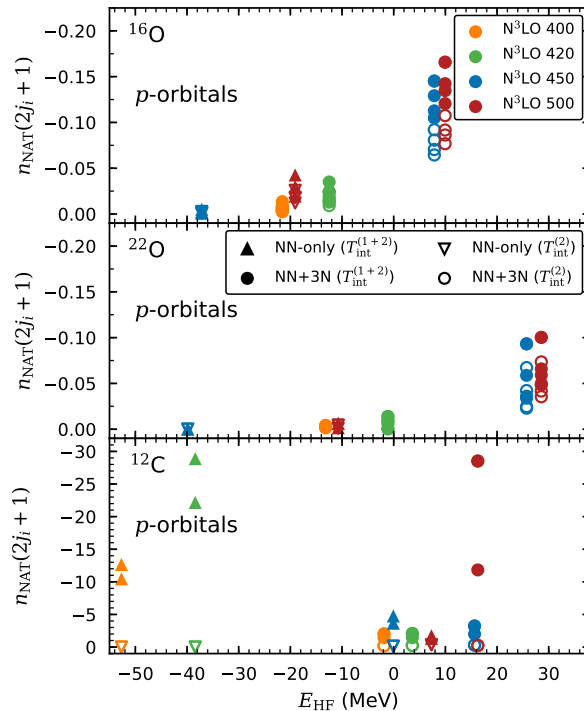


Figure 4.4: Negative occupations of the p orbitals scaled by $(2j_i + 1)$ in the NAT basis for ^{16}O (top), ^{22}O (middle), and ^{12}C (bottom) as a function of the HF energy. We show results for various cutoffs $\Lambda = 400\text{--}500$ MeV with the NN-only N^3LO EMN and NN+3N N^3LO interactions indicated by triangles and circles, respectively. We apply both choices for the kinetic energy operator, $T_{\text{int}}^{(1+2)}$ (solid symbols) and $T_{\text{int}}^{(2)}$ (open symbols), and use a model space of $e_{\text{max}}/E_{3\text{max}} = 14/14$ with $\hbar\omega = 20$ MeV. All negative occupations arise only for high radial quantum number. Note that there are no negative occupations for the softer NN-only EMN 400 and 420 interactions for the oxygen isotopes.

significantly reducing, though not fully resolving, the large negative occupations. The results of this analysis for the occupation numbers is also evidence for the challenges of the single reference-state starting point for a description of ^{12}C .

4.3 Natural orbital basis in the IMSRG

Before discussing IMSRG applications using natural orbitals, it is worth addressing the interplay of the correlations built into the MP2 density matrix and the correlations that are resummed within the IMSRG flow. Using a natural orbital reference determinant yields a higher ground-state energy at $s = 0$ compared to an HF vacuum due to the variational optimization of the HF orbitals in the space of single Slater-determinant reference states [see Eq. (4.28)]. Moreover, the ground-state energy at $s = \infty$ using the MP2 density matrix does not improve upon the IMSRG(2) results obtained in any other single-particle basis. The MP2 density matrix only incorporates correlations to one-particle-one-hole and two-particle-two-hole excitations. Within the IMSRG(2) approximation such effects are resummed to all orders [31] such that no improvement on the final observable is expected. Once higher-body excitations are included, additional correlations will enter the description which are absent in the IMSRG(2) scheme. Practically, this is achieved by including third-order terms

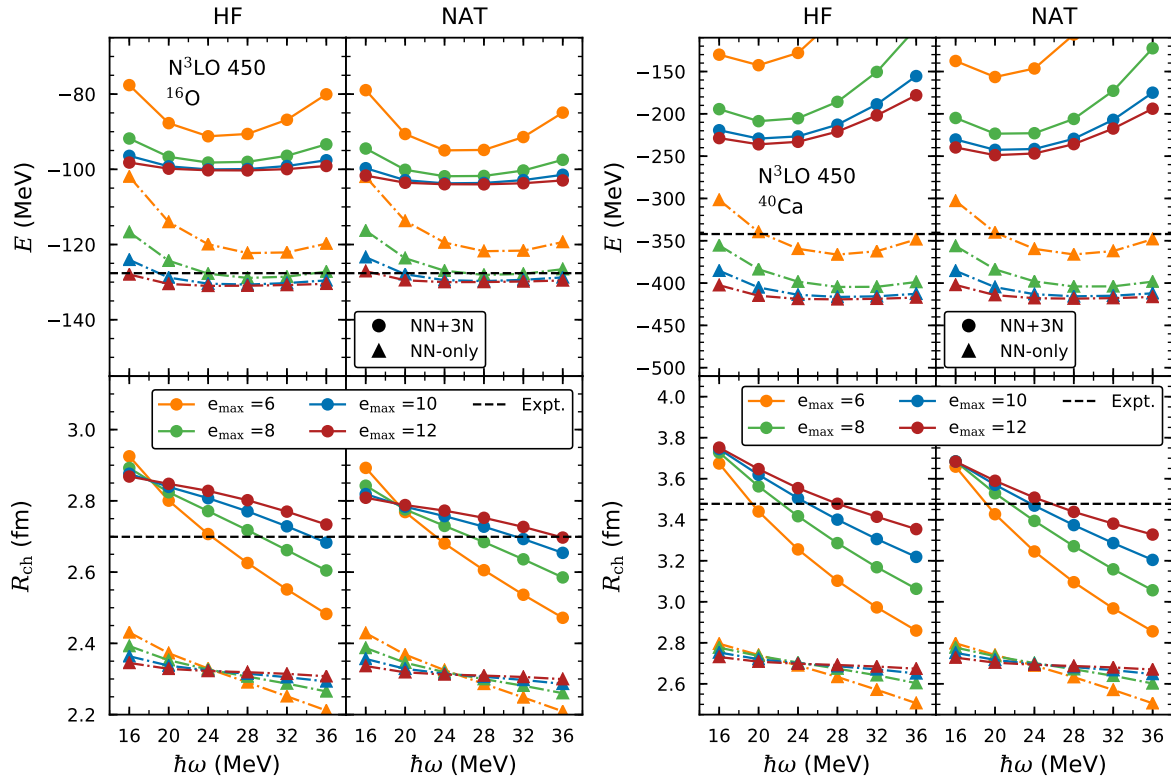


Figure 4.5: Ground-state energies (upper rows) and charge radii (lower rows) of ^{16}O and ^{40}Ca in the left and right plots, respectively, as a function of the oscillator frequency $\hbar\omega$, for the NN-only (triangles) and NN+3N (circles) $\text{N}^3\text{LO 450}$ interactions. We show results for the HF and NAT bases in the left and right panels of each plot, respectively, using various single-particle truncations e_{max} with $E_{3\text{max}} = 14$. Experimental values are taken from Refs. [48, 267].

in the MBPT expansion, i.e., λ^3 , or allowing three-body operators in the normal-ordered Hamiltonian, thus generating additional contributions in the first-order state correction. Both options will generate the leading contributions to three-particle-three-hole excitations (see also Sec. 3.5 for the IMSRG(3) truncation).

After addressing in detail properties of the single-particle basis itself, the various choices are benchmarked for medium-mass closed-shell systems using the IMSRG framework, focusing on ^{16}O , ^{40}Ca , and ^{78}Ni . All many-body calculations employed the publicly available IMSRG solver by Stroberg [247]. We compare results for ground-state energies and charge radii of ^{16}O and ^{40}Ca in the HF and NAT bases in Fig. 4.5 for a large range of oscillator frequencies for the NN-only and NN+3N $\text{N}^3\text{LO 450}$ interactions. For the NN-only potential, we observe nearly no change when going from the HF to the NAT basis on this scale. Since the HF solution is bound, bulk properties are well captured at the mean-field level and applying the NAT basis does not yield an improvement in final results. Both energies and radii are almost flat as a function of $\hbar\omega$ for the largest model space and rapidly converge with model-space size in both the HF and natural orbital bases. When 3N forces are included, the NN+3N results similarly to the NN-only case show almost no change from the HF to the NAT basis, but the $\hbar\omega$ dependence becomes more pronounced for the radii.

In order to systematically understand the difference between the basis sets, we examine the converged IMSRG(2) ground-state energies in greater detail. In Fig. 4.6, we show the difference of the results in the HF and NAT bases as a function of the SRG evolution scale

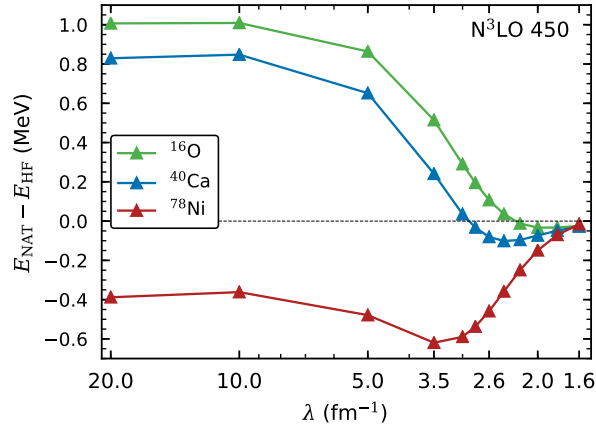


Figure 4.6: Difference of the ground-state energies in the NAT and HF bases for ^{16}O , ^{40}Ca , and ^{78}Ni as a function of the SRG resolution scale λ using the NN-only N^3LO EMN 450 interaction and a model space of $e_{\text{max}} = 14$ with $\hbar\omega = 20$ MeV.

for three closed-shell nuclei ^{16}O , ^{40}Ca , and ^{78}Ni for the NN-only interaction. The analysis is performed in absence of three-body interactions to eliminate the sensitivity of the different reference states to the NO2B approximation. For harder interactions (large λ) the difference is of the order of 1 MeV with the natural orbitals yielding stronger binding for ^{16}O and ^{40}Ca and slightly weaker binding for ^{78}Ni . Softening the potential (small λ) significantly reduces the effect such that, eventually, only differences of the order of tens of keV remain at $\lambda = 1.6 \text{ fm}^{-1}$. These differences are marginally enhanced when including 3N forces; i.e., natural orbitals provide slightly more binding compared to the HF basis and lead to a minor decrease of the $\hbar\omega$ dependence of charge radii. We emphasize again that this NN+3N interaction leads to an unbound HF solution, such that the total binding has to be produced by correlation effects during the IMSRG flow and the mean field provides a poor reference state as discussed in Sec. 4.2.1. The minor differences in converged energies are assumed to be driven by induced many-body contributions that differ in HF and natural orbital bases. A further investigation requires systematic evaluation of leading three-body contributions beyond the IMSRG(2) approximation which is beyond the scope of this thesis.

In summary, we do not observe the desired independence of the oscillator frequency in the smaller model spaces, which one could have guessed from the left plot of Fig. 4.3, and do not improve on the frequency dependence in the largest model spaces shown here compared to the HF basis.

4.3.1 Differences between NCSM and IMSRG

Given the great performance of MP2 natural orbitals in NCSM results, as shown in Ref. [250], the above results seem surprising at first since no substantial improvement over HF orbitals is obtained. The key difference between the IMSRG calculations performed in this thesis so far and the NCSM calculations is the model space in which the many-body solution is obtained.

In the NCSM, one conveniently employs an N_{max} truncation, where only many-body configurations up to a given relative excitation level are included [23]. In this case, constructing the correlated one-body density matrix in a large single-particle basis includes excitations that are absent from the NCSM configuration space and, therefore, improves the frequency dependence. On the other hand, this is inherently different from an IMSRG application, where

both the reference-state construction and IMSRG flow typically take place in the same model space, parametrized by e_{\max} . Since the high-lying states are included already in the initial single-particle basis for the HF calculation, we cannot expect significant improvement for the simplest natural-orbital-based IMSRG calculations over HF-based IMSRG calculations.

Consequently, the key idea in the following will be the construction of the MP2 density matrix in a large space, while solving the many-body problem in a reduced space in the presence of the full-space correlations embedded into the basis transformation.

4.3.2 Reduced-basis calculations from NAT/HF constructed in full space

In the following, the initial MP2 density matrix is built in a large model space $\mathcal{M}_{\text{full}}$, while a smaller subspace $\mathcal{M}_{\text{reduced}} \subseteq \mathcal{M}_{\text{full}}$ is used for performing the IMSRG evolution. While the basis transformation is performed according to

$$|n\alpha_p\rangle_{\text{NAT}} = \sum_{n'}^{\text{NAT/HF}} C_{nn'}^{\alpha_p} |n'\alpha_p\rangle_{\text{HO}}, \quad (4.29)$$

we construct a reduced basis set by keeping only a small number of the natural orbital states e_{\max} even though the density matrix construction is performed in a large space characterized by $e_{\max}^{\text{NAT/HF}}$. With this approach, the orthonormalization of the individual basis states in the reduced space is still guaranteed.

As an example, the construction of the NAT basis states in Eq. (4.29) in an $e_{\max}^{\text{NAT/HF}} = 10$ model space gives the optimized s orbitals $0s_{1/2}$ through $5s_{1/2}$, based on the transformation of the HO states up to the $5s_{1/2}$ orbitals. A subsequent truncation to an $e_{\max} = 6$ model space discards the $4s_{1/2}$ and $5s_{1/2}$ NAT orbitals after the unitary transformation. This is to be contrasted with the construction of the $e_{\max} = 6$ NAT basis in an $e_{\max}^{\text{NAT/HF}} = 6$ model space, where there are no $4s_{1/2}$ and $5s_{1/2}$ HO orbitals present in the transformation for the natural orbital basis states.

Even though parts of the information contained in the natural orbital basis are lost during this reduction process, the resulting matrix representation of operators in $\mathcal{M}_{\text{reduced}}$ still contains information about the large space due to the mixing of radial excitations up to a maximum radial quantum number n_{full} included in $\mathcal{M}_{\text{full}}$ that are otherwise not contained in $\mathcal{M}_{\text{reduced}}$. As a result, this approach accounts for high radial excitations in the construction of the reduced NAT basis and leads to a better optimization of the low-lying wave functions. Excluding higher-lying states from $\mathcal{M}_{\text{reduced}}$ is also motivated by the intuition that for low-resolution Hamiltonians we expect the many-body expansion to be dominated by excitations to low-lying states.

For the following calculations, $\mathcal{M}_{\text{reduced}}$ and $\mathcal{M}_{\text{full}}$ will be parametrized by two values, e_{\max} for the IMSRG evolution (in $\mathcal{M}_{\text{reduced}}$) and $e_{\max}^{\text{HF/NAT}}$ for the basis construction (in $\mathcal{M}_{\text{full}}$). We employ $e_{\max}^{\text{HF/NAT}} = 14$ for the 1.8/2.0 EM interaction, corresponding to the radial wave functions in the last column in the right plot of Fig. 4.3 that show the desired frequency independence for this soft interaction (see Sec. 4.2.1). Comparable results are expected for the consistently SRG-evolved N^3LO interactions. We investigate the impact on ground-state energies and charge radii by considering IMSRG calculations in various reduced model spaces with truncations $e_{\max} = 6, 8, \text{ and } 10$ for ^{16}O , ^{40}Ca , and ^{78}Ni in Figs. 4.7 and 4.8.

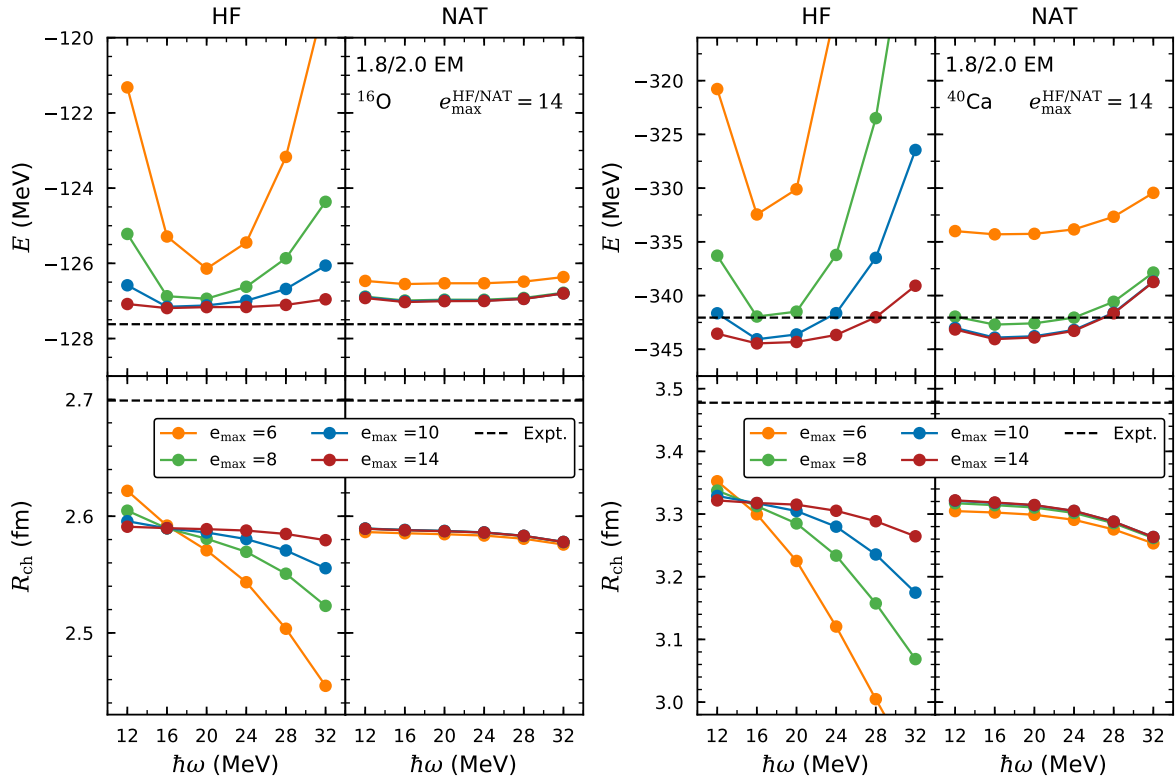


Figure 4.7: Ground-state energies (upper rows) and charge radii (lower rows) of ^{16}O and ^{40}Ca in the left and right plots, respectively, as a function of the oscillator frequency in the HF and NAT bases for the 1.8/2.0 EM interaction. We use a model space $\mathcal{M}_{\text{full}}$ with $e_{\text{max}}^{\text{HF/NAT}} = 14$ to construct the NAT basis, whereas the IMSRG calculations are performed for $e_{\text{max}} = 6, 8, 10, 14$, with $E_{3\text{max}} = 16$ in both cases. Experimental values are taken from Refs. [48, 267].

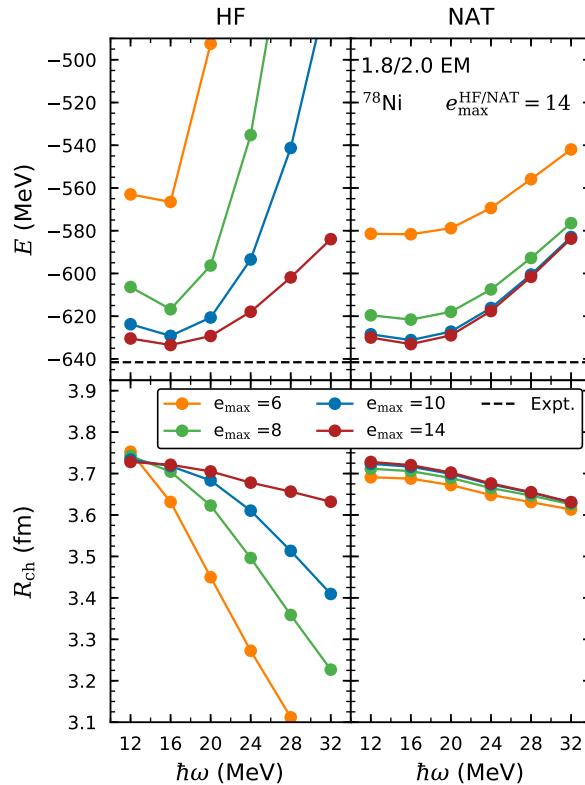


Figure 4.8: Same as Fig. 4.7 but for ^{78}Ni . Note that the experimental ground-state energy taken from Ref. [48] is extrapolated.

Constructing the NAT basis in the full space leads to a significant reduction of the $\hbar\omega$ dependence for both ground-state energies and charge radii as well as improved convergence behavior with respect to e_{\max} . The resulting improvement is similar to what was seen in NCSM calculations for ^{16}O [250] with nearly frequency-independent energies and radii, shown in the right column of the first plot in Fig. 4.7.

Analogous conclusions hold for heavier nuclei, where the convergence pattern is improved and we obtain converged results already in smaller model spaces e_{\max} . Although we cannot improve the results beyond the model space of $e_{\max}^{\text{HF/NAT}}$ employed for the initial transformation, we only have to solve for the natural orbital basis once in the largest possible $e_{\max}^{\text{HF/NAT}}$ space without having to solve the computationally more expensive IMSRG equations in the full space. Assuming we can obtain comparable results in $e_{\max} = 10$ (1140 single-particle states) using an MP2 density matrix constructed in $e_{\max} = 14$ (2720 single-particle states), we save a factor $R \approx 2\text{--}3$ in single-particle dimension. Consequently, the use of large-space natural orbitals combined with reduced-space many-body expansions provides a computationally efficient alternative to the full-space IMSRG calculations.

4.4 Exploration of Skyrme EDF basis sets

In addition to the HF and NAT single-particle bases discussed in great detail in the previous sections, we explore the effects of applying single-particle basis sets stemming from a density functional theory (DFT) calculation [268, 269] together with chiral interactions in the IMSRG. In particular, the orbitals are constructed from a Skyrme-HF calculation with the SLy4 EDF parametrization [270–272]. We subsequently apply these orbitals to the 1.8/2.0 EM interaction in IMSRG applications. The Skyrme orbitals have the possible advantages that they are available even for heavy nuclei and can easily be calculated for large model spaces. Furthermore, the underlying EDF yields a good description of ground-state energies and leads to realistic density profiles. Therefore, predicted charge radii are in good agreement with experiment for a large range of medium-mass to heavy nuclei.

We additionally explore the effects of mixed single-particle basis sets by combining the occupied Skyrme orbitals with the unoccupied NAT orbitals, where the goal is to capitalize on the advantages of both basis sets for the occupied and unoccupied orbitals, respectively. As these two basis sets are not orthonormal to each other, we carry out an orthogonalization with minimal adjustment (OMA) of the new basis by using the “cos-max” version outlined in Ref. [273]. This procedure generates a set of orthonormal orbitals where the overlap of the i -th generated orbital and the i -th input orbital is maximized and we weight all input orbitals equally. In general, this approach can be applied for any combination of basis sets.

The squared absolute value of the radial wave function for selected orbitals in the HO, HF, NAT, SLy4, and combined SLy4 + NAT basis is shown in Fig. 4.9. As expected, the occupied Skyrme orbitals are frequency independent, based on the underlying HF calculation, whereas the unoccupied orbitals show a frequency dependence that is comparable to the unoccupied HF orbitals. This issue is resolved for the combined OMA orbitals that are frequency independent in all shown cases. As a next step, we perform IMSRG calculations, comparing the HF, NAT, SLy4, and OMA basis for three test case nuclei, ^{40}Ca , ^{48}Ca , and ^{132}Sn . In Table 4.1, we show the normal-ordered zero-body part of the Hamiltonian and charge radius operator as well as the corresponding results after the IMSRG evolution. We

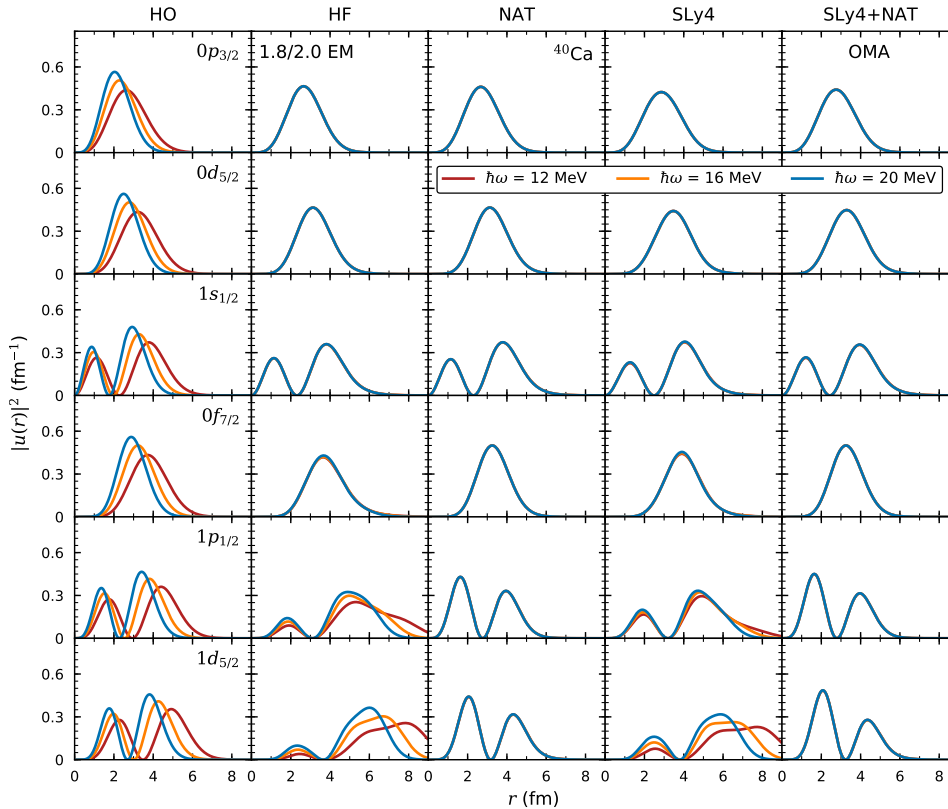


Figure 4.9: Same as Fig. 4.3 but for ^{40}Ca and $e_{\text{max}} = 14$ using the 1.8/2.0 EM interaction. We show the HO, HF, NAT, SLy4, and combined SLy4 + NAT OMA bases (see text for details) in the first through fifth columns, respectively. The first three rows ($0p_{3/2}$, $0d_{5/2}$, and $1s_{1/2}$) correspond to occupied orbitals in ^{40}Ca , whereas the fourth through sixth rows ($0f_{7/2}$, $1p_{1/2}$, and $1d_{5/2}$) are unoccupied.

find that the normal-ordered zero-body part for the Skyrme SLy4 basis is always slightly smaller for the energies and larger for the radii, which is expected as the consistent HF solution of the chiral interaction by construction yields the lowest reference-state expectation value for this interaction. However, the final results for both energies and radii are very close in all three basis sets and the combined OMA basis lies between the NAT and SLy4 basis. In particular, the charge radii remain too small compared to experiment for the SLy4 basis that leads to a more realistic density profile. Even though the SLy4 and combined OMA orbitals do not immediately yield a benefit over the HF or NAT basis, they can still serve as a measure for the reference-state dependence in the IMSRG, based on a reasonable (physically motivated) reference state.

In order to investigate the reference-state dependence in more detail, we compare ground-state energies and charge radii for ^{16}O and ^{12}C in Figs. 4.10 and 4.11, respectively, for a large set of model-space truncations e_{max} and oscillator frequencies. The energies for ^{16}O are very similar for all three basis sets, with the Skyrme SLy4 results showing similar convergence behavior as the HF results and leading to slightly more binding and slightly larger radii compared to the HF and NAT basis. This changes drastically for ^{12}C in Fig. 4.11. While the HF and NAT basis lead to comparable results close to the value suggested by NCSM calculations in small N_{max} model spaces (extrapolated to approximately -91 MeV but not shown here), the SLy4 orbitals lead to about 7 MeV more binding and about 0.5 fm larger

^{40}Ca	HF	NAT	SLy4	OMA
E_0 (MeV)	-247.181	-247.023	-235.234	-243.866
$R_{\text{ch},0}$ (fm)	3.292	3.287	3.495	3.391
E_{IMSRG} (MeV)	-344.458	-344.049	-344.538	-344.043
R_{ch} (fm)	3.320	3.318	3.325	3.323
^{48}Ca	HF	NAT	SLy4	OMA
E_0 (MeV)	-303.475	-303.188	-286.189	-298.723
$R_{\text{ch},0}$ (fm)	3.260	3.273	3.509	3.390
E_{IMSRG} (MeV)	-415.838	-415.424	-416.695	-415.862
R_{ch} (fm)	3.299	3.297	3.306	3.302
^{132}Sn	HF	NAT	SLy4	OMA
E_0 (MeV)	-759.558	-759.141	-706.452	-744.020
$R_{\text{ch},0}$ (fm)	4.342	4.358	4.681	4.516
E_{IMSRG} (MeV)	-1058.384	-1057.868	-1064.818	-1061.076
R_{ch} (fm)	4.392	4.390	4.409	4.402

Table 4.1: Normal-ordered zero-body part E_0 and $R_{\text{ch},0}$ of the Hamiltonian and the charge radius operator, respectively, in the HF, NAT, SLy4, and OMA basis for ^{40}Ca , ^{48}Ca , and ^{132}Sn . The ground-state energy and the charge radius after solving the IMSRG in each basis is shown by E_{IMSRG} and R_{ch} , respectively. All results use the 1.8/2.0 EM interaction and a model space of $e_{\text{max}} = 14$ with $\hbar\omega = 16$ MeV.

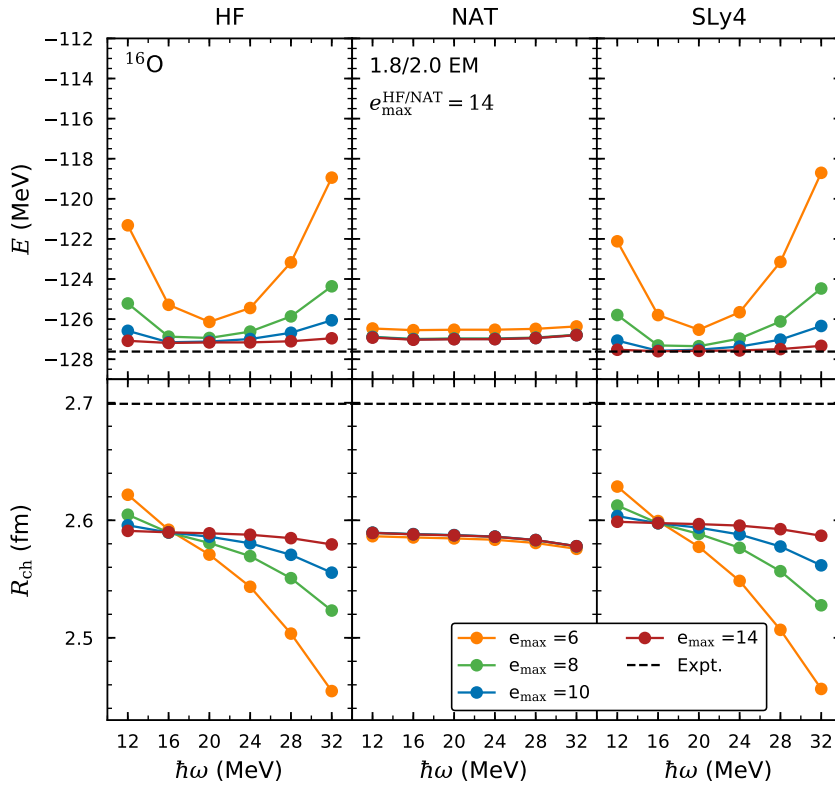


Figure 4.10: Same as the left plot of Fig. 4.7 but we additionally show the results for using the Skyrme SLy4 orbitals in the rightmost panel.

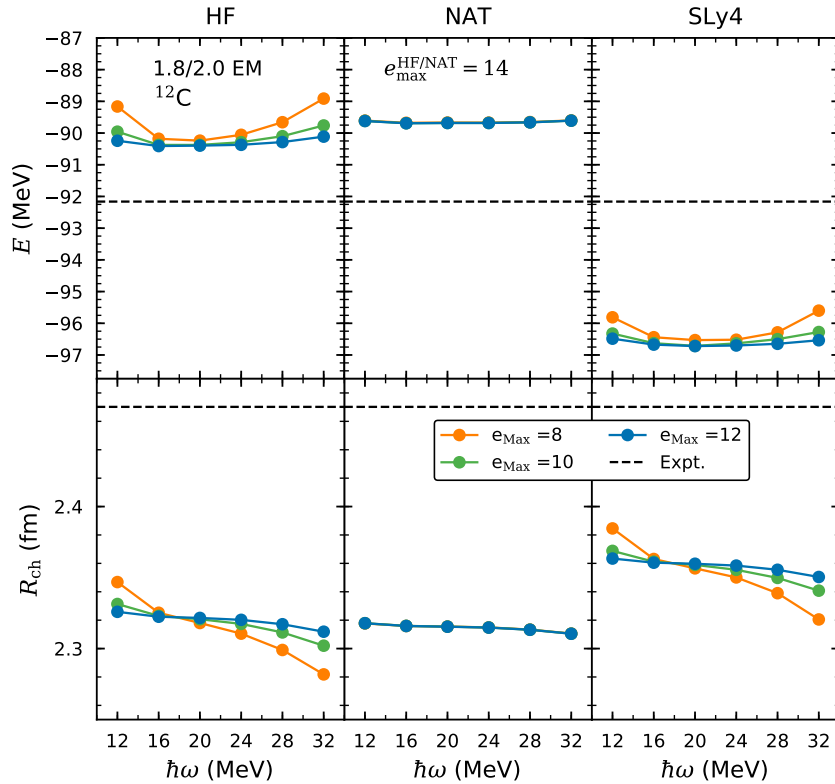


Figure 4.11: Same as Fig. 4.10 but for ^{12}C .

charge radii. By comparing the individual orbitals in each basis, we find that the squared radial wave function of the occupied orbitals in the HF (NAT) and SLy4 basis have the largest differences for the $0s_{1/2}$ orbital. Constructing an artificial reference state with the $0s_{1/2}$ HF orbital for the SLy4 basis brings the results in the different bases in better agreement (-92.2 MeV), but still showing a nonnegligible difference in energy. The missing difference is probably related to the weak or even vanishing shell closure and cluster structure of ^{12}C , making single-reference calculations of this nucleus extremely challenging compared to doubly closed-shell nuclei, such as ^{16}O .

4.5 Systematic study of IMSRG(3) truncations

In the following, we investigate the solution of the full IMSRG(3) and its approximate truncation schemes introduced in Sec. 3.5 for ground-state energies of ^4He and ^{16}O using the HF and NAT basis. The natural orbitals are constructed in a large model space $e_{\text{max}}^{\text{NAT}} = 14$ and truncated to a smaller model space $e_{\text{max}} = 2$ for the many-body calculation. All results shown in this section are based on our publication in Ref. [241], where I in particular contributed to the application of the NAT basis for the implementation of the IMSRG(3). The following calculations employ the imaginary time generator of Eq. (3.95) with the three-body part of Eq. (3.129) and directly integrate the flow equations without using the Magnus expansion approach. We tested the sensitivity of our results to the generator choice and found differences of only less than 1 keV for each truncation scheme. Due to the tremendous computational cost, the calculations are limited to small model spaces of $e_{\text{max}} = 2$.

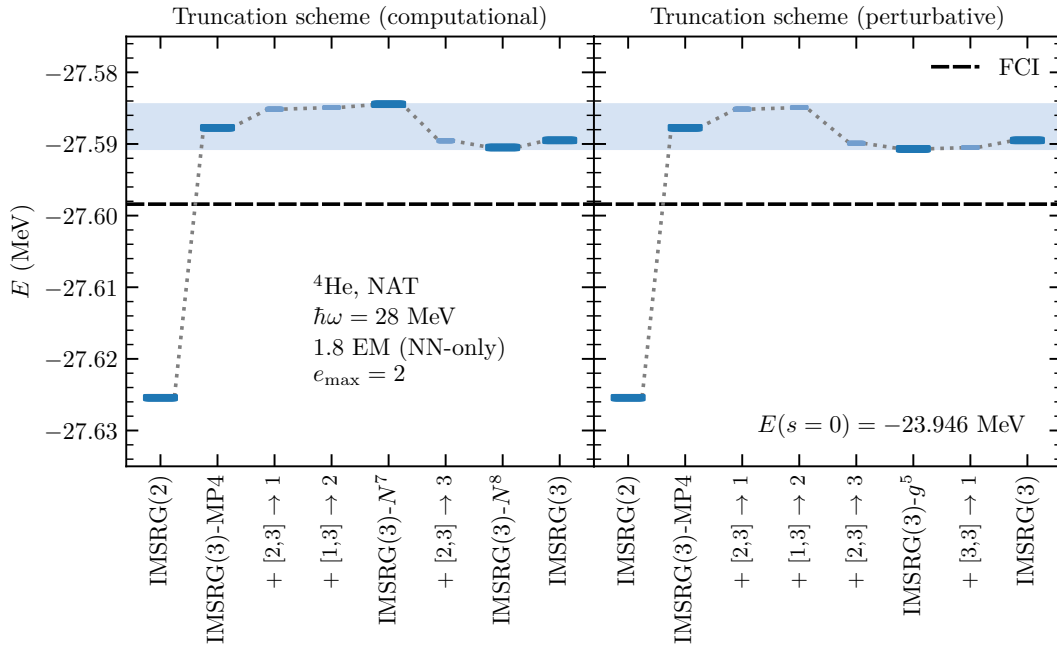


Figure 4.12: Ground-state energies of ${}^4\text{He}$ obtained in various truncation schemes using the 1.8 EM NN-only Hamiltonian and a NAT reference state with an oscillator frequency of $\hbar\omega = 28$ MeV, following the computational (left panel) and perturbative (right panel) truncation ordering for the fundamental commutators. Thicker, darker bars correspond to the major truncations summarized in Fig. 3.3. Thinner, lighter bars correspond to intermediate truncations where a single fundamental commutator has been added relative to the truncation scheme to the left. The dashed line indicates the $e_{\max} = 2$ FCI result obtained for this Hamiltonian. The blue band indicates the range spanned by the results obtained from the IMSRG(3)- N^7 and IMSRG(3)- g^5 truncations. The NAT reference-state expectation value is provided in the bottom right corner.

4.5.1 Application to ${}^4\text{He}$ and ${}^{16}\text{O}$

Figure 4.12 shows the ground-state energies of ${}^4\text{He}$ for the major truncations introduced in Fig. 3.3 by thick bars, using the NN-only interaction 1.8 EM of Ref. [46], SRG evolved to $\lambda = 1.8 \text{ fm}^{-1}$. We additionally introduce minor truncations that include additional fundamental commutators on top of a major truncation specified on the x axis and visualized by thinner bars. For example, one minor truncation scheme we consider is the IMSRG(3)- $N^7 + [2, 3] \rightarrow 3$ truncation, which has all $\mathcal{O}(N^7)$ commutators and the $[2, 3] \rightarrow 3$ commutator, which is $\mathcal{O}(N^8)$. For the NN-only calculations we provide exact results from a full configuration interaction (FCI) diagonalization of the $e_{\max} = 2$ Hamiltonian. In the absence of a many-body truncation, the IMSRG would be able to obtain the exact result, and comparing against this result for different approximations allows us to gain insight into the effect of the many-body truncations at play. In both panels of Fig. 4.12, we start from the IMSRG(2) truncation and add commutators until we reach the IMSRG(3) truncation on the right.

In the left panel, we follow the computational approach to organizing the IMSRG(3) fundamental commutators. At the IMSRG(2)-truncation level, the ground-state energy only differs from the FCI result by 27 keV. The first truncation we consider beyond the IMSRG(2) is always the IMSRG(3)-MP4 truncation in both panels, which in all systems we investigated delivered a sizable repulsive correction to the energy. This is consistent with our understanding

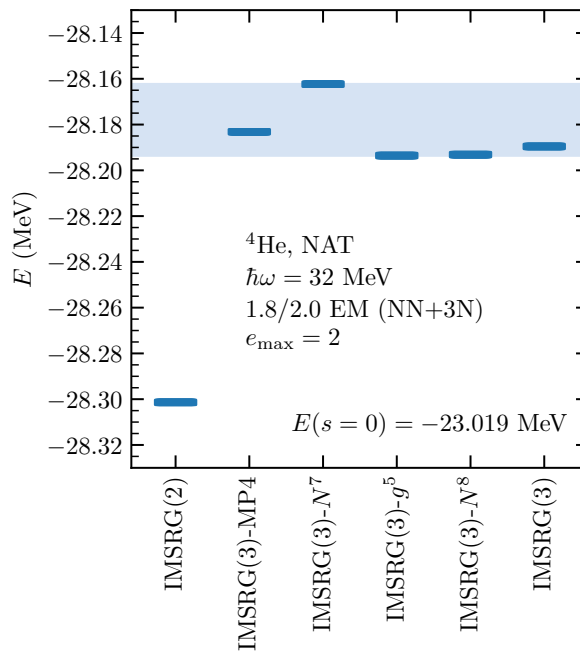


Figure 4.13: Ground-state energies of ${}^4\text{He}$ obtained in various truncation schemes using the 1.8/2.0 EM Hamiltonian and a NAT reference state with an oscillator frequency of $\hbar\omega = 32$ MeV. The blue band indicates the range spanned by the results obtained from the IMSRG(3)- N^7 and IMSRG(3)- g^5 truncations. The NAT reference-state expectation value is provided in the bottom right corner.

of the diagrammatic content of the IMSRG(2) and the nature of the missing fourth-order MBPT energy corrections. The inclusion of fundamental commutators up to the IMSRG(3)- N^7 truncation gives only small repulsive shifts to the energy. The next two commutators that are included in the IMSRG(3)- N^8 truncation provide slightly larger attractive contributions and the contribution of the $[3, 3] \rightarrow 3$ commutator to arrive at the full IMSRG(3) truncation is repulsive and only small. The final IMSRG(3) ground-state energy differs from the FCI result by 9 keV, which is a considerable improvement over the IMSRG(2) result, although all of the results discussed here are close to the exact result (sub-1% error). In the right panel, we show the same information for the case where the perturbative ordering of fundamental commutators is used. We see that the general size of energy contributions follows the perturbative counting. In particular, because the sixth-order commutator contributions are so small, the IMSRG(3)- g^5 approximates the full IMSRG(3) extremely well.

When discussing the contributions of commutators, it is worth noting that the contribution of an added commutator to the energy also depends on which other commutators are also included in that truncation. In this context, the one-by-one inclusion of fundamental commutators formally does not commute. In practice, however, we see that the size of the contribution of a specific commutator is not strongly sensitive to the order in which it is included relative to other commutators. One can see this behavior when comparing the two panels of Fig. 4.12.

In Fig. 4.13, we present ${}^4\text{He}$ ground-state energies obtained using the NN+3N 1.8/2.0 EM Hamiltonian and a NAT reference state for various IMSRG truncation schemes. For the treatment of the three-body part of the NN+3N Hamiltonian we use the NO2B approximation. Overall, the corrections offered by approximate IMSRG(3) truncations are larger in magnitude

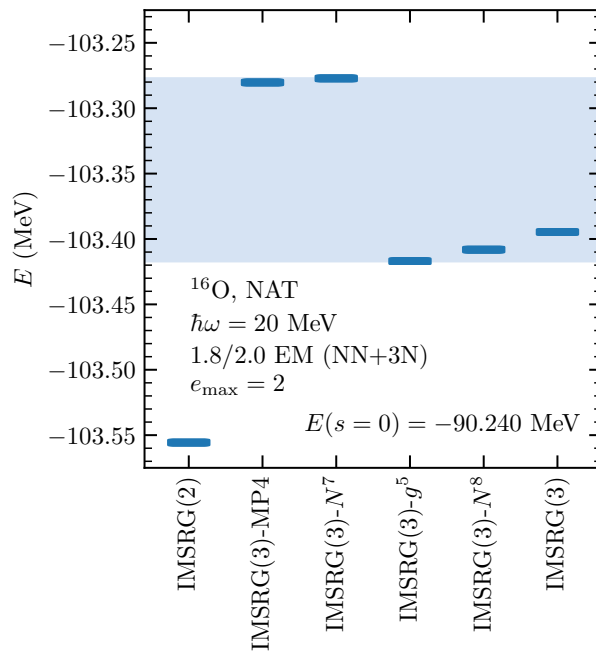


Figure 4.14: Ground-state energies of ^{16}O obtained in various truncation schemes using the 1.8/2.0 EM Hamiltonian and a NAT reference state with an oscillator frequency of $\hbar\omega = 20$ MeV. The blue band indicates the range spanned by the results obtained from the IMSRG(3)- N^7 and IMSRG(3)- g^5 truncations. The NAT reference state energy is provided in the bottom right corner.

than in the NN-only case, with the IMSRG(2) and IMSRG(3) results differing by 112 keV (compared to the difference of 36 keV in the NN-only case). We see similar trends as in the NN-only case, with a large repulsive correction from the IMSRG(3)-MP4 truncation and a smaller repulsive correction from the IMSRG(3)- N^7 . The $\mathcal{O}(N^8)$ fifth-order commutators provide attractive corrections, and the final IMSRG(3) result lands between the IMSRG(3)- N^7 and IMSRG(3)- g^5 results, as indicated by the blue band spanned by the results of these two truncations.

Next, we investigate the IMSRG solution for the ground-state energy of ^{16}O and compare the IMSRG(3) and its approximate truncation schemes to the IMSRG(2) for the NN+3N 1.8/2.0 EM Hamiltonian and the NAT basis in Fig. 4.14. In this case, the IMSRG(3)-MP4 truncation result is about 270 keV more repulsive than the IMSRG(2) result, and the IMSRG(3)- N^7 provides only small corrections to the IMSRG(3)-MP4 result. These results differ substantially from those obtained from the remaining truncation schemes, which contain all the $\mathcal{O}(N^8)$ fifth-order commutators. Of the systems we studied, this is the system with the largest contribution by these commutators, making the IMSRG(3)- g^5 , for example, a substantial improvement over the IMSRG(3)- N^7 due to its inclusion of these higher-cost fifth-order commutators that are neglected in the IMSRG(3)- N^7 . We see that again the large band resulting from the IMSRG(3)- N^7 and IMSRG(3)- g^5 results includes the IMSRG(3) result as for ^4He in Figs. 4.12 and 4.13. Note that the final IMSRG(3) energy differs by about 160 keV from the IMSRG(2) result.

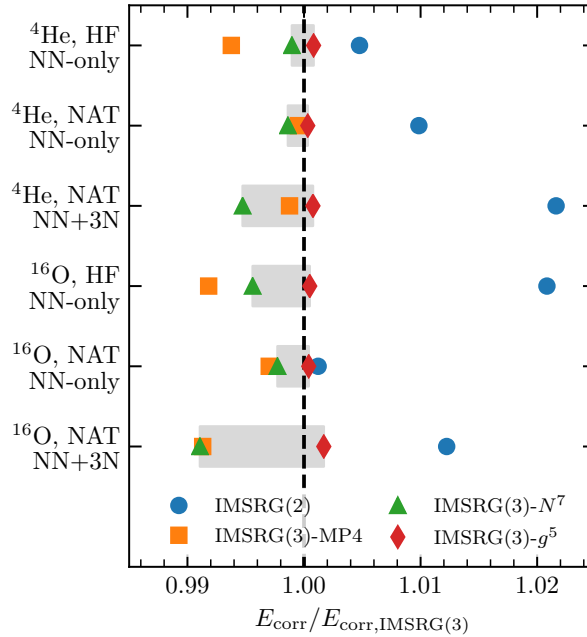


Figure 4.15: Ratios of correlation energies obtained in IMSRG(2) and approximate IMSRG(3) calculations relative to the IMSRG(3) correlation energies for ^4He and ^{16}O in the HF and NAT basis, using the NN-only 1.8 EM and NN+3N 1.8/2.0 EM Hamiltonian for $e_{\max} = 2$. We show results for the major truncations given in Fig. 3.3 and include the results of Figs. 4.12-4.14. The gray band indicates the range spanned by the IMSRG(3)- N^7 and IMSRG(3)- g^5 results.

4.5.2 Analysis of truncation performance

We consider the relative performance of the different IMSRG truncations for both nuclei studied above, the HF and NAT basis, as well as the NN-only and NN+3N Hamiltonian and summarize the observed trends in Fig. 4.15. We compare the correlation energy, defined as

$$E_{\text{corr}} = E(s \rightarrow \infty) - E(s = 0), \quad (4.30)$$

for the IMSRG(2) and approximate IMSRG(3) truncations relative to the IMSRG(3) correlation energy. The vertical line at $x = 1.0$ indicates the IMSRG(3) correlation energy. In the previous section, we saw that for ^4He and the NN-only Hamiltonian the IMSRG(3) energy was closer to the exact result obtained via FCI calculations. This intuitively matches the expected behavior of the many-body expansion, where including higher many-body ranks in the many-body expansion allows the truncated methods to systematically approach the exact result. In Fig. 4.15 and the following discussion, we frame things relative to the IMSRG(3) results, as the IMSRG(3) truncation is the “most complete” IMSRG result we have available.

Considering the performance of the IMSRG(2) relative to the IMSRG(3), we see that the difference in the correlation energy is about 1–2% for most systems, with the exception of about 0.1% difference for the ^{16}O NN-only NAT case. We also see that the IMSRG(2) results are systematically overbound relative to the IMSRG(3) results.

Turning our attention to the IMSRG(3)-MP4 truncation, we find that these results differ from the IMSRG(3) results by up to 1%. The results are also all less bound than the IMSRG(3) results, making the IMSRG(2) and IMSRG(3)-MP4 results lower and upper bounds on the IMSRG(3) result. Considering that the IMSRG(3)-MP4 is the least computationally expensive

approximate IMSRG(3) truncation we considered, this provides a relatively cheap way to set a weak bound on where the IMSRG(3) result lands. Turning our attention to the next two truncations, the IMSRG(3)- N^7 and IMSRG(3)- g^5 truncations, we find that the IMSRG(3)- N^7 results are generally less bound than the IMSRG(3) results by about 0.5% (1% in one case) and the IMSRG(3)- g^5 results are generally more bound by about 0.1%. The gray bands in Fig. 4.15 show the range of energies bounded by the results from these two truncations, where we see that these bands always contain the IMSRG(3) results. The IMSRG(3)- N^7 is of comparable expense and quality to the IMSRG(3)-MP4 truncation. However, the IMSRG(3)- g^5 is considerably more expensive and nearly as expensive as the full IMSRG(3). This means that even once large-scale IMSRG(3)-MP4 and IMSRG(3)- N^7 calculations are possible, IMSRG(3)- g^5 calculations may still be out of reach. Still, if both IMSRG(3)- N^7 and IMSRG(3)- g^5 calculations are possible, then these can be used to provide a robust bound on what the IMSRG(3) results could be and offer possibilities for studying uncertainties due to the many-body truncation in IMSRG calculations.

5

Importance Truncation

Ab initio nuclear many-body frameworks require extensive computational resources, especially when targeting heavier nuclei or more exotic systems. Even though impressive results have been obtained, e.g., *ab initio* calculations of systems with approximately 100 particles [49, 50] or calculations of a diverse set of nuclear observables [51, 55, 86, 91, 274, 275], several frontiers still remain: the extension of *ab initio* nuclear theory to heavy nuclei well above mass numbers $A \approx 100$; many-body calculations for deformed nuclei that are not well approximated by a spherical reference state; and the systematic inclusion of higher-order terms in the many-body expansion for high-precision studies. Some of the limiting factors common to all of these efforts are the computational and storage costs of the many-body calculation. Calculations of larger systems require larger single-particle bases to converge calculations. Similarly, calculations using symmetry-broken reference states (for instance, with axial symmetry rather than spherical symmetry) have to employ single-particle bases about an order of magnitude larger than standard spherically restricted calculations [74, 83]. Additionally, relaxing the many-body truncation in methods like the IMSRG and CC theory increases the scaling of both the computational and storage costs with respect to the basis size, as e.g., discussed for the IMSRG(3) in Sec. 4.5. Significant truncations have to be employed to make these calculations tractable [74, 241]. Considering the computational challenges shared among the points above, strategies to temper the storage and computational costs of the many-body expansion method would accelerate the progress for all of these developments.

It is well known that correlations are not uniformly distributed in the A -body Hilbert space and that certain configurations are more important for a quantitative reproduction of a given observable than others. In a simplistic picture this is already implicitly used in the N_{\max} truncation commonly employed in the NCSM that favors many-body states with low-lying excitations. A more refined selection of the configuration space was first employed by the IT-NCSM, which uses a perturbative selection measure to *a priori* gauge the relevance of a given configuration for the final NCSM eigenstate. With the aid of the IT it was first possible to extend the accessible mass range of configuration-interaction-based techniques to the oxygen drip line [68]. Similar ideas have since been employed in open-shell studies using particle-number-broken Hartree-Fock-Bogoliubov reference states. While initially applied to Bogoliubov MBPT (BMBPT) [169], the IT concept was recently extended to nonperturbative Gorkov SCGF calculations [276]. Simpler selection ideas based on natural orbital occupation numbers were used with great success in deformed CC applications [74]. Alternative approaches, such as the SVD introduced in Sec. 2.4, based on tensor-factorization techniques to decompose the many-body operators and therefore lower the storage and

computational requirements are, e.g., studied in Refs. [169–171, 277, 278] for applications in nuclear structure calculations.

In this chapter, we develop the IT ideas to the IMSRG framework and especially focus on the sensitivity of the importance-truncated results on the selection procedure and the interaction details for a wide range of IT measures. All results presented here have been published in Ref. [279]. Based on our findings, we identify the importance-truncated IMSRG (IT-IMSRG) as a promising candidate to reduce the costs of many-body calculations and, thus, extend the scope of *ab initio* studies along the lines discussed above.

We introduce the general IT approach in Sec. 5.1 with different interaction blocks and importance measures applied to the IMSRG in Sec. 5.2 and present results for selected mid-mass systems using different IT measures and chiral interactions in Sec. 5.3. All results shown in this chapter use the NAT single-particle basis. We employ the 1.8/2.0 EM [54] and N³LO 500 NN+3N [56, 57] Hamiltonians and study both the unevolved and consistently SRG-evolved interaction for the latter.

5.1 Basic principle

The aim of importance-truncation techniques is to effectively reduce the size of the problem by only considering the most important contributions based on a predefined importance measure. Significant benefits are obtained by combining measures that are computationally cheap to construct with computationally more challenging many-body methods. By truncating unimportant parts of the many-body problem the cost of the IT-adapted many-body method is reduced. The discarded information can further be approximately accounted for in a perturbative way in order to minimize the information loss due to the IT. Improving the quality of the IT measure or the approximation used to account for truncation effects can be used to reduce the systematic error introduced by the IT. In practice, however, a reasonable balance between accuracy and complexity of the IT measure construction and the approximate treatment of IT-truncated parts has to be found.

To understand how we approach IT in the IMSRG, it is instructive to review how importance truncation is performed with great success in the IT-NCSM [21, 280]. In the NCSM, the matrix elements of the Hamiltonian are evaluated in a basis of Slater determinants (configurations) $\{|\Phi\rangle\}$, and a subsequent diagonalization provides access to low-lying energies and corresponding eigenstates. The IT approach is based on defining an importance measure κ that gives an estimate of the importance of a particular configuration $|\Phi\rangle$. This measure is used to find the corresponding subspace \mathcal{M}^{IT} of the A -body Hilbert space $\mathcal{H}^{(A)}$

$$\mathcal{M}^{\text{IT}}(\kappa_{\text{min}}) \equiv \{|\Phi\rangle : \kappa(|\Phi\rangle) \geq \kappa_{\text{min}}\} \subset \mathcal{H}^{(A)} \quad (5.1)$$

of the most important configurations with $\kappa(|\Phi\rangle)$ above a chosen threshold κ_{min} .

The reduced size of the IT-selected subspace crucially reduces the computational cost of the following diagonalization, which roughly scales like the size of the subspace squared. Residual effects from truncated configurations are approximately incorporated via a low-order multi-configuration perturbation theory treatment [281, 282]. In the limit of $\kappa_{\text{min}} \rightarrow 0$ the full configuration space is recovered and no approximation is induced by the importance truncation.

Nuclear Hamiltonians obey a set of symmetries that one can explicitly exploit to lower computational requirements when storing operator matrix elements and performing many-body calculations. These symmetries are rotational invariance ($[H, J^2] = [H, J_z] = 0$), parity conservation ($[H, \Pi] = 0$), and isospin conservation ($[H, T_z] = 0$). Exploiting these symmetries leads to a block-diagonal structure, where we store the two-body matrix elements in separate ($J^{\Pi} T_z$) blocks. This block structure is preserved for the normal-ordered Hamiltonian if a symmetry-conserving reference state is employed, which is the case for all systems and computational bases we consider in this thesis. Application of symmetry-broken reference states leads to many-body operators with lesser symmetries compared to their non-normal-ordered representations [220, 221].

Many-body operators in a single-particle basis can be further decomposed in terms of their individual single-particle labels. For a Slater-determinant reference state $|\Phi\rangle$, single-particle states [see Eqs. (3.4), (3.24), and (3.28)] can be characterized as hole (h) or particle (p) states, depending on their occupation number in the reference state. In the case of the two-body part of the operator, this leaves us with six interaction blocks of single-particle index combinations: hhhh, hhhp, hhpp, hphp, hppp, and pppp (plus their Hermitian conjugates and symmetry related blocks). The notation we use here indicates that, e.g., for the hhpp block the two single-particle states in the bra two-body state are hole states and the two single-particle states in the ket two-body state are particle states. In model-space sizes required for converged calculations, the number of particle states typically significantly exceeds the number of hole states. Consequently, the pppp and hppp blocks drive the computational complexity of the many-body calculation, and blocks like the hhhh or hhhp blocks have a relatively small cost in terms of memory and computation. We investigate the various two-body interaction blocks, their contributions to the perturbative energy corrections and different diagrams in the IMSRG, and their role in the IT-IMSRG in more detail in the following.

5.1.1 Perturbative analysis

When following the standard Rayleigh-Schrödinger formulation of perturbation theory using the Møller-Plesset partitioning [35, 199] as outlined in Sec. 3.3.3, the canonical second-order (MP2) energy correction is given by Eq. (3.72). Here and in the following we use the same notation as before, with indices i, j, \dots (a, b, \dots) denoting hole (particle) states, while p, q, \dots denote generic single-particle states. From Eq. (3.72) we see that the second-order energy correction is only sensitive to the hhpp block of the interaction. The third-order (MP3) energy correction in a canonical basis, as defined in Eq. (3.74), consists of three terms

$$E_{\text{pp}}^{(3)} = \frac{1}{8} \sum_{abcdij} \frac{\Gamma_{ijab} \Gamma_{abcd} \Gamma_{cdij}}{\varepsilon_{ij}^{ab} \varepsilon_{ij}^{cd}}, \quad (5.2a)$$

$$E_{\text{hh}}^{(3)} = \frac{1}{8} \sum_{abijkl} \frac{\Gamma_{ijab} \Gamma_{abkl} \Gamma_{kl ij}}{\varepsilon_{ij}^{ab} \varepsilon_{kl}^{ab}}, \quad (5.2b)$$

$$E_{\text{ph}}^{(3)} = - \sum_{abcijk} \frac{\Gamma_{ijab} \Gamma_{kbic} \Gamma_{ackj}}{\varepsilon_{ij}^{ab} \varepsilon_{kj}^{ac}}, \quad (5.2c)$$

defining the pp (particle-particle), hh (hole-hole), and ph (particle-hole) diagrams, respectively. Consequently, the third-order energy correction is sensitive to the hphp, pppp, and hhhh blocks in addition to the hhpp block. Through a wide range of mass numbers it was shown

that correlation effects from the particle-hole diagram dominate the third-order contribution for Hamiltonians that are amenable to MBPT [18]. This will become important later for selecting the most relevant subblocks for the preprocessing in the IT approach.

When working in a noncanonical basis, e.g., the NAT basis, the one-body part of the Hamiltonian is not diagonal anymore and additional contributions to the perturbative energy corrections have to be considered that also include one-body vertices. For the second-order energy correction, there is one additional diagram [see Eq. (3.73)], and at third order eleven new diagrams arise [199] [see Eq. (3.75)]. The new third-order diagrams are now also sensitive to the two-body matrix elements in the hppp and hhpp blocks. Consequently, all interaction blocks contribute to the energy correction up to third order in a noncanonical basis.

5.2 Application to the IMSRG

The IMSRG differs from the NCSM by employing a Fock space rather than a configuration space formulation. As a result, the implementation of the IT approach in the IMSRG needs to be adapted to work with many-body operators. In the following, we focus the discussion of our approach on its application to two-body operators as in the IMSRG(2) they dominate the storage costs and contribute to the computationally dominating commutators. The approach is, however, general and could be easily applied to one-body operators or three-body operators in IMSRG(3) calculations (with appropriately adapted importance measures).

To implement IT on two-body operator matrix elements, we analyze whether the matrix element at the single-particle index combination $pqrs$ is important or not. The result of this analysis is a “mask” based on our importance measure and chosen importance-truncation threshold:

$$\kappa_{pqrs}^{\text{mask}} = \begin{cases} 1 & \text{if } pqrs \text{ is important,} \\ 0 & \text{otherwise.} \end{cases} \quad (5.3)$$

This is similar to how in the IT-NCSM configurations are analyzed and are either kept or removed (“masked”) from the model space. The task is then to figure out which index combinations are “important.” We use importance measures κ that take as input two-body matrix elements of some operator (typically the Hamiltonian) and give a value for the measure κ_{pqrs} for each single-particle index combination. If $\kappa_{pqrs} \geq \kappa_{\text{min}}$ for our chosen threshold κ_{min} , we say that the index combination $pqrs$ is important, and the mask $\kappa_{pqrs}^{\text{mask}}$ in Eq. (5.3) takes on a value of one. In Sec. 5.2.2, we discuss different possible importance measures.

Given such a mask, the matrix elements of a two-body operator O_{pqrs} can be split into an important part,

$$O_{pqrs}^{\text{imp.}} = \kappa_{pqrs}^{\text{mask}} O_{pqrs}, \quad (5.4)$$

and a residual part,

$$O_{pqrs}^{\text{res.}} = (1 - \kappa_{pqrs}^{\text{mask}}) O_{pqrs}. \quad (5.5)$$

Keeping only the important part of all two-body matrix elements in the IMSRG amounts to solving the flow equation for only a subset of single-particle index combinations, which

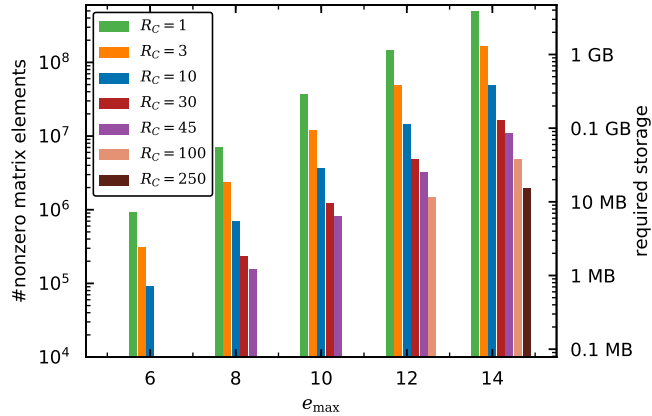


Figure 5.1: Total number (left y axis) and corresponding storage requirements (right y axis) of nonzero two-body matrix elements for different compression ratios R_C [see Eq. (5.6)] as a function of the model-space size e_{\max} . For $R_C = 1$ the number of matrix elements corresponds to the initial Hamiltonian without any IT.

gives us the IT-IMSRG. The residual part may be treated approximately independent of the IT-IMSRG solution to capture the main effects neglected by its removal.

More concretely, in the IMSRG(2) we apply the IT approach discussed above to the two-body part Γ of the Hamiltonian, see Eq. (3.19). Additionally, the same truncation (i.e., using the same κ^{mask}) is applied to the two-body part of the generator and any two-body parts arising from commutator evaluations. The initially removed matrix elements from the Hamiltonian will be treated perturbatively, and are not considered in the IMSRG solution. Moreover, the evaluation of commutators in the IMSRG induces contributions to IT-neglected matrix elements in the resulting operator. These are discarded and not treated further in our approach.

The storage benefits of an IT-preprocessed operator are conveniently characterized by defining a compression ratio

$$R_C = \frac{\# \text{ of nonzero MEs}}{\# \text{ of nonzero MEs} - \# \text{ of IT-neglected MEs}}, \quad (5.6)$$

given by the ratio of the number of initial nonzero two-body matrix elements (MEs) over the number of remaining nonzero two-body matrix elements after the IT. In the case of no truncation $R_C = 1$ and no compression is obtained. Once the IT selection is performed, R_C exceeds unity indicating a possibly lower memory footprint; truncating 90% of the matrix elements gives $R_C = 10$ and truncating 99% of the matrix elements gives $R_C = 100$. In this way the compression ratio provides an estimate of the scaling gained by the IT. For example, a compression ratio of $R_C = 70$ in an $e_{\max} = 14$ model space corresponds to truncating approximately 485.7 million of the total 492.7 million matrix elements. The displayed dimensionalities assume full exploitation of rotational invariance, parity and isospin conservation, and permutation symmetries. This leaves just 7 million nonvanishing matrix elements, which is roughly equivalent to an effective single-particle model space of $e_{\max} = 8$. This feature can also be clearly identified in the scaling example in Fig. 5.1, where we show the number of nonvanishing two-body matrix elements for different compression ratios R_C obtained in different model-space sizes e_{\max} . In general, the application of IT techniques is expected to be most efficient in large model spaces since high-lying excitations typically

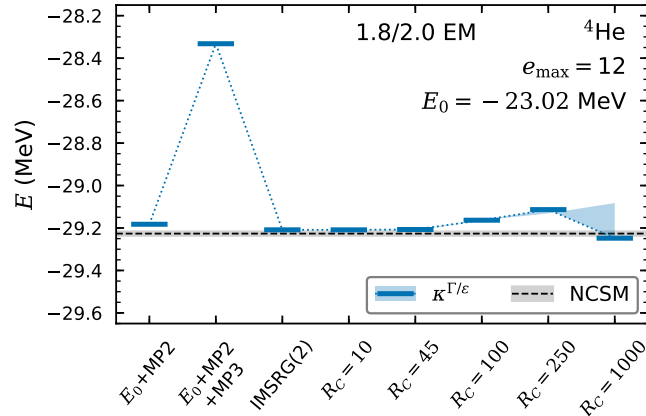


Figure 5.2: Ground-state energy of ${}^4\text{He}$ in the optimized $e^{\text{NAT}} = 14$ NAT basis truncated to $e_{\text{max}} = 12$ for different IT compression ratios R_C and the IT measure $\kappa^{\Gamma/\varepsilon}$ (see Sec. 5.2.2) compared to the full IMSRG(2) result and MBPT results up to second and third order, using the 1.8/2.0 EM interaction. The third-order energy correction of the IT-neglected entries (as introduced in Sec. 5.2.3) is given by the (cyan) colored band. The black dashed line indicates the extrapolated NCSM result (see text for details).

contribute less to ground-state observables and, thus, larger compression ratios can be obtained without introducing significant errors with respect to the exact result.

A first example for what can be expected from the IT-IMSRG is shown in Fig. 5.2. While the specific details are explained in the following, the general trends we observe from IT-IMSRG(2) calculations at different R_C are clear. We compare ground-state energies of ${}^4\text{He}$ for a chosen IT measure, which is detailed in Sec. 5.2.2, to the full IMSRG(2) result as well as to the second and third-order MBPT energy. The colored band perturbatively incorporates the IT-neglected matrix elements, as outlined in Sec. 5.2.3. We additionally show the extrapolated NCSM result for comparison, which is obtained by an extrapolation to $N_{\text{max}} \rightarrow \infty$ based on calculations up to $N_{\text{max}} = 14$ using the BIGSTICK code [283].

5.2.1 Interaction blocks

Before introducing the individual IT measures and investigating them in detail, we perform a more careful analysis of how sensitive the IT-IMSRG(2) solution is to truncations in the different two-body interaction blocks. In all following applications, we use the IMSRG(2) solver by Stroberg [247] as in the previous chapter. We note that the IT-IMSRG(2) implementation used in this thesis does not profit from the potential computational benefits of the IT framework by evaluating only important matrix-element index combinations in the flow. Instead, we use the standard solver and set unimportant matrix elements to zero. First computational studies for the advantages of an IT-IMSRG(2) solver using a sparse storage format are discussed in Sec. 5.3.3.

In Fig. 5.3, we consider the IT-IMSRG(2) solution of ${}^{40}\text{Ca}$ when different combinations of blocks are truncated (indicated by the different lines) using the IT measure κ^{Γ} based on the magnitude of the two-body matrix elements, which is introduced in Sec. 5.2.2. For each line, each point corresponds to a chosen κ_{min} , which gives a compression ratio R_C and produces an error to the exact IMSRG(2) solution. This error is shown in terms of the relative error on the correlation energy E_{corr} [see Eq. (4.30)] on the left y axis and in terms of the absolute

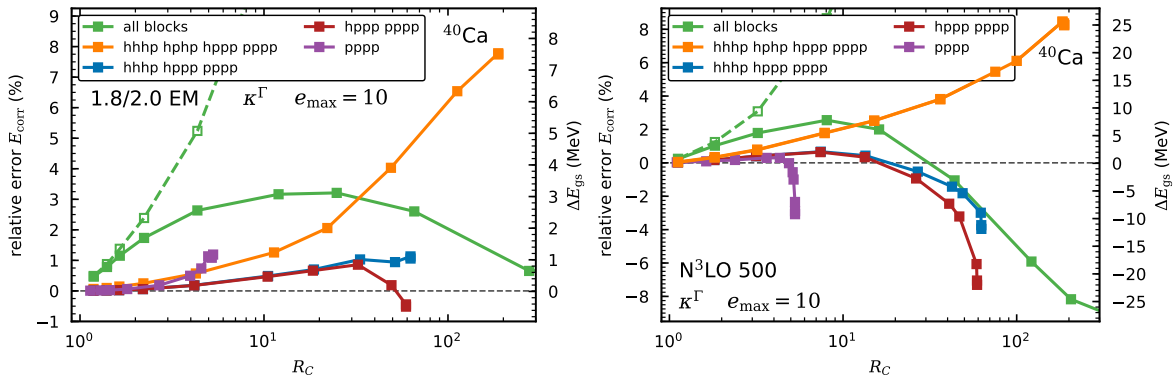


Figure 5.3: Relative error on the correlation energy of ^{40}Ca as a function of compression ratio R_C for IT-IMSRG(2) calculations truncating in various two-body interaction blocks. The green curve for truncating in all two-body interaction blocks additionally incorporates the second-order energy correction of the neglected matrix elements. For comparison, we also show the results without the energy correction by the green dashed line with open squares. In the left (right) panel the 1.8/2.0 EM ($N^3\text{LO 500}$) Hamiltonian is used. The left y axis indicates the relative error on the correlation energy E_{corr} , and the right y axis shows the absolute error on the ground-state energy. For comparison the correlation energy is given by $E_{\text{corr}} = -96.88$ MeV and $E_{\text{corr}} = -303.02$ MeV for the left and right panel, respectively. All calculations are performed in an $e_{\text{max}} = 10$ model space using the NAT basis and the IT measure κ^Γ (see Sec. 5.2.2 for details).

error on the ground-state energy on the right y axis. The two panels differ in the interaction used: the left panel features the 1.8/2.0 EM Hamiltonian and the right panel the $N^3\text{LO 500}$ Hamiltonian. In this figure, the truncated residual part of the two-body Hamiltonian is not treated approximately except when all blocks are truncated. In this case, the second-order energy correction based on the hphp block of the residual part is added to the IT-IMSRG(2) result.

In both panels, truncating all interaction blocks (the green curve) leads to the largest error at small and intermediate compression ratios. Fully truncating the entire two-body part of the Hamiltonian causes the IT-IMSRG(2) to produce a ground-state energy that is exactly $E_0 + E^{(2)}$ thanks to the perturbative treatment of the truncated hphp part of the Hamiltonian. In the left panel this is remarkably close to the full IMSRG(2) result, but in the right panel the relative error to the full IMSRG(2) correlation energy is nearly 10%. This behavior can be systematically improved by restricting importance truncation to selected blocks.

The first blocks we remove from the importance truncation are the hphp and hhhh blocks, which gives the orange curves in Fig. 5.3. We observed that truncating the hphp block leads to large errors at intermediate compression ratios, motivating its exclusion from the IT. The hphp block [and the hhhppp block in the IMSRG(3)] have previously been observed to be quite important for the IMSRG [31, 241], and this finding supports that intuition further. The hhhh block is the smallest block and, as a result, does not offer much room for compression, so we also leave it untruncated. We find that the removal of these two blocks from the IT reduces the error at intermediate compressions substantially. Still, the error grows large as we approach the maximum compression ratio.

Additionally removing the hphp block from the truncation yields the blue curve, which offers a substantial reduction in the error relative to the orange curve at all compression ratios. As a reminder, the hphp block contributes at third order in MBPT (see Sec. 5.1.1), and in

MBPT studies it was found that the third-order particle-hole diagram, which is sensitive to this block, dominates the third-order contribution [18]. In the IMSRG, it has been observed that the high-order generalizations of the particle-hole diagram, the ph-ring diagrams, which are resummed nonperturbatively in the IMSRG(2), are particularly important [31, 32]. The substantial reduction in the IT-induced error we find when the hphp block is excluded is consistent with these observations. Further restricting the IT to only the hppp and pppp blocks (leaving the small hhhp block untruncated) gives the red line, and truncating only in the pppp block gives the purple line. In our studies, we found that restricting the IT to just the hppp and pppp blocks (i.e., the red curves in Fig. 5.3) allowed us to achieve large compression ratios while introducing relatively small errors for appropriate IT thresholds. Hence, in the following we concentrate on this approach.

5.2.2 Definition of importance measures

In the following, various importance measures for the flowing two-body part of the Hamiltonian in the IMSRG(2) approach are investigated. We note that in principle similar studies can be performed for the one-body part as well. However, since the computational gain is negligible, we will focus on the two-body part here. All measures are constructed once at the beginning of the flow based on the initial Hamiltonian at $s = 0$. Important combinations of single-particle indices p, q, r , and s of Γ_{pqrs} are identified by the IT measure and kept over the course of the flow, while matrix elements with unimportant index combinations are set to zero throughout the flow. Note that this also includes matrix elements which are potentially induced during the flow by the IMSRG. An alternative approach would be to dynamically update the measure during the IMSRG evolution, which could possibly better account for the changing structure of the evolving Hamiltonian. We leave the exploration of such strategies to future studies and focus instead on different measure choices and their relative performance for different systems.

Matrix-element-based measures

The simplest way of estimating the relevance of a given two-body matrix element is its initial magnitude, giving rise to the first importance measure,

$$\kappa_{pqrs}^{\Gamma}(\Gamma) = \left| \Gamma_{pqrs} \right|. \quad (5.7)$$

This measure encodes the expectation that the largest matrix elements are expected to be most important for the evolution of the Hamiltonian and the smallest ones will be relatively unimportant. However, this naive estimate does not take into account specific information about the target nucleus (beyond the information from the single-particle basis transformation when working with matrix elements in an HF or NAT basis).

A more refined measure can be obtained by taking inspiration from MBPT. In MBPT, the matrix elements that are summed over are accompanied by energy denominators, and our measure based on this idea is

$$\kappa_{pqrs}^{\Gamma/\varepsilon}(\Gamma) = \left| \Gamma_{pqrs} / \varepsilon_{\text{sum}} \right|. \quad (5.8)$$

The additional appearance of an energy denominator ε_{sum} accounts for the lower importance of highly excited configurations associated with large single-particle energies. The measure

$\kappa^{\Gamma/\varepsilon}$ is very closely related to the first-order estimate of the MBPT wave-function expansion and similar in spirit to previously used measures in importance-truncated NCSM [21], BMBPT [169], or Gorkov SCGF [276] frameworks.

The energy denominator for the hhpp block is simply given by ε_{ij}^{ab} , defined in Eq. (3.70) and used in the second-order MBPT energy correction in Eq. (3.72). However, in the IMSRG other interaction blocks than only the hhpp block are present and the energy denominator of the importance measure has to be generalized accordingly. This is done by defining

$$\varepsilon_{\text{sum}} = \begin{cases} 4\varepsilon_{\text{F}} - \varepsilon_a - \varepsilon_b - \varepsilon_c - \varepsilon_d & \text{for pppp,} \\ 2\varepsilon_{\text{F}} + \varepsilon_i - \varepsilon_a - \varepsilon_b - \varepsilon_c & \text{for hppp,} \end{cases} \quad (5.9)$$

where ε_{F} is the Fermi energy, i.e., the energy of the energetically highest-lying hole orbital and the indices a , b , c , and d (i) denote particle (hole) states. Generally, the Fermi energy ε_{F} is different for protons and neutrons in proton-rich or neutron-rich systems. While in this thesis, we show results for the simple definition of an isospin-independent Fermi energy given above, we have explored using isospin-differentiated Fermi energies and found that the different approaches give quantitatively very similar results in a broad range of systems. Equation (5.9) can be trivially extended to include the hphp, hhhp, and hhhh blocks, but we focus our discussion in this thesis on truncations of the pppp and hppp blocks, as explained in Sec. 5.2.1.

Occupation-based measures

In the natural orbital basis, additional information about the system is available in the form of the noninteger occupation numbers $n^{\text{NAT}} \in [0, 1]$ of the individual orbitals (see Sec. 4.1.3). We can use this information to construct alternative truncation measures that only work when such noninteger occupation numbers, resulting from the diagonalization of an improved one-body density matrix beyond the mean-field level, are available. The simplest choice is the use of products of occupation numbers, as used in CC applications to improve convergence in the triples amplitudes truncation [74],

$$\kappa_{pqrs}^n = \prod_{i \in \{p, q, r, s\}} \begin{cases} |n_i^{\text{NAT}}| & \text{if } i \text{ is a particle state,} \\ |1 - n_i^{\text{NAT}}| & \text{if } i \text{ is a hole state,} \end{cases} \quad (5.10)$$

where the product is given by the natural orbital occupation numbers n^{NAT} for the p , q , r , and s orbitals, with n_i^{NAT} for particle states and $\bar{n}_i^{\text{NAT}} = (1 - n_i^{\text{NAT}})$ for hole states. This measure gives the greatest importance to matrix elements where bra and ket indices lie close to the Fermi surface. This reflects the intuition that for low-resolution Hamiltonians the correlation expansion is dominated by low-energy excitations around the Fermi surface. Again, this measure is rather simplistic since no explicit information from the two-body matrix elements enters the IT selection.

A further refinement is obtained by accounting for the magnitude of the associated two-

body matrix element as is done in Eqs. (5.7) and (5.8) via

$$\kappa_{pqrs}^{\Gamma n}(\Gamma) = |\Gamma_{pqrs}| \times \prod_{i \in \{p,q,r,s\}} \begin{cases} |n_i^{\text{NAT}}| & \text{if } i \text{ is a particle state,} \\ |1 - n_i^{\text{NAT}}| & \text{if } i \text{ is a hole state.} \end{cases} \quad (5.11)$$

In both cases, the natural orbital occupation numbers contain additional information about the shell structure, such that contributions from, e.g., high orbital angular momentum (large l) or high radial excitations (large n) will typically be suppressed.

Derivative-based measures

While the matrix-element- and occupation-based measures above are inspired by other many-body frameworks, the notion of derivative-based measures is specific to the IMSRG approach. By defining the IT measure as

$$\kappa_{pqrs}^{\partial\Gamma}(\Gamma) = \left| \left(\frac{dH}{ds} \right)_{pqrs}^{(2)} \right| = \left| [\eta, H]_{pqrs}^{(2)} \right|, \quad (5.12)$$

the importance of two-body matrix elements is based on the magnitude of their expected change. Matrix elements with a large derivative are expected to change significantly over the course of the evolution, and the initial value will be a poor approximation. Note, however, that this measure does not directly account for the size of the matrix element but only its expected dynamics independent of the starting value. It is also worth mentioning that the construction of this measure is more expensive than the previously discussed measures, as the evaluation of the required commutator scales like $\mathcal{O}(N^6)$ in the size of the single-particle basis N .

5.2.3 Perturbative treatment of truncated Hamiltonian

In order to perturbatively consider the IT-neglected contributions, we apply a modified version of the MP3 energy correction with all diagrams sensitive to the pppp and hppp truncated interaction blocks. We consider the pp-ladder diagram $E_{\text{pp}}^{(3)}$ shown in Eq. (5.2a), which is sensitive to the pppp matrix elements, as well as the two noncanonical diagrams that are sensitive to the hppp matrix elements [see Eq. (3.75)], when working in a natural orbital basis. Combining the IT matrix elements of the two relevant interaction blocks with the initial hppp elements results in an adapted third-order IT energy correction of the neglected contributions

$$E_{\text{IT}}^{(3)} = \tilde{E}_{\text{pp}}^{(3)} + \tilde{E}_{\text{hppp}}^{(3)}, \quad (5.13)$$

with the two parts given by

$$\tilde{E}_{\text{pp}}^{(3)} = \frac{1}{8} \sum_{abcdij} \frac{\Gamma_{ijab} \Gamma_{abcd}^{\text{res.}} \Gamma_{cdij}}{\varepsilon_{ij}^{ab} \varepsilon_{ij}^{cd}}, \quad (5.14a)$$

$$\tilde{E}_{\text{hppp}}^{(3)} = \frac{1}{2} \sum_{abcij} \frac{\Gamma_{ijab} \Gamma_{abcj}^{\text{res.}} f_{ci}}{\varepsilon_{ij}^{ab} \varepsilon_i^c} + \frac{1}{2} \sum_{abcij} \frac{f_{ai} \Gamma_{ajcb}^{\text{res.}} \Gamma_{cbij}}{\varepsilon_i^a \varepsilon_{ij}^{bc}}, \quad (5.14b)$$

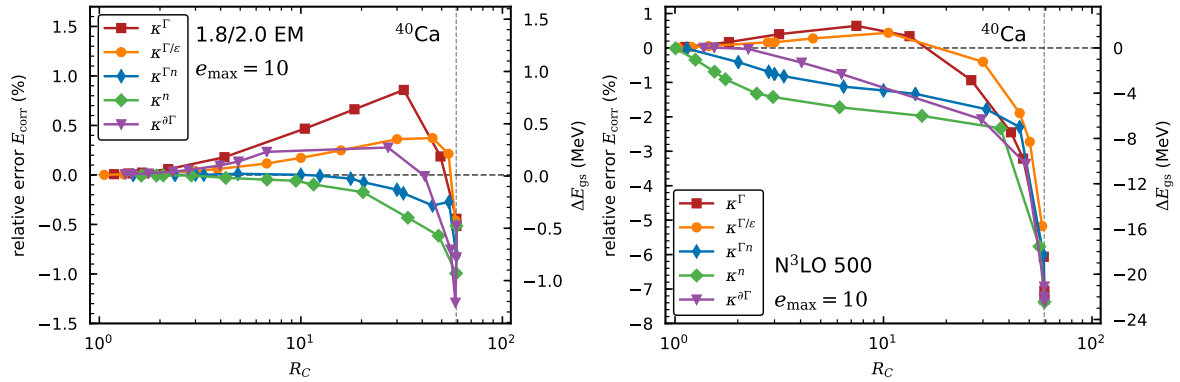


Figure 5.4: Relative error on the correlation energy of ^{40}Ca as a function of compression ratio R_C for IT-IMSRG(2) calculations using the five IT measures defined in Eqs. (5.7)-(5.12). In the left (right) panel the 1.8/2.0 EM ($\text{N}^3\text{LO 500}$) Hamiltonian is used. The left y axis indicates the relative error on the correlation energy E_{corr} , and the right y axis shows the absolute error on the ground-state energy. All calculations are performed in an $e_{\text{max}} = 10$ model space using the NAT basis and the dashed vertical line indicates the maximum compression ratio for truncating in the hppp and pppp blocks.

where the IT-neglected matrix elements are given by Γ^{res} , as defined in Eq. (5.5) and the matrix elements Γ and f without superscript correspond to the initial two- and one-body contributions of the normal-ordered Hamiltonian in Eq. (3.19).

5.3 Medium-mass applications

The five different IT measures κ introduced in Sec. 5.2.2 are studied for ^{40}Ca using two different Hamiltonians in Fig. 5.4. For both Hamiltonians one finds that at the maximum compression accessible for the chosen interaction blocks (indicated by the dashed vertical line) all measures give the same error to the exact IMSRG(2) result, which reflects that at this compression κ_{min} for each measure has been chosen such that the hppp and pppp blocks are completely truncated. At intermediate compressions, however, the various measures give different results. Of particular interest is the growth in the error to the exact IMSRG(2) result when going from small to intermediate compressions. Concentrating first on the matrix-element-based measures (red squares and orange circles), we find that they follow the same qualitative trend. The more refined $\kappa^{\Gamma/\epsilon}$ gives smaller errors than κ^{Γ} at small and intermediate compressions, especially for the 1.8/2.0 Hamiltonian. The fact that $\kappa^{\Gamma/\epsilon}$ works so well for the 1.8/2.0 Hamiltonian reflects the perturbativeness of the Hamiltonian, but the MBPT-inspired refinement over κ^{Γ} seems to be effective for harder interactions as well.

Turning to the occupation-based measures (green diamonds and blue thin diamonds), we find that they produce smaller errors than $\kappa^{\Gamma/\epsilon}$ and κ^{Γ} for the 1.8/2.0 EM Hamiltonian and larger errors for the $\text{N}^3\text{LO 500}$ Hamiltonian. This can also be understood due to the relative softness of the two Hamiltonians, as the natural orbitals are constructed using second-order MBPT. It is likely that for harder Hamiltonians this construction does not approximate the one-body density matrix well enough for the IT measure based on its occupation numbers to be effective. We also find that refining κ^n by including the matrix element size to give $\kappa^{\Gamma n}$ produces smaller errors at all compression ratios. We find that the derivative-based measure $\kappa^{\partial\Gamma}$ (purple triangles) performs similarly to the other measures investigated, but

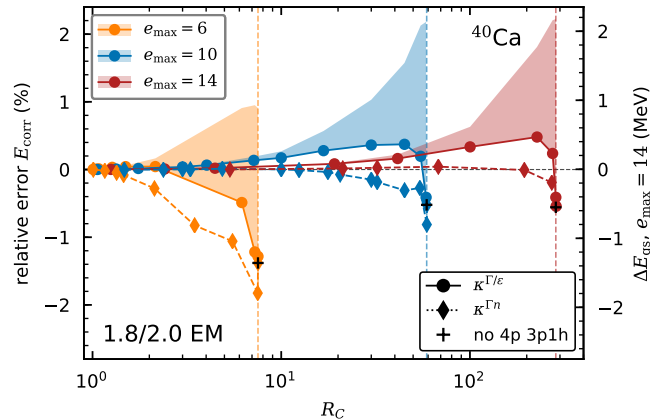


Figure 5.5: Relative error on the correlation energy of ^{40}Ca as a function of the compression ratio R_C for the model-space sizes $e_{\max} = 6, 10,$ and 14 in orange, blue, and red, respectively, using the NAT basis and the 1.8/2.0 EM Hamiltonian. We show results for the IT measures $\kappa^{\Gamma/\varepsilon}$ (circles) and $\kappa^{\Gamma n}$ (diamonds). The right y axis indicates the absolute energy difference between the $e_{\max} = 14$ IT-IMSRG(2) results and the exact IMSRG(2) result. The MP3 energy correction for the $\kappa^{\Gamma/\varepsilon}$ IT-neglected contributions is indicated by the corresponding band for each model-space truncation and the vertical dashed lines correspond to the maximum R_C for the given model spaces.

costs substantially more to construct.

As outlined in Sec. 5.1, we utilize the underlying symmetry of the Hamiltonian to store the two-body matrix elements in a $(J\text{IT}_z)$ block structure and apply the IT in the individual symmetry blocks. Although the resulting energy can be quite different depending on the chosen IT measure, we observe nearly identical suppression of the number of matrix elements in the $(J\text{IT}_z)$ blocks for the three IT measures κ^{Γ} , $\kappa^{\Gamma/\varepsilon}$, and $\kappa^{\Gamma n}$ at comparable compression ratios. In the rest of this thesis, we focus our explorations mostly on the two best performing measures, $\kappa^{\Gamma/\varepsilon}$ and $\kappa^{\Gamma n}$ [see Eqs. (5.8) and (5.11)].

In Fig. 5.5, we study the effect of going to different model-space sizes on the achievable compression ratios and their associated errors on the correlation and ground-state energy of ^{40}Ca with the 1.8/2.0 EM Hamiltonian. Going from $e_{\max} = 10$ to $e_{\max} = 14$ increases the number of two-body matrix elements by a factor of roughly 15, which allows for higher maximum compression. However, at the same compression ratio, the $e_{\max} = 14$ IT-IMSRG(2) calculations have much smaller errors to the exact result, because many of the matrix elements that are added when going from $e_{\max} = 10$ to $e_{\max} = 14$ can be truncated. This also means that the IT-IMSRG(2) is less effective in small model spaces (such as $e_{\max} = 6$ in Fig. 5.5) because in these model spaces the maximum compression is lower and truncating a lot of matrix elements quickly leads to larger errors.

In Fig. 5.5, we include the perturbative treatment of the truncated part of the Hamiltonian introduced in Sec. 5.2.3 for $\kappa^{\Gamma/\varepsilon}$. The points on the lines are the result of IT-IMSRG(2) calculations without any extra treatment of the truncated part. The MP3 correction due to the IT-neglected matrix elements is included as a band on top of this IT-IMSRG(2) result. We understand this correction to be an indication of the magnitude of the missing third-order and higher-order contributions that are discarded by the truncation. This can be used as an estimate of the IT uncertainty relative to the full IMSRG(2) for a given truncation threshold, which is important in cases where exact results are not readily available for comparison. We see that in this case the uncertainty indicated by the MP3 correction is reasonable up to

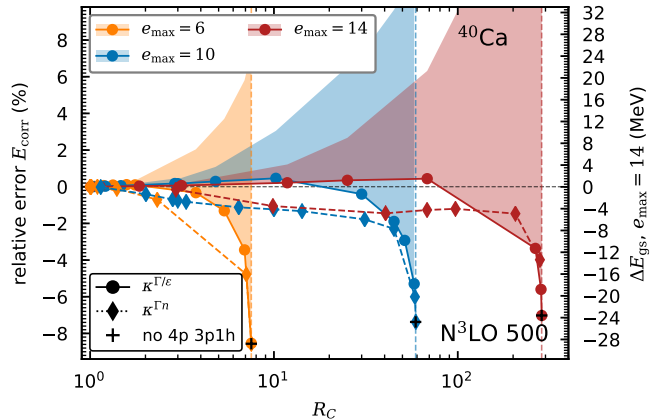


Figure 5.6: Same as Fig. 5.5 but for the $N^3\text{LO } 500$ Hamiltonian.

relatively high compression ratios. As an example, for an $e_{\text{max}} = 14$ IT-IMSRG(2) calculation, we can achieve a compression ratio of 100 while keeping the IT uncertainty below 0.5% on the correlation energy.

5.3.1 Interaction sensitivity

We now turn our attention to how the observed trends are affected by the choice of Hamiltonian. In Fig. 5.6, we again show the IT-IMSRG(2) errors in several model-space sizes for ^{40}Ca , this time using the $N^3\text{LO } 500$ Hamiltonian. We see that, compared to the softer 1.8/2.0 EM Hamiltonian, the relative error on the correlation energy is similar, which is due to the large correlation energy for the $N^3\text{LO } 500$ Hamiltonian. Accordingly, the absolute errors in the energy are larger than in Fig. 5.5. We see that the IT-IMSRG(2) results based on $\kappa^{\Gamma/\varepsilon}$ are better than using $\kappa^{\Gamma n}$, and the uncorrected results for $\kappa^{\Gamma/\varepsilon}$ lie very close to the exact IMSRG(2) results up to compressions near 100 for $e_{\text{max}} = 14$. However, the MP3 correction due to the IT-neglected matrix elements is much larger for the harder $N^3\text{LO } 500$ Hamiltonian, suggesting a sizable uncertainty in the IT-IMSRG(2) results even at relatively small compression ratios.

In Fig. 5.7, we compare ground-state energies for ^{40}Ca obtained via various different many-body approaches for the $N^3\text{LO } 500$ and 1.8/2.0 EM Hamiltonians in an $e_{\text{max}} = 10$ model space. We compare IT-IMSRG(2) results at different compression ratios against untruncated IMSRG(2) results and provide results from second- and third-order MBPT for comparison. Looking first at the results for the 1.8/2.0 Hamiltonian, we see that second- and third-order MBPT energies differ from the IMSRG(2) result by less than 5 MeV. Overall, the IT-IMSRG(2) results also agree well with the IMSRG(2) results. In particular, for intermediate compression ratios ($R_C = 10$, for instance) the estimated uncertainty from the treatment of IT-neglected matrix elements is very small. For the $N^3\text{LO } 500$ Hamiltonian, this picture changes substantially. The second-order MBPT, third-order MBPT, and IMSRG(2) results span an energy range of about 65 MeV. Here the IT-IMSRG(2) performs quite well, giving errors to the IMSRG(2) of up to roughly 7 MeV for the largest compression ratio considered in Fig. 5.7. The estimated uncertainty, however, is much larger than the actually observed errors. It seems that the correction we obtain from the IT-neglected matrix elements for this interaction overestimates the size of the missing physics, which we understand to

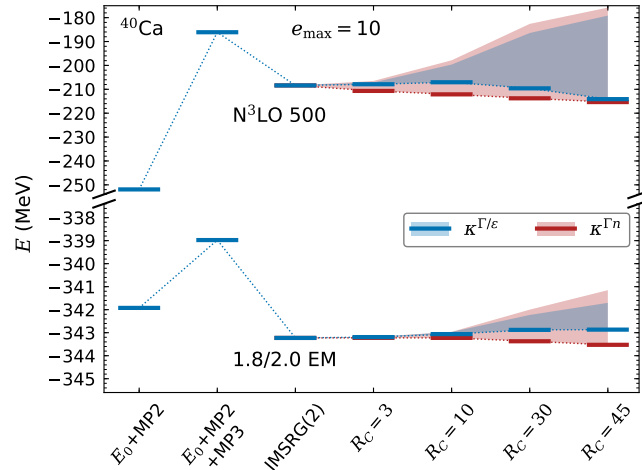


Figure 5.7: Ground-state energy of ^{40}Ca for the IT measures $\kappa^{\Gamma/\varepsilon}$ (blue) and $\kappa^{\Gamma n}$ (red) for different compression ratios R_C compared to the full IMSRG(2) result and calculations from second- and third-order MBPT. We show results for the $N^3\text{LO } 500$ interaction (top) and the 1.8/2.0 EM interaction (bottom) for a model-space size of $e_{\max} = 10$ in the NAT basis. The third-order energy correction of the IT-neglected contributions for both measures is given by the correspondingly colored band.

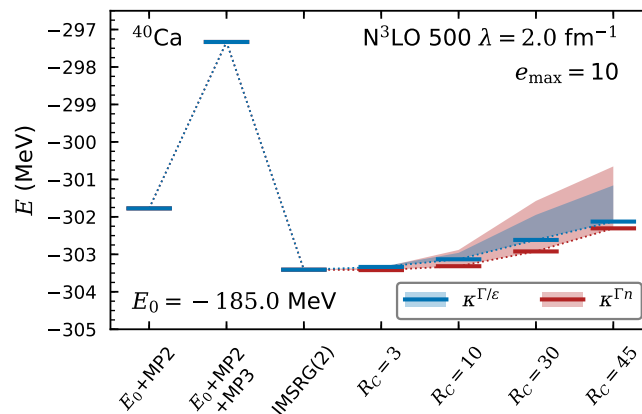


Figure 5.8: Same as Fig. 5.7 but for the consistently SRG-evolved $N^3\text{LO } 500$ interaction to $\lambda = 2.0 \text{ fm}^{-1}$.

be an artifact of the perturbative approach we take in conjunction with a nonperturbative Hamiltonian.

To confirm this, we consider the same system using the $N^3\text{LO } 500$ Hamiltonian consistently SRG evolved to a resolution scale of $\lambda = 2.0 \text{ fm}^{-1}$ in Fig. 5.8. This SRG-evolved potential is very soft, as also suggested by the small differences between second-order MBPT, third-order MBPT, and IMSRG(2) results. Here the difference between the IT-IMSRG(2) and the IMSRG(2) results is about 1.5 MeV for $R_C = 45$, and the estimated uncertainty is also of approximately the same size as the error. This suggests that our uncertainty estimate is quite reasonable for soft Hamiltonians and the IT results for an intermediate compression ratio of about $R_C = 10$ lie very close to the full IMSRG(2) result for such interactions.

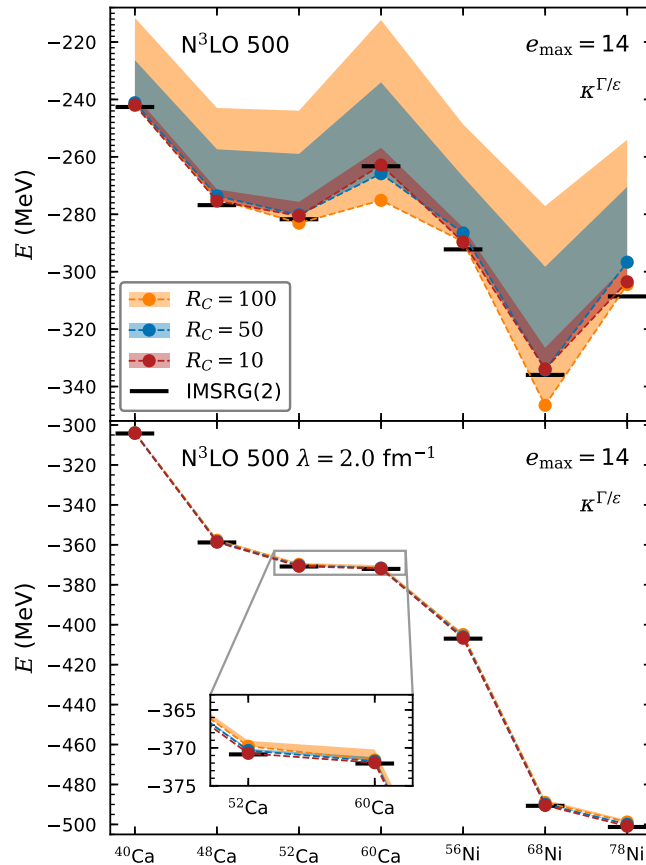


Figure 5.9: Ground-state energies for selected calcium and nickel isotopes in the IT-IMSRG with compression ratios $R_C = 10, 50,$ and 100 for the measure $\kappa^{\Gamma/\varepsilon}$. Results are shown for the NAT basis and the unevolved (top) and SRG-evolved to $\lambda = 2.0 \text{ fm}^{-1}$ (bottom) $\text{N}^3\text{LO } 500$ interaction in $e_{\text{max}} = 14$.

5.3.2 Mass number sensitivity

After our investigation of the interaction blocks and IT measures for ^{40}Ca as a reasonable test case, we extend our studies to closed-shell nuclei ranging from ^{40}Ca up to ^{78}Ni . In the top panel of Fig. 5.9, we show ground-state energies for different compression ratios in the IT-IMSRG(2) compared to the full IMSRG(2) result when using the $\text{N}^3\text{LO } 500$ Hamiltonian. At intermediate compressions (here $R_C = 10$), we find that the IT-IMSRG(2) results match the exact IMSRG(2) results within a few MeV. The largest deviation is found for ^{78}Ni with an error of 5 MeV. The uncertainty indicated by our third-order treatment of truncated matrix elements is also of about the same size. Going to larger compressions, we find that at $R_C = 50$ the IT-IMSRG(2) results still lie remarkably close to the exact IMSRG(2) results. The 12 MeV error for ^{78}Ni is the exception here, and most errors are still below 5 MeV. For $R_C = 100$, the deviation to exact IMSRG(2) results tends to be larger. However, for both $R_C = 50$ and $R_C = 100$ the indicated uncertainty is much larger than the observed error, growing to beyond 50 MeV in some systems. We emphasize that for these results $R_C = 50$ and $R_C = 100$ are being used to explore the truncation error for heavily truncated calculations and would not be considered adequate for practical nuclear structure calculations.

We perform the same study across a variety of systems in the lower panel of Fig. 5.9, but this time using the SRG-evolved $\text{N}^3\text{LO } 500 \lambda = 2.0 \text{ fm}^{-1}$ Hamiltonian, which in the last

section showed substantially smaller errors in IT-IMSRG(2) calculations than the unevolved $N^3\text{LO}$ 500 Hamiltonian. For this Hamiltonian, we see that even with $R_C = 100$ the error to the exact IMSRG(2) result is very small in all systems (with a maximum of 2.5 MeV for ^{78}Ni). Moreover, the uncertainty indicated by the third-order treatment of truncated matrix elements is also quite small, only growing up to 1.4 MeV for ^{68}Ni with $R_C = 100$. These results show the promising performance of the IT-IMSRG over a wide range of mass numbers and up to large compression ratios when using softer or SRG-evolved interactions. While Fig. 5.9 only shows results obtained using the $\kappa^{\Gamma/\varepsilon}$ measure, the results are very similar for $\kappa^{\Gamma n}$.

5.3.3 First computational investigations

For all results shown in this chapter, we applied the IT-IMSRG formalism by taking the IMSRG solver by Stroberg [247] and explicitly setting truncated matrix elements to zero. However, an implementation that fully takes advantage of the new structure of importance-truncated operators will be necessary to take advantage of the storage and computational benefits of the IT-IMSRG. We performed an initial exploration of this by adapting the solver mentioned above to use a modified storage format.

An optimized IT-IMSRG solver must not store the zeros associated with truncated matrix elements, and it must be able to do so flexibly as different IT measures will truncate different matrix elements. This naturally suggests the use of sparse matrices and sparse linear algebra operations (as is available in, e.g., the C++ ARMADILLO library [284, 285]). We were able to adapt the storage format of our IT-IMSRG(2) solver to use sparse matrices, and the computational operations were adapted to use sparse linear algebra routines. We observed the expected reduction in memory requirements in our calculations, but our initial implementation was unable to substantially speed up the IT-IMSRG(2) solution over the IMSRG(2) solution. Profiling and detailed benchmarks led us to suspect that this lack of performance is due to suboptimal handling of data around the sparse matrix format (e.g., random matrix element access in sparse matrices is slow, unlike with dense matrices). These computational slow downs affected our implementation most heavily in the particle-hole part of the two-body commutator (see, e.g., Ref. [31]), where the Pandya transformation is naturally implemented using unordered accesses in the input and output matrices. However, given the speed-ups observed in other parts of the solver when using sparse matrices (e.g., the particle-particle and hole-hole parts of the two-body commutator), we fully expect an optimized IT-IMSRG(2) solver to also reduce the computational cost of IMSRG(2) calculations in addition to the memory savings.

6

Normal Ordering in the Jacobi Basis

Three-nucleon interactions play an important role in nuclear theory calculations, not only to obtain reasonable saturation properties in nuclear matter [54], but also for realistic predictions of finite nuclei with good agreement to experiment [22, 52, 66–68]. However, the memory requirements for storing three-body operators and the computational demands in large model spaces significantly complicate their use in *ab initio* many-body methods and necessitate approximate treatments. Normal-ordering techniques to approximate 3N interactions by density-dependent 2N interactions have proven to be a powerful and efficient tool to include the effects of the three-body force. This is accomplished by summing one particle over occupied states in the reference state. In particular, the NO2B approximation, which discards residual 3N contributions is very successful for calculations of nuclear matter [211, 259, 286, 287] and studies of finite nuclei [29, 190, 213, 214].

Most many-body methods, e.g., the IMSRG, CC theory, or MBPT, rely on many-body operator inputs in a single-particle basis. Usually, the 3N matrix elements calculated in a plane-wave Jacobi basis [135, 286] are transformed to a relative HO basis, antisymmetrized in this basis, and then transformed to a single-particle HO basis using a three-body Talmi-Moshinsky transformation [288–291]. Note that the antisymmetrization step can as well be carried out already in the Jacobi basis. Only after these steps, the normal ordering of the three-body operator with respect to a given reference state, e.g., an HO, HF, or NAT state, is performed in the single-particle basis.

Due to the tremendous computational requirements for incorporating 3N interactions, in practice, approximate treatments and truncations have to be employed. One possible way is to introduce a truncation in the space of three-body single-particle orbitals $e_1 + e_2 + e_3 \leq E_{3\max}$, as discussed in Sec. 4.2.2. Figure 6.1 shows the required memory for storing three-body operators in different bases as a function of $E_{3\max}$. Clearly, storing matrix elements for all angular-momentum quantum numbers of the single-particle basis in the m -scheme format (blue points in Fig. 6.1) does not present a feasible choice. Exploiting symmetries and working in an angular-momentum and isospin coupled JT basis [see Eq. (3.144)] is beneficial (red triangles in Fig. 6.1) and has become the standard approach for storing three-body matrix elements in a single-particle basis. Nevertheless, memory requirements still grow rapidly as a function of $E_{3\max}$ and exceed current memory limitations for high $E_{3\max}$. Typically used values of $E_{3\max} = 16$ already require ≈ 20 GB of memory. Especially for heavy nuclei, where large model spaces are required to obtain converged results, the storage cost can easily exceed 100 GB for large $E_{3\max}$. Just recently, the range of accessible $E_{3\max}$ was significantly increased

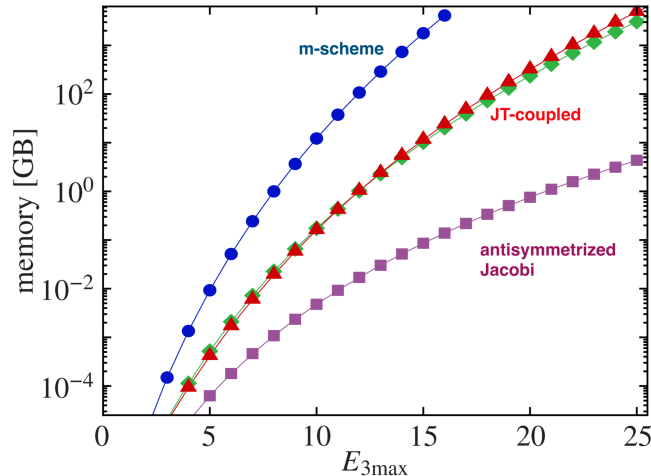


Figure 6.1: Memory requirements for storing 3N matrix elements in different computational bases as a function of $E_{3\max}$, assuming single-precision floating-point values. We compare three-body operators stored in the m -scheme (blue), JT -coupled scheme (red), and antisymmetrized Jacobi scheme (purple). Figure taken from Ref. [291].

to values of $E_{3\max} = 28$ at the NO2B level in Ref. [50]. This allowed for converged calculations in nuclei as heavy as ^{132}Sn and enabled first exploratory *ab initio* studies for even heavier systems, such as ^{208}Pb [51]. Even though performing the normal ordering in the single-particle basis is computationally cheap, the major drawback of high memory consumption for large $E_{3\max}$ still hinders the full inclusion of 3N interactions without an active $E_{3\max}$ truncation. Incorporating these contributions provides an important step towards converged calculations of heavier nuclei, where they become particularly important.

In this chapter, following Ref. [95], we develop an alternative way of obtaining the normal-ordered two-body contribution of the 3N interaction by performing the normal ordering directly in the plane-wave Jacobi basis. This framework has the substantial benefit that we do not rely on a single-particle representation of the 3N force and consequently allows for calculations without an $E_{3\max}$ truncation. The difference in the required memory can be clearly seen in Fig. 6.1 by comparing the purple squares and red triangles for the antisymmetrized Jacobi basis and JT -coupled basis, respectively. Normal-ordering in the Jacobi basis introduces a cm dependence for the effective two-body interaction and new quantum numbers arise to describe this additional dependence. The only possibly remaining effect of the $E_{3\max}$ truncation in the new framework is given by the dependence on the reference state, which is calculated in the single-particle basis. In the following, we investigate the performance of the novel framework in detail by benchmarking calculations against the standard single-particle approach and investigating the convergence behavior with respect to truncating the new quantum numbers.

This chapter is structured as follows. In Sec. 6.1, we outline how 3N interactions are normal ordered in the plane-wave Jacobi basis, and how the additional cm dependence is considered by the new quantum numbers. Afterwards, the effective two-body interaction is transformed to the Jacobi HO and eventually to the single-particle basis, yielding a suitable input for most *ab initio* many-body calculations. First benchmark calculations of ground-state energies using the IMSRG are performed in Sec. 6.2 for light and medium-mass nuclei and compared to the single-particle normal ordering, before targeting heavier systems in Sec. 6.3.

6.1 Normal ordering in plane-wave Jacobi basis

The computationally most time-consuming operation in the normal-ordering procedure outlined in Sec. 3.1 is the calculation of the contributions from 3N interactions to the two-body operator Γ [see Eq. (3.20c)]

$$\Gamma_{ijkl}^{3N} \equiv \sum_m n_m \langle ij m | V_{3N}^{\text{as}} | k l m \rangle, \quad (6.1)$$

where we use single-particle labels i, j, \dots , the 3N superscript indicates the three-body contribution to the normal-ordered two-body operator $\langle ij | \Gamma^{3N} | kl \rangle = \Gamma_{ijkl}^{3N}$, $\langle ij m | V_{3N}^{\text{as}} | k l m \rangle$ are the antisymmetrized three-body matrix elements, and n_m is the occupation number of the single-particle state m in the reference state. We emphasize that the reference state is given by a single Slater determinant, as shown in Eq. (3.4). This formally requires the representation of the 3N force in a single-particle basis, ideally sufficiently large to converge many-body calculations. All further 3N contributions that enter the normal-ordered Hamiltonian in Eqs. (3.20b) and (3.20a) can be easily computed in a computationally inexpensive way once Γ^{3N} is calculated. Successively performing the additional contractions over one and two densities yields the normal-ordered one- and zero-body part, respectively.

We now turn to the novel Jacobi-based framework [95] that circumvents the need to represent 3N interactions in a single-particle basis at any point of the normal-ordering procedure. To do so we perform the normal ordering in a Jacobi momentum representation and only transform to a single-particle HO basis at the end in Secs. 6.1.1 and 6.1.2. As a first step, we formulate the three-body contribution to the normal-ordered two-body interaction in a single-particle momentum-space basis, before using the benefits of representing the 3N interaction in the Jacobi basis. In the following, we use single-particle states defined by

$$|\tilde{\mathbf{k}}_i\rangle = |\mathbf{k}_i m_{s_i} m_{t_i}\rangle, \quad (6.2)$$

where \mathbf{k}_i denotes the momentum of particle i , and m_{s_i} and m_{t_i} are the spin and isospin projection quantum numbers, respectively. Hence, we can write the normal-ordered expression Γ^{3N} as

$$\Gamma_{\tilde{\mathbf{k}}'_1 \tilde{\mathbf{k}}'_2 \tilde{\mathbf{k}}_1 \tilde{\mathbf{k}}_2}^{3N} = \int \frac{d\mathbf{k}_3 d\mathbf{k}'_3}{(2\pi)^6} \sum_{\substack{m_{s_3} m'_{s_3} \\ m_{t_3} m'_{t_3}}} \gamma(\tilde{\mathbf{k}}_3, \tilde{\mathbf{k}}'_3) \langle \tilde{\mathbf{k}}'_1 \tilde{\mathbf{k}}'_2 \tilde{\mathbf{k}}'_3 | V_{3N}^{\text{as}} | \tilde{\mathbf{k}}_1 \tilde{\mathbf{k}}_2 \tilde{\mathbf{k}}_3 \rangle, \quad (6.3)$$

with the density matrix $\gamma(\tilde{\mathbf{k}}_3, \tilde{\mathbf{k}}'_3)$ defined as

$$\gamma(\tilde{\mathbf{k}}_3, \tilde{\mathbf{k}}'_3) = \delta_{m_{t_3} m'_{t_3}} \sum_{nl_3 j_3 m_{j_3}} n_3 \langle \tilde{\mathbf{k}}'_3 | \Phi_{nl_3 j_3 m_{j_3} m_{t_3}} \rangle \langle \Phi_{nl_3 j_3 m_{j_3} m_{t_3}} | \tilde{\mathbf{k}}_3 \rangle, \quad (6.4)$$

where we specified the single-particle states in the reference state $|\Phi\rangle$ by $|\Phi_3\rangle = |\Phi_{nl_3 j_3 m_{j_3} m_{t_3}}\rangle$ with occupation numbers n_3 . The occupation number n_3 should not be confused with the radial quantum number n of the single-particle state $|\Phi_3\rangle$. Note that the density matrix is diagonal in the isospin projection m_t but not in the spin projection quantum number m_s . Projecting the reference state onto the single-particle momentum-space basis defined in

Eq. (6.2) leads to

$$\langle \mathbf{k}_i m_{s_i} m_{t_i} | \Phi_{nl_j i m_{j_i} m_{t_i}} \rangle = \sum_{m_i} \mathcal{C}_{l_i m_i \frac{1}{2} m_{s_i}}^{j_i m_{j_i}} Y_{l_i m_i}(\hat{\mathbf{k}}) \Phi_{nl_j i m_{j_i} m_{t_i}}(k), \quad (6.5)$$

where $Y_{lm_i}(\hat{\mathbf{k}})$ is the spherical harmonic of degree l and order m_l with the angular orientation $\hat{\mathbf{k}}$ of \mathbf{k} and we introduced the shorthand notation of the Clebsch-Gordan coefficients

$$\mathcal{C}_{l_i m_i \frac{1}{2} m_{s_i}}^{j_i m_{j_i}} = \left(\begin{array}{cc|c} l_i & \frac{1}{2} & j_i \\ m_i & m_{s_i} & m_{j_i} \end{array} \right), \quad (6.6)$$

for the sake of simpler presentation in the following.

For practical calculations, Eq. (6.3) is however not very useful due to the complexity and redundancy of the representation of the 3N interaction in the single-particle momentum basis. Significant benefits can be obtained by exploiting the symmetries of the three-body interaction, i.e., Galilean, rotational, and isospin invariance. In particular, we explicitly make use of the Galilean invariance of the nuclear force by representing it in terms of the relative and cm momenta, with the interaction being independent of the (three-body) cm momentum \mathbf{P}_{3N} . We therefore switch to a Jacobi momentum-space representation, as already introduced for the regulator of the 3N interaction in Eq. (2.15), by defining the relative Jacobi momenta

$$\mathbf{p} = \frac{1}{2}(\mathbf{k}_1 - \mathbf{k}_2), \quad (6.7a)$$

$$\mathbf{q} = \frac{2}{3} \left[\mathbf{k}_3 - \frac{1}{2}(\mathbf{k}_1 + \mathbf{k}_2) \right]. \quad (6.7b)$$

The corresponding states including the spin and isospin quantum numbers are given by

$$|\tilde{\mathbf{p}}\rangle = |\mathbf{p} S M_S T M_T\rangle, \quad (6.8)$$

$$|\tilde{\mathbf{q}}\rangle = |\mathbf{q} m_s m_t\rangle = |\mathbf{q} m_{s_3} m_{t_3}\rangle, \quad (6.9)$$

with S (T) denoting the two-body spin (isospin) and its projection M_S (M_T), and m_s (m_t) the spin (isospin) quantum number of the third particle. We highlight that the spin and isospin quantum numbers of the third particle are identical to m_{s_3} and m_{t_3} , respectively, of $|\tilde{\mathbf{k}}_3\rangle$ defined in Eq. (6.2). The cm momenta for the two-body subsystem and three-body system read

$$\mathbf{P} = \mathbf{k}_1 + \mathbf{k}_2, \quad (6.10a)$$

$$\mathbf{P}_{3N} = \mathbf{k}_1 + \mathbf{k}_2 + \mathbf{k}_3, \quad (6.10b)$$

respectively, and we can write the momentum of the third particle by $\mathbf{k}_3 = 3/2\mathbf{q} + 1/2\mathbf{P}$. We reexpress the 3N interaction in the single-particle momentum-space basis in Eq. (6.3) by the Jacobi momenta. The resulting V_{3N}^{as} in the Jacobi basis only depends on four momenta instead of six by factoring out the cm dependence on $\mathbf{P}_{3N} = \mathbf{P} + \mathbf{k}_3$ of the interaction

$$\Gamma_{\tilde{\mathbf{p}}\tilde{\mathbf{p}}'\tilde{\mathbf{q}}\tilde{\mathbf{q}}'}^{3N} = \int \frac{d\mathbf{k}_3 d\mathbf{k}_3'}{(2\pi)^6} \sum_{\substack{m_{s_3} m'_{s_3} \\ m_{t_3} m'_{t_3}}} \gamma(\tilde{\mathbf{k}}_3, \tilde{\mathbf{k}}_3') \langle \tilde{\mathbf{p}}' \tilde{\mathbf{q}}' | V_{3N}^{\text{as}} | \tilde{\mathbf{p}} \tilde{\mathbf{q}} \rangle (2\pi)^3 \delta(\mathbf{P} + \mathbf{k}_3 - \mathbf{P}' - \mathbf{k}_3'). \quad (6.11)$$

Note however that only the three-body cm momentum is conserved, while the two-body cm momentum \mathbf{P} does not have to be conserved, as $\mathbf{k}_3 \neq \mathbf{k}'_3$, and consequently, the two-body interaction Γ^{3N} will depend on \mathbf{P} and \mathbf{P}' .

Our starting point for all applications and transformations of the three-body interactions are partial-wave decomposed 3N matrix elements computed in the Jacobi momentum-state basis (see, e.g., Refs. [135, 211, 286] for details). Advances for deriving three-body interactions in a partial-wave decomposed form allow for a complete consideration of 3N interactions up to N³LO [135]. The 3N matrix elements are conveniently written by using a shorthand notation for the three-body partial-wave states

$$|pq\alpha\rangle \equiv |[pq(LS)J(ls)j]\mathcal{J}(Tt)\mathcal{T}\rangle, \quad (6.12)$$

here $p = |\mathbf{p}|$ and $q = |\mathbf{q}|$ are given by the magnitudes of the Jacobi momenta, L is the relative two-body angular momentum, J the total relative two-body angular momentum, lowercase letters ($l, s = 1/2, j$, and $t = 1/2$) denote the quantum numbers of the third particle with momentum q , and J and j as well as T and t are coupled to the total three-body angular momentum \mathcal{J} and total three-body isospin \mathcal{T} , respectively. We emphasize that the three-body force is diagonal in \mathcal{J} and \mathcal{T} and independent of the corresponding projections $M_{\mathcal{J}}$ and $M_{\mathcal{T}}$ due to rotational and isospin invariance.

Our next steps involve the partial-wave decomposition of the 3N interaction in the Jacobi momentum-space basis, with the goal to obtain a partial-wave decomposed two-body interaction Γ^{3N} on the right-hand side of Eq. (6.11). Using the notation of Eq. (6.12), we decompose the plane-wave Jacobi basis states into partial waves

$$\begin{aligned} |\tilde{\mathbf{p}}\tilde{\mathbf{q}}\rangle &= \sum_{LM_L} \sum_{lm_l} Y_{LM_L}^*(\hat{\mathbf{p}}) Y_{lm_l}^*(\hat{\mathbf{q}}) \\ &\times \sum_{SM_S} \sum_{m_s} \sum_{JM_J} \sum_{jm_j} C_{LM_L SM_S}^{JM_J} C_{lm_l \frac{1}{2} m_s}^{jm_j} \\ &\times \sum_{\mathcal{J}M_{\mathcal{J}}} \sum_{\mathcal{T}M_{\mathcal{T}}} \sum_{m_t} \sum_{\mathcal{T}M_{\mathcal{T}}} C_{\mathcal{J}M_{\mathcal{J}} jm_j}^{\mathcal{J}M_{\mathcal{J}}} C_{\mathcal{T}M_{\mathcal{T}} \frac{1}{2} m_t}^{\mathcal{T}M_{\mathcal{T}}} |pq\alpha\rangle, \end{aligned} \quad (6.13)$$

with capital (lowercase) M (m) letters denoting projections of the corresponding index for two- or three-body (single-particle) quantum numbers as given in Eq. (6.12). The partial-wave decomposed interaction hence reads

$$\begin{aligned} \langle \tilde{\mathbf{p}}'\tilde{\mathbf{q}}' | V_{3N}^{\text{as}} | \tilde{\mathbf{p}}\tilde{\mathbf{q}} \rangle &= \sum_{LL'L'} \sum_{M_L M'_L} \sum_{m_l m'_l} Y_{LM_L}^*(\hat{\mathbf{p}}) Y_{lm_l}^*(\hat{\mathbf{q}}) Y_{L'M'_L}(\hat{\mathbf{p}}') Y_{l'm'_l}(\hat{\mathbf{q}}') \\ &\times \sum_{M_J M'_J} \sum_{m_j m'_j} \sum_{J'J'j'j'} C_{LM_L SM_S}^{JM_J} C_{L'M'_L S'M'_S}^{J'M'_J} C_{lm_l \frac{1}{2} m_s}^{jm_j} C_{l'm'_l \frac{1}{2} m'_s}^{j'm'_j} \\ &\times \sum_{\mathcal{J}M_{\mathcal{J}}} C_{\mathcal{J}M_{\mathcal{J}} jm_j}^{\mathcal{J}M_{\mathcal{J}}} C_{J'M'_J j'm'_j}^{\mathcal{J}M_{\mathcal{J}}} \sum_{\mathcal{T}M_{\mathcal{T}}} C_{\mathcal{T}M_{\mathcal{T}} \frac{1}{2} m_{t3}}^{\mathcal{T}M_{\mathcal{T}}} C_{T'M'_{\mathcal{T}} \frac{1}{2} m'_{t3}}^{\mathcal{T}M_{\mathcal{T}}} \\ &\times \langle p'q'\alpha' | V_{3N}^{\text{as}} | pq\alpha \rangle, \end{aligned} \quad (6.14)$$

where we used m_{s_3} and m_{t_3} for the quantum numbers of $\tilde{\mathbf{q}}$. Note that there are no sums over S, M_S, m_s, T, M_T , and m_t , and that the 3N interaction in general is off-diagonal in T and M_T .

As already discussed for Eq. (6.11), the normal-ordered 3N contribution to the two-body force breaks Galilean invariance and we have to explicitly incorporate additional quantum numbers that describe the cm dependence. In the following, we indicate quantum numbers of the two-body basis by an overline to distinguish them from the three-body basis and use a collective index β for the two-body states. The modified partial-wave decomposed two-body state including the additional quantum numbers \bar{L}_{cm} and \bar{J}_{tot} [see Eq. (2.28) for the standard notation] is defined as

$$|pP\beta\rangle \equiv |pP \left[(\bar{L}\bar{S})\bar{J}\bar{L}_{\text{cm}} \right] \bar{J}_{\text{tot}} M_{\bar{J}_{\text{tot}}} \bar{T} M_{\bar{T}} \rangle, \quad (6.15)$$

with the total two-body angular momentum \bar{J}_{tot} obtained by coupling the relative angular momentum \bar{J} and the two-body cm orbital angular momentum \bar{L}_{cm} . The effective two-body interaction $\Gamma^{3\text{N}}$ transforms like a scalar under rotations in spin and space, is diagonal in the total angular momentum \bar{J}_{tot} , does not depend on its projection $M_{\bar{J}_{\text{tot}}}$, and is diagonal in the isospin projection $M_{\bar{T}}$, as long as the reference state is spherical.

By inserting the partial-wave decomposed interaction of Eq. (6.14) into Eq. (6.11) and projecting the two-body states of $\Gamma^{3\text{N}}$ onto the partial-wave decomposed states, taking into account the additional cm dependence in Eq. (6.15), we obtain the final expression of the normal-ordered three-body contribution in the relative momentum-space basis

$$\begin{aligned} & \langle p'P'\beta' | \Gamma^{3\text{N}} | pP\beta \rangle \\ &= \frac{1}{2\bar{J}_{\text{tot}} + 1} \sum_{M_{\bar{J}_{\text{tot}}}} \sum_{\substack{M_{\bar{L}}, M_{\bar{S}}, M_{\bar{J}}, M_{\bar{L}_{\text{cm}}} \\ M'_{\bar{L}}, M'_{\bar{S}}, M'_{\bar{J}}, M'_{\bar{L}_{\text{cm}}}}} C_{\bar{L}\bar{M}_{\bar{L}} \bar{S} M_{\bar{S}}}^{\bar{J} M_{\bar{J}}} C_{\bar{L}'\bar{M}'_{\bar{L}} \bar{S}' M'_{\bar{S}}}^{\bar{J}' M'_{\bar{J}}} C_{\bar{J} M_{\bar{J}} \bar{L}_{\text{cm}} M_{\bar{L}_{\text{cm}}}}^{\bar{J}_{\text{tot}} M_{\bar{J}_{\text{tot}}}} C_{\bar{J}' M'_{\bar{J}} \bar{L}'_{\text{cm}} M'_{\bar{L}'_{\text{cm}}}}^{\bar{J}'_{\text{tot}} M'_{\bar{J}'_{\text{tot}}}} \\ & \times \int d\hat{\mathbf{P}} \int d\hat{\mathbf{P}}' Y_{\bar{L}_{\text{cm}} M_{\bar{L}_{\text{cm}}}}(\hat{\mathbf{P}}) Y_{\bar{L}'_{\text{cm}} M'_{\bar{L}'_{\text{cm}}}}^*(\hat{\mathbf{P}}') \int \frac{d\mathbf{k}_3}{(2\pi)^3} \\ & \times \sum_{\substack{nl_3 j_3 m_{j_3} m_{t_3} \\ m_{i_3} m'_{i_3} m_{s_3} m'_{s_3}}} C_{l_3 m_{i_3} \frac{1}{2} m_{s_3}}^{j_3 m_{j_3}} C_{l_3 m'_{i_3} \frac{1}{2} m'_{s_3}}^{j_3 m_{j_3}} \Phi_3(k_3) \Phi_3(k'_3) Y_{l_3 m_{i_3}}(\hat{\mathbf{k}}'_3) Y_{l_3 m_{i_3}}^*(\hat{\mathbf{k}}_3) \\ & \times \sum_{\mathcal{J} M_{\mathcal{J}}} \sum_{\mathcal{T} M_{\mathcal{T}}} \sum_{LL'U'} \sum_{JJ'j'j'} \sum_{M_L M'_L} \sum_{m_i m'_i} \sum_{M_J M'_J} \sum_{m_j m'_j} \delta_{L\bar{L}} \delta_{M_L M_{\bar{L}}} \delta_{L'\bar{L}'} \delta_{M'_L M'_{\bar{L}'}} Y_{lm_i}^*(\hat{\mathbf{q}}) Y_{l'm'_i}(\hat{\mathbf{q}}') \\ & \times C_{LM_L \bar{S} M_{\bar{S}}}^{\mathcal{J} M_{\mathcal{J}}} C_{L'M'_L \bar{S}' M'_{\bar{S}'}}^{\mathcal{J}' M'_{\mathcal{J}'}} C_{lm_i \frac{1}{2} m_{s_3}}^{j m_j} C_{l'm'_i \frac{1}{2} m'_{s_3}}^{j' m'_j} C_{JM_{\mathcal{J}} j m_j}^{\mathcal{J} M_{\mathcal{J}}} C_{J'M'_{\mathcal{J}'} j' m'_j}^{\mathcal{J}' M'_{\mathcal{J}'}} C_{\bar{T} M_{\bar{T}} \frac{1}{2} m_{t_3}}^{\mathcal{T} M_{\mathcal{T}}} C_{\bar{T}' M'_{\bar{T}'} \frac{1}{2} m'_{t_3}}^{\mathcal{T}' M'_{\mathcal{T}'}} \\ & \times \langle p'q'\alpha' | V_{3\text{N}} | pq\alpha \rangle, \end{aligned} \quad (6.16)$$

where we used the orthonormality of the spherical harmonics, the delta function in Eq. (6.11) to evaluate the \mathbf{k}'_3 integral, and that the two-body spin is given by $S = \bar{S}$ and $S' = \bar{S}'$. Multiple sums in Eq. (6.16) can be simplified analytically, e.g., the combination of Clebsch-Gordan coefficients [222]. The remaining sums and integrals have to be solved numerically.

The simplified expression of Eq. (6.16) can be written as

$$\begin{aligned}
\langle p'P'\beta'|\Gamma^{3N}|pP\beta\rangle &= \sum_{\substack{\mathcal{J}\mathcal{T} \\ l'j'j'}} \int d\hat{\mathbf{P}}d\hat{\mathbf{P}}' \frac{d\mathbf{k}_3}{(2\pi)^3} \langle p'q'\alpha'|V_{3N}|pq\alpha\rangle \\
&\times \sum_{\substack{j_xj_yj_z \\ m_y m_z}} \sum_{M_{\bar{L}_{\text{cm}}} M'_{\bar{L}_{\text{cm}}}} \sum_{m_l m'_l} A_{j_xj_yj_z}^{\alpha\alpha'\beta\beta'} B_{j_xj_yj_zm_y m_z}^{\bar{T}\bar{T}'M_{\bar{T}}\mathcal{T}}(\mathbf{k}_3, \mathbf{k}'_3) \\
&\times C_{lm_l\bar{L}'_{\text{cm}}M'_{\bar{L}'_{\text{cm}}}}^{j_y m_y} C_{l'm'_l\bar{L}'_{\text{cm}}M'_{\bar{L}'_{\text{cm}}}}^{j_z m_z} Y_{\bar{L}_{\text{cm}}M_{\bar{L}_{\text{cm}}}}^*(\hat{\mathbf{P}}) Y_{\bar{L}'_{\text{cm}}M'_{\bar{L}'_{\text{cm}}}}(\hat{\mathbf{P}}') Y_{lm_l}^*(\hat{\mathbf{q}}) Y_{l'm'_l}(\hat{\mathbf{q}}'),
\end{aligned} \tag{6.17}$$

where the superscripts α and β indicate the dependence on any of the quantum numbers as defined in Eqs. (6.12) and (6.15). In the above equation, we introduced the abbreviations

$$\begin{aligned}
A_{j_xj_yj_z}^{\alpha\alpha'\beta\beta'} &= (-1)^{-\bar{J}+\bar{J}'+j+j'+2j_x+j_y-j_z} \hat{\mathcal{J}}^2 \hat{j}_j \hat{j}_y \hat{j}_z \hat{j}_x^2 \\
&\times \left\{ \begin{array}{ccc} \bar{L}'_{\text{cm}} & l & j_y \\ \frac{1}{2} & j_x & j \end{array} \right\} \left\{ \begin{array}{ccc} \bar{L}_{\text{cm}} & l' & j_z \\ \frac{1}{2} & j_x & j' \end{array} \right\} \left\{ \begin{array}{ccc} j_x & \bar{L}'_{\text{cm}} & j \\ \bar{L}_{\text{cm}} & \bar{J}_{\text{tot}} & \bar{J} \\ j' & \bar{J}' & \mathcal{J} \end{array} \right\},
\end{aligned} \tag{6.18}$$

and

$$\begin{aligned}
&B_{j_xj_yj_zm_y m_z}^{\bar{T}\bar{T}'M_{\bar{T}}\mathcal{T}}(\mathbf{k}_3, \mathbf{k}'_3) \\
&= \sum_{M_{\mathcal{T}}} \sum_{j_u m_u} \sum_{\substack{n l_3 j_3 m_{j_3} \\ m_{l_3} m'_{l_3} m_{t_3}}} \hat{j}_3^2 C_{l_3 m_{l_3} j_3 m_{j_3}}^{j_u m_u} C_{l_3 m'_{l_3} j_3 m_{j_3}}^{j_u m_u} C_{\bar{T}M_{\bar{T}}\frac{1}{2}m_{t_3}}^{\mathcal{T}M_{\mathcal{T}}} C_{\bar{T}'M_{\bar{T}'}\frac{1}{2}m_{t_3}}^{\mathcal{T}M_{\mathcal{T}}} \\
&\times \left\{ \begin{array}{ccc} j_x & \frac{1}{2} & j_y \\ \frac{1}{2} & j_3 & l_3 \\ j_z & l_3 & j_u \end{array} \right\} Y_{l_3 m'_{l_3}}(\hat{\mathbf{k}}'_3) Y_{l_3 m_{l_3}}^*(\hat{\mathbf{k}}_3) \Phi_3(k_3) \Phi_3(k'_3),
\end{aligned} \tag{6.19}$$

where the simplification of the product of Clebsch-Gordan coefficients leads to $J = \bar{J}$ and $J' = \bar{J}'$. We employed the additional intermediate quantum numbers j_x , j_y , j_z , and j_u as well as their projections m_y , m_z , and m_u . These intermediate quantities are obtained by coupling l with \bar{L}'_{cm} to j_y , l' with \bar{L}_{cm} to j_z , l_3 with j_y or j_z to j_u , and $s = 1/2$ with j_y or j_z to j_x .

We further used the notation of $6j$ and $9j$ symbols in Eqs. (6.18) and (6.19) and refer to Ref. [222] for a more in-depth discussion of these symbols and their symmetries and properties. Note that the values of the Jacobi momenta \mathbf{q} and \mathbf{q}' are implicitly fixed by the relations $\mathbf{k}_3 = 3/2\mathbf{q} + 1/2\mathbf{P}$ and $\mathbf{k}'_3 = \mathbf{P} + \mathbf{k}_3 - \mathbf{P}'$. Furthermore, $A_{j_xj_yj_z}^{\alpha\alpha'\beta\beta'}$ does not depend on m_y , m_z , or any of the momenta in the spherical harmonics, such that it can be precalculated and evaluated independently of the sums and integrals in Eq. (6.17) and easily be prestored. All other quantities that involve those quantum numbers, like $M_{\bar{L}_{\text{cm}}}$ and m_l , that also enter the spherical harmonics need to be recomputed for each point of the momentum integrals. Numerically, we solve the momentum integrals in Eq. (6.17) on a finite mesh system with N_P , N_p , N_q , and N_{k_3} grid points for the corresponding integrals. Typical values for the number of momentum mesh points are $N_P \approx 18$, $N_p \approx 14$, $N_q \approx 50$ and $N_{k_3} \approx 15$.

In order to take into account all possible recoupling contributions from the Jacobi representation to a single-particle representation, matrix elements for sufficiently large values of the angular-momentum quantum numbers in the three-body basis need to be computed for a given single-particle basis size e_{max} . In practice, however, the matrix elements of Γ^{3N} get

quantum number	description	employed truncation values
\bar{L}_{cm}	cm two-body angular momentum in 2N basis	8-13
\bar{J}_{tot}	total angular momentum in the 2N basis	8-13
J	rel two-body angular momentum in 3N PW basis	5-6
l	orbital angular momentum of third particle in 3N PW basis	5-7
j	total angular momentum of third particle in 3N PW basis	-
\mathcal{J}	total three-body angular momentum	9/2 - 15/2
\mathcal{T}	total three-body isospin	-
\bar{L}	rel orbital angular momentum in 2N basis	-
\bar{T}	total isospin in 2N basis	-
l_3	sp orbital angular momentum in reference state	-
j_3	sp total angular momentum in reference state	-

Table 6.1: Selected quantum numbers in the Jacobi normal-ordering framework. We use the shorthand notations rel for relative, cm for center-of-mass, sp for single-particle, and PW for partial wave. For quantum numbers truncated in practical applications, we additionally give reasonable maximal truncation values in the third column. Some quantum numbers depend on each other, e.g., the maximum value of j depends on the truncation in l , and we only show truncation values for the actually truncated quantities here.

suppressed as the values of \bar{J} or \bar{L}_{cm} increase. In fact, the matrix elements of the partial-wave 3N matrix elements are typically only computed up to values of $J \simeq 5\text{--}8$ depending on the three-body quantum number \mathcal{J} . Such values are typically sufficient for converged many-body calculations [130]. We again summarize the most important angular-momentum quantum numbers for the Jacobi normal ordering in Table 6.1 for the sake of clarity and additionally give a range of employed truncation values for those quantum numbers which are truncated in the novel framework. In Secs. 6.2 and 6.3, we present detailed benchmarks and investigate the convergence behavior with respect to the employed truncations for different mass numbers, specifically focusing on variations of \bar{L}_{cm} and \bar{J}_{tot} . Besides these truncations, we employ the constraints $\bar{J}_{\text{max}} = l_{\text{max}} = 5$ (if not stated otherwise), where \bar{J}_{max} denotes the maximum total relative angular momentum in the bases $|\alpha\rangle$ and $|\beta\rangle$ defined in Eqs. (6.12) and (6.15), and l_{max} is the maximum value of the orbital angular momentum of the particle with Jacobi momentum q in the three-body basis $|\alpha\rangle$. These values have been shown to be sufficient to obtain well-converged results in light and medium-mass nuclei as well as nuclear matter [130].

6.1.1 Transformation to Jacobi HO basis

In the next step, we transform the normal-ordered two-body interaction from the Jacobi basis to the relative HO basis. This is similar to the standard transformation of the partial-wave decomposed NN interaction from momentum-space to the relative HO basis (see, e.g., Ref. [254]). However, in this case we have to consider the additional cm dependence. The

corresponding HO basis is given by

$$|NN_{\text{cm}}\beta\rangle, \quad (6.20)$$

where N and N_{cm} are the radial oscillator quantum numbers of the relative momentum p and cm momentum P , respectively, and β is the collective index of Eq. (6.15). The plane-wave Jacobi states are transformed to the relative HO basis by

$$|NN_{\text{cm}}\beta\rangle = \int dp \int dP p^2 P^2 R_{N\bar{L}}(p, b) R_{N_{\text{cm}}\bar{L}_{\text{cm}}}(P, b) |pP\beta\rangle, \quad (6.21)$$

with the oscillator length parameter $b = \sqrt{\frac{(\hbar c)^2}{M\hbar\omega}}$ and the radial part $R_{N\bar{L}}$ of the harmonic oscillator wave function in momentum space given by the overlap

$$\begin{aligned} R_{N\bar{L}}(p, b) &= \langle p\bar{L} | N\bar{L} \rangle, \\ &= (-1)^n \sqrt{\frac{2n!b^3}{\Gamma(n+l+\frac{3}{2})}} (pb)^l \exp\left(-\frac{1}{2}(pb)^2\right) L_n^{l+\frac{1}{2}}\left((pb)^2\right), \end{aligned} \quad (6.22)$$

where Γ is the gamma function and $L_n^{l+\frac{1}{2}}$ are the associated Laguerre polynomials. We emphasize that the dependence on the cm quantum number \bar{L}_{cm} allows for more complicated angular-momentum coupling patterns. Consequently, the number of possible partial-wave channels is significantly increased compared to the standard two-body transformation. The total energy quantum number now involves cm and relative quantum numbers and is given by

$$\bar{E}^{(2)} = 2N_{\text{cm}} + \bar{L}_{\text{cm}} + 2N + \bar{L}. \quad (6.23)$$

This implies that in order to perform a complete calculation in a given single-particle basis space e_{max} , we need to choose $\bar{E}_{\text{max}}^{(2)} \geq 2e_{\text{max}}$. There are no additional limits on the total energy quantum number $\bar{E}^{(2)}$. In particular, the values of the radial quantum numbers N_{cm} and N are not truncated for a given choice of e_{max} and can be easily pushed to large values.

6.1.2 Transformation to single-particle basis

The final step to arrive at JT -coupled two-body matrix elements is the transformation from the relative to the single-particle HO basis. Towards this goal, we use Talmi-Moshinsky or so-called HO transformation brackets [288–290]. The (JT -uncoupled) two-body single-particle basis can be written using the collective index introduced in Eq. (3.28)

$$|ab\rangle = \left| n(l_a \frac{1}{2}) j_a m_a \frac{1}{2} m_{t_a} n'(l_b \frac{1}{2}) j_b m_b \frac{1}{2} m_{t_b} \right\rangle, \quad (6.24)$$

where we explicitly show the isospin (spin) $t_i = 1/2$ ($s_i = 1/2$), its projection m_{t_i} , and the radial quantum numbers n and n' for particles a and b , respectively. The final JT -coupled matrix elements of the form

$$\langle (ab) \bar{J}_{\text{tot}} \bar{T}' M_{\bar{T}} | \Gamma^{3N} | (cd) \bar{J}_{\text{tot}} \bar{T} M_{\bar{T}} \rangle, \quad (6.25)$$

are obtained by coupling the single-particle angular momenta and isospins of particle a and b (as well as c and d) to the total two-body angular momentum \bar{J}_{tot} and total isospin \bar{T} , respectively. Note that in general Γ^{3N} has nonvanishing matrix elements for off-diagonal \bar{T} and \bar{T}' and will depend on $M_{\bar{T}}$, while it is diagonal in \bar{J}_{tot} and independent of $M_{\bar{J}_{\text{tot}}}$, as discussed for Eq. (6.15). However, since the transformation to the single-particle basis does not modify the isospin dependence of the states, we will in the following suppress the isospin quantum numbers for simplicity.

In the first step of the transformation, we factorize the spin part of the states by recoupling the two-body states to from j - to ls -coupling scheme, using a $9j$ -symbol

$$\left| [n(l_a s_a) j_a n' (l_b s_b) j_b] \bar{J}_{\text{tot}} \right\rangle = \sum_{\lambda \bar{S}} \hat{j}_a \hat{j}_b \hat{\lambda} \hat{S} \begin{Bmatrix} l_a & s_a & j_a \\ l_b & s_b & j_b \\ \lambda & \bar{S} & \bar{J}_{\text{tot}} \end{Bmatrix} \left| [(n l_a n' l_b) \lambda (s_a s_b) \bar{S}] \bar{J}_{\text{tot}} \right\rangle, \quad (6.26)$$

where the orbital angular momenta l_a and l_b couple to the total orbital angular momentum λ . In order to make use of the standard definitions of the Talmi-Moshinsky transformation brackets of Ref. [290], which are given by

$$\left| (n l_a n' l_b) \lambda \right\rangle = \sum_{N_{\text{cm}} \bar{L}_{\text{cm}} N \bar{L}} \left\langle (N_{\text{cm}} \bar{L}_{\text{cm}} N \bar{L}) \lambda \mid (n l_a n' l_b) \lambda \right\rangle \left| (N_{\text{cm}} \bar{L}_{\text{cm}} N \bar{L}) \lambda \right\rangle, \quad (6.27)$$

we need to recouple also the angular momenta of the Jacobi HO basis defined in Eq. (6.20) to first couple the relative and cm angular momenta to the total orbital angular momentum:

$$\begin{aligned} \left| N N_{\text{cm}} [(\bar{L}_{\text{cm}} \bar{L}) \lambda \bar{S}] \bar{J}_{\text{tot}} \right\rangle &= \sum_{\bar{J}} (-1)^{\bar{L} + \bar{S} + \bar{J}} \hat{J} \hat{\lambda} \begin{Bmatrix} \bar{S} & \bar{L} & \bar{J} \\ \bar{L}_{\text{cm}} & \bar{J}_{\text{tot}} & \lambda \end{Bmatrix} \\ &\times \left| N N_{\text{cm}} [(\bar{L} \bar{S}) \bar{J} \bar{L}_{\text{cm}}] \bar{J}_{\text{tot}} \right\rangle, \end{aligned} \quad (6.28)$$

where we changed the coupling order of \bar{L} and \bar{L}_{cm} , which introduces an additional phase of $(-1)^{\bar{L}_{\text{cm}} + \bar{L} - \lambda}$. Summarizing, this leads to the final transformation relation for the two-body states:

$$\begin{aligned} \left| (ab) \bar{J}_{\text{tot}} \right\rangle &= \sum_{\lambda \bar{S}} \hat{j}_a \hat{j}_b \hat{\lambda}^2 \hat{S} \hat{J} \begin{Bmatrix} l_a & s_a & j_a \\ l_b & s_b & j_b \\ \lambda & \bar{S} & \bar{J}_{\text{tot}} \end{Bmatrix} \sum_{N_{\text{cm}} \bar{L}_{\text{cm}} N \bar{L}} \left\langle (N_{\text{cm}} \bar{L}_{\text{cm}} N \bar{L}) \lambda \mid (n_a l_a n_b l_b) \lambda \right\rangle \\ &\times \sum_{\bar{J}} (-1)^{\bar{L} + \bar{S} + \bar{J}} \begin{Bmatrix} \bar{S} & \bar{L} & \bar{J} \\ \bar{L}_{\text{cm}} & \bar{J}_{\text{tot}} & \lambda \end{Bmatrix} \left| N N_{\text{cm}} [(\bar{L} \bar{S}) \bar{J} \bar{L}_{\text{cm}}] \bar{J}_{\text{tot}} \right\rangle. \end{aligned} \quad (6.29)$$

The resulting Γ^{3N} two-body matrix elements in the JT -coupled single-particle basis can now be directly used in *ab initio* many-body applications, e.g., the IMSRG.

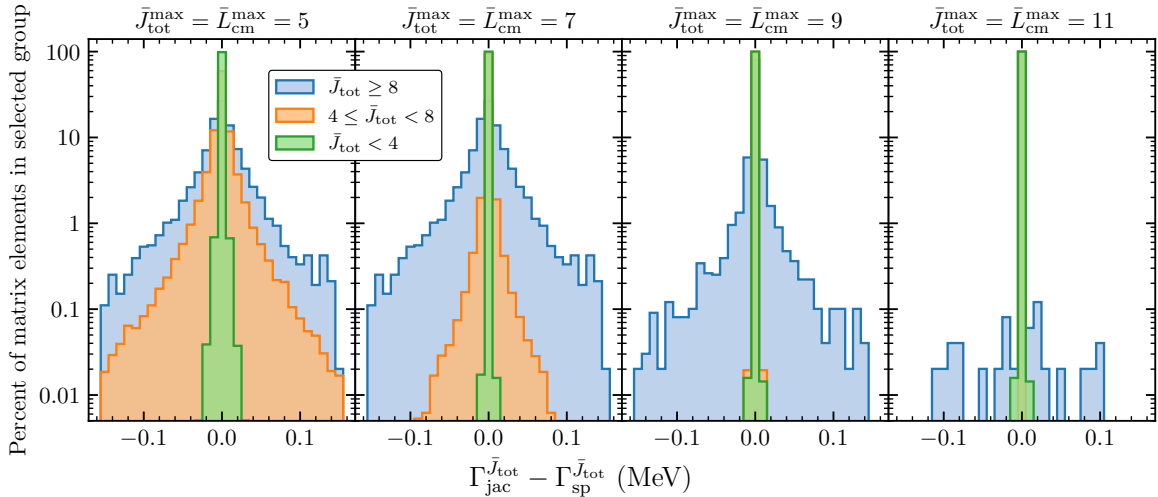


Figure 6.2: Difference $\Gamma_{\text{jac}} - \Gamma_{\text{sp}}$ of the normal-ordered two-body matrix element from the 3N contribution in the Jacobi and single-particle normal ordering for different \bar{J}_{tot} blocks of $\bar{J}_{\text{tot}} < 4$ (green), $4 \leq \bar{J}_{\text{tot}} < 8$ (orange) and $\bar{J}_{\text{tot}} \geq 8$ (blue) in the two-body interaction. We show results for different truncations in the Jacobi normal ordering, using $\bar{J}_{\text{tot}}^{\text{max}} = \bar{L}_{\text{cm}}^{\text{max}} = 5, 7, 9$, and 11 in the first through fourth panel, respectively. The y-axis shows the percentage of matrix elements with the difference specified on the x-axis in the selected \bar{J}_{tot} block. Results are shown for the 1.8/2.0 EM 3N interaction with $e_{\text{max}} = 6$, $E_{3\text{max}} = 18$, and $\hbar\omega = 16$ MeV using an ^{16}O HF reference state.

6.2 Truncation benchmark for light nuclei

6.2.1 Matrix-element comparison

As a first step, we study the performance of the Jacobi normal ordering (NO) by explicitly comparing matrix elements of the effective two-body operator $\Gamma^{3\text{N}}$ in the single-particle and Jacobi approaches. The reference state employed for all normal-ordering applications in the Jacobi basis in this work is given by an HF reference state calculated in the single-particle basis using the 1.8/2.0 EM interaction. The corresponding model space is characterized by e_{max} and $E_{3\text{max}}$ and the HF orbitals, which are a linear combination of HO orbitals, can then be applied in the Jacobi normal ordering.

In Fig. 6.2, we show the difference between the normal-ordered two-body matrix elements $\Gamma^{3\text{N}}$ resulting from the three-body contribution in the Jacobi and single-particle basis for an ^{16}O reference state. We employ a model space of $e_{\text{max}} = 6$ with $E_{3\text{max}} = 18$, such that there is no active $E_{3\text{max}}$ cut. The maximum total three-body angular momentum is set to $\mathcal{J} = 9/2$, which is typically enough to obtain converged results for finite nuclei and nuclear matter [130]. Using the same HF reference state in both frameworks allows for a clean comparison of the normal-ordered matrix elements. For a better understanding of the different contributions to the two-body interaction, we divide the set of matrix elements into three blocks of total angular momentum \bar{J}_{tot} in the two-body basis. We consider blocks of $\bar{J}_{\text{tot}} < 4$, $4 \leq \bar{J}_{\text{tot}} \leq 8$, and $\bar{J}_{\text{tot}} \geq 8$ and show on the y-axis the percentage of matrix elements with the specified difference on the x-axis in the corresponding blocks. By consistently varying

the $\bar{J}_{\text{tot}}^{\text{max}}$ and $\bar{L}_{\text{cm}}^{\text{max}}$ truncations in the Jacobi framework from 5 to 11, we see that increasing \bar{J}_{tot} and \bar{L}_{cm} systematically brings the matrix elements in the Jacobi NO in better agreement with the single-particle NO. In general, both truncations can be varied independently and we truncate them at the same value for simplicity. Smaller \bar{J}_{tot} blocks are already more accurate at smaller $\bar{J}_{\text{tot}}^{\text{max}}$ and $\bar{L}_{\text{cm}}^{\text{max}}$, and larger \bar{J}_{tot} blocks are more accurately reproduced for increased truncations. For the highest truncation of $\bar{J}_{\text{tot}}^{\text{max}} = \bar{L}_{\text{cm}}^{\text{max}} = 11$ shown here, both methods yield nearly identical matrix elements with only minor deviations, mostly for high \bar{J}_{tot} contributions. This can be understood by the generalized transformation to the single-particle basis in Sec. 6.1.2 for the Jacobi framework. The two-body cm quantum number \bar{L}_{cm} couples with \bar{L} and \bar{S} to the total angular momentum \bar{J}_{tot} , such that for a complete basis we would need to take $\bar{L}_{\text{cm}}^{\text{max}}$ to $\bar{J}_{\text{tot}}^{\text{max}} + \bar{L}^{\text{max}} + \bar{S}^{\text{max}}$, with $\bar{J}_{\text{tot}}^{\text{max}} = 13$ in an $e_{\text{max}} = 6$ model space and $\bar{S}^{\text{max}} = 1$. However, the contributions from very high \bar{L}_{cm} are found to be only small and the rightmost panel in Fig. 6.2 shows nearly exact agreement for $\bar{J}_{\text{tot}}^{\text{max}} = \bar{L}_{\text{cm}}^{\text{max}} = 11$ in all \bar{J}_{tot} blocks.

We emphasize that the remaining small deviations for the matrix elements could also be caused by different truncations of the relative two-body angular momentum J in the 3N basis in Eq. (6.12). While the Jacobi framework uses $J = 5$ for all three-body partial waves, the single-particle approach uses a truncation of $J = 8$, $J = 7$, and $J = 6$ for channels with total three-body angular momenta of $\mathcal{J} \leq 5/2$, $\mathcal{J} = 7/2$, and $\mathcal{J} = 9/2$, respectively. However, the impact of matrix elements beyond $J = 5$ for calculations of finite nuclei and nuclear matter is observed to be typically only small [130].

6.2.2 Ground-state properties

We extend our benchmark calculations from a detailed comparison of matrix elements to ground-state energies of light and medium-mass nuclei using the IMSRG, again comparing the Jacobi and single-particle NO. For all following calculations, we use a model-space size of $e_{\text{max}} = 14$, which is sufficient to obtain converged results for light, medium-mass, and medium-heavy nuclei [55]. We emphasize that in general the mean-field solution converges faster than the many-body solution with respect to $E_{3\text{max}}$ and that any residual dependence for the ground-state or correlation energy on $E_{3\text{max}}$ in the single-particle framework is purely based on correlation effects in the many-body expansion. It is therefore beneficial to study the convergence behavior of the correlation energy, which cancels out the dependence on the HF energy. Figure 6.3 shows the correlation energy in the single-particle normal ordering as a function of $E_{3\text{max}}$ and in the Jacobi normal ordering as a function of $\bar{L}_{\text{cm}}^{\text{max}}$ and $\bar{J}_{\text{tot}}^{\text{max}}$ for ^{16}O and ^{48}Ca . In contrast to the matrix-element comparison for small model spaces in Fig. 6.2, without an active $E_{3\text{max}}$ truncation, we employ a significant cut on the three-body matrix elements by using $E_{3\text{max}} = 18$ in an $e_{\text{max}} = 14$ model space (only $E_{3\text{max}} = 42$ would be complete). The effect of the $E_{3\text{max}}$ truncation for light and medium-mass nuclei in the single-particle normal ordering is however known to be only small and we show results up to $E_{3\text{max}} = 18$ in the left panels of Fig. 6.3, and use a $E_{3\text{max}} = 16$ reference state for the Jacobi normal ordering in the right panels.

Converged correlation (and ground-state) energies in the single-particle approach are observed around $E_{3\text{max}} \approx 13$ and $E_{3\text{max}} \approx 18$ for ^{16}O and ^{40}Ca in the top and bottom plot, respectively. The HF energy is already converged for smaller truncations of $E_{3\text{max}} = 10$ for ^{16}O and $E_{3\text{max}} = 12$ for ^{48}Ca (not shown). In the Jacobi framework we find that truncating the additional quantum numbers at $\bar{L}_{\text{cm}}^{\text{max}} = \bar{J}_{\text{tot}}^{\text{max}} \approx 5$ ($\bar{L}_{\text{cm}}^{\text{max}} = \bar{J}_{\text{tot}}^{\text{max}} \approx 8$) is enough to obtain

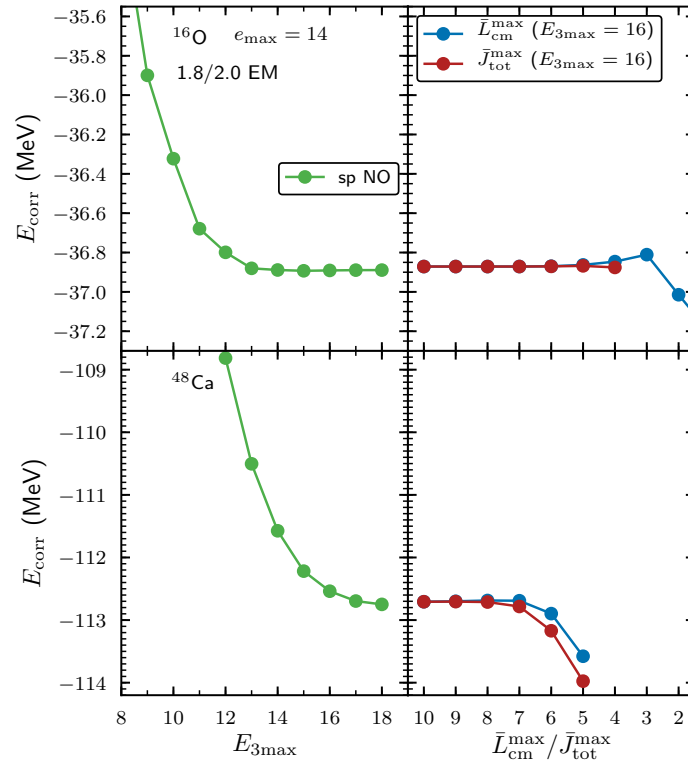


Figure 6.3: Correlation energy in the single-particle (left panel) and Jacobi normal ordering (right panel) as a function of $E_{3\max}$ (left panel) and $\bar{L}_{\text{cm}}^{\max}$ or $\bar{J}_{\text{tot}}^{\max}$ (right panel), keeping the nonvaried parameter at the maximal value of $\bar{L}_{\text{cm}}^{\max} = 10$ or $\bar{J}_{\text{tot}}^{\max} = 10$, respectively. We show results for ^{16}O and ^{48}Ca in the top and bottom plot, using the 1.8/2.0 EM interaction, an $e_{\max} = 14$ model space, and an oscillator frequency of $\hbar\omega = 16$ MeV in the HF basis. The Jacobi normal ordering employs an $E_{3\max} = 16$ HF reference state.

converged energies for ^{16}O (^{40}Ca). The slightly larger truncations for ^{40}Ca indicate that increased truncations are required for converged results of higher mass numbers. Comparing the results in the Jacobi and single-particle normal ordering, we observe perfect agreement of converged energies in both frameworks. The only remaining dependence on $E_{3\max}$ in the Jacobi framework is given by the reference-state calculation in the single-particle basis. While we observe no residual dependence on the $E_{3\max}$ cut for the ground-state energies of ^{16}O and ^{48}Ca when using an $E_{3\max} = 16$ reference state, the dependence on the reference state could become recognizable when going to higher mass numbers. This will be investigated in more detail in the following, moving to heavier systems.

6.3 Application to heavy systems

We now turn our attention to heavier nuclei, first exploring the correlation energy of ^{78}Ni in Fig. 6.4. As discussed before, increasing the $E_{3\max}$ cut becomes important to obtain converged ground-state energies in the single-particle NO when approaching heavier systems. This can be seen in the left panel of Fig. 6.4, where we study the correlation energy up to $E_{3\max} = 24$ and find converged results for $E_{3\max} \approx 20$. Increasing the $E_{3\max}$ cut to higher values was

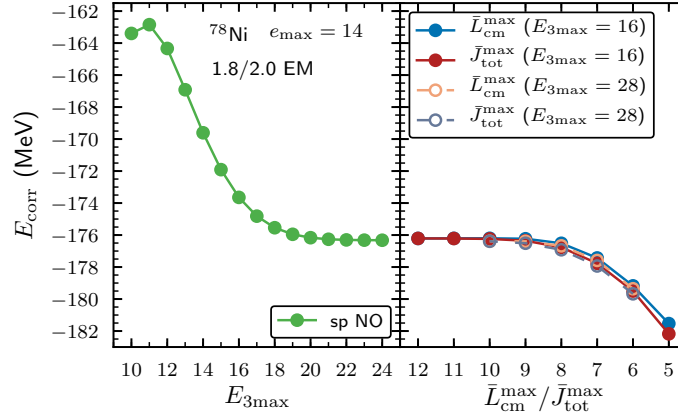


Figure 6.4: Same as Fig. 6.3 but for ^{78}Ni . In addition to using an $E_{3\text{max}} = 16$ reference state in the Jacobi normal ordering, we show results when using an $E_{3\text{max}} = 28$ reference state by the dashed lines with open circles in the right plot. The resulting correlation energies lie on top of the calculations using the reference state constructed with a smaller $E_{3\text{max}}$ truncation.

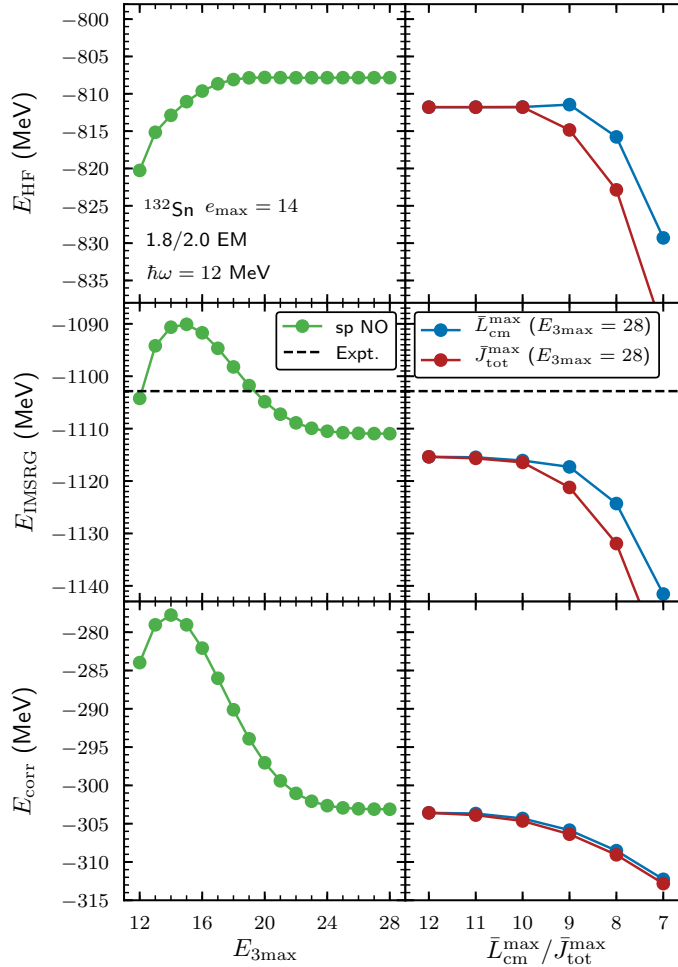


Figure 6.5: Same as Fig. 6.4 but for ^{132}Sn and $\hbar\omega = 12$ MeV. The Jacobi normal ordering (right) uses an $E_{3\text{max}} = 28$ HF reference state. We additionally show the HF energy and IMSRG energy in the top and middle panel, respectively, and increased the $E_{3\text{max}}$ range in the single-particle normal ordering (left) to $E_{3\text{max}} = 28$.

possible due to Ref. [50] and 3N matrix elements in the single-particle basis were provided by T. Miyagi. In contrast to previous calculations in Sec. 6.2.2, which only employed an $E_{3\max} = 16$ HF reference states in the Jacobi normal ordering, we additionally show results when using a reference state constructed in a significantly larger space of $E_{3\max} = 28$ (the currently largest available cut [50]). Remarkably, even though the correlation expansion based on the single-particle NO is not converged for $E_{3\max} = 16$, the results in the Jacobi framework show no difference for using an $E_{3\max} = 16$ or $E_{3\max} = 28$ reference state. This can be understood by the HF calculation converging faster than the IMSRG calculation, where we find converged HF energies already around $E_{3\max} \approx 14$ for ^{78}Ni (not shown). Consequently, no high-quality reference states of $E_{3\max} \approx 28$ are needed in the Jacobi NO and a converged HF reference state is sufficient to obtain converged energies, once $\bar{L}_{\text{cm}}^{\max}$ and $\bar{J}_{\text{tot}}^{\max}$ are large enough. This is in contrast to the single-particle NO, where increased $E_{3\max}$ values are required to obtain converged calculations.

Again, the Jacobi and single-particle framework lead to the same converged energies, even when just using an $E_{3\max} = 16$ reference state in the Jacobi NO. We note that by going to heavier mass numbers, also the truncations $\bar{L}_{\text{cm}}^{\max}$ and $\bar{J}_{\text{tot}}^{\max}$ in the Jacobi NO have to be increased and we observe converged results for $\bar{L}_{\text{cm}}^{\max} = \bar{J}_{\text{tot}}^{\max} \approx 9$, slightly larger than what was observed for ^{16}O or ^{48}Ca . Increasing these truncations leads to increased computation times in the Jacobi framework, which is why one wants to keep them to the minimal required values in practical applications.

The trends observed for ^{78}Ni can be further verified for even heavier systems. In Fig. 6.5, we show a detailed comparison of the HF, IMSRG, and correlation energies of ^{132}Sn in the single-particle and Jacobi normal ordering. The results in the single-particle basis are shown up to $E_{3\max} = 28$ based on the recent developments in Ref. [50], and we here show calculations for a slightly different oscillator frequency of $\hbar\omega = 12$ MeV. We increased the total three-body angular momentum to maximal values of $\mathcal{J}^{\max} = 15/2$, however effects of higher total angular momenta beyond $\mathcal{J} = 9/2$ are expected to be only small [50, 130]. As anticipated, the HF energy converges rapidly with respect to $E_{3\max}$, clearly visible in the top panel of Fig. 6.5. Consequently, we assume that a reference state with $E_{3\max} \approx 18$, where the HF calculation is converged, is enough to obtain converged ground-state and correlation energies in the Jacobi approach. Nevertheless, for a better comparison, we employ an $E_{3\max} = 28$ reference state in the Jacobi NO. The ground-state and correlation energy in the single-particle NO still depend on the $E_{3\max}$ truncation beyond $E_{3\max} = 18$ and cuts of $E_{3\max} \approx 24$ are required to obtain converged results.

In the Jacobi NO, the $\bar{L}_{\text{cm}}^{\max}$ and $\bar{J}_{\text{tot}}^{\max}$ truncations required for converged calculations follow the trends observed for ^{78}Ni in Fig. 6.4 and slightly increase to $\bar{L}_{\text{cm}}^{\max} = \bar{J}_{\text{tot}}^{\max} \approx 11$. We checked that the remaining difference of the HF and ground-state energy between the single-particle and Jacobi NO is not caused by too small truncations for J and l in the three-body partial-wave basis in Eq. (6.12). Increasing the maximum quantum numbers from $J^{\max} = l^{\max} = 5$ to $J^{\max} = 6$ and $l^{\max} = 7$ leads to nearly no change, with only a couple hundred keV more binding for the HF and ground-state energy. Possible reasons for the deviation could be that larger mesh systems are required for the momentum integrations in heavier nuclei to describe the occurring highly oscillating functions. However, studies in this direction are still work in progress.

We further investigate the benefits of the Jacobi normal ordering for even heavier systems, studying ^{208}Pb in Fig. 6.6. We additionally show calculations for using an increased model-

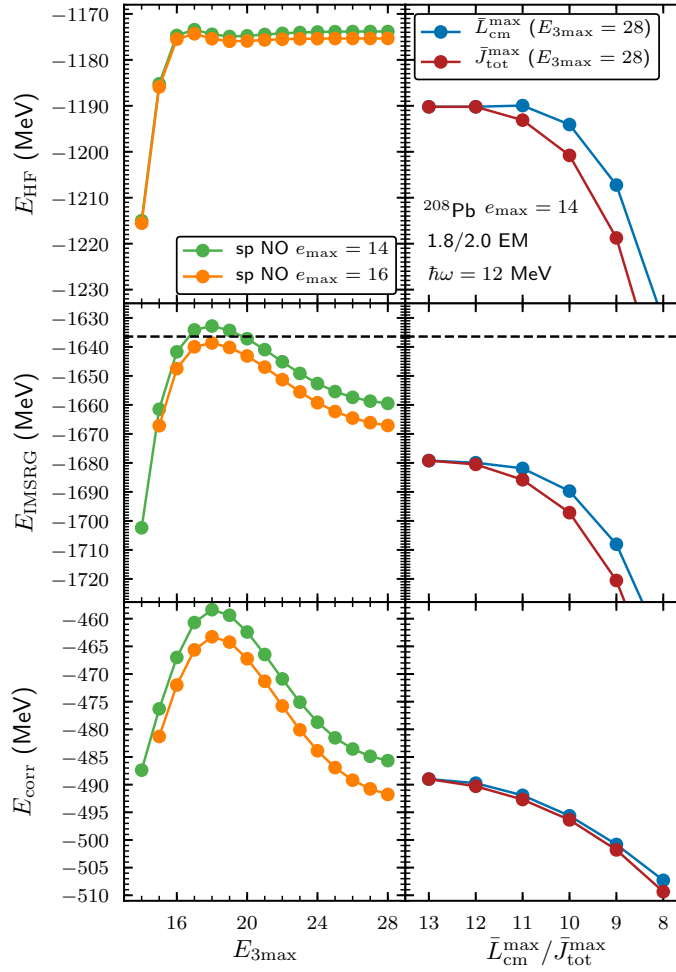


Figure 6.6: Same as Fig. 6.5 but for ^{208}Pb . The Jacobi normal ordering (right) uses an $e_{\max} = 14$ and $E_{3\max} = 28$ HF reference state. We additionally show results in the single-particle normal ordering (left) when using an $e_{\max} = 16$ model space by the orange curve.

space of $e_{\max} = 16$ in the single-particle approach. As before, the HF energy is well converged around $E_{3\max} \approx 20$ and we find only small effects of using the larger e_{\max} truncation for the mean-field solution. This changes for the many-body solution, where the ground-state and, thus, the correlation energy are not fully converged with respect to e_{\max} and still show an $E_{3\max}$ -sensitivity beyond $E_{3\max} = 28$. The Jacobi framework shows similar trends as for ^{132}Sn in Fig. 6.5 employing an $e_{\max} = 14$ and $E_{3\max} = 28$ reference state. We observe more binding for the HF and IMSRG energy compared to the single-particle normal ordering and only slight differences for the correlation energy. Possible reasons for this differences could again be that larger mesh systems are required in the Jacobi normal ordering, especially when describing heavier nuclei. Converged results are obtained for $\bar{L}_{\text{cm}}^{\max} = \bar{J}_{\text{tot}}^{\max} \approx 13$, being only slightly larger than in ^{132}Sn . It will be interesting to see what reference states with increased e_{\max} and calculations with larger mesh systems predict in the Jacobi normal ordering. We emphasize again that the reference-state construction is computationally cheap and that the final e_{\max} truncation for the effective two-body interaction can be scaled up in the Jacobi framework.

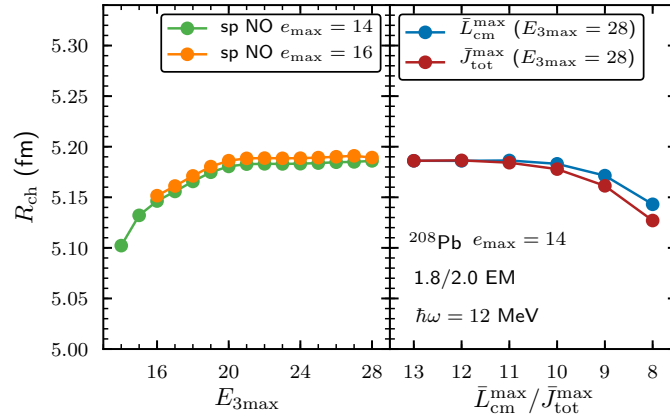


Figure 6.7: Same as Fig. 6.6 but for the charge radius of ^{208}Pb and an oscillator frequency of $\hbar\omega = 12$ MeV.

6.3.1 Charge radii

In addition to ground-state properties, the interactions derived within the new framework can be straightforwardly applied to study other observables. We here highlight the application to the charge radius operator in the IMSRG, following the calculation of the charge radius as outlined in Sec. 3.4.3, and again compare results in the Jacobi and single-particle normal ordering for ^{208}Pb in Fig. 6.7.

The charge radius operator is known to be already quite well described at the HF level. With a HF charge radius of $R_{\text{ch}} = 5.141$ fm, we find only small contributions from the correlation expansion to the charge radius for both normal-ordering frameworks. The single-particle normal ordering shows only minor differences when increasing the model space to $e_{\text{max}} = 16$ and the results are converged in $E_{3\text{max}}$. We find excellent agreement between both normal-ordering approaches and slightly faster convergence in the Jacobi framework with respect to $\bar{L}_{\text{cm}}^{\text{max}}$ and $\bar{J}_{\text{tot}}^{\text{max}}$ compared to the energies in Fig. 6.6.

All these results highlight the versatility of the novel normal-ordering approach, being able to target heavy nuclei in good agreement with standard normal-ordering methods and without being limited by an $E_{3\text{max}}$ truncation. The only remaining dependence on the single-particle basis, due to the reference-state construction, was found to be resolved once the HF solution is converged.

7

Summary and Outlook

In this thesis, we addressed current challenges in contemporary *ab initio* nuclear structure theory. In particular, we presented advances for the IMSRG and method developments to target the challenges of increased computational cost and memory requirements that provide strong frontiers for *ab initio* many-body methods moving to higher mass numbers with more precision.

Especially the improvements for wave-function expansion methods allowed many-body methods to advance to systems up to heavy nuclei. Improving calculations for these expansion methods goes in two directions: first, improving the reference state; and second, improving the many-body method. Both approaches have been studied in detail in this thesis, exploring ground-state observables of closed-shell nuclei using chiral NN and 3N interactions in the *ab initio* IMSRG.

Aiming at the first point, improving the reference state provides a powerful tool to optimize *ab initio* calculations. Due to computational limitations, calculations of nuclear observables typically depend on basis set parameters of the underlying basis, such as the oscillator frequency. We showed that natural orbital reference states, which are defined as the eigenstates of the one-body density matrix, can be beneficial to improve the many-body solution. Specifically, we studied NAT basis states stemming from a perturbatively improved density matrix up to second order in perturbation theory. These orbitals led to frequency-independent single-particle wave functions. This makes them superior to standard single-particle basis choices, such as the HO basis, which does not optimize any frequency dependence, and the HF basis, which only optimizes occupied orbitals. Additionally, the natural orbital occupation numbers can serve as a diagnostic to indicate when the NAT construction might be ill-behaved. We found that a reasonable mean-field solution and low-resolution Hamiltonians are key factors to construct well-performing natural orbitals based on a perturbatively improved density matrix. Significant benefits were obtained when constructing the NAT states in a large model space and truncating them to a smaller space for performing the many-body calculation. This approach resulted in frequency-independent results and improved model-space convergence, by informing the basis in the small space about information from the large model space. Converged results of ground-state energies and charge radii are already obtained in considerably smaller model spaces of $e_{\max} \approx 10$, instead of requiring to go to $e_{\max} = 14$. This saves a factor of approximately 2-3 in single-particle dimension.

Next, we turned our attention to tensor-factorization and importance-truncation techniques to decompose and compress many-body operators and effectively lower the corresponding memory requirements. This hopefully enables many-body methods to incorporate many-body operators of high rank at reduced computational and storage cost.

We showed that singular-value decomposed approximations of the two-body potential lead to excellent reproduction of ground-state energies over a large range of nuclei. This is already true for low truncation of the SVD rank, leading to a compression of around 10 compared to the initial storage cost. It will be interesting to see how advanced many-body methods that are reformulated to explicitly take advantage of the low-rank structure will perform in future applications. Work along these lines is already in progress.

In addition to tensor-factorization techniques, importance-truncation techniques have been applied for the first time to the IMSRG in the IT-IMSRG. Neglecting unimportant contributions and performing many-body calculations only based on the most important contributions resulted in significantly compressed many-body operators and computational benefits at the price of introducing (small) errors compared to the full result. In this thesis, we focused on applications of the IT to two-body operators. We investigated multiple IT measures and studied how different truncations affect ground-state energies of finite nuclei in the IMSRG. Perturbative approaches at third order in perturbation theory using the neglected two-body matrix elements were used to estimate the error introduced by the IT. For soft interactions, these error estimates provided a reasonable correction in agreement with the actually observed error. The IT generally was observed to perform better in larger model spaces and yielded best results for soft interactions. Overall, we found that a large part of the interaction can be neglected while introducing only small errors for the total ground-state energy, e.g., neglecting 99% of all two-body matrix elements in large model spaces led to calculations with less than 1 MeV error to the exact IMSRG(2) result in mid-mass systems. Applications to various mid-mass systems finally showed the great applicability of the IT framework for a large range of mass numbers. All these results establish the IT-IMSRG as a promising tool to compress and accelerate many-body calculations. We expect that the IT-IMSRG approach can also be adapted to work with extensions of the IMSRG that target open-shell systems, such as the MR- or VS-IMSRG, with appropriately selected importance measures. Extending the IT approach to other operators and observables in the IMSRG is a next natural step, where either the same measure as for the Hamiltonian can be applied or new operator-specific measures can be developed.

The standard IMSRG approach truncates all operators at the normal-ordered two body-level, yielding the IMSRG(2). Triple corrections, not included in the IMSRG(2), however have been observed to be important for many observables. Targeting the second point mentioned above of improving the many-body method, we showed how the IMSRG can be extended to the next truncation order in the many-body expansion, including three-body operators in the IMSRG(3). We additionally derived approximate IMSRG(3) truncation schemes of lower computational cost and presented results for full and approximate IMSRG(3) truncations for ${}^4\text{He}$ and ${}^{16}\text{O}$. The IMSRG(3) systematically improves over the IMSRG(2) compared to exact results. However, given the tremendous computational cost, calculations are limited to small $e_{\text{max}} = 2$ model spaces and converged calculations in large model spaces are still outside of reach. Consequently, improving the scaling behavior or providing appropriate approximation techniques is a key goal towards more precise calculations.

The benefits observed for truncated natural orbitals are of strong interest for the IMSRG(3), where further improving the construction of single-particle basis sets will significantly help to advance to heavier nuclei and higher precision in *ab initio* applications. Based on the observed savings in single-particle dimension for the IMSRG(2), naive speed-ups of around 10^3 - 10^4 can be anticipated for the IMSRG(3). Advantages for high-order calculations

using the natural orbital basis, have also been observed in other many-body methods. In Ref. [74], natural orbital occupation numbers are used in CC calculations to tame the dimensionality of the space of three-body cluster amplitudes. Moreover, the developments for using importance-truncation techniques in the IMSRG are especially of great interest for the IMSRG(3) in order to lower the computational cost of evaluating the additional commutators and reducing the storage cost of handling three-body operators. In preliminary studies on three-body matrix elements, we have found that similar choices as for the IT-IMSRG(2) yield three-body compression ratios of about 100-1000, approximately an order of magnitude larger than in the two-body case. These substantial reductions in the number of three-body matrix elements could bring memory requirements associated with three-body operators into the range accessible with standard supercomputing nodes. An IT-IMSRG(3) solver tuned to handle the extremely sparse structure of the resulting operators could extend the range of the many-body method and make large model-space truncations or more expensive approximate IMSRG(3) truncations accessible.

Additionally, the input interactions, in particular the explicit inclusion of three-body interactions presents computational challenges for *ab initio* calculations. Normal-ordering techniques, which approximate the effect of three-body interactions by an effective two-body interaction, have been proven to be a key concept to systematically account for three-body contributions in a computationally efficient way. However, traditional normal-ordering frameworks require the representation of $3N$ interactions in a large single-particle basis, which leads to massive storage costs and necessitates an additional truncation $E_{3\max}$ in three-body space. Effects of this truncation become significant when approaching heavy systems.

In this thesis, we presented a novel normal-ordering framework in the Jacobi plane-wave basis that circumvents this drawback by requiring substantially less memory and allows to perform calculations without any truncation on three-body energy quantum numbers. Benchmark calculations for ground-state energies of light and medium-mass systems, comparing both frameworks, showed perfect agreement already for rather small truncations in the Jacobi normal ordering. Exploring heavier systems, we found that a fairly converged HF reference state, at $E_{3\max}$ values where ground-state energies in the single-particle normal ordering are still far from convergence, is sufficient to obtain converged results in the Jacobi framework. This is based on the mean-field solution converging faster than the many-body solution with respect to the model-space size. Comparing converged results in both frameworks again led to good agreement of ground-state and correlation energies. These findings were highlighted by calculations of ^{78}Ni , ^{132}Sn , and ^{208}Pb , demonstrating the versatility and benefits of the new normal-ordering approach. The framework can in future be straightforwardly applied to more refined reference states, such as a natural orbital reference state. Next steps and extensions of the Jacobi framework involve the application to open-shell systems, hence additionally being able to study excited-state properties. One possible approach towards this goal is, e.g., an equal-filling approximation with fractional occupied orbitals in the reference state, as applied in the VS-IMSRG in Ref. [94].

In summary, we accomplished improvements for some of the major challenges of rapidly increasing computational cost and memory demands in *ab initio* theory today. All the developments presented in this thesis pave the way for more precise many-body calculations and possibly allow to push the range of *ab initio* methods to higher mass numbers and more exotic systems.

List of Abbreviations

Abbreviation	Complete text
BCH	Baker-Campbell-Hausdorff
(B)MBPT	(Bogoliubov) many-body perturbation theory
CC	coupled-cluster
center-of-mass	cm
FCI	full configuration interaction
EFT	effective field theory
HF	Hartree-Fock
HO	harmonic oscillator
IMSRG	in-medium similarity renormalization group
IT	importance truncation
LEC	low-energy constant
LO	leading order
MP2/MP3	many-body perturbation theory up to second/third order
NAT	natural orbitals
NCSM	no-core shell model
NLO	next-to-leading order
N²LO	next-to-next-to-leading order
N³LO	next-to-next-to-next-to-leading order
NN	nucleon nucleon
NO	normal ordering
NO2B	normal-ordered two-body approximation
<i>npnh</i>	n-particle-n-hole
ODE	ordinary differential equation
QCD	quantum chromodynamics
QMC	quantum Monte Carlo
SCGF	self-consistent Green's function
SPE	single-particle energy
(S)RG	(similarity) renormalization group
SVD	singular value decomposition
3N	three nucleon

Table 7.1: List of used abbreviations in this thesis.

Bibliography

- [1] J. Erler, N. Birge, M. Kortelainen, W. Nazarewicz, E. Olsen, A. M. Perhac, and M. Stoitsov, “The limits of the nuclear landscape,” *Nature* **486**, 509 (2012).
- [2] M. Thoennessen, “Current status and future potential of nuclide discoveries,” *Rep. Prog. Phys.* **76**, 056301 (2013).
- [3] X. W. Xia, Y. Lim, P. W. Zhao, H. Z. Liang, X. Y. Qu, Y. Chen, H. Liu, L. F. Zhang, S. Q. Zhang, Y. Kim, *et al.*, “The limits of the nuclear landscape explored by the relativistic continuum Hartree–Bogoliubov theory,” *At. Data Nucl. Data Tables* **121-122**, 1 (2018).
- [4] C. Drischler and S. K. Bogner, “A Brief Account of Steven Weinberg’s Legacy in *ab initio* Many-Body Theory,” *Few-Body Syst.* **62**, 109 (2021).
- [5] S. R. Beane, W. Detmold, K. Orginos, and M. J. Savage, “Nuclear physics from lattice QCD,” *Prog. Part. Nucl. Phys.* **66**, 1 (2011).
- [6] S. Aoki *et al.* (FLAG Collaboration), “Review of lattice results concerning low-energy particle physics,” *Eur. Phys. J. C* **77**, 112 (2017).
- [7] S. R. Beane, E. Chang, S. D. Cohen, W. Detmold, H. W. Lin, T. C. Luu, K. Orginos, A. Parreño, M. J. Savage, and A. Walker-Loud (NPLQCD Collaboration), “Light nuclei and hypernuclei from quantum chromodynamics in the limit of SU(3) flavor symmetry,” *Phys. Rev. D* **87**, 034506 (2013).
- [8] S. R. Beane, E. Chang, S. Cohen, W. Detmold, H. W. Lin, K. Orginos, A. Parreño, M. J. Savage, and B. C. Tiburzi (NPLQCD Collaboration), “Magnetic Moments of Light Nuclei from Lattice Quantum Chromodynamics,” *Phys. Rev. Lett.* **113**, 252001 (2014).
- [9] S. Weinberg, “Nuclear forces from chiral lagrangians,” *Phys. Lett. B* **251**, 288 (1990).
- [10] S. Weinberg, “Effective chiral lagrangians for nucleon-pion interactions and nuclear forces,” *Nucl. Phys. B* **363**, 3 (1991).
- [11] S. Weinberg, “Three-body interactions among nucleons and pions,” *Phys. Lett. B* **295**, 114 (1992).
- [12] E. Epelbaum, H.-W. Hammer, and U.-G. Meißner, “Modern theory of nuclear forces,” *Rev. Mod. Phys.* **81**, 1773 (2009).
- [13] V. G. J. Stoks, R. A. M. Klomp, M. C. M. Rentmeester, and J. J. de Swart, “Partial-wave analysis of all nucleon-nucleon scattering data below 350 MeV,” *Phys. Rev. C* **48**, 792 (1993).
- [14] R. B. Wiringa, V. G. J. Stoks, and R. Schiavilla, “Accurate nucleon-nucleon potential with charge-independence breaking,” *Phys. Rev. C* **51**, 38 (1995).

- [15] R. Machleidt, “High-precision, charge-dependent Bonn nucleon-nucleon potential,” *Phys. Rev. C* **63**, 024001 (2001).
- [16] S. K. Bogner, R. J. Furnstahl, and R. J. Perry, “Similarity renormalization group for nucleon-nucleon interactions,” *Phys. Rev. C* **75**, 061001(R) (2007).
- [17] R. J. Furnstahl and K. Hebeler, “New applications of renormalization group methods in nuclear physics,” *Rep. Prog. Phys.* **76**, 126301 (2013).
- [18] A. Tichai, J. Langhammer, S. Binder, and R. Roth, “Hartree-Fock many-body perturbation theory for nuclear ground-states,” *Phys. Lett. B* **756**, 283 (2016).
- [19] H. Hergert, “A Guided Tour of *ab initio* Nuclear Many-Body Theory,” *Front. Phys.* **8**, 379 (2020).
- [20] P. Navrátil, S. Quaglioni, I. Stetcu, and B. R. Barrett, “Recent developments in no-core shell-model calculations,” *J. Phys. G* **36**, 083101 (2009).
- [21] R. Roth, “Importance truncation for large-scale configuration interaction approaches,” *Phys. Rev. C* **79**, 064324 (2009).
- [22] R. Roth, J. Langhammer, A. Calci, S. Binder, and P. Navrátil, “Similarity-Transformed Chiral NN+3N Interactions for the *Ab Initio* Description of ^{12}C and ^{16}O ,” *Phys. Rev. Lett.* **107**, 072501 (2011).
- [23] B. R. Barrett, P. Navrátil, and J. P. Vary, “*Ab initio* no core shell model,” *Prog. Part. Nucl. Phys.* **69**, 131 (2013).
- [24] A. Gezerlis, I. Tews, E. Epelbaum, S. Gandolfi, K. Hebeler, A. Nogga, and A. Schwenk, “Quantum Monte Carlo Calculations with Chiral Effective Field Theory Interactions,” *Phys. Rev. Lett.* **111**, 032501 (2013).
- [25] J. Carlson, S. Gandolfi, F. Pederiva, S. C. Pieper, R. Schiavilla, K. E. Schmidt, and R. B. Wiringa, “Quantum Monte Carlo methods for nuclear physics,” *Rev. Mod. Phys.* **87**, 1067 (2015).
- [26] J. E. Lynn, I. Tews, S. Gandolfi, and A. Lovato, “Quantum Monte Carlo Methods in Nuclear Physics: Recent Advances,” *Ann. Rev. Nucl. Part. Sci.* **69**, 279 (2019).
- [27] D. Lonardoni, S. Gandolfi, J. E. Lynn, C. Petrie, J. Carlson, K. E. Schmidt, and A. Schwenk, “Auxiliary field diffusion Monte Carlo calculations of light and medium-mass nuclei with local chiral interactions,” *Phys. Rev. C* **97**, 044318 (2018).
- [28] G. Hagen, T. Papenbrock, M. Hjorth-Jensen, and D. J. Dean, “Coupled-cluster computations of atomic nuclei,” *Rep. Prog. Phys.* **77**, 096302 (2014).
- [29] S. Binder, J. Langhammer, A. Calci, and R. Roth, “*Ab initio* path to heavy nuclei,” *Phys. Lett. B* **736**, 119 (2014).
- [30] K. Tsukiyama, S. K. Bogner, and A. Schwenk, “In-Medium Similarity Renormalization Group For Nuclei,” *Phys. Rev. Lett.* **106**, 222502 (2011).
- [31] H. Hergert, S. K. Bogner, T. D. Morris, A. Schwenk, and K. Tsukiyama, “The In-Medium Similarity Renormalization Group: A novel *ab initio* method for nuclei,” *Phys. Rept.* **621**, 165 (2016).
- [32] S. R. Stroberg, H. Hergert, S. K. Bogner, and J. D. Holt, “Nonempirical Interactions for the Nuclear Shell Model: An Update,” *Annu. Rev. Nucl. Part. Sci.* **69**, 307 (2019).

- [33] W. H. Dickhoff and C. Barbieri, “Self-consistent Green’s function method for nuclei and nuclear matter,” *Prog. Part. Nucl. Phys.* **52**, 377 (2004).
- [34] V. Somà, P. Navrátil, F. Raimondi, C. Barbieri, and T. Duguet, “Novel chiral Hamiltonian and observables in light and medium-mass nuclei,” *Phys. Rev. C* **101**, 014318 (2020).
- [35] A. Tichai, R. Roth, and T. Duguet, “Many-Body Perturbation Theories for Finite Nuclei,” *Front. Phys.* **8**, 164 (2020).
- [36] J. D. Holt, J. Menéndez, J. Simonis, and A. Schwenk, “Three-nucleon forces and spectroscopy of neutron-rich calcium isotopes,” *Phys. Rev. C* **90**, 024312 (2014).
- [37] A. Tichai, P. Arthuis, T. Duguet, H. Hergert, V. Somà, and R. Roth, “Bogoliubov many-body perturbation theory for open-shell nuclei,” *Phys. Lett. B* **786**, 195 (2018).
- [38] E. Epelbaum, H. Krebs, and U.-G. Meißner, “Improved chiral nucleon-nucleon potential up to next-to-next-to-next-to-leading order,” *Eur. Phys. J. A* **51**, 53 (2015).
- [39] R. J. Furnstahl, D. R. Phillips, and S. Wesolowski, “A recipe for EFT uncertainty quantification in nuclear physics,” *J. Phys. G* **42**, 034028 (2015).
- [40] J. A. Melendez, S. Wesolowski, and R. J. Furnstahl, “Bayesian truncation errors in chiral effective field theory: Nucleon-nucleon observables,” *Phys. Rev. C* **96**, 024003 (2017).
- [41] J. A. Melendez, R. J. Furnstahl, D. R. Phillips, M. T. Pratola, and S. Wesolowski, “Quantifying correlated truncation errors in effective field theory,” *Phys. Rev. C* **100**, 044001 (2019).
- [42] D. R. Phillips, R. J. Furnstahl, U. Heinz, T. Maiti, W. Nazarewicz, F. M. Nunes, M. Plumlee, M. T. Pratola, S. Pratt, F. G. Viens, *et al.*, “Get on the BAND Wagon: a Bayesian framework for quantifying model uncertainties in nuclear dynamics,” *J. Phys. G* **48**, 072001 (2021).
- [43] D. Frame, R. He, I. Ipsen, D. Lee, D. Lee, and E. Rrapaj, “Eigenvector Continuation with Subspace Learning,” *Phys. Rev. Lett.* **121**, 032501 (2018).
- [44] S. König, A. Ekström, K. Hebeler, D. Lee, and A. Schwenk, “Eigenvector continuation as an efficient and accurate emulator for uncertainty quantification,” *Phys. Lett. B* **810**, 135814 (2020).
- [45] A. Ekström and G. Hagen, “Global Sensitivity Analysis of Bulk Properties of an Atomic Nucleus,” *Phys. Rev. Lett.* **123**, 252501 (2019).
- [46] D. R. Entem and R. Machleidt, “Accurate charge-dependent nucleon-nucleon potential at fourth order of chiral perturbation theory,” *Phys. Rev. C* **68**, 041001(R) (2003).
- [47] P. Navrátil, “Local three-nucleon interaction from chiral effective field theory,” *Few Body Syst.* **41**, 117 (2007).
- [48] M. Wang, G. Audi, F. G. Kondev, W. J. Huang, S. Naimi, and X. Xu, “The AME2016 atomic mass evaluation (II). Tables, graphs and references,” *Chin. Phys. C* **41**, 030003 (2017).
- [49] T. D. Morris, J. Simonis, S. R. Stroberg, C. Stumpf, G. Hagen, J. D. Holt, G. R. Jansen, T. Papenbrock, R. Roth, and A. Schwenk, “Structure of the Lightest Tin Isotopes,” *Phys. Rev. Lett.* **120**, 152503 (2018).

- [50] T. Miyagi, S. R. Stroberg, P. Navrátil, K. Hebeler, and J. D. Holt, “Converged *ab initio* calculations of heavy nuclei,” *Phys. Rev. C* **105**, 014302 (2022).
- [51] B. Hu, W. Jiang, T. Miyagi, Z. Sun, A. Ekström, C. Forssén, G. Hagen, J. D. Holt, T. Papenbrock, S. R. Stroberg, *et al.*, *Ab initio predictions link the neutron skin of ^{208}Pb to nuclear forces*, 2021, [arXiv:2112.01125](https://arxiv.org/abs/2112.01125).
- [52] J. Hoppe, C. Drischler, K. Hebeler, A. Schwenk, and J. Simonis, “Probing chiral interactions up to next-to-next-to-next-to-leading order in medium-mass nuclei,” *Phys. Rev. C* **100**, 024318 (2019).
- [53] T. Hübner, K. Vobig, K. Hebeler, R. Machleidt, and R. Roth, “Family of chiral two-plus three-nucleon interactions for accurate nuclear structure studies,” *Phys. Lett. B* **808**, 135651 (2020).
- [54] K. Hebeler, S. K. Bogner, R. J. Furnstahl, A. Nogga, and A. Schwenk, “Improved nuclear matter calculations from chiral low-momentum interactions,” *Phys. Rev. C* **83**, 031301(R) (2011).
- [55] J. Simonis, S. R. Stroberg, K. Hebeler, J. D. Holt, and A. Schwenk, “Saturation with chiral interactions and consequences for finite nuclei,” *Phys. Rev. C* **96**, 014303 (2017).
- [56] D. R. Entem, R. Machleidt, and Y. Nosyk, “High-quality two-nucleon potentials up to fifth order of the chiral expansion,” *Phys. Rev. C* **96**, 024004 (2017).
- [57] C. Drischler, K. Hebeler, and A. Schwenk, “Chiral Interactions up to Next-to-Next-to-Next-to-Leading Order and Nuclear Saturation,” *Phys. Rev. Lett.* **122**, 042501 (2019).
- [58] A. Ekström, G. R. Jansen, K. A. Wendt, G. Hagen, T. Papenbrock, B. D. Carlsson, C. Forssén, M. Hjorth-Jensen, P. Navrátil, and W. Nazarewicz, “Accurate nuclear radii and binding energies from a chiral interaction,” *Phys. Rev. C* **91**, 051301(R) (2015).
- [59] B. D. Carlsson, A. Ekström, C. Forssén, D. F. Strömberg, G. R. Jansen, O. Lilja, M. Lindby, B. A. Mattsson, and K. A. Wendt, “Uncertainty Analysis and Order-by-Order Optimization of Chiral Nuclear Interactions,” *Phys. Rev. X* **6**, 011019 (2016).
- [60] A. Ekström, G. Hagen, T. D. Morris, T. Papenbrock, and P. D. Schwartz, “ Δ isobars and nuclear saturation,” *Phys. Rev. C* **97**, 024332 (2018).
- [61] W. G. Jiang, A. Ekström, C. Forssén, G. Hagen, G. R. Jansen, and T. Papenbrock, “Accurate bulk properties of nuclei from $A = 2$ to ∞ from potentials with Δ isobars,” *Phys. Rev. C* **102**, 054301 (2020).
- [62] M. Piarulli and I. Tews, “Local Nucleon-Nucleon and Three-Nucleon Interactions Within Chiral Effective Field Theory,” *Front. Phys.* **7**, 245 (2020).
- [63] E. Epelbaum, J. Golak, K. Hebeler, T. Hübner, H. Kamada, H. Krebs, P. Maris, U.-G. Meißner, A. Nogga, R. Roth, *et al.* (LENPIC Collaboration), “Few- and many-nucleon systems with semilocal coordinate-space regularized chiral two- and three-body forces,” *Phys. Rev. C* **99**, 024313 (2019).
- [64] P. Maris, E. Epelbaum, R. J. Furnstahl, J. Golak, K. Hebeler, T. Hübner, H. Kamada, H. Krebs, U.-G. Meißner, J. A. Melendez, *et al.* (LENPIC Collaboration), “Light nuclei with semilocal momentum-space regularized chiral interactions up to third order,” *Phys. Rev. C* **103**, 054001 (2021).

- [65] T. Djärv, A. Ekström, C. Forssén, and H. T. Johansson, “Bayesian predictions for $A = 6$ nuclei using eigenvector continuation emulators,” *Phys. Rev. C* **105**, 014005 (2022).
- [66] T. Otsuka, T. Suzuki, J. D. Holt, A. Schwenk, and Y. Akaishi, “Three-Body Forces and the Limit of Oxygen Isotopes,” *Phys. Rev. Lett.* **105**, 032501 (2010).
- [67] G. Hagen, M. Hjorth-Jensen, G. R. Jansen, R. Machleidt, and T. Papenbrock, “Continuum Effects and Three-Nucleon Forces in Neutron-Rich Oxygen Isotopes,” *Phys. Rev. Lett.* **108**, 242501 (2012).
- [68] H. Hergert, S. Binder, A. Calci, J. Langhammer, and R. Roth, “*Ab Initio* Calculations of Even Oxygen Isotopes with Chiral Two-Plus-Three-Nucleon Interactions,” *Phys. Rev. Lett.* **110**, 242501 (2013).
- [69] V. Somà, T. Duguet, and C. Barbieri, “*Ab initio* self-consistent Gorkov-Green’s function calculations of semimagic nuclei: Formalism at second order with a two-nucleon interaction,” *Phys. Rev. C*, 064317.
- [70] K. Tsukiyama, S. K. Bogner, and A. Schwenk, “In-medium similarity renormalization group for open-shell nuclei,” *Phys. Rev. C* **85**, 061304(R) (2012).
- [71] G. R. Jansen, J. Engel, G. Hagen, P. Navrátil, and A. Signoracci, “*Ab Initio* Coupled-Cluster Effective Interactions for the Shell Model: Application to Neutron-Rich Oxygen and Carbon Isotopes,” *Phys. Rev. Lett.* **113**, 142502 (2014).
- [72] H. Hergert, “In-medium similarity renormalization group for closed and open-shell nuclei,” *Phys. Scr.* **92**, 023002 (2017).
- [73] J. M. Yao, J. Engel, L. J. Wang, C. F. Jiao, and H. Hergert, “Generator-coordinate reference states for spectra and $0\nu\beta\beta$ decay in the in-medium similarity renormalization group,” *Phys. Rev. C* **98**, 054311 (2018).
- [74] S. J. Novario, G. Hagen, G. R. Jansen, and T. Papenbrock, “Charge radii of exotic neon and magnesium isotopes,” *Phys. Rev. C* **102**, 051303(R) (2020).
- [75] S. R. Stroberg, J. D. Holt, A. Schwenk, and J. Simonis, “*Ab Initio* Limits of Atomic Nuclei,” *Phys. Rev. Lett.* **126**, 022501 (2021).
- [76] Q. Yuan, S. Q. Fan, B. S. Hu, J. G. Li, S. Zhang, S. M. Wang, Z. H. Sun, Y. Z. Ma, and F. R. Xu, *Deformed in-medium similarity renormalization group*, 2022, [arXiv:2204.07301](https://arxiv.org/abs/2204.07301).
- [77] V. Somà, A. Cipollone, C. Barbieri, P. Navrátil, and T. Duguet, “Chiral two- and three-nucleon forces along medium-mass isotope chains,” *Phys. Rev. C* **89**, 061301(R) (2014).
- [78] P. Demol, M. Frosini, A. Tichai, V. Somà, and T. Duguet, “Bogoliubov many-body perturbation theory under constraint,” *Ann. Phys.* **424**, 168358 (2021).
- [79] A. Signoracci, T. Duguet, G. Hagen, and G. R. Jansen, “*Ab initio* Bogoliubov coupled cluster theory for open-shell nuclei,” *Phys. Rev. C* **91**, 064320 (2015).
- [80] M. Frosini, T. Duguet, J.-P. Ebran, and V. Somà, “Multi-reference many-body perturbation theory for nuclei I – Novel PGCM-PT formalism,” *Eur. Phys. J. A* **58**, 62 (2022).

- [81] M. Frosini, T. Duguet, J.-P. Ebran, B. Bally, T. Mongelli, T. R. Rodríguez, R. Roth, and V. Somà, “Multi-reference many-body perturbation theory for nuclei II – Ab initio study of neon isotopes via PGCM and IM-NCSM calculations,” *Eur. Phys. J. A* **58**, 63 (2022).
- [82] M. Frosini, T. Duguet, J.-P. Ebran, B. Bally, H. Hergert, T. R. Rodríguez, R. Roth, J. Yao, and V. Somà, “Multi-reference many-body perturbation theory for nuclei III – Ab initio calculations at second order in PGCM-PT,” *Eur. Phys. J. A* **58**, 64 (2022).
- [83] G. Hagen, S. J. Novario, Z. H. Sun, T. Papenbrock, G. R. Jansen, J. G. Lietz, T. Duguet, and A. Tichai, *Angular-momentum projection in coupled-cluster theory: structure of ^{34}Mg* , 2022, [arXiv:2201.07298](https://arxiv.org/abs/2201.07298).
- [84] F. T. Avignone, S. R. Elliott, and J. Engel, “Double beta decay, Majorana neutrinos, and neutrino mass,” *Rev. Mod. Phys.* **80**, 481 (2008).
- [85] B. R. Holstein, “Precision frontier in semileptonic weak interactions: theory,” *J. Phys. G: Nucl. Part. Phys.* **41**, 114001 (2014).
- [86] S. R. Stroberg, “Beta Decay in Medium-Mass Nuclei with the In-Medium Similarity Renormalization Group,” *Particles* **4**, 521 (2021).
- [87] J. Engel and J. Menéndez, “Status and future of nuclear matrix elements for neutrinoless double-beta decay: a review,” *Rep. Prog. Phys.* **80**, 046301 (2017).
- [88] J. M. Yao, B. Bally, J. Engel, R. Wirth, T. R. Rodríguez, and H. Hergert, “*Ab Initio* Treatment of Collective Correlations and the Neutrinoless Double Beta Decay of ^{48}Ca ,” *Phys. Rev. Lett.* **124**, 232501 (2020).
- [89] A. Belley, C. G. Payne, S. R. Stroberg, T. Miyagi, and J. D. Holt, “*Ab Initio* Neutrinoless Double-Beta Decay Matrix Elements for ^{48}Ca , ^{76}Ge , and ^{82}Se ,” *Phys. Rev. Lett.* **126**, 042502 (2021).
- [90] G. Hagen, G. R. Jansen, and T. Papenbrock, “Structure of ^{78}Ni from First-Principles Computations,” *Phys. Rev. Lett.* **117**, 172501 (2016).
- [91] N. M. Parzuchowski, S. R. Stroberg, P. Navrátil, H. Hergert, and S. K. Bogner, “*Ab initio* electromagnetic observables with the in-medium similarity renormalization group,” *Phys. Rev. C* **96**, 034324 (2017).
- [92] S. R. Stroberg, J. Henderson, G. Hackman, P. Ruotsalainen, G. Hagen, and J. D. Holt, “Systematics of $E2$ strength in the sd shell with the valence-space in-medium similarity renormalization group,” *Phys. Rev. C* **105**, 034333 (2022).
- [93] S. K. Bogner, H. Hergert, J. D. Holt, A. Schwenk, S. Binder, A. Calci, J. Langhammer, and R. Roth, “Nonperturbative Shell-Model Interactions from the In-Medium Similarity Renormalization Group,” *Phys. Rev. Lett.* **113**, 142501 (2014).
- [94] S. R. Stroberg, A. Calci, H. Hergert, J. D. Holt, S. K. Bogner, R. Roth, and A. Schwenk, “Nucleus-Dependent Valence-Space Approach to Nuclear Structure,” *Phys. Rev. Lett.* **118**, 032502 (2017).
- [95] V. Durant, “*Chiral interactions for nuclear reactions and heavy nuclei*,” PhD thesis (Technische Universität Darmstadt 2019).

- [96] R. Machleidt, “The Meson Theory of Nuclear Forces and Nuclear Structure,” in *Advances in nuclear physics*, edited by J. W. Negele and E. Vogt (Springer US, Boston, MA, 1989), p. 189.
- [97] H. Yukawa, “On the Interaction of Elementary Particles I,” *Proc. Phys. Math. Soc. Jap.* **17**, 48 (1955).
- [98] D. B. Kaplan, “Five lectures on effective field theory,” in *Lectures delivered at the 17th National Nuclear Physics Summer School, Berkeley, June 6-17* (2005).
- [99] R. Machleidt and D. R. Entem, “Chiral effective field theory and nuclear forces,” *Phys. Rep.* **503**, 1 (2011).
- [100] I. Hinchliffe and A. Manohar, “The QCD Coupling Constant,” *Annu. Rev. Nucl. Part. Sci.* **50**, 643 (2000).
- [101] S. Bethke, “Experimental tests of asymptotic freedom,” *Prog. Part. Nucl. Phys.* **58**, 351 (2007).
- [102] P. A. Zyla, R. M. Barnett, J. Beringer, O. Dahl, D. A. Dwyer, D. E. Groom, C.-J. Lin, K. S. Lugovsky, E. Pianori, D. J. Robinson, *et al.* (Particle Data Group), “Review of Particle Physics,” *Prog. Theor. Exp. Phys.* **2020**, 083C01 (2020).
- [103] R. Aaij, B. Adeva, M. Adinolfi, A. Affolder, Z. Ajaltouni, S. Akar, J. Albrecht, F. Alessio, M. Alexander, S. Ali, *et al.* (LHCb Collaboration), “Observation of $J/\psi p$ Resonances Consistent with Pentaquark States in $\Lambda_b^0 \rightarrow J/\psi K^- p$ Decays,” *Phys. Rev. Lett.* **115**, 072001 (2015).
- [104] R. Aaij, C. Abellán Beteta, B. Adeva, M. Adinolfi, Z. Ajaltouni, S. Akar, J. Albrecht, F. Alessio, M. Alexander, S. Ali, *et al.* (LHCb Collaboration), “Model-Independent Evidence for $J/\psi p$ Contributions to $\Lambda_b^0 \rightarrow J/\psi p K^-$ Decays,” *Phys. Rev. Lett.* **117**, 082002 (2016).
- [105] R. Aaij, C. Abellán Beteta, B. Adeva, M. Adinolfi, C. A. Aidala, Z. Ajaltouni, S. Akar, P. Albicocco, J. Albrecht, F. Alessio, *et al.* (LHCb Collaboration), “Observation of a Narrow Pentaquark State, $P_c(4312)^+$, and of the Two-Peak Structure of the $P_c(4450)^+$,” *Phys. Rev. Lett.* **122**, 222001 (2019).
- [106] R. Aaij, B. Adeva, M. Adinolfi, Z. Ajaltouni, S. Akar, J. Albrecht, F. Alessio, M. Alexander, S. Ali, G. Alkhazov, *et al.* (LHCb Collaboration), “Observation of $J/\psi \phi$ Structures Consistent with Exotic States from Amplitude Analysis of $B^+ \rightarrow J/\psi \phi K^+$ Decays,” *Phys. Rev. Lett.* **118**, 022003 (2017).
- [107] R. Aaij, B. Adeva, M. Adinolfi, Z. Ajaltouni, S. Akar, J. Albrecht, F. Alessio, M. Alexander, S. Ali, G. Alkhazov, *et al.* (LHCb Collaboration), “Amplitude analysis of $B^+ \rightarrow J/\psi \phi K^+$ decays,” *Phys. Rev. D* **95**, 012002 (2017).
- [108] S. L. Olsen, T. Skwarnicki, and D. Zieminska, “Nonstandard heavy mesons and baryons: Experimental evidence,” *Rev. Mod. Phys.* **90**, 015003 (2018).
- [109] S. R. Beane, E. Chang, S. D. Cohen, W. Detmold, P. Junnarkar, H. W. Lin, T. C. Luu, K. Orginos, A. Parreño, M. J. Savage, *et al.* (NPLQCD Collaboration), “Nucleon-nucleon scattering parameters in the limit of SU(3) flavor symmetry,” *Phys. Rev. C* **88**, 024003 (2013).
- [110] N. Ishii, S. Aoki, and T. Hatsuda, “Nuclear Force from Lattice QCD,” *Phys. Rev. Lett.* **99**, 022001 (2007).

- [111] S. Aoki and T. Doi, “Lattice QCD and Baryon-Baryon Interactions: HAL QCD Method,” *Front. Phys.* **8**, 307 (2020).
- [112] C. C. Chang, A. N. Nicholson, E. Rinaldi, E. Berkowitz, N. Garron, D. A. Brantley, H. Monge-Camacho, C. J. Monahan, C. Bouchard, M. A. Clark, *et al.*, “A per-cent-level determination of the nucleon axial coupling from quantum chromodynamics,” *Nature* **558**, 91 (2018).
- [113] C. Gattringer and C. B. Lang, *Quantum chromodynamics on the lattice*, Vol. 788 (Springer, Berlin, 2010).
- [114] J. Goldstone, A. Salam, and S. Weinberg, “Broken Symmetries,” *Phys. Rev.* **127**, 965 (1962).
- [115] E. Epelbaum, H. Krebs, and P. Reinert, “High-Precision Nuclear Forces From Chiral EFT: State-of-the-Art, Challenges, and Outlook,” *Front. Phys.* **8**, 98 (2020).
- [116] N. Barnea, L. Contessi, D. Gazit, F. Pederiva, and U. van Kolck, “Effective Field Theory for Lattice Nuclei,” *Phys. Rev. Lett.* **114**, 052501 (2015).
- [117] J. Kirscher, N. Barnea, D. Gazit, F. Pederiva, and U. van Kolck, “Spectra and scattering of light lattice nuclei from effective field theory,” *Phys. Rev. C* **92**, 054002 (2015).
- [118] A. Bansal, S. Binder, A. Ekström, G. Hagen, G. R. Jansen, and T. Papenbrock, “Pionless effective field theory for atomic nuclei and lattice nuclei,” *Phys. Rev. C* **98**, 054301 (2018).
- [119] L. Contessi, A. Lovato, F. Pederiva, A. Roggero, J. Kirscher, and U. van Kolck, “Ground-state properties of ^4He and ^{16}O extrapolated from lattice QCD with pionless EFT,” *Phys. Lett. B* **772**, 839 (2017).
- [120] I. Tews, Z. Davoudi, A. Ekström, J. D. Holt, and J. E. Lynn, “New ideas in constraining nuclear forces,” *J. Phys. G: Nucl. Part. Phys* **47**, 103001 (2020).
- [121] A. Nogga, R. G. E. Timmermans, and U. van Kolck, “Renormalization of one-pion exchange and power counting,” *Phys. Rev. C* **72**, 054006 (2005).
- [122] M. Pavón Valderrama and D. R. Phillips, “Power Counting of Contact-Range Currents in Effective Field Theory,” *Phys. Rev. Lett.* **114**, 082502 (2015).
- [123] M. Pavón Valderrama, “Power counting and Wilsonian renormalization in nuclear effective field theory,” *Int. J. Mod. Phys. E* **25**, 1641007 (2016).
- [124] B. Long, “Power counting for nuclear forces in chiral effective field theory,” *Int. J. Mod. Phys. E* **25**, 1641006 (2016).
- [125] M. Drissi, T. Duguet, and V. Somà, “Renormalization of pionless effective field theory in the A-body sector,” *Eur. Phys. J. A* **56** (2020).
- [126] H.-W. Hammer, S. König, and U. van Kolck, “Nuclear effective field theory: Status and perspectives,” *Rev. Mod. Phys.* **92**, 025004 (2020).
- [127] M. Fierz, “Zur Fermischen Theorie des β -Zerfalls,” *Z. Phys* **104**, 553 (1937).
- [128] L. Huth, I. Tews, J. E. Lynn, and A. Schwenk, “Analyzing the Fierz rearrangement freedom for local chiral two-nucleon potentials,” *Phys. Rev. C* **96**, 054003 (2017).
- [129] C. Drischler, W. Haxton, K. McElvain, E. Mereghetti, A. Nicholson, P. Vranas, and A. Walker-Loud, “Towards grounding nuclear physics in QCD,” *Prog. Part. Nucl. Phys.* **121**, 103888 (2021).

- [130] K. Hebeler, “Three-nucleon forces: Implementation and applications to atomic nuclei and dense matter,” *Phys. Rep.* **890**, 1 (2021).
- [131] U. van Kolck, “Few-nucleon forces from chiral Lagrangians,” *Phys. Rev. C* **49**, 2932 (1994).
- [132] V. Bernard, E. Epelbaum, H. Krebs, and U.-G. Meißner, “Subleading contributions to the chiral three-nucleon force: Long-range terms,” *Phys. Rev. C* **77**, 064004 (2008).
- [133] V. Bernard, E. Epelbaum, H. Krebs, and U.-G. Meißner, “Subleading contributions to the chiral three-nucleon force. II. Short-range terms and relativistic corrections,” *Phys. Rev. C* **84**, 054001 (2011).
- [134] S. Ishikawa and M. R. Robilotta, “Two-pion exchange three-nucleon potential: $\mathcal{O}(q^4)$ chiral expansion,” *Phys. Rev. C* **76**, 014006 (2007).
- [135] K. Hebeler, H. Krebs, E. Epelbaum, J. Golak, and R. Skibiński, “Efficient calculation of chiral three-nucleon forces up to N³LO for *ab initio* studies,” *Phys. Rev. C* **91**, 044001 (2015).
- [136] C. Drischler, A. Carbone, K. Hebeler, and A. Schwenk, “Neutron matter from chiral two- and three-nucleon calculations up to N³LO,” *Phys. Rev. C* **94**, 054307 (2016).
- [137] BUGEYE collaboration, <https://buqeye.github.io/> (2021).
- [138] P. F. Bedaque and U. van Kolck, “Effective Field Theory for Few-Nucleon Systems,” *Annu. Rev. Nucl. Part. Sci.* **52**, 339 (2002).
- [139] H. Krebs, E. Epelbaum, and U.-G. Meißner, “Nuclear forces with Δ excitations up to next-to-next-to-leading order, part I: Peripheral nucleon-nucleon waves,” *Eur. Phys. J. A* **32**, 127 (2007).
- [140] H. Krebs, A. M. Gasparyan, and E. Epelbaum, “Three-nucleon force in chiral effective field theory with explicit $\Delta(1232)$ degrees of freedom: longest-range contributions at fourth order,” *Phys. Rev. C* **98**, 014003 (2018).
- [141] J. Fujita and H. Miyazawa, “Pion Theory of Three-Body Forces,” *Prog. Theor. Phys.* **17**, 360 (1957).
- [142] I. Tews, T. Krüger, K. Hebeler, and A. Schwenk, “Neutron Matter at Next-to-Next-to-Next-to-Leading Order in Chiral Effective Field Theory,” *Phys. Rev. Lett.* **110**, 032504 (2013).
- [143] S. Schulz, “*Four-Nucleon Forces in Ab Initio Nuclear Structure*,” PhD thesis (Technische Universität Darmstadt 2018).
- [144] A. Gezerlis, I. Tews, E. Epelbaum, M. Freunek, S. Gandolfi, K. Hebeler, A. Nogga, and A. Schwenk, “Local chiral effective field theory interactions and quantum Monte Carlo applications,” *Phys. Rev. C* **90**, 054323 (2014).
- [145] M. Piarulli, L. Girlanda, R. Schiavilla, A. Kievsky, A. Lovato, L. E. Marcucci, S. C. Pieper, M. Viviani, and R. B. Wiringa, “Local chiral potentials with Δ -intermediate states and the structure of light nuclei,” *Phys. Rev. C* **94**, 054007 (2016).
- [146] E. Epelbaum, H. Krebs, and U.-G. Meißner, “Precision Nucleon-Nucleon Potential at Fifth Order in the Chiral Expansion,” *Phys. Rev. Lett.* **115**, 122301 (2015).
- [147] P. Reinert, H. Krebs, and E. Epelbaum, “Semilocal momentum-space regularized chiral two-nucleon potentials up to fifth order,” *Eur. Phys. J. A* **54**, 86 (2018).

- [148] J. Hoppe, C. Drischler, R. J. Furnstahl, K. Hebeler, and A. Schwenk, “Weinberg eigenvalues for chiral nucleon-nucleon interactions,” *Phys. Rev. C* **96**, 054002 (2017).
- [149] E. Epelbaum, A. Nogga, W. Glöckle, H. Kamada, U.-G. Meißner, and H. Witała, “Three-nucleon forces from chiral effective field theory,” *Phys. Rev. C* **66**, 064001 (2002).
- [150] J. Tjon, “Bound states of ^4He with local interactions,” *Phys. Lett. B* **56**, 217 (1975).
- [151] L. Platter, H.-W. Hammer, and U.-G. Meißner, “Four-boson system with short range interactions,” *Phys. Rev. A* **70**, 052101 (2004).
- [152] D. Gazit, S. Quaglioni, and P. Navrátil, “Three-Nucleon Low-Energy Constants from the Consistency of Interactions and Currents in Chiral Effective Field Theory,” *Phys. Rev. Lett.* **103**, 102502 (2009). [Erratum: *Phys. Rev. Lett.* **122**, 029901 (2019)].
- [153] Y. Nosyk, D. R. Entem, and R. Machleidt, “Nucleon-nucleon potentials from Δ -full chiral effective-field-theory and implications,” *Phys. Rev. C* **104**, 054001 (2021).
- [154] S. Wesolowski, I. Svensson, A. Ekström, C. Forssén, R. J. Furnstahl, J. A. Melendez, and D. R. Phillips, “Rigorous constraints on three-nucleon forces in chiral effective field theory from fast and accurate calculations of few-body observables,” *Phys. Rev. C* **104**, 064001 (2021).
- [155] S. K. Bogner, A. Schwenk, R. J. Furnstahl, and A. Nogga, “Is nuclear matter perturbative with low-momentum interactions?” *Nucl. Phys. A* **763**, 59 (2005).
- [156] F. Wegner, “Flow-equations for Hamiltonians,” *Ann. Phys.* **506**, 77 (1994).
- [157] F. Wegner, “Flow equations for Hamiltonians,” *Nucl. Phys. B Proc. Suppl.* **90**, 141 (2000).
- [158] S. D. Glazek and K. G. Wilson, “Renormalization of Hamiltonians,” *Phys. Rev. D* **48**, 5863 (1993).
- [159] S. D. Glazek and K. G. Wilson, “Perturbative renormalization group for Hamiltonians,” *Phys. Rev. D* **49**, 4214 (1994).
- [160] A. J. Tropiano, S. K. Bogner, and R. J. Furnstahl, “Operator evolution from the similarity renormalization group and the Magnus expansion,” *Phys. Rev. C* **102** (2020).
- [161] A. J. Tropiano, S. K. Bogner, and R. J. Furnstahl, “Short-range correlation physics at low renormalization group resolution,” *Phys. Rev. C* **104** (2021).
- [162] E. Anderson, S. K. Bogner, R. J. Furnstahl, E. D. Jurgenson, R. J. Perry, and A. Schwenk, “Block diagonalization using similarity renormalization group flow equations,” *Phys. Rev. C* **77**, 037001 (2008).
- [163] W. Li, E. R. Anderson, and R. J. Furnstahl, “Similarity renormalization group with novel generators,” *Phys. Rev. C* **84**, 054002 (2011).
- [164] N. M. Dicaire, C. Omand, and P. Navrátil, “Alternative similarity renormalization group generators in nuclear structure calculations,” *Phys. Rev. C* **90**, 034302 (2014).
- [165] E. Epelbaum, W. Glöckle, and U.-G. Meißner, “Improving the convergence of the chiral expansion for nuclear forces - II: Low phases and the deuteron,” *Eur. Phys. J. A* **19**, 401 (2004).

- [166] K. Hebeler, “Momentum-space evolution of chiral three-nucleon forces,” *Phys. Rev. C* **85**, 021002(R) (2012).
- [167] K. Hebeler, J. D. Holt, J. Menéndez, and A. Schwenk, “Nuclear Forces and Their Impact on Neutron-Rich Nuclei and Neutron-Rich Matter,” *Annu. Rev. Nucl. Part. Sci.* **65**, 457 (2015).
- [168] T. G. Kolda and B. W. Bader, “Tensor Decompositions and Applications,” *SIAM Rev.* **51**, 455 (2009).
- [169] A. Tichai, J. Ripoché, and T. Duguet, “Pre-processing the nuclear many-body problem,” *Eur. Phys. J. A* **55**, 90 (2019).
- [170] A. Tichai, R. Schutski, G. E. Scuseria, and T. Duguet, “Tensor-decomposition techniques for *ab initio* nuclear structure calculations: From chiral nuclear potentials to ground-state energies,” *Phys. Rev. C* **99**, 034320 (2019).
- [171] A. Tichai, P. Arthuis, K. Hebeler, M. Heinz, J. Hoppe, and A. Schwenk, “Low-rank matrix decompositions for *ab initio* nuclear structure,” *Phys. Lett. B* **821**, 136623 (2021).
- [172] G. F. Bertsch, B. Sabbey, and M. Uusnäkki, “Fitting theories of nuclear binding energies,” *Phys. Rev. C* **71**, 054311 (2005).
- [173] B. A. Brown and W. A. Richter, “New “USD” Hamiltonians for the *sd* shell,” *Phys. Rev. C* **74**, 034315 (2006).
- [174] Y. Jaganathen, R. M. I. Betan, N. Michel, W. Nazarewicz, and M. Płoszajczak, “Quantified Gamow shell model interaction for *psd*-shell nuclei,” *Phys. Rev. C* **96**, 054316 (2017).
- [175] J. M. R. Fox, C. W. Johnson, and R. Navarro Pérez, “Uncertainty quantification of an empirical shell-model interaction using principal component analysis,” *Phys. Rev. C* **101**, 054308 (2020).
- [176] S. N. More, S. K. Bogner, and R. J. Furnstahl, “Scale dependence of deuteron electrodisintegration,” *Phys. Rev. C* **96**, 054004 (2017).
- [177] L. M. Robledo and G. F. Bertsch, “Global systematics of octupole excitations in even-even nuclei,” *Phys. Rev. C* **84**, 054302 (2011).
- [178] S. K. Bogner, R. J. Furnstahl, S. Ramanan, and A. Schwenk, “Convergence of the Born series with low-momentum interactions,” *Nucl. Phys. A* **773**, 203 (2006).
- [179] S. Ramanan, S. K. Bogner, and R. J. Furnstahl, “Weinberg eigenvalues and pairing with low-momentum potentials,” *Nucl. Phys. A* **797**, 81 (2007).
- [180] C. Eckart and G. Young, “The approximation of one matrix by another of lower rank,” *Psychometrika* **1**, 211 (1936).
- [181] H. Hergert, S. K. Bogner, T. D. Morris, S. Binder, A. Calci, J. Langhammer, and R. Roth, “*Ab initio* multireference in-medium similarity renormalization group calculations of even calcium and nickel isotopes,” *Phys. Rev. C* **90**, 041302(R) (2014).
- [182] N. M. Parzuchowski, T. D. Morris, and S. K. Bogner, “*Ab initio* excited states from the in-medium similarity renormalization group,” *Phys. Rev. C* **95**, 044304 (2017).
- [183] J. C. Slater, “The Theory of Complex Spectra,” *Phys. Rev.* **34**, 1293 (1929).

- [184] S. K. Bogner, R. J. Furnstahl, and A. Schwenk, "From low-momentum interactions to nuclear structure," *Prog. Part. Nucl. Phys.* **65**, 94 (2010).
- [185] W. Kutzelnigg and D. Mukherjee, "Normal order and extended Wick theorem for a multiconfiguration reference wave function," *J. Chem. Phys.* **107**, 432 (1997).
- [186] L. Kong, M. Nooijen, and D. Mukherjee, "An algebraic proof of generalized Wick theorem," *J. Chem. Phys.* **132**, 234107 (2010).
- [187] G. C. Wick, "The Evaluation of the Collision Matrix," *Phys. Rev.* **80**, 268 (1950).
- [188] A. Szabo and N. Ostlund, *Modern Quantum Chemistry: Introduction to Advanced Electronic Structure Theory*, Dover Books on Chemistry (Dover Publications, 1989).
- [189] R. R. Whitehead, A. Watt, B. J. Cole, and I. Morrison, "Computational Methods for Shell-Model Calculations," in *Advances in nuclear physics* (Springer US, Boston, MA, 1977), pp. 123–176.
- [190] E. Gebrerufael, A. Calci, and R. Roth, "Open-shell nuclei and excited states from multireference normal-ordered Hamiltonians," *Phys. Rev. C* **93**, 031301(R) (2016).
- [191] F. Coester, "Bound states of a many-particle system," *Nucl. Phys.* **7**, 421 (1958).
- [192] F. Coester and H. Kümmel, "Short-range correlations in nuclear wave functions," *Nucl. Phys.* **17**, 477 (1960).
- [193] J. Čížek, "On the Correlation Problem in Atomic and Molecular Systems. Calculation of Wavefunction Components in Ursell-Type Expansion Using Quantum-Field Theoretical Methods," *J. Chem. Phys.* **45**, 4256 (1966).
- [194] J. Čížek, "On the Use of the Cluster Expansion and the Technique of Diagrams in Calculations of Correlation Effects in Atoms and Molecules," in *Advances in chemical physics: correlation effects in atoms and molecules, volume 14* (John Wiley & Sons, Inc., 1969), p. 35.
- [195] K. Kowalski, D. J. Dean, M. Hjorth-Jensen, T. Papenbrock, and P. Piecuch, "Coupled Cluster Calculations of Ground and Excited States of Nuclei," *Phys. Rev. Lett.* **92**, 132501 (2004).
- [196] G. Hagen, D. J. Dean, M. Hjorth-Jensen, T. Papenbrock, and A. Schwenk, "Benchmark calculations for ^3H , ^4He , ^{16}O and ^{40}Ca with *ab initio* coupled-cluster theory," *Phys. Rev. C* **76**, 044305 (2007).
- [197] R. J. Bartlett, J. D. Watts, S. A. Kucharski, and J. Noga, "Non-iterative fifth-order triple and quadruple excitation energy corrections in correlated methods," *Chem. Phys. Lett.* **165**, 513 (1990).
- [198] A. G. Taube and R. J. Bartlett, "Improving upon CCSD(T): ACCSD(T). I. Potential energy surfaces," *J. Chem. Phys.* **128**, 044110 (2008).
- [199] I. Shavitt and R. J. Bartlett, *Many-Body Methods in Chemistry and Physics: MBPT and Coupled-Cluster Theory*, Cambridge Molecular Science (Cambridge University Press, 2009).
- [200] J. Goldstone, "Derivation of the Brueckner many-body theory," *Proc. Math. Phys. Eng. Sci.* **239**, 267 (1957).
- [201] P. D. Stevenson, "Automatic generation of vacuum amplitude many-body perturbation series," *Int. J. Mod. Phys. C* **14**, 1135 (2003).

- [202] P. Arthuis, T. Duguet, A. Tichai, R.-D. Lasserri, and J.-P. Ebran, “ADG: Automated generation and evaluation of many-body diagrams I. Bogoliubov many-body perturbation theory,” *Comput. Phys. Commun.* **240**, 202 (2019).
- [203] P. Arthuis, A. Tichai, J. Ripoché, and T. Duguet, “ADG: Automated generation and evaluation of many-body diagrams II. Particle-number projected Bogoliubov many-body perturbation theory,” *Comput. Phys. Commun.* **261**, 107677 (2021).
- [204] A. Tichai, P. Arthuis, H. Hergert, and T. Duguet, *ADG: Automated generation and evaluation of many-body diagrams III. Bogoliubov in-medium similarity renormalization group formalism*, 2021, [arXiv:2102.10889](https://arxiv.org/abs/2102.10889).
- [205] A. Tichai, R. Wirth, J. Ripoché, and T. Duguet, <https://github.com/radnut/amc>, [10.5281/zenodo.3663059](https://zenodo.org/record/3663059) (2020).
- [206] A. Tichai, R. Wirth, J. Ripoché, and T. Duguet, “Symmetry reduction of tensor networks in many-body theory I. Automated symbolic evaluation of $SU(2)$ algebra,” *Eur. Phys. J. A* **56**, 272 (2020).
- [207] R. Roth and J. Langhammer, “Padé-resummed high-order perturbation theory for nuclear structure calculations,” *Phys. Lett. B* **683**, 272 (2010).
- [208] J. Langhammer, R. Roth, and C. Stumpf, “Spectra of open-shell nuclei with Padé-resummed degenerate perturbation theory,” *Phys. Rev. C* **86**, 054315 (2012).
- [209] L. Coraggio, J. W. Holt, N. Itaco, R. Machleidt, L. E. Marcucci, and F. Sammarruca, “Nuclear-matter equation of state with consistent two- and three-body perturbative chiral interactions,” *Phys. Rev. C* **89**, 044321 (2014).
- [210] C. Wellenhofer, J. W. Holt, and N. Kaiser, “Divergence of the isospin-asymmetry expansion of the nuclear equation of state in many-body perturbation theory,” *Phys. Rev. C* **93**, 055802 (2016).
- [211] C. Drischler, K. Hebeler, and A. Schwenk, “Asymmetric nuclear matter based on chiral two- and three-nucleon interactions,” *Phys. Rev. C* **93**, 054314 (2016).
- [212] J. W. Holt and N. Kaiser, “Equation of state of nuclear and neutron matter at third-order in perturbation theory from chiral EFT,” *Phys. Rev. C* **95**, 034326 (2017).
- [213] G. Hagen, T. Papenbrock, D. J. Dean, A. Schwenk, A. Nogga, M. Włoch, and P. Piecuch, “Coupled-cluster theory for three-body Hamiltonians,” *Phys. Rev. C* **76**, 034302 (2007).
- [214] R. Roth, S. Binder, K. Vobig, A. Calci, J. Langhammer, and P. Navrátil, “Medium-Mass Nuclei with Normal-Ordered Chiral NN+3N Interactions,” *Phys. Rev. Lett.* **109**, 052501 (2012).
- [215] T. D. Morris, “*Systematic improvements of ab-initio in-medium similarity renormalization group calculations*,” *PhD thesis (Michigan State University, East Lansing, 2016)* (2016).
- [216] C. Runge, “Ueber die numerische Auflösung von Differentialgleichungen,” *Math. Ann.* **46**, 167 (1895).
- [217] W. Kutta, “Beitrag zur näherungsweise Integration totaler Differentialgleichungen,” *Z. Math. Phys.* **46**, 435 (1901).
- [218] J. C. Butcher, *Numerical methods for ordinary differential equations* (Wiley, 2016).

- [219] S. R. White, “Numerical canonical transformation approach to quantum many-body problems,” *J. Chem. Phys.* **117**, 7472 (2002).
- [220] J. Ripoché, A. Tichai, and T. Duguet, “Normal-ordered k -body approximation in particle-number-breaking theories,” *Euro. Phys. Jour. A* **56**, 02 (2020).
- [221] M. Frosini, T. Duguet, B. Bally, Y. Beaujeault-Taupère, J.-P. Ebran, and V. Somà, “In-medium k -body reduction of n -body operators,” *Eur. Phys. J. A* **57**, 151 (2021).
- [222] D. A. Varshalovich, A. N. Moskalev, and V. K. Khersonskii, *Quantum Theory Of Angular Momentum* (World Scientific, Singapore, 1988).
- [223] S. P. Pandya, “Nucleon-Hole Interaction in jj Coupling,” *Phys. Rev.* **103**, 956 (1956).
- [224] L. L. Foldy and S. A. Wouthuysen, “On the Dirac Theory of Spin 1/2 Particles and Its Non-Relativistic Limit,” *Phys. Rev.* **78**, 29 (1950).
- [225] J. D. Bjorken and S. D. Drell, *Relativistic quantum mechanics*, International series in pure and applied physics (1964).
- [226] J. L. Friar, J. Martorell, and D. W. L. Sprung, “Nuclear sizes and the isotope shift,” *Phys. Rev. A* **56**, 4579 (1997).
- [227] A. Ong, J. C. Berengut, and V. V. Flambaum, “Effect of spin-orbit nuclear charge density corrections due to the anomalous magnetic moment on halonuclei,” *Phys. Rev. C* **82**, 014320 (2010).
- [228] R. Pohl, A. Antognini, F. Nez, F. D. Amaro, F. Biraben, J. M. R. Cardoso, D. S. Covita, A. Dax, S. Dhawan, L. M. P. Fernandes, *et al.*, “The size of the proton,” *Nature* **466**, 213 (2010).
- [229] R. Pohl, R. Gilman, G. A. Miller, and K. Pachucki, “Muonic Hydrogen and the Proton Radius Puzzle,” *Ann. Rev. Nucl. Part. Sci.* **63**, 175 (2013).
- [230] P. J. Mohr, D. B. Newell, and B. N. Taylor, “CODATA recommended values of the fundamental physical constants: 2014,” *Rev. Mod. Phys.* **88**, 035009 (2016).
- [231] A. Beyer, L. Maisenbacher, A. Matveev, R. Pohl, K. Khabarova, A. Grinin, T. Lamour, D. C. Yost, T. W. Hänsch, N. Kolachevsky, *et al.*, “The Rydberg constant and proton size from atomic hydrogen,” *Science* **358**, 79 (2017).
- [232] N. Bezginov, T. Valdez, M. Horbatsch, A. Marsman, A. C. Vutha, and E. A. Hessels, “A measurement of the atomic hydrogen Lamb shift and the proton charge radius,” *Science* **365**, 1007 (2019).
- [233] W. Xiong, A. Gasparian, H. Gao, D. Dutta, M. Khandaker, N. Liyanage, E. Pasyuk, C. Peng, X. Bai, L. Ye, *et al.*, “A small proton charge radius from an electron–proton scattering experiment,” *Nature* **575**, 147 (2019).
- [234] J.-P. Karr, D. Marchand, and E. Voutier, “The proton size,” *Nat. Rev. Phys.* **2**, 601 (2020).
- [235] H. Gao and M. Vanderhaeghen, “The proton charge radius,” *Rev. Mod. Phys.* **94**, 015002 (2022).
- [236] W. Magnus, “On the exponential solution of differential equations for a linear operator,” *Commun. Pure Appl. Math.* **7**, 649 (1954).

- [237] T. D. Morris, N. M. Parzuchowski, and S. K. Bogner, “Magnus expansion and in-medium similarity renormalization group,” *Phys. Rev. C* **92**, 034331 (2015).
- [238] S. J. Novario, P. Gysbers, J. Engel, G. Hagen, G. R. Jansen, T. D. Morris, P. Navrátil, T. Papenbrock, and S. Quaglioni, “Coupled-Cluster Calculations of Neutrinoless Double- β Decay in ^{48}Ca ,” *Phys. Rev. Lett.* **126**, 182502 (2021).
- [239] M. Miorelli, S. Bacca, G. Hagen, and T. Papenbrock, “Computing the dipole polarizability of ^{48}Ca with increased precision,” *Phys. Rev. C* **98**, 014324 (2018).
- [240] S. Kaufmann, J. Simonis, S. Bacca, J. Billowes, M. L. Bissell, K. Blaum, B. Cheal, R. F. G. Ruiz, W. Gins, C. Gorges, *et al.*, “Charge Radius of the Short-Lived ^{68}Ni and Correlation with the Dipole Polarizability,” *Phys. Rev. Lett.* **124**, 132502 (2020).
- [241] M. Heinz, A. Tichai, J. Hoppe, K. Hebeler, and A. Schwenk, “In-medium similarity renormalization group with three-body operators,” *Phys. Rev. C* **103**, 044318 (2021).
- [242] Y. S. Lee, S. A. Kucharski, and R. J. Bartlett, “A coupled cluster approach with triple excitations,” *J. Chem. Phys.* **81**, 5906 (1984).
- [243] W. Kutzelnigg, “Error analysis and improvements of coupled-cluster theory,” *Theor. Chim. Acta* **80**, 349 (1991).
- [244] J. D. Watts and R. J. Bartlett, “Economical triple excitation equation-of-motion coupled-cluster methods for excitation energies,” *Chem. Phys. Lett.* **233**, 81 (1995).
- [245] S. Binder, P. Piecuch, A. Calci, J. Langhammer, P. Navrátil, and R. Roth, “Extension of coupled-cluster theory with a noniterative treatment of connected triply excited clusters to three-body Hamiltonians,” *Phys. Rev. C* **88**, 054319 (2013).
- [246] S. R. Stroberg, *IMSRG with flowing 3N operators*, talk given at TRIUMF Workshop: Progress in *Ab Initio* Techniques in Nuclear Physics, 2020.
- [247] S. R. Stroberg, <https://github.com/ragnarstroberg/imsrg> (Nov 23, 2019).
- [248] A. Tichai, P. Arthuis, K. Hebeler, M. Heinz, J. Hoppe, A. Schwenk, and L. Zurek, in prep., (2022).
- [249] M. A. Caprio, P. Maris, and J. P. Vary, “Coulomb-Sturmian basis for the nuclear many-body problem,” *Phys. Rev. C* **86**, 034312 (2012).
- [250] A. Tichai, J. Müller, K. Vobig, and R. Roth, “Natural orbitals for *ab initio* no-core shell model calculations,” *Phys. Rev. C* **99**, 034321 (2019).
- [251] G. Hagen, T. Papenbrock, and D. J. Dean, “Solution of the Center-Of-Mass Problem in Nuclear Structure Calculations,” *Phys. Rev. Lett.* **103**, 062503 (2009).
- [252] J. Hoppe, A. Tichai, M. Heinz, K. Hebeler, and A. Schwenk, “Natural orbitals for many-body expansion methods,” *Phys. Rev. C* **103**, 014321 (2021).
- [253] A. Nogga, P. Navrátil, B. R. Barrett, and J. P. Vary, “Spectra and binding energy predictions of chiral interactions for ^7Li ,” *Phys. Rev. C* **73**, 064002 (2006).
- [254] J. Simonis, “*Ab initio* calculations of nuclei using chiral interactions with realistic saturation properties,” PhD thesis (Technische Universität Darmstadt 2017).
- [255] J. Langhammer, “*Chiral Three-Nucleon Interactions in Ab-Initio Nuclear Structure and Reactions*,” PhD thesis (Technische Universität Darmstadt 2014).

- [256] P. J. Hay, “On the calculation of natural orbitals by perturbation theory,” *J. Chem. Phys.* **59**, 2468 (1973).
- [257] A. K. Q. Siu and E. F. Hayes, “Configuration interaction procedure based on the calculation of perturbation theory natural orbitals: Applications to H₂ and LiH,” *J. Chem. Phys.* **61**, 37 (1974).
- [258] M. R. Strayer, W. H. Bassichis, and A. K. Kerman, “Correlation Effects in Nuclear Densities,” *Phys. Rev. C* **8**, 1269 (1973).
- [259] A. Carbone, A. Cipollone, C. Barbieri, A. Rios, and A. Polls, “Self-consistent Green’s functions formalism with three-body interactions,” *Phys. Rev. C* **88**, 054326 (2013).
- [260] C. Constantinou, M. A. Caprio, J. P. Vary, and P. Maris, “Natural orbital description of the halo nucleus ⁶He,” *Nucl. Sci. Tech.* **28**, 179 (2017).
- [261] S. B. Khadkikar and V. B. Kamble, “Centre of mass motion and single particle separation energies in Hartree-Fock theory,” *Nucl. Phys. A* **225**, 352 (1974).
- [262] L. Jaqua, M. A. Hasan, J. P. Vary, and B. R. Barrett, “Kinetic-energy operator in the effective shell-model interaction,” *Phys. Rev. C* **46**, 2333 (1992).
- [263] H. Hergert and R. Roth, “Treatment of the intrinsic Hamiltonian in particle-number nonconserving theories,” *Phys. Lett. B* **682**, 27 (2009).
- [264] E. Gebrerufael, K. Vobig, H. Hergert, and R. Roth, “*Ab Initio* Description of Open-Shell Nuclei: Merging No-Core Shell Model and In-Medium Similarity Renormalization Group,” *Phys. Rev. Lett.* **118**, 152503 (2017).
- [265] R. J. Furnstahl, “The Renormalization Group in Nuclear Physics,” *Nucl. Phys. Proc. Suppl.* **228**, 139 (2012).
- [266] M. S. Gordon, M. W. Schmidt, G. M. Chaban, K. R. Glaesemann, W. J. Stevens, and C. Gonzalez, “A natural orbital diagnostic for multiconfigurational character in correlated wave functions,” *J. Chem. Phys.* **110**, 4199 (1999).
- [267] I. Angeli and K. P. Marinova, “Table of experimental nuclear ground state charge radii: An update,” *At. Data Nucl. Data Tables* **99**, 69 (2013).
- [268] P. Hohenberg and W. Kohn, “Inhomogeneous Electron Gas,” *Phys. Rev.* **136**, B864 (1964).
- [269] W. Kohn and L. J. Sham, “Self-Consistent Equations Including Exchange and Correlation Effects,” *Phys. Rev.* **140**, A1133 (1965).
- [270] E. Chabanat, P. Bonche, P. Haensel, J. Meyer, and R. Schaeffer, “A Skyrme parametrization from subnuclear to neutron star densities Part II. Nuclei far from stabilities,” *Nucl. Phys. A* **635**, 231 (1998); *ibid.* **643**, 441(E) (1998).
- [271] M. Bender, P.-H. Heenen, and P.-G. Reinhard, “Self-consistent mean-field models for nuclear structure,” *Rev. Mod. Phys.* **75**, 121 (2003).
- [272] B. G. Carlsson, J. Dobaczewski, J. Toivanen, and P. Veselý, “Solution of self-consistent equations for the N³LO nuclear energy density functional in spherical symmetry. The program HOSPHE (v1.02),” *Comput. Phys. Commun.* **181**, 1641 (2010).
- [273] P. H. Garthwaite, F. Critchley, K. Anaya-Izquierdo, and E. Mubwandarikwa, “Orthogonalization of vectors with minimal adjustment,” *Biometrika* **99**, 787 (2012).

- [274] F. Bonaiti, S. Bacca, and G. Hagen, “*Ab initio* coupled-cluster calculations of ground and dipole excited states in ^8He ,” *Phys. Rev. C* **105**, 034313 (2022).
- [275] S. Malbrunot-Ettenauer, S. Kaufmann, S. Bacca, C. Barbieri, J. Billowes, M. L. Bissell, K. Blaum, B. Cheal, T. Duguet, R. F. G. Ruiz, *et al.*, “Nuclear Charge Radii of the Nickel Isotopes $^{58-68,70}\text{Ni}$,” *Phys. Rev. Lett.* **128**, 022502 (2022).
- [276] A. Porro, V. Somà, A. Tichai, and T. Duguet, “Importance truncation in non-perturbative many-body techniques,” *Eur. Phys. J. A* **57**, 297 (2021).
- [277] T. Papenbrock and D. J. Dean, “Density matrix renormalization group and wavefunction factorization for nuclei,” *J. Phys. G: Nucl. Part. Phys.* **31**, S1377 (2005).
- [278] B. Zhu, R. Wirth, and H. Hergert, “Singular value decomposition and similarity renormalization group evolution of nuclear interactions,” *Phys. Rev. C* **104**, 044002 (2021).
- [279] J. Hoppe, A. Tichai, M. Heinz, K. Hebeler, and A. Schwenk, “Importance truncation for the in-medium similarity renormalization group,” *Phys. Rev. C* **105**, 034324 (2022).
- [280] R. Roth and P. Navrátil, “*Ab Initio* Study of ^{40}Ca with an Importance-Truncated No-Core Shell Model,” *Phys. Rev. Lett.* **99**, 092501 (2007).
- [281] Z. Rolik, Á. Szabados, and P. R. Surján, “On the perturbation of multiconfiguration wave functions,” *J. Chem. Phys.* **119**, 1922 (2003).
- [282] P. R. Surján, Z. Rolik, Á. Szabados, and D. Köhalmi, “Partitioning in multiconfiguration perturbation theory,” *Ann. Phys.* **13**, 223 (2004).
- [283] C. W. Johnson, W. E. Ormand, K. S. McElvain, and H. Shan, *BIGSTICK: A flexible configuration-interaction shell-model code*, 2018, [arXiv:1801.08432](https://arxiv.org/abs/1801.08432).
- [284] C. Sanderson and R. Curtin, “Armadillo: a template-based C++ library for linear algebra,” *J. Open Source Softw.* **1**, 26 (2016).
- [285] C. Sanderson and R. Curtin, “A User-Friendly Hybrid Sparse Matrix Class in C++,” in *Mathematical Software – ICMS 2018*, edited by J. H. Davenport, M. Kauers, G. Labahn, and J. Urban (2018), p. 422.
- [286] K. Hebeler and A. Schwenk, “Chiral three-nucleon forces and neutron matter,” *Phys. Rev. C* **82**, 014314 (2010).
- [287] J. W. Holt, N. Kaiser, and W. Weise, “Density-dependent effective nucleon-nucleon interaction from chiral three-nucleon forces,” *Phys. Rev. C* **81**, 024002 (2010).
- [288] I. Talmi, “Nuclear spectroscopy with harmonic-oscillator wave functions,” *Helv. Phys. Acta* **25**, 185 (1952).
- [289] M. Moshinsky, “Transformation brackets for harmonic oscillator functions,” *Nucl. Phys.* **13**, 104 (1959).
- [290] G. P. Kamuntavičius, R. K. Kalinauskas, B. R. Barrett, S. Mickevičius, and D. Germanas, “The general harmonic-oscillator brackets: compact expression, symmetries, sums and Fortran code,” *Nucl. Phys. A* **695**, 191 (2001).
- [291] R. Roth, A. Calci, J. Langhammer, and S. Binder, “Evolved chiral NN+3N Hamiltonians for *ab initio* nuclear structure calculations,” *Phys. Rev. C* **90**, 024325 (2014).

Acknowledgments

I want to express my deepest gratitude to my supervisor Achim Schwenk for his constant support from my Bachelors degree on and for offering me the possibility to do my PhD in his group. His outstanding knowledge of physics and always encouraging attitude were an integral part for the success of the work presented in this thesis. Thank you for numerous fruitful discussion and for always pointing out new points of view. Moreover, I am thankful for the awesome possibilities of traveling, visiting conferences, summer schools, and workshops, this really was something special for me.

I am deeply grateful to Kai Hebler for always making time and promoting me with his profound physics understanding. Thank you for multiple prolific discussions about physics and many other topics beyond that. May the canteen portions increase some day and you always find some Carolina Reaper to add to your curry.

A special thanks goes to Matthias Heinz and Alex Tichai for countless fruitful discussions and strong collaboration. Thank you for the productive working environment you produced with your in-depth understanding of physics and computational problems, as well as for pushing *ab initio* theory applications in our small local many-body group.

I would like to thank my office mates Marco Knöll, Julius Müller, Rodric Seutin, and Lars Zurek for creating a fun and productive office atmosphere. Lars and Rodric thank you for the wonderful time we had in China and Vancouver, learning new things, discovering new places, and getting to know new people. I always enjoyed our small discussions and that we kept them alive even in complicated pandemic times. Lars, thank you for always sharing an apartment with me, being a perfect room mate, and the great time in Trento. Rodric, thank you for all the discussions and talks over small walks or coffee breaks and for being friends outside of work.

During the writing process of this thesis, I received helpful feedback and comments from Pierre Arthuis, Christian Drischler, Matthias Heinz, Alexander Tichai, Rodric Seutin, and Lars Zurek. Thank you for your careful proofreading and multiple improvements of this thesis. Additionally, I received helpful comments from Kai Hebler and Achim Schwenk.

Moreover, I would like to thank all former and current members of the strongint group I had the pleasure to get to know or work together with. You all contributed to a very nice and familiar atmosphere during multiple trips, rehearsal sessions, and group events. I am very happy to be a part of this group.

My thank goes to Christian Drischler for supporting me already during my Bachelors thesis and staying in touch even after. I appreciated our remote Christmas markets and hope we continue this tradition.

I would also like to express my gratitude to Johannes Simonis, who kindly shared his sound knowledge about the IMSRG code and his transformation codes with me. Thank you for being open for questions and providing me with all the skills and tools to execute calculations and introducing me to the computational aspects of the IMSRG.

I want to thank Stephanie Müller, for taking care of all the administration and making processes and communication so effortless.

I am grateful for being supported by the Deutsche Forschungsgemeinschaft (DFG, German Research Foundation) – Project-ID 279384907 – SFB 1245.

I would like to thank my family for their constant encouragement, especially my mother and brother for always offering me a place where I feel at home and can come to rest.

Last but definitely not least, I am deeply grateful to Julia for always having my back and for her continuous support. Thank you for motivating and encouraging me even in difficult times, for putting up with my moods when I was hungry or something didn't work out as planned, and for being my beloved partner and best friend. Bis zum Ende des Universums...

Erklärung zur Dissertation

Gemäß §9 Promotionsordnung:

Hiermit versichere ich, dass ich die vorliegende Dissertation selbstständig angefertigt und keine anderen als die angegebenen Quellen und Hilfsmittel verwendet habe. Alle wörtlichen und paraphrasierten Zitate wurden angemessen kenntlich gemacht. Die Arbeit hat bisher noch nicht zu Prüfungszwecken gedient.

Darmstadt, den 9. Mai 2022

(Jan Hoppe)